Turkish Journal of Civil Engineering

formerly
Teknik Dergi

Turkish Journal of Civil Engineering (formerly Teknik Dergi) Publication Principles

Turkish Journal of Civil Engineering (TJCE), a non-profit, open access scientific and technical periodical of UCTEA Chamber of Civil Engineers, publishes papers reporting original research work and major projects of interest in the area of civil engineering. TJCE annually publishes six issues and is open to papers in English and Turkish. It should be noted that TJCE (formerly, Teknik Dergi/ Technical Journal of Turkish Chamber of Civil Engineers) is being published regularly for more than 30 years since 1990. Main publication principles of TJCE are summarized below:

1. Articles reporting original scientific research and those reflecting interesting engineering applications are accepted for publication. To be classified as original, the work should either produce new scientific knowledge or add a genuinely new dimension to the existing knowledge or develop a totally new method or substantially improve an existing method.

2. Articles reporting preliminary results of scientific studies and those which do not qualify as full articles but provide useful information for the reader can be considered for publication as technical notes.

3. Discussions received from the readers of the published articles within three months from publication are reviewed by the Editorial Board and then published together with the closing remarks of the author.

4. Manuscripts submitted for publication are evaluated by two or three reviewers unknown to the authors. In the light of their reports, final decision to accept or decline is taken by the Editorial Board. General policy of the Board is to get the insufficient manuscripts improved in line with the reviewers' proposals. Articles that fail to reach the desired level are declined. Reasons behind decisions are not declared.

5. A signed statement is taken from the authors, declaring that the article has not been published as a "journal article or book chapter". In case the Editorial Board is in the opinion that the article has already been published elsewhere with minor changes or suspects plagiarism or a similar violation of ethics, then not only that article, but none of the articles of the same authors are published.

6. Papers reporting works presented as conference papers and developed further may be considered for publication. The conference it was presented to is given as a footnote in the first page.

7. Additionally, a document signed by all authors, transferring the copyright to UCTEA Chamber of Civil Engineers is submitted together with the manuscript.

Turkish Journal of Civil Engineering

(formerly Teknik Dergi)

Reviewers:

This list is renewed each year and includes reviewers who served in the last two years of publication.

Turkish Journal of Civil Engineering (formerly Teknik Dergi)

Volume 34   Issue 3   May 2023

CONTENTS

RESEARCH ARTICLE

THE RECENT EARTHQUAKE DISASTER IN TURKEY

On February 6, 2023 two disastrous earthquakes, the first with a moment magnitude of 7.7 and the second with a magnitude of 7.6 occurred nine hours apart on two different faults in the East Anatolian Fault Zone within the boundaries of the province of Kahramanmaraş, Turkey. Besides more than fifty thousand lives lost, the two earthquakes and their aftershocks caused enormous material damage in the eleven provinces comprising the disaster area. We remember those who lost their lives, express our sympathies to their families and loved ones and wish quick recovery to the survivors.

The most recent disaster of comparable scale is the 1999 İzmit Earthquake of 7.4 magnitude, which caused around seventeen thousand casualties. At the time, it was presumed that the tragic experience of the İzmit Earthquake would serve as a lesson and a warning sign to the planners, designers and constructors in the field of civil engineering to improve their evidently deficient practices. Indeed, several new versions of the seismic code, each introducing stricter rules than the preceding one, were drafted in the years following the İzmit Earthquake. New legal documents were issued to improve the construction supervision system. Moreover, a variety of design software were developed. The quality of concrete and reinforcing steel has relatively improved as the result of recent technological advances.

Regrettably the preliminary reconnaissance reports indicate a rather heavy structural damage resembling that of the İzmit Earthquake. Besides other contributors, the Turkish civil engineering practice of the last two decades is also accountable for the damage. However, a fair criticism should also acknowledge the fact that the recent disaster was a combination of several earthquakes of enormous damaging power, stemming primarily from their exceptionally high spectral accelerations. It would be a fair judgement to observe the improvements in the structural performance since the İzmit disaster; however, they are still far from satisfactory.

Among other factors leading to deficiencies in the civil engineering practice, the following two appear to be the most critical:

1. Deterioration in civil engineering education: The standards of civil engineering education have been significantly lowered. Consequently, the number of civil engineering graduates has excessively increased at the cost of deterioration in their professional qualifications.

2. Failure to introduce a professional civil engineering system: The Higher Earthquake Council (Deprem Şurası, 2004) inspired by the İzmit Earthquake had firmly endorsed the introduction of a professional engineering system in Turkey. Despite tireless efforts of the Turkish Chamber of Civil Engineering, such a system could not be implemented.

Considering the need for a rapid information flow, the Turkish Journal of Civil Engineering decided to publish a special issue to disseminate the preliminary data on the Kahramanmaraş Earthquakes. The November 2023 issue will be devoted to this purpose. This special issue will include mainly technical notes of a descriptive nature which can be drafted in a short while and submitted soon. Naturally, full papers on the earthquakes will also be considered, provided they have the required solid scientific content. As required by the publication policy of the Turkish Journal of Civil Engineering, the papers in the special issue will have to be confined to the civil engineering aspect of the problem.

Best wishes,

Editorial Board, Turkish Journal of Civil Engineering

Building's Controlled Seismic Isolation by Using Upper Horizontal Dampers and Stiff Core

Kourosh TALEBI JOUNEGHANI[1]
Mahmood HOSSEINI[2]
Mohammad Sadegh ROHANIMANESH[3]
Morteza RAISSI[4]

ABSTRACT

The fundamental period of the seismically isolated buildings may be close to that of the long period pulses of near-field earthquakes, leading to very large lateral displacements in isolators, which in turn can considerably reduce the stability of isolators, increase the chance of collision of the isolated buildings to adjacent buildings, or even result in overturning of the isolated buildings. Therefore, it is important to control these types of buildings and reduce the amount of lateral displacement in their isolating system. In this study, by conducting a series of time history analyses for a set of five multi-story steel buildings with various numbers of stories from 3 to 14. Each building is considered to have a very stiff core structure and a set of crosswise viscous dampers, connecting the building structure to the core structure at the lowest and the top floors, as well as the same structures without the core structure and dampers. The effect of stiff core and dampers in reducing the lateral displacement at isolators has been shown. Results indicate that by the proposed technique, the lateral displacement of the base isolation system is significantly decreased particularly for low-rise buildings.

Keywords: Control of displacement, base-isolated structures, crosswise dissipators, central rigid support.

1 Department of Civil Engineering, Central Tehran Branch, Islamic Azad University, Tehran, Iran
  kou.talebijouneghani.eng@iauctb.ac.ir - https://orcid.org/0000-0003-4340-0381

2 Eastern Mediterranean University, Department of Civil Engineering, Famagusta, North Cyprus
  mahmood.hosseni@emu.edu.tr - https://orcid.org/0000-0003-3142-4087

3 Department of Civil Engineering, Central Tehran Branch, Islamic Azad University, Tehran, Iran
  m.s.rohanimanesh@iauctb.ac.ir - https://orcid.org/0000-0002-8426-8906

4 University of Science and Technology, Department of Civil Engineering, Tehran, Iran
  mraissi@iust.ac.ir - https://orcid.org/0000-0003-2364-1268

1. INTRODUCTION

Considering the significant interest in structurally controlling the base-isolated buildings, the fundamental model for a specific type of building was established in [1] and [2]. The eight-story building had a length of 82.4m and a width of 54.3m, a replica of a structure in Los Angeles. The model package is a result of the cooperative study between various researchers. Hence, a realistic and detailed 3D modelling was obtained for a base-isolated building model. Researchers could use an exact structural model to compare and design numerous control systems. Various controllers were utilized during the Engineering Mechanics Conference (Newark, Delaware, June 2004), and different investigators contributed to the benchmark study and provided their preliminary results [3–10].

Recognizing the importance of earthquake improvement and building retrofitting and attempts to achieve these goals is of great concern for many researchers. Seismic isolators and viscous dampers rank as two of the most effective solutions among these techniques. These gadgets differ from one another in that each has benefits and drawbacks. Dampers are tools for releasing energy generated by an earthquake inside a building. There are many different kinds of dampers, but viscous dampers are particularly popular because of their simple installation and extended lifespan [11–14].

Seismic isolators with significant lateral deformation capability support the building. When there is an earthquake, the column often bears the brunt of the displacements, with the rest of the building functioning more like a solid object oscillating with minor displacements. By extending the time and dampening the structure, installing an isolator causes seismic loads to decrease rather than improve the structure's bearing capability. Active, passive, and semi-active control systems, which employ techniques other than enhancing the structure's strength and capacity, might be noted among the methods for regulating the reaction of structures. They reduce the force on the structure during an earthquake. For example, vibration isolation systems increase the natural period and damping of the design and effectively reduce the force on the structure. This isolation is achieved by increasing the system's flexibility and providing proper damping. In this method, since the force of the earthquake is not supposed to enter the structure or a small part of it is transferred to the structure, it can be expected that the displacement of the floors will be reduced, the acceleration of the floor will be reduced, and the failures of the building and also the failures of the property will be significantly reduced. Moreover, fewer architectural problems will arise in the plans, and the cost of implementing huge structures will decrease due to the use of finer sections [15, 16]. According to the functioning of isolation systems, the use of these systems in soils with low shear wave velocity (soft), although they increase the damping of the entire system and, as a result, less energy is introduced into the structure, but due to the increase in the need to change the location that one of the main criteria for using these systems is that it always faces limitations. Therefore, the need to change location and move a lot in earthquakes near the fault due to the frequency content and special features of these records is one of the limitations of this system [17]. In recent years this issue may have been solved to some extent with additional dampers added to the isolation system, especially in bridges [18]. Wu et al. [19] studied the failure of structures on sandstone and mudstone. In another study [20], they numerically studied water inrush from rock strata separation space. However, the research on the effects of these dampers on isolated systems is one of the essential issues in this research on the damping effect of viscose add-on dampers in isolated structures. The seismic

isolation of buildings was aimed at saving the structure and avoiding damage to the contents, including its residents [21, 22]. The superstructure response is reduced by base isolation systems like elastomeric bearing systems and sliding.

However, the base displacements were increased in near-fault earthquakes. Recently, many studies have been devoted to limiting bearing displacements. Protecting the base-isolated buildings from long-period and intense pulses in near-field earthquakes is challenging. Heaton et al. [23] showed that large drifts were observed in a near-field earthquake in a base-isolated building. Rupture or buckling of the isolation bearings was noted when the structure was subject to a strong earthquake [24, 25]. However, isolator displacements are reduced by large damping levels in the fundamental mode since forces are imparted into the structure, thus, increasing the structural deformations and accelerations in higher modes [26, 27]. Different kinds of systems were proposed to address the requirement for higher damping and limit the low damping and isolation drift to enhance the isolation effectiveness at higher frequencies.

Detailed reviews have been provided on the studies on structural response control [28-33]. In active structural control, the control force is straightly exerted on the model in terms of a definite algorithm. For this purpose, to obtain certain response control objectives under the device capacity limitation, state estimation or response measurements are used along with direct actuation tools (hydraulic actuators). Among other benefits of active control systems are applicability to multi-risk situations (such as wind and earthquakes), relative insensitivity to site circumstances and ground motions, and selectivity of control objectives like safety during severe dynamic loading and human comfort during non-critical times. Wu et al. [34] studied the deformation and failure of structures using convolutional neural networks.

Seismic excitations are traditionally ignored or assumed as white noise in designing optimal active control systems. Therefore, it is impossible to guarantee these 'optimal' controllers' optimality while existing seismic excitations have significant pulse performance. Yang [35] recommended designing controllers in terms of the augmented system, including the filter and the structure, to model filtered white noise. He used the same method to control the nonlinear hysteretic structures [36]. Various studies propose other structural control methods [37-45]. Optimal structural control was proposed by Panariello et al. [46] by conducting an experiment using artificial neural networks. In order to design a smart base isolation system, Yoshioka et al. [47] and Ramallo et al. [48] modelled the earthquake excitations by using Kanai–Tajimi filter [49]. For the input shaping filter, the recorded earthquake's PSD is fitted with a second-order transfer function to obtain the transfer function. The shaping filter of Kanai–Tajimi was employed by Ramallo et al. to model the ground. Thus, the structural excitation augmented system is obtained to design an MR damper controller. Using filters from [50] for modelling input excitation was proved to be the overall result. However, these filters overestimated the energy within the lower frequency range while affecting the longer-period structures' response. Nagarajaiah and Narasimhan [2] proposed a modified model [38]. A lower overestimating is achieved for energy by the modified model within the lower range of frequency in comparison with the original model. He [51] and He and Agrawal [52] proposed an analytical model for control systems in near-field ground motions [53]. He and Agrawal extensively studied the use of the analytical pulse model for the benchmark cable-stayed bridge model [54]. A frequency-domain pulse filter was established by converting the analytical pulse model in the Laplace domain. An active pulse filter (APF) controller can be

designed by further augmentation of the pulse filter into state-space form through the structural system [55]. APF (Active Pulse Filter) is the name of the active controller. To conduct a parametric study independent of noise disturbances, the measurement of noise disturbances hasn't been considered when designing and simulating controllers in this paper. APF controllers are however investigated in [55-57] for their effects on white noise disturbances. APF controllers have been shown to be robust according to simulation results in the benchmark package for base-isolated buildings [2].

A previous study determined that weighting parameters in semi-active and active control algorithms such as Linear Quadratic Regulators (LQR) and H2/LQG are constant during earthquake loading, while in the MH2/LQG control algorithm, a variable weighting parameter is considered at each time step for the purpose of designing the semi-active control system and determining appropriate damper forces for the MR. The MH2/LQG control algorithm adjusts the weighting parameter at time steps where the MR damper is not required to apply excessive damping forces to the structure in order to prevent this.

According to some seismologists, buildings that are isolated from the base may be subject to significant impulsive ground movements that are produced by nearby faults. Large insulator displacements caused by long-period pulses linked to movement near the fault might cause the buildings that are separated from the base to operate poorly. Researchers were quite interested in this, and lately, several studies have been published on the dynamic behavior of base-insulated structures during near-fault motions [58]. It has been shown that bearing displacements in near-fault motions can be quite considerable, which can cause the isolation system to become unstable. According to the research above, the LRB (Lead Rubber Bearings) system's performance with specific attributes was unsuitable for movements close to faults. Since the LRB system is a popular isolation system with all the features needed for fundamental isolation, it is important to research how the LRB system behaves dynamically and what its best settings are when the fault is moving [58].

This study presents the method of using four cross-horizontal viscous dampers at the level of the roof of the structures, which is connected to a rigid central core in the center of the structures. Also, they are equipped with seismic isolators to restrain the lateral displacement of the structures under the effect of pulses in the near field.

2. MODULATION

In this research, five types of 3, 5, 8, 11, and 14-story steel bending frame structures with Chevron braces with square plans have been designed using ETABS 2016 software using the LRFD method. Then, for each building, rigid concrete central support structure was designed using ETABS 2016 software and transferred to the Perform3D simulator software.

Then, in this software, base isolators and specific horizontal viscous dampers are added to the structures. Each type of building is divided into two categories. The first category is equipped with a base isolator without a hard-central support structure, and the second category is equipped with a base isolator with a hard-central support structure. These structures have been subjected to nonlinear dynamic analysis under seven distant and seven near-earth records. The outputs of all structures have been examined, and the following results have been obtained.

2.1. Designing the Structures

All the structures have a Chevron brace and have a yard to establish the supportive structures. The design of the structures was performed by the AISC 360-05 [59] LRFD technique and UBC-97 in ETABS 2016 Provided Seismic zone factor (Z) =0.4. The load combinations under Strength level (U) =1.2D+0.5L+E were used, where D, L and E are dead load, live load, and lateral load, respectively. Site soil profile types are (stiff soil profile) by the shear wave velocity 180 to 360 meter/second. ST37 type steel is used for all structures with 370 mega Pascal ultimate tensile strength. They were then transported to PERFORM3D to analyze the nonlinear time history. The types of structures are shown in Fig. 1, and the section properties are given in Table 1.
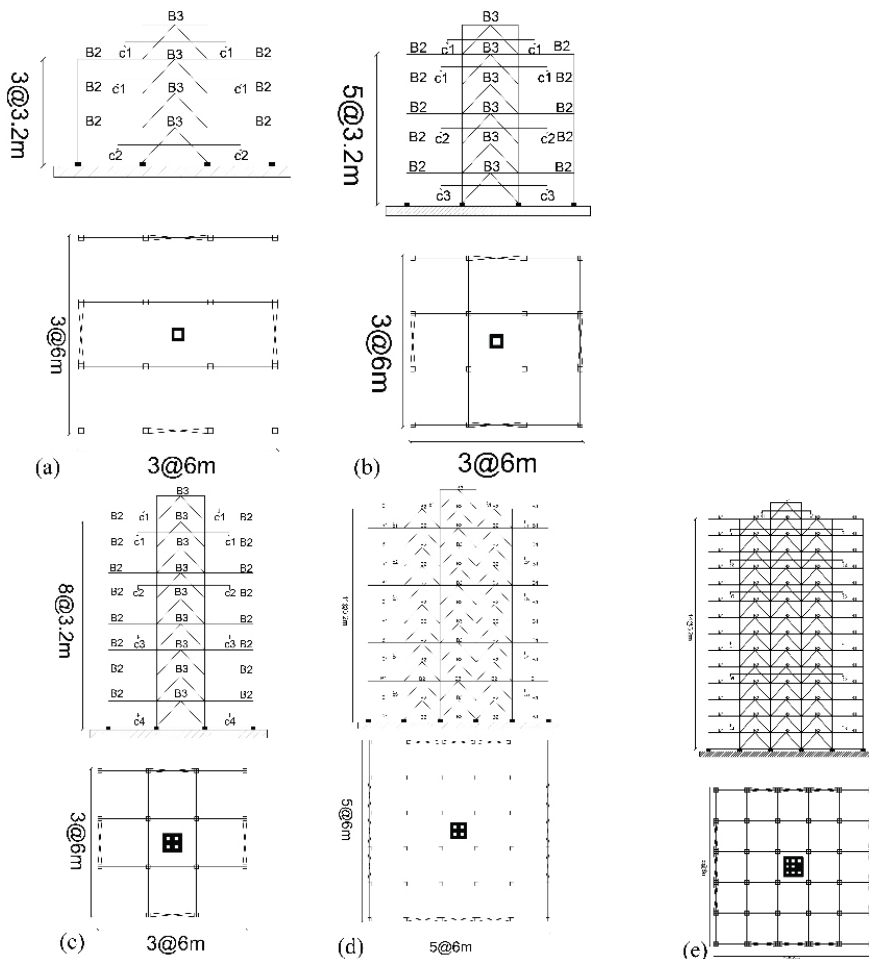
Fig. 1 - The structures with no rigid support of (a) 3 stories, (b) 5 stories, (c) 8 stories, (d) 11 stories, and (e) 14 stories

Table 1 - Section properties for Fig. 1.

Column section		Beam section
$B \times t$ (cm)		$[(h_w \times t_w) + (b_f \times t_f)]$ (cm)
$c_1 = 35 \times 2$	$c_4 = 50 \times 3$	$B_1 = (40 \times 1) + (20 \times 1.5)$
$c_2 = 40 \times 2.5$	$c_5 = 60 \times 3.5$	$B_2 = (45 \times 1.5) + (25 \times 2)$
$c_3 = 45 \times 3$	$c_6 = 80 \times 5$	$B_3 = (50 \times 2) + (30 \times 3)$
$B = width$		$t_w = web\ thickness$
$t = thickness$		$b_f = flange\ width$
$h_w = web\ height$		$t_f = flange\ thickness$

2.2. Designing the Stiff Core (Rigid Support Structure)

The current survey of the United Nations approximated that more than half of the people accommodate in cities [60]. Furthermore, it was also estimated that more people will be living in the cities by the end of 2050. Therefore, the number of houses and apartment complexes is rising in urban areas. Normally, tall buildings are more susceptible to wind actions and ground motions than low-rise buildings. Hence, effective lateral force-resisting systems should be used to reduce lateral demands. In order to solve this problem, reinforced concrete (RC) is utilized in high-rise structures. This provides the benefits of flexible architecture, faster construction, and commodious area [61].

The columns in an RC-supported structure have the flexibility to transfer the gravity loads. One of the most accurate and precise numerical approaches is the nonlinear response history analysis (NLRHA) process, which computes the high-rise structures' dynamic responses. However, it is computationally expensive, time-consuming, and needs expertise in nonlinear modelling. Mehmood et al. [62] revealed that the NLRHA procedure requires a computation time of about 30 hours for predicting a building's seismic responses for a certain case. Moreover, another 5 hours is required for the post-processing. Thus, various simplified analysis processes have been developed to avoid the issues related to the NLRHA process. Nonlinear modelling is required by some of the simplified processes, while the linear elastic modelling option is served for others. However, these approaches have less accuracy in comparison to the NLRHA technique. The simplified techniques were mostly adopted in different codes [63-65]. Recently, more analysis processes have been proposed [66-73]. However, the present study has concentrated on more developed models.

No study exists examining the simplified procedures, particularly for high-rise core wall buildings. The present study is aimed to compare all the simplified methods for their computational efforts, computation time, and relative accuracy for high-rise core wall structures. It provides the demerits and merits of different simplified analysis procedures in detail. Moreover, a modified simple analysis procedure is presented using modal decomposition methods based on an in-depth analysis of modal responses.

The rigid support structure is a central square core wall with high-strength steel (HSS) with 650 mega Pascal ultimate tensile strength and high-strength concrete (HSC) with 60 mega Pascal compressive strength. It was designed via the ACI 363R-92 [74]. This structure is connected rigidly to the foundation. Moreover, by horizontally crosswise viscous dampers, the structures are linked to the support structure in the roof, as shown in Fig 2.
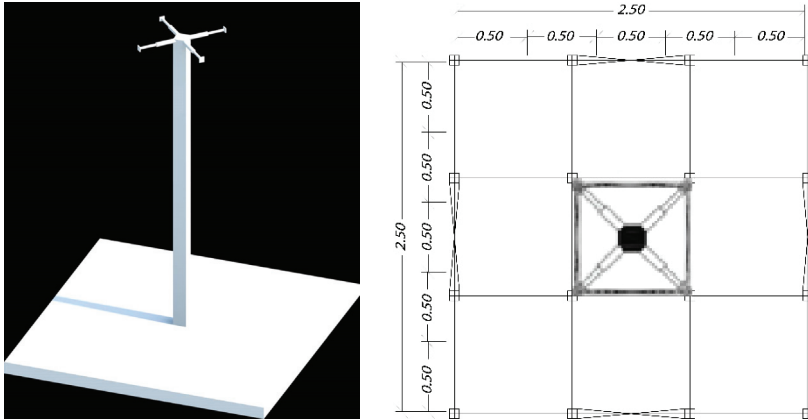
Fig. 2 - Schematic configuration of rigid support structure

Fig. 3 shows the details of the support system.
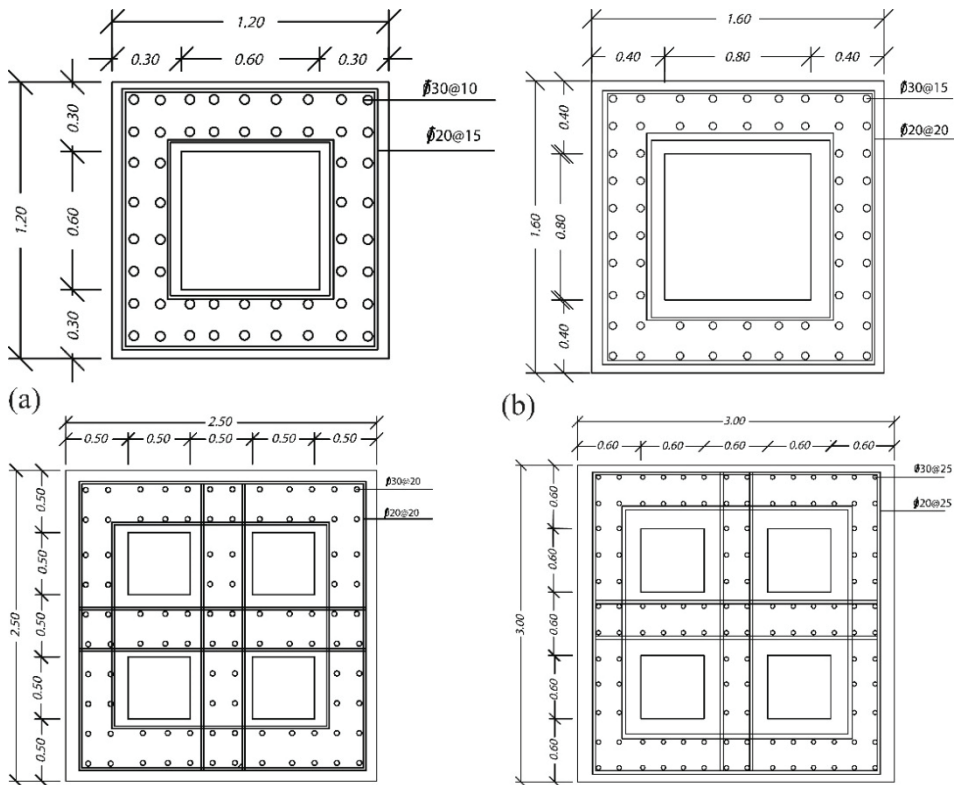
Fig 3 - The details of rigid supports for (a) 3 stories, (b) 5 stories, (c) 8 stories, (d) 11 stories, and (e) 14 stories

(e)
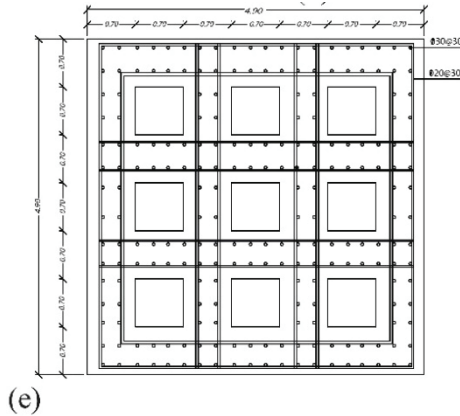
Fig 3 - The details of rigid supports for (a) 3 stories, (b) 5 stories, (c) 8 stories,
(d) 11 stories, and (e) 14 stories (continued)

2.3. Base Isolation System

Among the influencing parameters in the response of isolated structures under near-field earthquakes, we can mention the important feature of LRB isolators, i.e., the stiffness ratio before and after yielding of rubber isolator with lead core, B_{ratio}. To investigate the effect of that parameter, it is considered as a variable to determine the value of the minimum response of the isolated structure under the influence of the nearby earthquake [75].

In this study, Wen and Bouc models are used for nonlinear modelling and expression of the hysteresis behavior of the LRB system [75].

One of the influential parameters in the response of the isolated system is the amount of damping of the isolated system with the behavior of the linear displacement force. Increasing the damping controls the deformation of the structure, but on the other hand, it increases the acceleration of the structure. Therefore, two parameters of acceleration and displacement of the separator system were studied simultaneously under near-field accelerometry. For this purpose, the structure with frequency characteristics ω_s, period T_s, and damping ς_s and separator with frequency characteristics ω_b, period T_b, damping ς_b and $\gamma = \frac{m}{(m+m_b)}$ were investigated [76].

Another important parameter in the response of the system under an earthquake is the normalized yield strength F_0 of the LRB isolator, which has been studied in [77]. For this purpose, an N-story building equipped with an LRB isolator was used. The yield strength parameter is normalized and is defined according to equation 1.

$$F_0 = \frac{F_y}{W} \qquad\qquad (1)$$

where F_y is the yield strength of the isolator, and W is the total weight of the isolated building. For more detail, in this regard, the study of Jangrid [77] is introduced.

The LRB yield strength ought to be such that it offers sufficient initial rigidity when there is no yielding in the lead core because, for relatively small values of the isolator yield strength, the efficient period of the isolated building is around 2.5 seconds, which is extremely similar to the interval time of the isolator pulse [77].

It can be said that in the design of the LRB separator, the optimal value for the LRB is slightly higher than the F_0 related to the acceleration of the minimum floors in order to achieve the maximum amount of separation with the least amount of floor displacement. This value of F_0 is considered to be about 0.1 to 0.15.

Typically, there are two kinds of seismic isolators, which are sliding bearings [78] and [79] and rubber bearings (LRBs) [80]. As previously stated, the present work aims to assess the effects of viscous dampers and lead rubber bearings' performance concerning the features of the near-field ground motion. The LRB isolator is able to neutralize the impact using a particular hysteretic lead plug. Thus, it supports the structure vertically and offers limited horizontal autonomy. The designed isolators of the present study are based on the Uniform Building Code (UBC-97) [80]. The present study's design parameters are introduced in Table 2.

Table 2 - The design parameters used in the present study

Parameter	Details
Q/W	The ratio of the characteristic strength to the total weight on the isolation system
D	The isolator diameter
F_y	The yield force
n	The number of rubber layers
d	The lead core diameter
t	The layer thickness
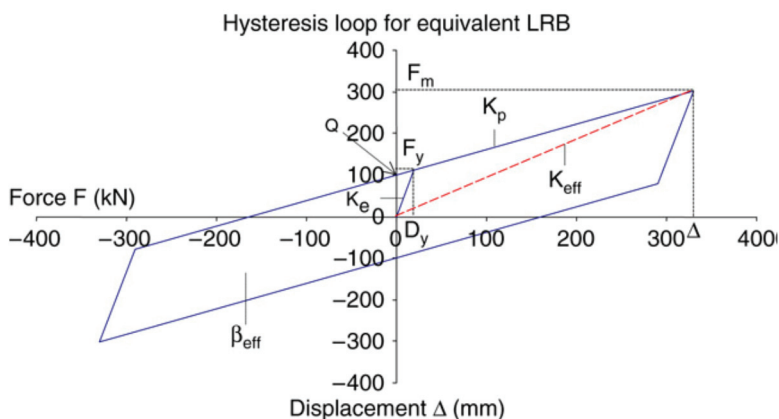
Fig. 4 - The typical bilinear LRB hysteresis

Fig. 4 demonstrates the bilinear curve used for analysis purposes in the present study. It specifies k_e and k_p which are the elastic and post-yield stiffness, respectively.

k_e and k_p are determined as follows:

$$k_e = \frac{F_y}{D_y} \tag{2}$$

$$k_p = \frac{G.A_r}{t_r} fL \tag{3}$$

where, D_y, G, and A_r are the yield displacement, the shear modulus, and the cross-sectional area of rubber, respectively. fL is a constant, which is set to be 1.5. The strength is also calculated by:

$$Q = A_{pb}\sigma_{y_{pb}} \tag{4}$$

where, A_{pb} and $\sigma_{y_{pb}}$ are the area and the yield strength of the lead core, respectively. Furthermore, the effective stiffness k_{eff} is calculated as follows:

$$k_{eff} = \frac{F_m}{\Delta} \tag{5}$$

where, F_m is the force and Δ is the displacement. The effective stiffness is also calculated as Eq. 6.

$$k_{eff} = \begin{cases} k_p + \frac{Q}{\Delta} & (if\ \Delta > D_y) \\ k_e & (if\ \Delta < D_y) \end{cases} \tag{6}$$

Also, the forces are formulated as:

$$F_m = Q + k_p\Delta \tag{7}$$

$$F_y = Q + k_pD_y \tag{8}$$

The area ED of the hysteretic loop, which corresponds to the amount of dissipated energy, is obtained as:

$$ED = 4Q(\Delta - D_y) \tag{9}$$

The amount of hysteretic energy that is dissipated by the isolator is defined as the effective damping ratio ζ_{eff}.

$$\zeta_{eff} = \frac{ED}{2\pi k_{eff}\Delta^2} \tag{10}$$

Ultimately, the fundamental isolation period T^{iso} is achieved as:

$$T^{iso} = 2\pi \sqrt{\frac{M}{\Sigma K_{eff}}} \qquad (11)$$

M is the overall mass of the system. Fig. 5 shows the hysteretic curves for different cases.
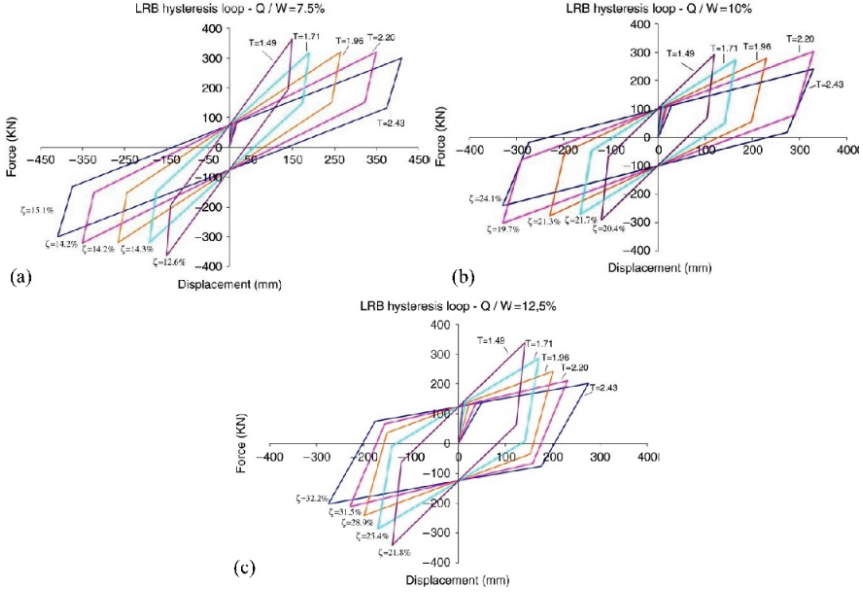
Fig. 5 - The LRB isolators hysteretic curve for the cases of (a) $Q/W = 7.5\%$, (b) $Q/W = 10.0\%$, and (c) $Q/W = 12.5\%$

The equation of motion is utilized to determine the maximum deformation of the isolation system to calculate the initial values [81]. This approximation of the maximum deformation is accurate [82].

$$M\ddot{x}_b(t) + C_{eff}\dot{x}_b(t) + K_{eff}x_b(t) + \sum_{q=1}^{Q} m_q a_q = -M\ddot{x}_g(t) \qquad (12)$$

Where, Eq. 12 is the equation of motion. $\ddot{x}_g(t)$, $x_b(t)$, m_q, a_q, and Q are the horizontal ground acceleration, the relative displacement of the isolator, mass, relative acceleration of the nth degree of freedom, and the number of superstructure's degrees of freedom, respectively.

C_{eff} is the effective damping coefficient which is formulated as follows:

$$C_{eff} = 2\zeta_{eff}\sqrt{MK_{eff}} \qquad (13)$$

Fig. 6 and Table 3 provide the properties of the isolators used in PERFORM3D.
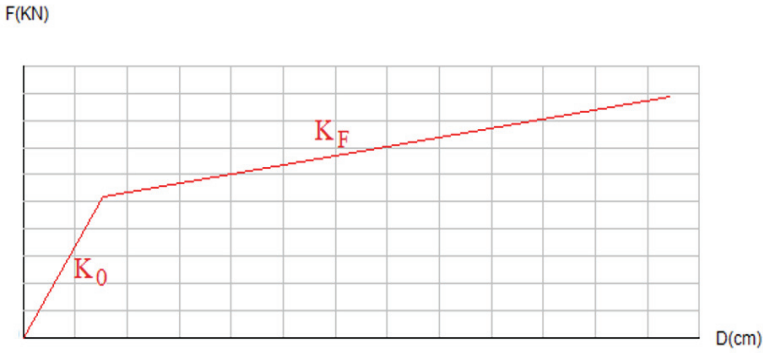
Fig. 6 - Force-displacement relationship for lead rubber bearing

Table 3 - The relationship of force/displacement for lead rubber bearing for T=2.43

Structures	$K_e = K_o$ (KN/M)	D_{max} (mm)	F_u (KN/M)	$K_p = K_F$ (KN/M)
3 story	400	400	14	0.200
5 story	485	485	16.5	0.225
8 story	530	530	19	0.255
11 story	605	605	22.5	0.311
14 story	675	675	26	0.311

Note that in Perform3D, K_e and K_p are introduced as K_o and K_f.

2.4. The Fluid Viscous Damper System

Viscous fluid dampers are frequently used as energy dissipation tools to protect structures from earthquakes. These dampers are made of a hollow cylinder filled with fluid, usually silicone-based fluid. Strong forces opposing the damper's relative motion can be produced by the pressure difference across the piston head [82]. Heat is produced as a result of energy dissipation caused by friction forces. When the damper is exposed to lengthy or large-amplitude vibrations, the resulting temperature increase can be severe [83, 84]. There are mechanisms to counteract the temperature increase such that the impact on damper behavior is minimal [85]. The possibility of heat-related harm to the damper seals increases the temperature [84]. Strangely, even though the damper is referred to as a viscous fluid damper, the fluid often has a low viscosity, such as silicone oil, which has a kinematic viscosity of around 0.001 m²/s at 20°C. The phrase "viscous fluid damper" refers to a damper's macroscopic behavior, nearly identical to that of an ideal linear or nonlinear viscous dashpot in that the resistive force is proportional to the velocity.

Viscous dampers present a resisting force to the velocity [86, 87]. In order to calculate the damper force, we use Eq. 14.

$$F_D = cV_c^{exp} \tag{14}$$

Where, c and V_c are the coefficient and the relative velocity. Also, exp is a constant ranging from 0.1 to 0.3. In the present study, the mentioned parameter is set to 1 for simplicity. Fig. 7 presents the relation between the applied force and the displacement of the viscous damper.
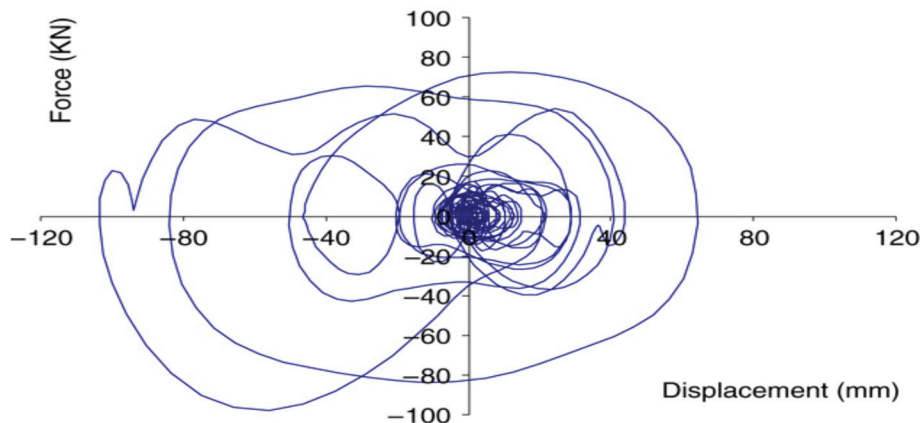
Fig.7 - The typical relation of the force and the displacement in a viscous damper

The viscous damper's parameters are represented in Fig.8.
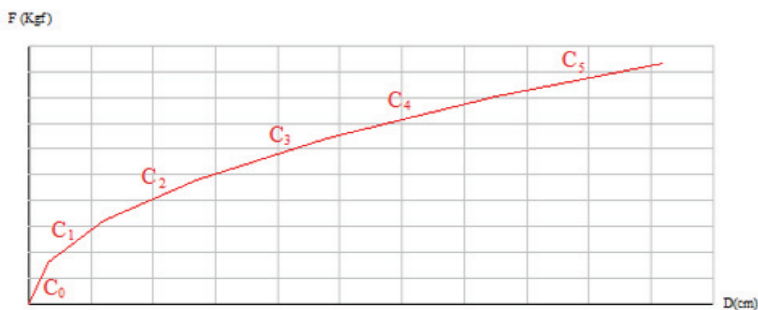
Fig. 8 - The force-displacement association for fluid and the viscous damper in a structure with 3 stories

The axial force in the viscous damper is calculated by:

$$Axial\ Force = C\ (Deformation\ rate)^{0.5} \tag{15}$$

The coefficient of each structure based on its number of stories and the force in the last segment is given in Table 4.

Table 4 - The value of C under different conditions (number of stories and the force at last segment)

Segment	Deformation rate	3 stories 20,000 Kgf	5 stories 40,000 Kgf	8 stories 60,000 Kgf	11 stories 80,000 Kgf	14 stories 100,000 Kgf
1	0.6	2222	4444	6667	8889	8889
2	2.4	1333	2667	4000	5333	5333
3	5.4	952.4	1905	2857	3810	3810
4	9.6	740.7	1481	2222	2963	2963
5	15	606.1	1212	1818	2424	2424

Regarding the equation of motion, a thorough explanation is given in our previous research [88-90], and the reader is referred to those papers.

2.5. Ground Motion Information

Ground motion components should be matched and scaled based on the design spectrum to avoid scattering the time history analysis results. The design spectrum is determined based on the ground motions components of the construction site and according to the hazard and soil characteristics in different site layers with a damping value of 5%. Initially, each record is scaled based on the maximum Peak Ground Acceleration (PGA) of gravity of the earth (g). Each scaled record's response spectra are calculated with a 5% damping value. The square root of the sum of squares (SRSS) of each response spectra was determined. The average of SRSS in the range of 0.2T to 1.5T of all the earthquakes under study is calculated (T is the fundamental period of the structure), and this number, which is the coefficient of scale, is introduced to the software. This average should not be less than 1.17 times the design spectrum. According to the national regulations of the building, the selected records must be in harmony with the desired building in terms of size, fault mechanism, and the distance from the fault to the place of registration. If the required records do not exist, modified or artificial records can be used. The number of records used and how to modify the records to match the existing conditions are important questions. For this research, earthquake records were selected based on FEMA P695 recommendation, where 22 earthquake records for the distant area and 28 records for the near area were mentioned.

In comparing spectra and codes of earthquakes, the desired return period should be the same for response spectra and the design spectrum of codes. In other words, to check each earthquake's effect on the structure and evaluate the tremors of the buildings, it is necessary that the response spectra be adapted or scaled with the spectra of the corresponding plan to a specific return period. SeismoSignal software was used for scaling, and all records were scaled for all modes.

Individual recorded events must be scaled and selected to determine the horizontal components of the ground motion. It is appropriate to use ground motions whose magnitudes, fault distances, and source mechanisms are consistent with those controlling the maximum earthquake considered. Whenever there are not enough recorded ground motion pairs to fulfill the requirement, simulated ground motion pairs will be used as a substitute to fulfill the requirement. The square root of the sum of squares (SRSS) spectrum for each pair of

horizontal ground motion components will be calculated by taking the SRSS spectra of five percent damped response spectra (where the same scale factor will be applied to both components of each pair).

In this study, the two methods of comparing the acceleration are the methods presented in the ASCE07-10. Each pair of acceleration maps must be scaled to their maximum value; for example, we have two acceleration maps of Tabas's earthquake with PGAs of 0.85 and 0.86. First, we multiply both records by a factor of 1/0.86= 1.16. The larger accelerometer's PGA equals 1g (the accelerometer numbers were based on a coefficient of g). And the record with a lower PGA will have a PGA equal to 0.98 (In the third edition of the 2800 standard, the amount of PGA in both acceleration maps was equal to one, which was changed in the fourth edition). In the SeismoSignal software, according to each couple, we extract the accelerometer scaled to the maximum with 5% damping. We obtain the response spectra of each map acceleration pair in each period by the root sum of squares method. In the range of 0.2T to 1.5T (where the period is the main), we get the root mean of the sum of squares. Important: only in the three-dimensional analysis should this average not be more than 10% less than 1.3 times according to the plan; that is, it should be more than 1.17 times the spectrum of the plan. The coefficient obtained in this way is entered as a scaling coefficient in the software.
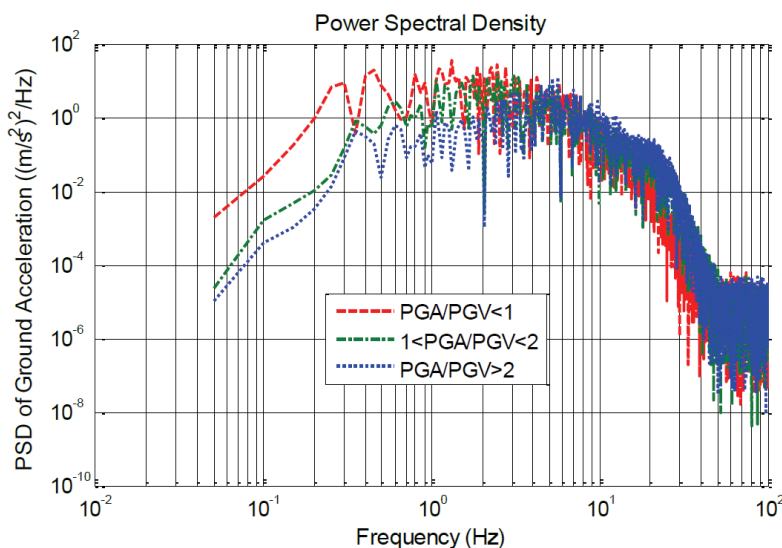
Fig. 9 - The power spectral density of different earthquakes

The ground motions whose PGA/PGV is smaller than one have been selected because of their highest intensity (Fig. 9). Table 5 illustrates the ground motions, and Figure 10 shows the spectral acceleration of the ground motions together with their mean.

Table 5 - The characteristics of different ground motions (PGA/PGV)

Earthquake Name	Year	Duration time	PGA (g)	PGV (m/s)	PGD (m)	PGA/PGV
TCGH13	2004	21	0.590	0.626	0.098	0.945
KOBE	1995	50	0.834	0.911	0.211	0.915
Imperial Valley-02	1940	55	0.280	0.309	0.087	0.905
Tabas	1978	40	0.027	0.034	0.31	0.768
Tabas	1978	33	0.861	1.234	0.936	0.698
Bam	2003	33	0.014	0.020	0.013	0.696
Imperial Valley-02	1940	55	0.210	0.313	0.241	0.670
El Mayor-Cucapah	2010	130	0.248	0.383	0.482	0.648
Northridge	1994	28	0.426	0.748	0.190	0.569
Kocaeli	1999	150	0.045	0.081	0.035	0.555
Tottori	2000	120	0.018	0.036	0.042	0.511
Duzce	1999	95	0.017	0.045	0.038	0.373
Northridge01	1994	30	0.410	1.114	0.446	0.368
Darfield	2010	140	0.194	0.591	0.491	0.328
Zealand	2010	120	0.209	0.671	0.599	0.311
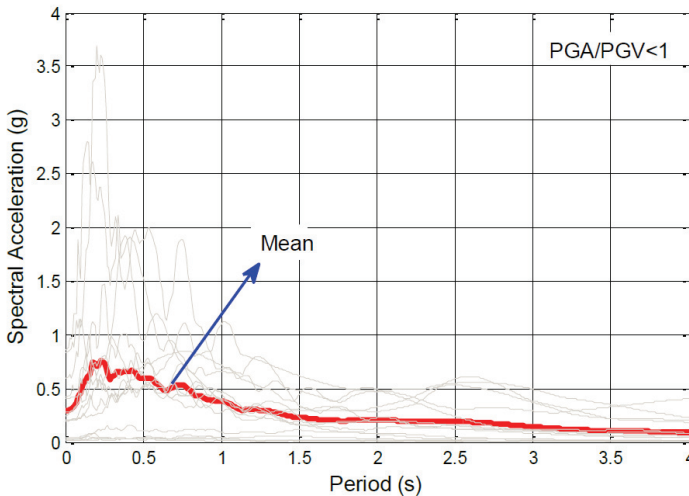
Fig. 10 - 5% damped acceleration spectra if the selected ground motions

The SeismoArtif software was used to create fake earthquakes based on the median spectrum ground movements in Fig. 10. (version 2018). The Saragoni and Hart [91] envelope curve approach was applied while considering the following requirements (Fig. 11).
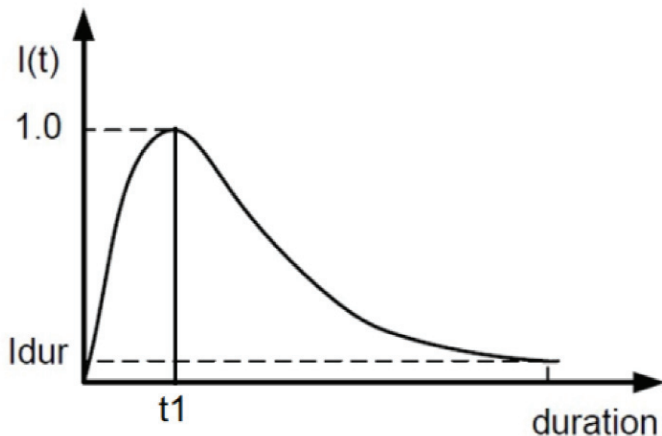
Fig. 11 - Saragoni and Hart envelope curve [91]

By executing the procedure mentioned above, it can be seen from Fig. 12 that the actual spectrum matches the specific target spectrum with 5% damping.
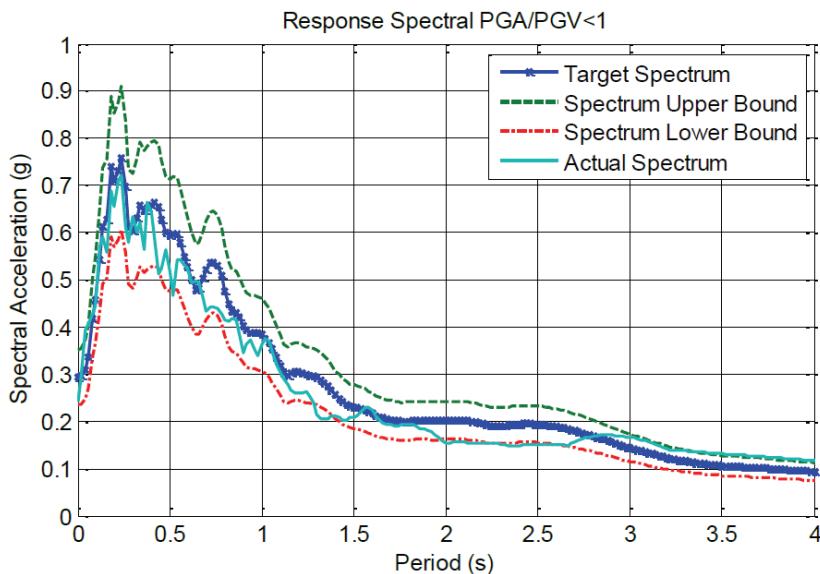
Fig. 12 - The response spectral matched the target spectrum

Tables 6 and 7 present the 7 near-field (N.F) and 7 far-field (F.F) ground motions used in the current study.

Table 6 - The features of N.F earthquake motions

No.	Earthquake	M	Station	Distance(km)	PGA(g)	PGV(cm/s)	PGD(cm)
1	Northridge	6.69	LA Dam	11.79	0.576	77.09	20.1
2	Chi Chi	7.62	TCU068	3.01	0.5	277.56	715.8
3	San Fernando	6.61	Pacoima Dam	11.86	0.827	34.43	18.67
4	Palm springs	6.06	North Palm springs	10.57	0.669	73.55	11.87
5	Kocaeli	7.4	Sakarya	3.2	0.41	82.05	205.9
6	Gazil	6.8	Karakyr	12.82	0.599	64.94	24.18
7	Whittier narrows	5.99	Santa-fe springs	11.73	0.398	23.75	1.76

Table 7 - The features of F.F earthquake motions

No.	Earthquake	M	Station	Distance(km)	PGA(g)	PGV(cm/s)	PGD(cm)
1	Imperial Valley	6.53	Brawley Airport	43	0.158	36.09	22.63
2	Loma Prieta	6.9	Richmond City Hall	87.87	0.124	17.34	3.58
3	Tabas	6.8	Tabas	55.24	0.851	121.22	95.06
4	Kobe	6.9	KJMA	18.27	0.854	95.75	24.56
5	Chi Chi	7.62	TCU065	26.67	0.831	129.55	93.85
6	Kocaeli	7.51	Sakarya	33.24	0.376	79.49	70.56
7	Northridge	6.7	Huntington BchWaikiki	69.5	0.086	5.01	1.63

3. SIMPLIFIED MODEL

In order to evaluate the performance of a base isolation construction, a single-degree-of-freedom (SDOF) model is suggested. A complete representation of this model is presented in Fig. 13.

The parameters needed for this procedure are shown in the following equations. The simplified SDOF model's mass, starting stiffness, yield deformation, and damping coefficient are denoted by the letters M_e, k_e, d_{ye}, and c_{main}, respectively.
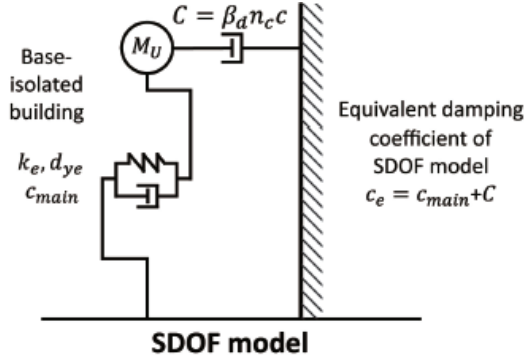
Fig. 13 - A Schematic of the reduced SDOF model

$$M_e = M_U \tag{16}$$

$$k_e = \frac{1}{\left(\frac{1}{k_I} + \frac{1}{k_U}\right)} \tag{17}$$

$$d_{ye} = \frac{K_I d_{yI}}{k_e} \tag{18}$$

$$\frac{1}{k_e + i\omega_e c_{main}} = \frac{1}{k_I + i\omega_e c_I} + \frac{1}{k_U + i\omega_e c_U} \tag{19}$$

$$\omega_e = \sqrt{M_e/k_e} \tag{20}$$

$$c_{main} = \frac{(k_I c_U + k_U c_I)(k_I + k_U) - (k_I k_U - \omega_e^2 c_I c_U)(c_I + c_U)}{(k_I + k_U)^2 + \omega_e^2 (c_I + c_U)^2} \tag{21}$$

β_d is the effect of the damper location.

m_U (kg)	1.70×10^6
c (Ns/m)	5×10^6
k_l (N/m)	2.61×10^6
d_{yl} (m)	0.01

In the design of isolators, performance point methods (PPM) are employed. Depending on the location of the building, spectral acceleration, and displacement are plotted for the 5 percent damped spectrum. In order to decrease the spectrum, equal viscous damping is considered. The isolation system is considered to be dampened by 15 percent in this section. Using the PPM method, the design spectrum has been changed in terms of force-displacement rather than acceleration displacement in light of the bilinear behavior of the isolator. Essentially, bilinear behavior refers to earthquake capacity, while force-displacement

spectrum refers to earthquake demand. A point should be identified in the PPM by plotting capacity and demand together in a diagram. The acceleration-displacement spectrum of the classified isolator is multiplied by 1601 kN, 957 kN, and 511 kN to create three force-displacement spectrums. By intersecting the demand and capacity curves, we are able to reach the isolator design parameters. To begin with, the period, damping, and characteristic strength were assumed, and iterations continued until the desired performance level was reached. Despite the fact that all parameters are the same as those defined in the previous section, post-elastic stiffness (K_2) is calculated based on the isolation period (T_{iso}).

4. NUMERICAL STUDY

This study used accelerograms related to the 7 scaled N.F and 7 scaled F.F earthquakes. Structure motion equations without controller and structure motion equations with central rigid support have been nonlinear time history analyses by PERFORM-3D. The average displacement of the base isolation upper level and stories velocity and acceleration were influenced by 14 earthquakes. These values are presented without a controller and with a central rigid support controller.

4.1. Results and Discussion

Table 8 shows the average absolute value of lateral displacement of the base isolation upper level in structures with and without rigid support. As seen in Table 9 and Table10, the structures' response followed by the time history analysis is extracted under far and near field scaled earthquake scaled records. Therefore, the decreased quantities in the most displacement of the base isolation upper level are presented in the following tables.

Table 11 shows the average absolute value of base shear of the base isolation's upper level in structures with and without rigid support under N.F and F.F earthquakes. As seen in Table 12 and Table13, these structures have the response as discussed in the former section. Moreover, the decreased quantities in the highest base shears are presented.

Table 8 - The average absolute value of lateral displacement of the base isolation upper level in structures with and without rigid support in N.F and F.F earthquakes (cm)

Field / Structure	N.F		F.F		D_{max}
	With rigid support	Without rigid support	With rigid support	Without rigid support	
3 stories	17	3.9	17.5	7.3	40
5 stories	10.8	1.55	19.6	1.82	48.5
8 stories	13.2	2	9.8	1.95	53
11 stories	14.5	3.7	17.9	9.9	60.5
14 stories	7.4	0.95	11.7	3.6	67.5

Table 9 - The percentage of decreased quantity of the lateral displacement of the base isolation upper level in structures with support under N.F earthquakes

Earthquake \ Structure	Chi Chi	San Fernando	Palm springs	Kocaeli	Gazil	Whittier narrows	Northridge
3 stories	89.1	89	90.1	83.2	81.2	88.2	87
5 stories	88.1	81.3	83.2	87.5	86	89.1	85.6
8 stories	82.2	88	86	81.9	84.1	79.6	84.8
11 stories	70.1	76.2	79.2	69.8	76.3	76	74.5
14 stories	81.1	78.9	76	81.3	78.8	72	77

Table 10 - The percentage of reduced quantity of lateral displacement of the base isolation's upper level in structures with support under F.F earthquakes

Earthquake \ Structure	Imperial Valley	Loma Prieta	Tabas	Kobe	Chi Chi	Kocaeli	Northridge
3 stories	92.2	88.1	90	78	89.3	84.4	88
5 stories	90.4	89.7	92.2	83.3	88.9	91.1	90.3
8 stories	84.8	91.1	86.8	90.1	92.2	89.9	90.6
11 stories	37.6	41.2	39.3	80.3	40.1	36.1	44.7
14 stories	50.2	56.6	53.4	88.7	51.1	50.4	58.3
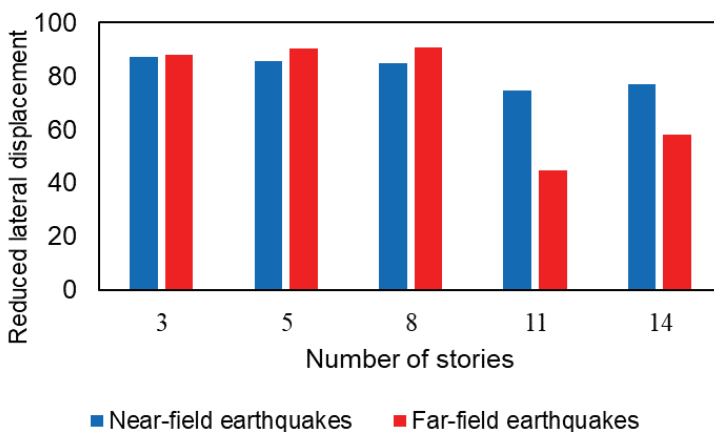
Fig. 14 - The percentage of reduced quantity of lateral displacement of the base isolation's upper level in structures with support under earthquakes

Table 11 - The average absolute value of base shear of the base isolation's upper level in structures with and without rigid support under N.F and F.F earthquakes (kg)

Field Structure	N.F		F.F	
	With rigid support	Without rigid support	With rigid support	Without rigid support
3 stories	41500	9950	52100	13200
5 stories	51100	19100	61300	20250
8 stories	54050	19050	61500	19600
11 stories	125100	90200	135300	115400
14 stories	133000	99100	130550	105200

Table 12 - The percentage of reduced quantity of base shear of the base isolation's upper level in structures with support under N.F earthquakes

Earthquake Structure	Chi Chi	San Fernando	Palm springs	Kocaeli	Gazil	Whittier narrows	Northridge
3 stories	78.8	80.1	76.6	82.4	75.3	79.9	78
5 stories	64.1	60.6	64.9	65.5	68	62.1	64
8 stories	47	42	41.1	48.8	44	48.3	45
11 stories	24.4	26	24.4	29.9	28.1	22.2	26
14 stories	26	22.6	20.1	30.7	28.5	23.1	25

Table 13 - The percentage of reduced quantity of the base shear of the base isolation upper level in structures with support under F.F earthquakes

Earthquake Structure	Imperial Valley	Loma Prieta	Tabas	Kobe	Chi Chi	Kocaeli	Northridge
3 stories	78.2	69.2	65.9	73	78.8	66.6	71
5 stories	59	71.1	67.7	58.8	64.1	68.8	66
8 stories	63.3	54	50.1	58.8	57	52.2	55
11 stories	11	16.9	21.2	12.6	14.4	10.1	15
14 stories	13.6	17	26.6	18.9	17	21.1	19
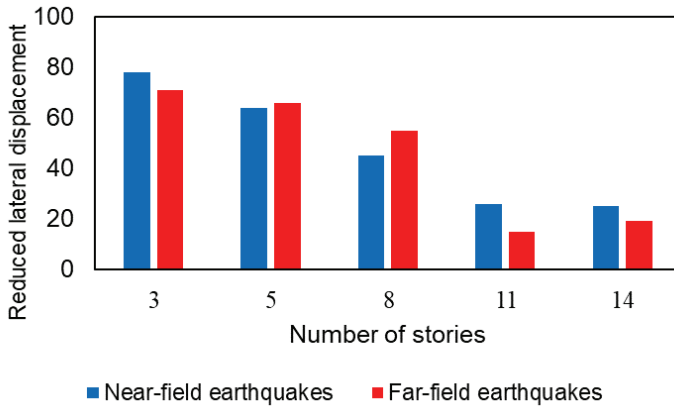
Fig. 15 - The percentage of reduced quantity of the base shear of the base isolation upper level in structures with support under earthquakes

According to the results, there are four main advantages for the structures with horizontal crosswise dissipators connected to the vertex of central rigid support. The first significant influence of support structures possessing dissipators in N.F earthquakes is the reduction of the displacement of the base isolation's upper level and reducing the base shear both in N.F and F.F earthquakes, particularly in buildings with lower numbers of stories.

As seen in Fig. 16, Fig. 17 and Fig. 18 the stories' velocity average in the structures are obtained as an average of F.F and N.F earthquakes records.
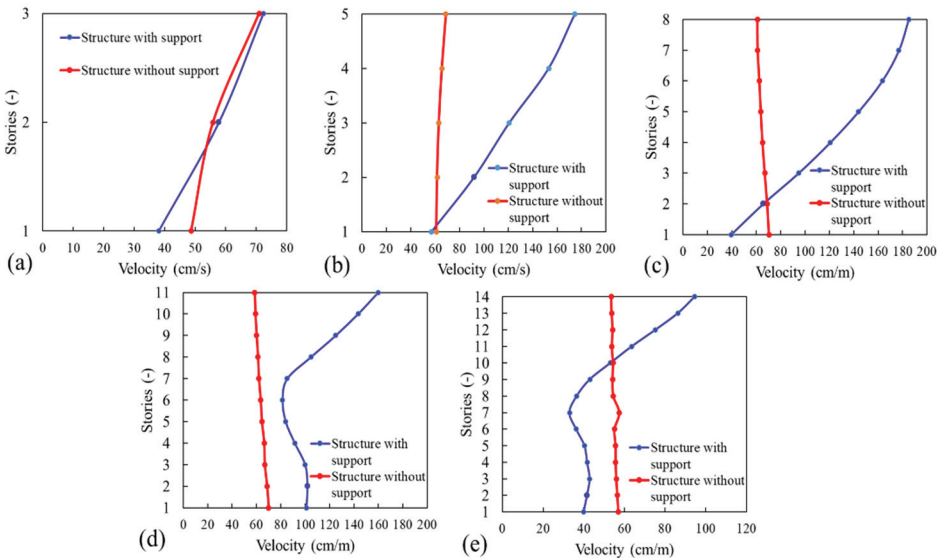
Fig. 16 - The F.F earthquake's stories velocity average for (a) 3-story, (b) 5-story, (c) 8-story, (d) 11-story, and (e) 14-story structure
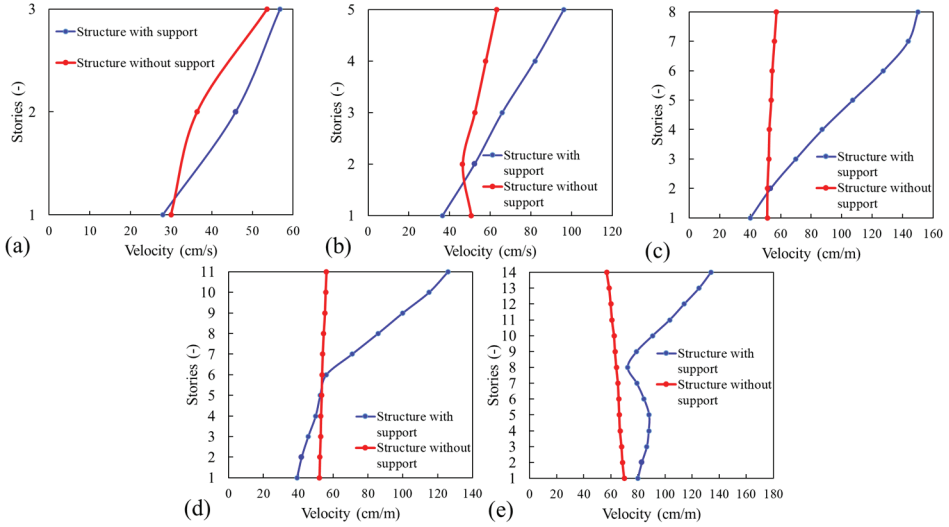
Fig. 17 - The N.F earthquake's stories velocity average for (a) 3-story, (b) 5-story, (c) 8-story, (d) 11-story, and (e) 14-story structure

Table 14 - The average absolute value of velocity of the base isolation upper level in structures with and without rigid support in N.F and F.F earthquakes

Field / Structure	N.F		F.F	
	With rigid support	Without rigid support	With rigid support	Without rigid support
3 stories	30	43.57	58.53	56.07
5 stories	54.08	66.66	63.94	119.48
8 stories	53.59	97.33	64.98	123.78
11 stories	53.76	71.21	63.66	107.08
14 stories	54.93	52.08	64.12	87.19

Table 15 - The percentage of average conversion of velocities in structures with support under N.F earthquakes

Earthquake / Structure	Chi Chi	San Fernando	Palm springs	Kocaeli	Gazil	Whittier narrows	Northridge
3 stories	5.7	11.1	8.8	9.1	6.6	8.2	8.2
5 stories	20.5	17.7	14.4	16.3	24.1	20.2	18.9
8 stories	50.1	39.8	42.7	43.3	51	53.3	45
11 stories	21	19	31.9	22.2	30.1	19.6	24.3
14 stories	-7	-7.9	-3.1	-4.7	6.8	-2.4	-5.2

Table 16 - The percentage of average conversion of velocities in structures with support under F.F earthquakes

Earthquake \ Structure	Imperial Valley	Loma Prieta	Tabas	Kobe	Chi Chi	Kocaeli	Northridge
3 stories	4.9	-5.9	-8	-4.7	5.6	-6.8	-4.2
5 stories	46	49.2	51	46.5	49.1	53.9	46.5
8 stories	49	39.8	51.1	33.3	54.4	61.6	48
11 stories	38.9	43.6	39	45.6	40.3	44.3	40.6
14 stories	36.3	27.8	30.9	27.8	31.1	33.6	31.4

The intention behind using base isolation system is to reduce the ground acceleration in the horizontal direction. This is achieved by adding stiffness between the building and its base leading to a lower frequency. The first dynamic mode of the isolated structure shows deformation in the isolators only. However, the higher modes affect the building itself. The purpose of the isolator is to deflect the earthquake energy. Damping is a favorable parameter in isolators, but too much damping could become an issue as well since it can be acting as a conduit for energy to be induced in the higher modes of the isolated structure. Obviously, by controlling the isolators' displacement, the amount of velocity and acceleration of the stories increases. However, using dissipators in N.F earthquakes leads to a drop in the velocity of the structures, particularly in tall structures. Under far-field earthquakes, similar effects are found.

■ Near-field earthquakes ■ Far-field earthquakes
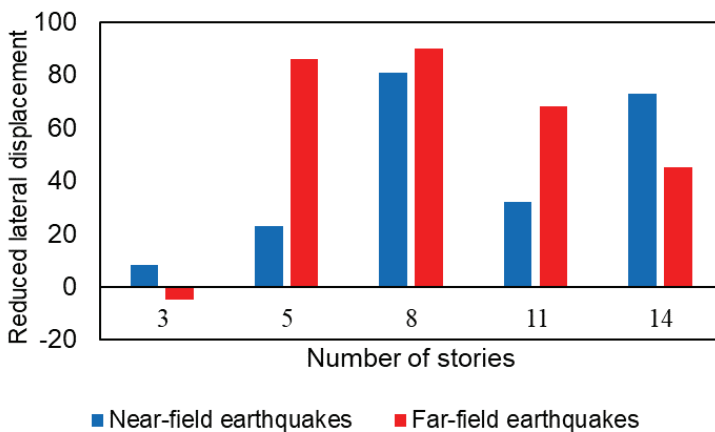
Fig. 18 - The percentage of average conversion of velocities in structures with support under earthquakes

According to Fig. 19, 20, and 21 and Table 17, 18, and 19, these structures' response is obtained as N.F and F.F scaled earthquakes records. The average conversion of the stories acceleration is presented in the following table and figures.
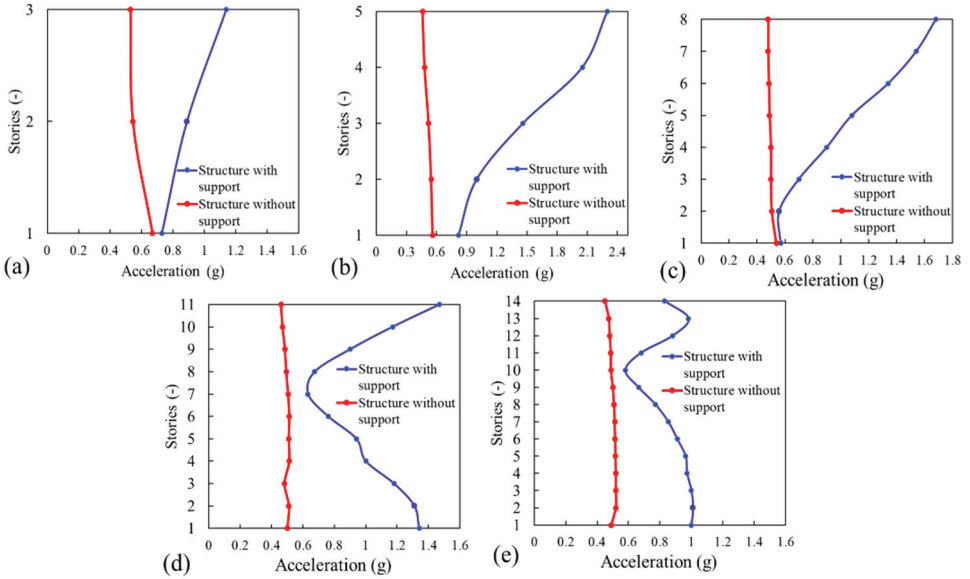
Fig. 19 - The F.F earthquake's stories acceleration average for (a) 3-story, (b) 5-story, (c) 8-story, (d) 11-story, and (e) 14-story structure
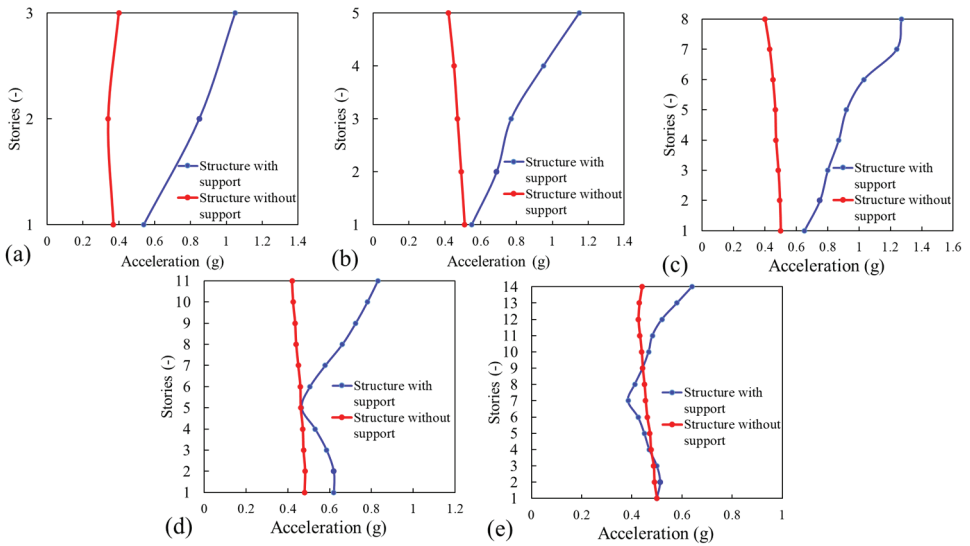
Fig. 20 - The N.F earthquake's stories acceleration average for (a) 3-story, (b) 5-story, (c) 8-story, (d) 11-story, and (e) 14-story structure

Table 17 - The average absolute value of accelerations of the base isolation upper level in structures with and without rigid support in N.F and F.F earthquakes

Field / Structure	N.F		F.F	
	With rigid support	**Without rigid support**	**With rigid support**	**Without rigid support**
3 stories	0.37	0.813	0.582	0.92
5 stories	0.468	0.822	0.513	1.526
8 stories	0.462	0.941	0.498	1.046
11 stories	0.455	0.627	0.494	1.034
14 stories	0.457	0.485	0.499	0.864

Table 18 - The percentage of average conversion of accelerations in rigid-support structures under N.F earthquakes

Earthquake / Structure	Chi Chi	San Fernando	Palm springs	Kocaeli	Gazil	Whittier narrows	Northridge
3 stories	46.7	67.8	48.8	44.1	49.9	68.1	54.5
5 stories	41.8	51.1	38.4	46.1	37.9	44.2	43
8 stories	57.9	60.6	56.6	43.8	62.6	57.1	56.3
11 stories	28.8	22.6	29.8	23.4	29.2	30.8	27.5
14 stories	4	7.1	6.7	6.1	4.9	5.7	5.7

Table 19 - The percentage of average conversion of accelerations in rigid-support structures under F.F earthquakes

Earthquake / Structure	Imperial Valley	Loma Prieta	Tabas	Kobe	Chi Chi	Kocaeli	Northridge
3 stories	38.7	43.9	39.9	35.3	39	23.3	36.8
5 stories	67.7	61.1	71.4	60.4	69	68.6	66.4
8 stories	57.1	49	59	55.7	45	49	52.4
11 stories	49.1	58.6	48.7	49.8	49	59	52.2
14 stories	40.1	45.3	47.1	32.4	58.7	29.3	42.3
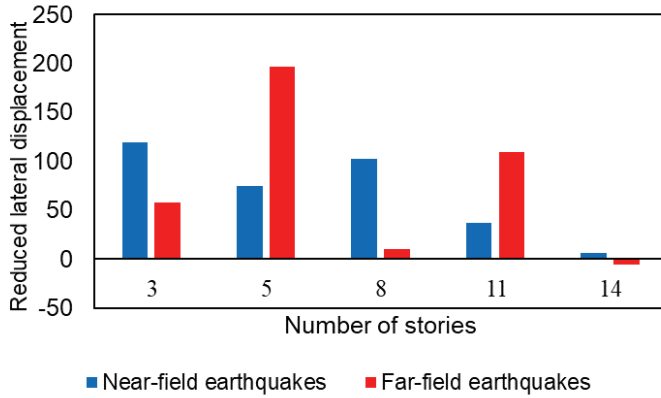
Fig. 21 - The percentage of average conversion of accelerations in rigid-support structures under earthquakes

The acceleration in N.F earthquakes is proved to be decreased by using the dissipators. Also, alteration of the structure's first modal shape from shear to torsional is achieved. This is significant in decreasing the modal mass effect on the structure's first action. Furthermore, it seems that the danger of buildings collapse has decreased dramatically in N.F earthquakes.

In Figs. 22 to 31, the hysteresis curve (force-displacement) of the upper level of the seismic isolators of buildings under study can be seen. The decreasing changes in the hysteresis curve of the structures equipped with the supporting structure are quite evident.
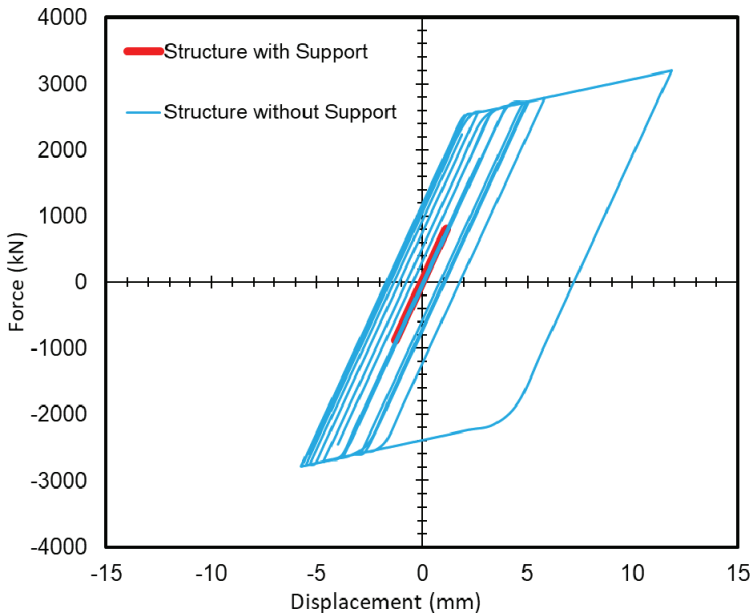
Fig. 22 - The F-D relation for the 3-strory structure in the far-field earthquake
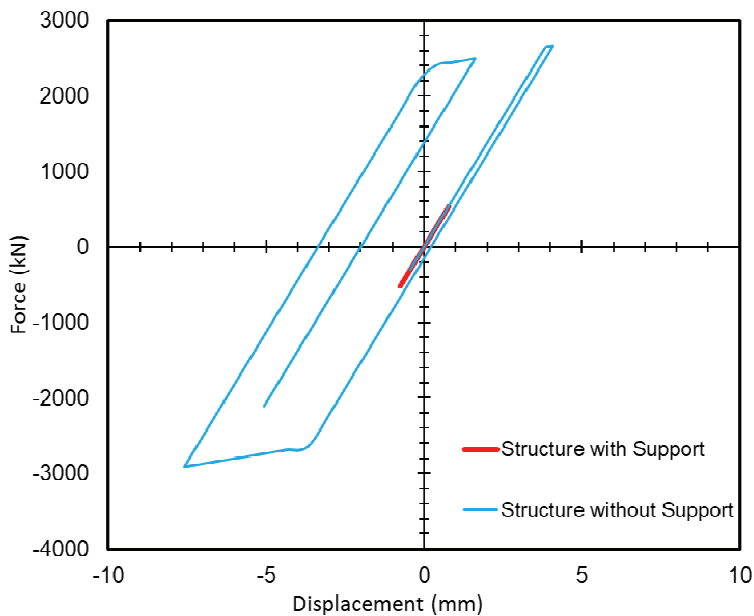
Fig. 23 - The F-D relation for the 3-strory structure in the near-field earthquake
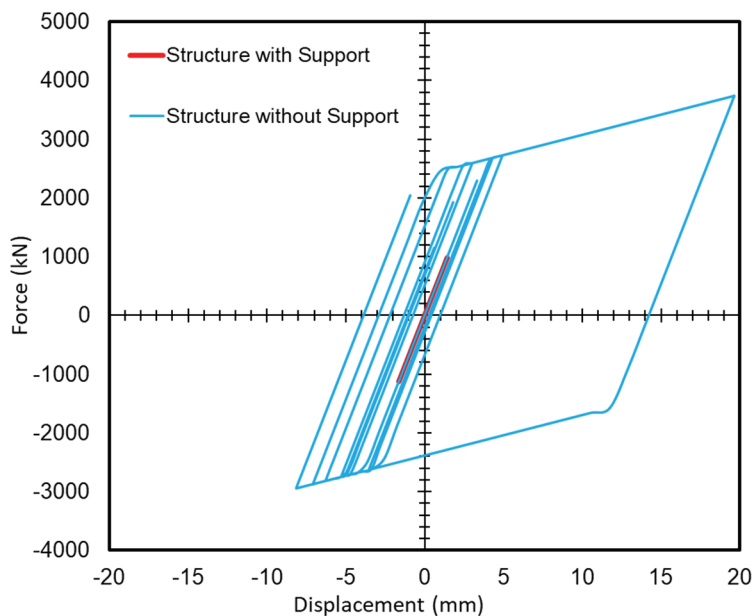
Fig. 24 - The F-D relation for the 5-strory structure in the far-field earthquake
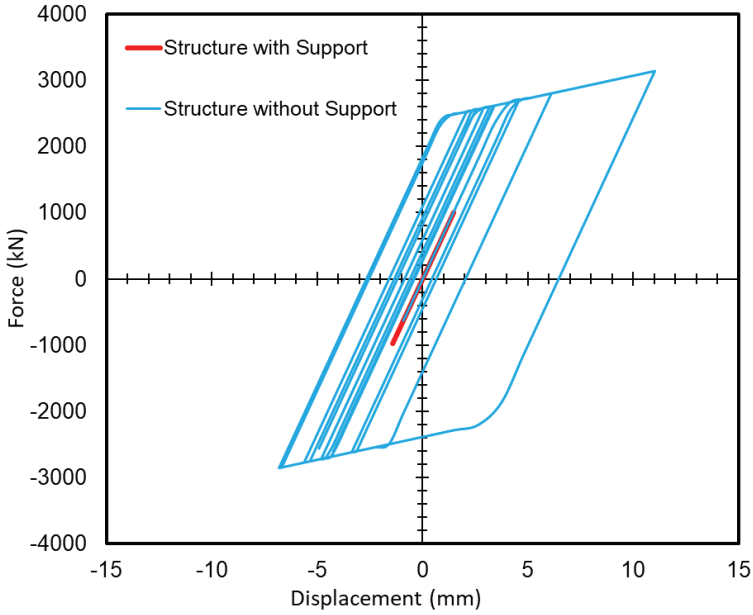
Fig. 25 - The F-D relation for the 5-strory structure in the near-field earthquake
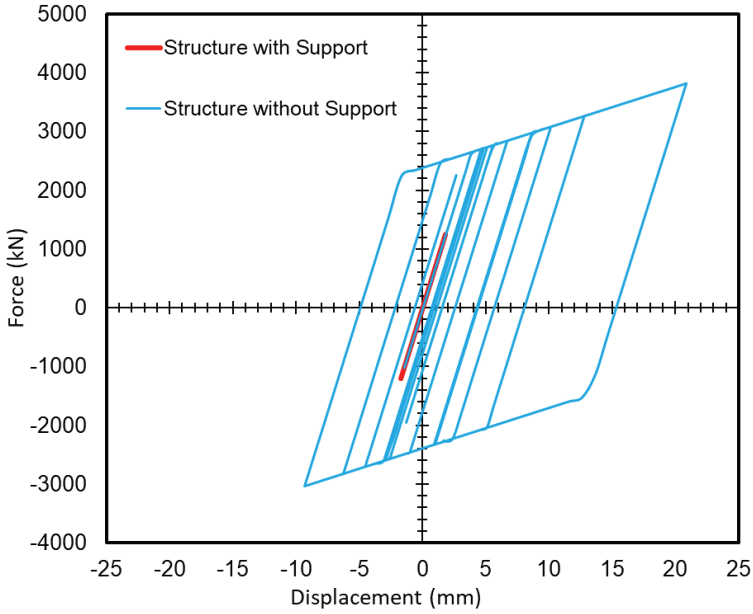
Fig. 26 - The F-D relation for the 8-strory structure in the far-field earthquake
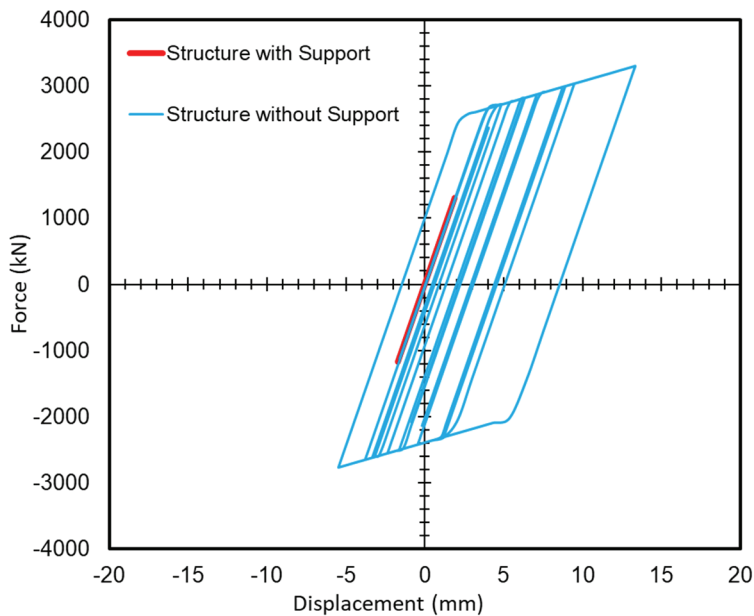
Fig. 27 - The F-D relation for the 8-strory structure in the near-field earthquake
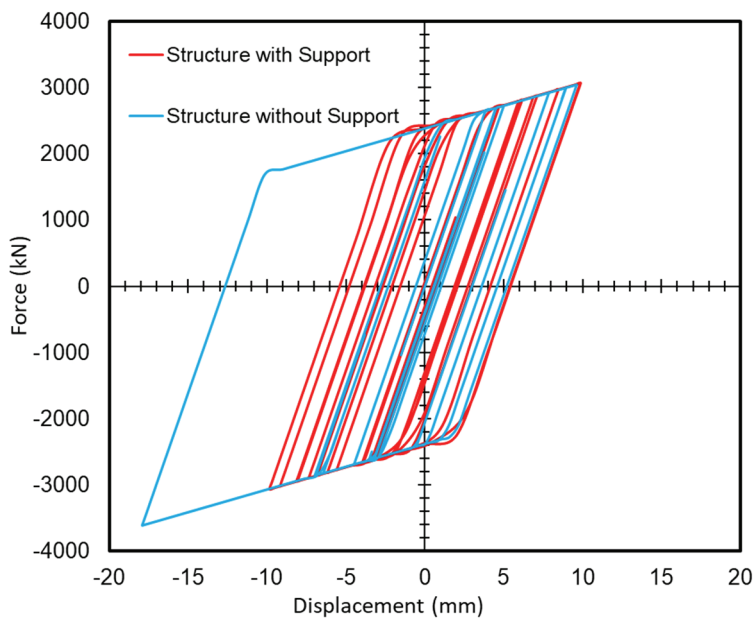
Fig. 28 - The F-D relation for the 11-strory structure in the far-field earthquake
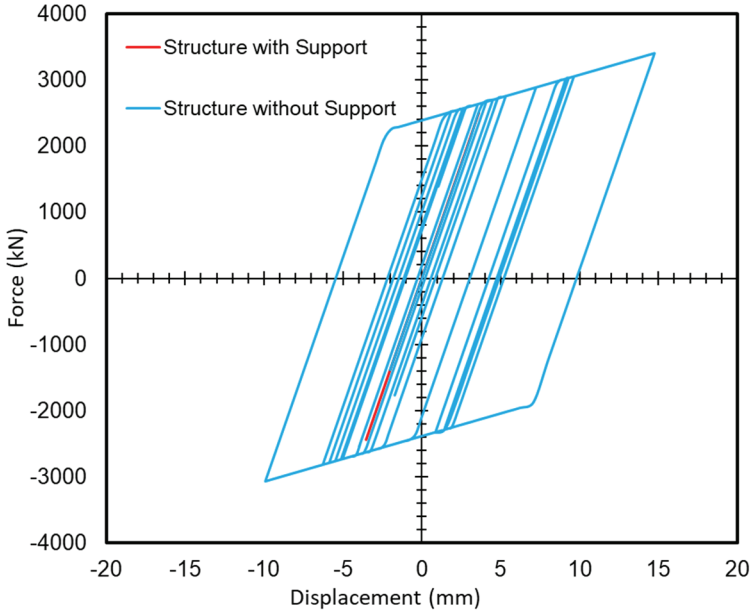
Fig. 29 - The F-D relation for the 11-strory structure in the near-field earthquake
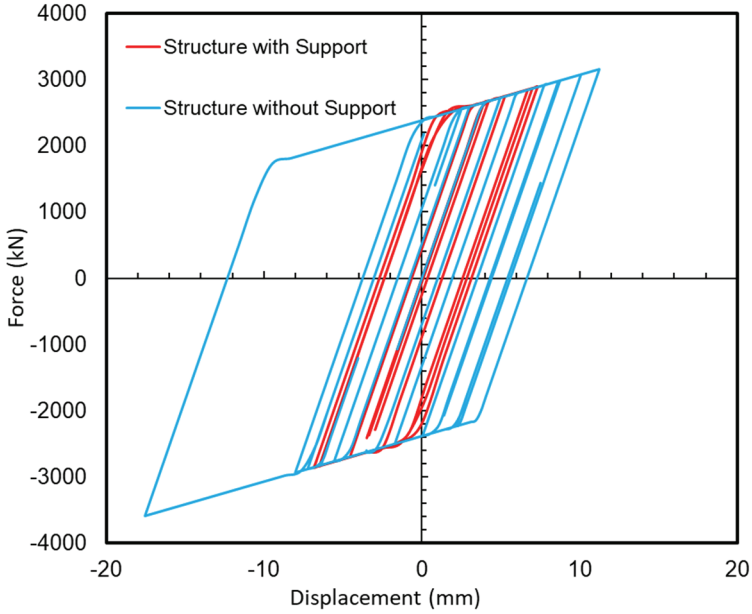
Fig. 30 - The F-D relation for the 14-strory structure in the far-field earthquake
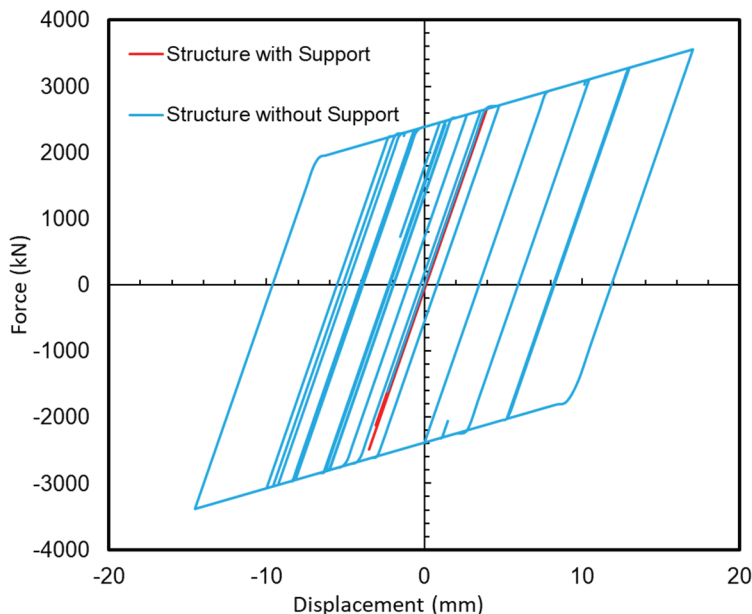
Fig. 31 - The F-D relation for the 14-strory structure in the near-field earthquake

5. CONCLUSION

Base isolation is the only anti-seismic technique that is able to save the building and its contents. In F.F earthquakes, acceptable performance is observed from the isolator, but in case of N.F ground motions they do not seem as helpful. Furthermore, utilizing such system is extremely expensive, which is in a controversy with the fundamental purpose of using seismic isolators. Normally, designing the base isolation, the destructive impacts of an earthquake are reduced, while prolonging the life of a structure and making a rigid body for the structures. Though the mentioned features can be improved through a base isolation system, regarding a near-field earthquake, a considerable drop may occur in the stability of the structures leading to the overturn and destruction of the building. According to the former studies, critical lateral displacement may be experienced by a building equipped with an isolator, and it could result in the overturn of the structure. A safe method is presented in the present study as a remedy to the stated problem to decrease the base isolation lateral displacement under near-field earthquakes. A supportive structure is designed, which is connected to the roof of the building by a viscous damper in a crosswise manner. It is also rigidly connected to the building's base. According to the results, there are five main advantages of implementing the proposed technique:

- Hybrid buildings consisting of base isolation and viscous dampers require a large number of dampers on each floor, and the sum total of the dampers used in those buildings, due to the high cost of viscous dampers and the high cost of servicing and maintaining these dampers, it creates a very high cost for the builders of those

buildings, perhaps this very high cost has been imposed, which has prevented the generalization of the use of these types of buildings.

- The biggest achievement of this research is the use of 4 viscous dampers in each building, which has significantly reduced the staggering costs of hybrid buildings.

- In all structures exposed to N.F earthquakes, the displacement of the base isolation is reduced significantly.

- It was proved that the base shear was decreased substantially under N.F earthquakes.

- By limiting the lateral displacement of the isolators, the floor velocity of all structures increased, with the least amount of velocity increase occurring in short and tall structures.

- By controlling the isolators' displacement, the amount of acceleration of the stories increases, with the least amount of acceleration increase occurring in tall structures.

- The structure's first modal shape was changed from shear to torsional.

Based on these benefits, the application of LRB isolators eliminated the impacts of N.F earthquakes. Furthermore, the present technique could decrease the near-field earthquake-caused mortality rates. Similarly, by utilizing the proposed technique, the damage to the property is also reduced considerably.

Nomenclature

A_{pb}	Area of the lead core
A_r	Cross-sectional area of rubber
a_q	Relative acceleration of the nth degree of freedom
c	Coefficient of velocity
C_{eff}	Effective damping coefficient
D	The isolator diameter
D_y	Yield displacement
d	The lead core diameter
ED	Area of the hysteretic loop
F_D	Viscous damper force
F_m	Force
F_y	Yield force
fL	Constant
G	Shear modulus

k_e	Elastic stiffness
k_{eff}	Effective stiffness
k_p	Yielded stiffness in isolation
M	Overall mass of the system
m_q	Mass of the nth degree of freedom
n	The number of rubber layers
Q	Strength
T^{iso}	Fundamental isolation period
V_c	Relative velocity

Greek Letters

Δ	Displacement
$\sigma_{y_{pb}}$	Yield strength of the lead core
ζ_{eff}	Damping ratio

References

[1] Erkus B, Johnson EA. Smart base-isolated benchmark building part III: a sample controller for bilinear isolation. Structural Control and Health Monitoring: The Official Journal of the International Association for Structural Control and Monitoring and of the European Association for the Control of Structures. 2006 Mar; 13(2-3):605-25; https://doi.org/10.1002/stc.101.

[2] Nagarajaiah S, Narasimhan S. Smart base isolated benchmark building part II: sample controllers for linear and friction isolation. InProc. 16th ASCE Engineering Mechanics Conference, July 2003 (pp. 16-18).

[3] He WL, Agrawal AK. Applications of several semi-active control systems to the benchmark base-isolated building. In Proceedings of the ASCE Engineering Mechanics Conference 2004 Jun.

[4] Huang, S., Huang, M., & Lyu, Y. (2021). Seismic performance analysis of a wind turbine with a monopile foundation affected by sea ice based on a simple numerical method. Engineering applications of computational fluid mechanics, 15(1), 1113-1133.

[5] Feng, Y., Zhang, B., Liu, Y., Niu, Z., Dai, B., Fan, Y., Chen, X. (2021). A 200-225-GHz Manifold-Coupled Multiplexer Utilizing Metal Wave guides. IEEE Transactions on Microwave Theory and Techniques, 1.

[6] Kim SB, Spencer Jr BF, Yun CB. Sliding mode fuzzy control for smart base isolated building. In17th ASCE Engineering Mechanics Conference (EM2004), Newark, USA 2004 Jun 13.

[7] Bai, Y., Nardi, D. C., Zhou, X., Picón, R. A., & Flórez-López, J. (2021). A new comprehensive model of damage for flexural subassemblies prone to fatigue. Computers & Structures, 256, 106639.

[8] Reigles D, Symans MD. Application of supervisory fuzzy logic controller to the base-isolated benchmark structure. In Proceedings of the ASCE Engineering Mechanics Conference 2004 Jun.

[9] Zhang, C., 2022. The active rotary inertia driver system for flutter vibration control of bridges and various promising applications. *Science China Technological Sciences*, pp.1-16.

[10] Choi KM, Jung HJ, Lee IW. Fuzzy control strategy for seismic response reduction of smart base isolated benchmark building. In17th ASCE Engineering Mechanics Conference 2004.

[11] Guo, Y., Yang, Y., Kong, Z., He, J., & Wu, H. (2022). Development of Similar Materials for Liquid-Solid Coupling and Its Application in Water Outburst and Mud Outburst Model Test of Deep Tunnel. Geofluids, 2022.

[12] Jung HJ, Moon YJ, Jang JE, Spencer BF. Robust hybrid control systems for seismic protection of benchmark base isolated building. Proceedings of the ASCE Engineering Mechanics Conference, June 2004, Newark, DE, CD-ROM.

[13] Huang, H., Li, M., Yuan, Y. and Bai, H., 2023. Experimental Research on the Seismic Performance of Precast Concrete Frame with Replaceable Artificial Controllable Plastic Hinges. *Journal of Structural Engineering*, *149*(1), p.04022222.

[14] Skinner RI, McVerry GH, Robinson WH. An Introduction to Seismic Isolation. Wiley, 1993 (ISBN: 047193433).

[15] Zhang, C. and Ali, A., 2021. The advancement of seismic isolation and energy dissipation mechanisms based on friction. *Soil Dynamics and Earthquake Engineering*, *146*, p.106746.

[16] Kakolvand, H., Ghazi, M., Mehrparvar, B. and Parvizi, S., 2022. Experimental and numerical study of a new proposed seismic isolator using steel rings (SISR). *Journal of Earthquake Engineering*, *26*(8), pp.4000-4029.

[17] Öncü-Davas, S. and Alhan, C., 2019. Reliability of semi-active seismic isolation under near-fault earthquakes. *Mechanical Systems and Signal Processing*, *114*, pp.146-164.

[18] Jiang, L., Zhong, J. and Yuan, W., 2020, October. The pulse effect on the isolation device optimization of simply supported bridges in near-fault regions. In *Structures* (Vol. 27, pp. 853-867). Elsevier.

[19] Wu, L.Y., Wang, Z., Ma, D., Zhang, J.W., Wu, G., Wen, S., Zha, M. and Wu, L., 2022. A continuous damage statistical constitutive model for sandstone and mudstone based on triaxial compression tests. *Rock Mechanics and Rock Engineering*, *55*(8), pp.4963-4978.

[20] Wu, L.Y., Ma, D., Wang, Z. and Zhang, J.W., 2022. Prediction and prevention of mining-induced water inrush from rock strata separation space by 3D similarity simulation testing: a case study of Yuan Zigou coal mine, China. *Geomechanics and Geophysics for Geo-Energy and Geo-Resources*, *8*(6), p.202.

[21] Kelly JM. Earthquake-Resistant Design with Rubber, 2nd ed. Springer: New York, 1997 (ISBN: 3540761314).

[22] Huang, Y., Zhang, W. and Liu, X., 2022. Assessment of diagonal macrocrack-induced debonding mechanisms in FRP-strengthened RC beams. *Journal of Composites for Construction*, *26*(5), p.04022056.

[23] Heaton TH, Hall JF, Wald DJ, Halling MW. Response of high-rise and base-isolated buildings to a hypothetical M w 7.0 blind thrust earthquake. Science. 1995 Jan 13; 267(5195):206-11; https://doi.org/10.1126/science.267.5195.206.

[24] Chen, J., Tong, H., Yuan, J., Fang, Y. and Gu, R., 2022. Permeability prediction model modified on Kozeny-Carman for building foundation of clay soil. *Buildings*, *12*(11), p.1798.

[25] Nagarajaiah S, Ferrell K. Stability of elastomeric seismic isolation bearings. Journal of Structural Engineering. 1999 Sep; 125(9):946-54; https://ascelibrary.org/doi/abs/10.1061/(ASCE)0733-9445(1999)125:9(946).

[26] Gu, M., Cai, X., Fu, Q., Li, H., Wang, X. and Mao, B., 2022. Numerical analysis of passive piles under surcharge load in extensively deep soft soil. *Buildings*, *12*(11), p.1988.

[27] Soong TT. Active Structural Control: Theory and Practice. Wiley: New York, ISBN 0-470-21670-0, 1991.

[28] Symans MD, Constantinou MC. Semi-active control systems for seismic protection of structures: a state-of-the-art review. Engineering structures. 1999 Jun 1; 21(6):469-87; https://doi.org/10.1016/S0141-0296(97)00225-3.

[29] Housner G, Bergman LA, Caughey TK, Chassiakos AG, Claus RO, Masri SF, Skelton RE, Soong TT, Spencer BF, Yao JT. Structural control: past, present, and future. Journal of engineering mechanics. 1997 Sep; 123(9):897-971; https://ascelibrary.org/doi/abs/10.1061/(ASCE)0733-9399(1997)123:9(897).

[30] Deng, E.F., Zhang, Z., Zhang, C.X., Tang, Y., Wang, W., Du, Z.J. and Gao, J.P., 2023. Experimental study on flexural behavior of UHPC wet joint in prefabricated multi-girder bridge. *Engineering Structures*, *275*, p.115314.

[31] Soong TT, Spencer Jr BF. Supplemental energy dissipation: state-of-the-art and state-of-the-practice. Engineering structures. 2002 Mar 1; 24(3):243-59; https://doi.org/10.1016/S0141-0296(01)00092-X.

[32] Zhai, S.Y., Lyu, Y.F., Cao, K., Li, G.Q., Wang, W.Y. and Chen, C., 2023. Seismic behavior of an innovative bolted connection with dual-slot hole for modular steel buildings. *Engineering Structures*, *279*, p.115619.

[33] Spencer Jr BF, Nagarajaiah S. State of the art of structural control. Journal of structural engineering. 2003 Jul; 129(7):845-56; https://ascelibrary.org/doi/abs/10.1061/(ASCE)0733-9445(2003)129:7(845).

[34] Wu, L., Ma, D., Wang, Z., Zhang, J., Zhang, B., Li, J., Liao, J. and Tong, J., 2023. An deep CNN-based constitutive model for describing of statics characteristics of rock materials. *Engineering Fracture Mechanics*, p.109054.

[35] Yang JN, Wu JC, Agrawal AK. Sliding mode control for nonlinear and hysteretic structures. Journal of Engineering Mechanics. 1995 Dec; 121(12):1330-9; https://ascelibrary.org/doi/abs/10.1061/(ASCE)0733-9399(1995)121:12(1330).

[36] Wang, G., Zhao, B., Wu, B., Wang, M., Liu, W., Zhou, H., Zhang, C., Wang, Y., Han, Y. and Xu, X., 2022. Research on the macro-mesoscopic response mechanism of multisphere approximated heteromorphic tailing particles. *Lithosphere*, *2022*(Special 10).

[37] Yang JN, Wu JC, Reinhorn AM, Riley M. Control of sliding-isolated buildings using sliding-mode control. Journal of Structural Engineering. 1996 Feb; 122(2):179-86; https://ascelibrary.org/doi/abs/10.1061/(ASCE)0733-9445(1996)122:2(179).

[38] Nagarajaiah S. Fuzzy controller for structures with hybrid isolation system. InProc. First World Conf. Struct. Control, Los Angeles, CA 1994 (pp. 67-76).

[39] Wang, G., Zhao, B., Wu, B., Zhang, C. and Liu, W., 2023. Intelligent prediction of slope stability based on visual exploratory data analysis of 77 in situ cases. *International Journal of Mining Science and Technology*, *33*(1), pp.47-59.

[40] Nagarajaiah S, Riley MA, Reinhorn A. Control of sliding-isolated bridge with absolute acceleration feedback. Journal of engineering Mechanics. 1993 Nov; 119(11):2317-32; https://ascelibrary.org/doi/abs/10.1061/(ASCE)0733-9399(1993)119%3A11(2317).

[41] Yang JN, Agrawal AK. Semi-active hybrid control systems for nonlinear buildings against near-field earthquakes. Engineering structures. 2002 Mar 1; 24(3):271-80; https://doi.org/10.1016/S0141-0296(01)00094-3.

[42] Yang JN. Application of optimal control theory to civil engineering structures. Journal of the engineering Mechanics Division. 1975 Dec;101(6):819-38; https://ascelibrary.org/doi/abs/10.1061/JMCEA3.0002075.

[43] Li, J., Cheng, F., Lin, G. and Wu, C., 2022. Improved hybrid method for the generation of ground motions compatible with the multi-damping design spectra. *Journal of Earthquake Engineering*, pp.1-27.

[44] Yang JN, Wu JC, Agrawal AK, Li Z. Sliding mode control for seismic-excited linear and nonlinear civil engineering structures. National Center for Earthquake Engineering Research, Technical Report NCEER-94-0017. 1994 Jun 21; https://ascelibrary.org/doi/abs/10.1061/%28ASCE%290733-9399%281995%29121%3A12%281386%29.

[45] Huang, S., Lyu, Y., Sha, H., & Xiu, L. (2021). Seismic performance assessment of unsaturated soil slope in different groundwater levels. Landslides, 18(8), 2813-2833.

[46] Panariello GF, Betti R, Longman RW. Optimal structural control via training on ensemble of earthquakes. Journal of engineering mechanics. 1997 Nov; 123(11):1170-9; https://ascelibrary.org/doi/abs/10.1061/(ASCE)0733-9399(1997)123:11(1170).

[47] Yoshioka H, Ramallo JC, Spencer Jr BF. "Smart" base isolation strategies employing magnetorheological dampers. Journal of engineering mechanics. 2002 May; 128(5):540-51; https://ascelibrary.org/doi/abs/10.1061/(ASCE)0733-9399(2002)128:5(540).

[48] Ramallo JC, Johnson EA, Spencer Jr BF. "Smart" base isolation systems. Journal of Engineering Mechanics. 2002 Oct; 128(10):1088-99; https://ascelibrary.org/doi/abs/10.1061/(ASCE)0733-9399(2002)128:10(1088).

[49] Alimoradi, H., Eskandari, E., Pourbagian, M. and Shams, M., 2022. A parametric study of subcooled flow boiling of Al2O3/water nanofluid using numerical simulation and artificial neural networks. *Nanoscale and Microscale Thermophysical Engineering*, *26*(2-3), pp.129-159.

[50] Soong TT, Grigoriu M. Random vibration of mechanical and structural systems. NASA STI/Recon Technical Report A. 1993; 93:14690; https://ui.adsabs.harvard.edu/abs/1993STIA...9314690S/abstract.

[51] He W. Smart energy dissipation systems for protection of civil infrastructures from near-field earthquakes. City University of New York; 2003; https://www.proquest.com/openview/0171ba4787fee2145cae0e21240e3fa2/1?pq-origsite=gscholar&cbl=18750&diss=y.

[52] He WL, Agrawal AK. An analytical model for ground motion pulses during near-field earthquakes for the design of smart protective systems. Journal of Structural Engineering (ASCE). 2005.

[53] Eskandari, E., Alimoradi, H., Pourbagian, M. and Shams, M., 2022. Numerical investigation and deep learning-based prediction of heat transfer characteristics and bubble dynamics of subcooled flow boiling in a vertical tube. *Korean Journal of Chemical Engineering*, *39*(12), pp.3227-3245.

[54] He WL, Agrawal AK. Passive and hybrid control systems for seismic protection of a benchmark cable-stayed bridge. Structural Control and Health Monitoring: The Official Journal of the International Association for Structural Control and Monitoring and of the European Association for the Control of Structures. 2007 Feb; 14(1):1-26; https://doi.org/10.1002/stc.81.

[55] Xu Z. Design and assessment of seismic protective systems for near-field ground motions. City University of New York; 2007; https://www.proquest.com/openview/d72dee3441cd311cd30c019d1718430a/1?pq-origsite=gscholar&cbl=18750.

[56] Agrawal, A.K., Xu, Z. and He, W.L., 2006. Ground motion pulse-based active control of a linear base-isolated benchmark building. *Structural Control and Health Monitoring: The Official Journal of the International Association for Structural Control and Monitoring and of the European Association for the Control of Structures*, *13*(2-3), pp.792-808.

[57] Xu, Z., Agrawal, A.K. and Yang, J.N., 2006. Semi-active and passive control of the phase I linear base-isolated benchmark building model. *Structural Control and Health Monitoring: The Official Journal of the International Association for Structural Control and Monitoring and of the European Association for the Control of Structures*, *13*(2-3), pp.626-648.

[58] Özuygur, A.R. and Noroozinejad Farsangi, E., 2021. Influence of pulse-like near-fault ground motions on the base-isolated buildings with LRB devices. *Practice Periodical on Structural Design and Construction*, *26*(4), p.04021027.

[59] AISC code, Specification for Structural Steel Buildings (ANSI/AISC 360-05), American Institute of Steel Construction, Inc., Chicago, IL., USA, 2005.

[60] International Herald Tribune, UN Says Half the World's Population will Live in Urban Areas by End of 2008, Associated Press, New York, NY, USA, 2009.

[61] Maffei J, Yuen N. Seismic performance and design requirements for high-rise buildings. Structural Magazine. 2007 Apr 28:28-32.

[62] Mehmood T, Warnitchai P, Suwansaya P. Seismic evaluation of tall buildings using a simplified but accurate analysis procedure. Journal of Earthquake Engineering. 2018 Mar 16; 22(3):356-81; https://doi.org/10.1080/13632469.2016.1224742.

[63] Code, U.B. UBC-97 in Structural Engineering Design Provisions, International Conference of Building Officials, Whittier, CA, USA, 1997.

[64] Prestandard FE. commentary for the seismic rehabilitation of buildings (FEMA356). Washington, DC: Federal Emergency Management Agency. 2000;7(2).

[65] Comartin CD. Seismic evaluation and retrofit of concrete buildings. Seismic Safety Commission, State of California; 1996.

[66] Soleimani S, Aziminejad A, Moghadam AS. Approximate two-component incremental dynamic analysis using a bidirectional energy-based pushover procedure. Engineering Structures. 2018 Feb 15; 157:86-95; https://doi.org/10.1016/j.engstruct.2017.11.056.

[67] Panyakapo P. Cyclic pushover analysis procedure to estimate seismic demands for buildings. Engineering Structures. 2014 May 1; 66:10-23; https://doi.org/10.1016/j.engstruct.2014.02.001.

[68] Poursha M, Khoshnoudian F, Moghadam AS. The extended consecutive modal pushover procedure for estimating the seismic demands of two-way unsymmetric-plan tall buildings under influence of two horizontal components of ground motions. Soil Dynamics and Earthquake Engineering. 2014 Aug 1; 63:162-73; https://doi.org/10.1016/j.soildyn.2014.02.001.

[69] Belejo A, Bento R. Improved modal pushover analysis in seismic assessment of asymmetric plan buildings under the influence of one and two horizontal components of ground motions. Soil Dynamics and Earthquake Engineering. 2016 Aug 1; 87:1-5; https://doi.org/10.1016/j.soildyn.2016.04.011.

[70] Soleimani S, Aziminejad A, Moghadam AS. Extending the concept of energy-based pushover analysis to assess seismic demands of asymmetric-plan buildings. Soil Dynamics and Earthquake Engineering. 2017 Feb 1; 93:29-41; https://doi.org/10.1016/j.soildyn.2016.11.014.

[71] Najam FA, Qureshi MI, Warnitchai P, Mehmood T. Prediction of nonlinear seismic demands of high-rise rocking wall structures using a simplified modal pushover analysis procedure. The Structural Design of Tall and Special Buildings. 2018 Oct 25; 27(15):e1506; https://doi.org/10.1002/tal.1506.

[72] Brozovič M, Dolšek M. Envelope-based pushover analysis procedure for the approximate seismic response analysis of buildings. Earthquake Engineering & Structural Dynamics. 2014 Jan; 43(1):77-96; https://doi.org/10.1002/eqe.2333.

[73] Sürmeli M, Yüksel E. An adaptive modal pushover analysis procedure (VMPA-A) for buildings subjected to bi-directional ground motions. Bulletin of Earthquake Engineering. 2018 Nov;16(11):5257-77; https://doi.org/10.1007/s10518-018-0324-x.

[74] Goel RK, Chopra AK. Role of higher-"mode" pushover analyses in seismic analysis of buildings. Earthquake Spectra. 2005 Nov; 21(4):1027-41; https://doi.org/10.1193%2F1.2085189.

[75] Attard, T. and Dhiradhamvit, K., 2009. Application and design of lead-core base isolation for reducing structural demands in short stiff and tall steel buildings and highway bridges subjected to near-field ground motions. *Journal of Mechanics of Materials and Structures*, *4*(5), pp.799-817.

[76] Jangid, R.S. and Kelly, J.M., 2001. Base isolation for near-fault motions. Earthquake engineering & structural dynamics, 30(5), pp.691-707.

[77] Jangid, R.S., 2007. Optimum lead–rubber isolation bearings for near-fault motions. Engineering structures, 29(10), pp.2503-2513.

[78] Kelly JM. The role of damping in seismic isolation. Earthquake engineering & structural dynamics. 1999 Jan; 28(1):3-20; https://doi.org/10.1002/(SICI)1096-9845(199901)28:1%3C3::AID-EQE801%3E3.0.CO;2-D.

[79] HITEC (Highway Innovation Technology Evaluation Center). Evaluation Findings for R.J. Watson Inc. Sliding Isolation Bearings. Reston (VA): Technical evaluation report, ASCE, 1998.

[80] Uniform Building Code. International Conference of Building Officials. Whittier, CA. 1997.

[81] Kelly JM. Earthquake-resistant design with rubber. 2nd ed. London: Springer-Verlag; 1997.

[82] Lee, D. and Taylor, D.P., 2001. Viscous damper development and future trends. *The structural design of tall buildings*, *10*(5), pp.311-320.

[83] Makris, N., 1998. Viscous heating of fluid dampers. I: Small-amplitude motions. *Journal of engineering mechanics*, *124*(11), pp.1210-1216.

[84] Makris, N., Roussos, Y., Whittaker, A.S. and Kelly, J.M., 1998. Viscous heating of fluid dampers. II: Large-amplitude motions. *Journal of Engineering Mechanics*, *124*(11), pp.1217-1223.

[85] Soong, T.T. and Dargush, G.F., 1997. Passive Energy Dissipation Systems in Structural Engineering Wiley. *Chichester, UK*.

[86] Skinner RI, Robinson WH, McVerry GH. An introduction to seismic isolation. London: John Wiley and Sons; 1993.

[87] Makris N. Rigidity–plasticity–viscosity: Can electrorheological dampers protect base-isolated structures from near-source ground motions? Earthquake Engineering & Structural Dynamics. 1997 May; 26(5):571-91; https://doi.org/10.1002/(SICI)1096-9845(199705)26:5%3C571::AID-EQE658%3E3.0.CO;2-6.

[88] Jouneghani KT, Hosseini M, Rohanimanesh MS, Dehkordi MR. Evaluating main parameters effects of near-field earthquakes on the behavior of concrete structures with moment frame system. Advances in Science and Technology. Research Journal. 2018; 12(3); http://dx.doi.org/10.12913/22998624/74135.

[89] Jouneghani KT, Hosseini M, Rohanimanesh MS, Dehkordi MR. Dynamic behavior of steel frames with tuned mass dampers. Advances in Science and Technology. Research Journal. 2017; 11(2); http://dx.doi.org/10.12913/22998624/70763.

[90] Jouneghani KT, Rohanimanesh MS, Hosseini M, Raissi M. Reducing the lateral displacement of lead rubber bearing isolators under the near field earthquakes by crosswise dissipaters connected to rigid support structure: earthquake engineering. Stavební obzor-Civil Engineering Journal. 2021 Dec 31; 30(4); https://doi.org/10.14311/CEJ.2021.04.0066.

[91] Rodolfo Saragoni, G. and Hart, G.C., 1973. Simulation of artificial earthquakes. *Earthquake Engineering & Structural Dynamics*, *2*(3), pp.249-267.

[92] Hayashi, K., Fujita, K., Tsuji, M. and Takewaki, I., 2018. A simple response evaluation method for base-isolation building-connection hybrid structural system under long-period and long-duration ground motion. *Frontiers in Built Environment*, *4*, p.2.

Nanomontmorillonite Reinforced Fibre Cements and Nanomontmorillonite-Nanosilica Reinforced Mortars

Styliani PAPATZANI[1]
Kevin PAINE[2]

ABSTRACT

In this study the effects of an organomodified nanomontmorillonite (nMt) dispersion (nC2) and of a powder type nMt (nC4), were compared in quaternary low carbon footprint fibre-reinforced cementitious nanocomposites and mortars. 60% Portland cement, 20% limestone (LS) and 20% fly ash plus fibres/superplasticizer comprised the reference paste. nMt was added at 1% by mass. Pastes were investigated in terms of flexural strength, thermal properties, density and water impermeability. Neither of the two types offered strength enhancement. nC2 showed some potentials at late ages (90 days). Thermal gravimetric analyses showed limited additional pozzolanic activity towards the production of additional C–S– H at day 90, in agreement with flexural strength results and X-ray diffraction analysis, which showed the consumption of $Ca(OH)_2$ even at day 28. No change in density was observed, whereas water impermeability tests showed that nC2 was more effectively organomodified not allowing water to be absorbed neither in the short nor in the long term, while nC4 at later ages seemed to be absorbing water back. Lastly, cubes of mortars were prepared and tested in compression in an attempt to fully investigate the potentials of the formulations. The effect of using simultaneously nMt and nanosilica (nS) was also recorded, however no increase in compressive strength was observed. The long-term density of the mortars was also investigated, results suggesting poor compaction which was not adjusted with the use of admixtures. These results are in support of previous studies undertaken in the field, showing that the purpose of use of organomodified nMt's must be clearly defined before any formulations are designed.

Keywords: Organomodified nanomontmorillonites, fibre cements, nanomontmorillonite and nanosilica enhanced mortars, characterization.

1 University of West Attica, Department of Surveying and Geoinformatics Engineering, Aigaleo, Greece
Hellenic Army Academy, Department of Mathematics and Engineering Sciences, Attika, Greece
spapatzani@uniwa.gr - spapatzani@sse.gr - https://orcid.org/0000-0001-8475-8975

2 Centre for Innovative Construction Materials University of Bath, Department of Architecture and Civil Engineering, Bath, England
k.paine@bath.ac.uk - https://orcid.org/0000-0001-7455-7002

1. INTRODUCTION

Under the European Union FP7 project (FIBCEM), different nanomontmorillonite (nMt) dispersions were produced by the project partners and tested in cementitious binders at the University of Bath, in an effort to produce low carbon footprint cements specifically for fibre cement applications [1,2]. Despite the availability of alternative cementitious systems [3–5], the carbon footprint of fibre cements is typically lowered by reducing the Portland cement content in binary combinations [6,7], as analytically reviewed elsewhere [8]. However, the downside to this is lower early-age strength and often lower long-term strength at the low water to cement (w/c) ratio required for manufacture. A potential solution to this is to use nanoparticles to nucleate and enhance the hydration processes, thus, in effect improving and maximising the cement hydration reactions [9–11]. The authors of the current paper have carried out exhaustive investigations on the level of CO_2 reduction that is technically achievable by minimizing Portland cement content and simultaneously, increasing the content of cement additions such as limestone, fly ash or silica fume in a number of different reference formulations, typical of the requirements for fibre cements [8], whilst trying to maintain performance through rational use of nanoparticles. In the process of finding the upper and lower limits of nanoparticle inclusion in these composite formulations, potential synergies amongst the constituents were determined, as well as antagonistic functionalities through a number of studies on different materials' combinations [8]. For example, in high fly ash content formulations, it was found that the inclusion of nanosilica did not exhaust the $Ca(OH)_2$ produced during the hydration of cement, but there was plenty of $Ca(OH)_2$ available for further reactions, given time. In fact, a direct correlation was observed between the $Ca(OH)_2$ available at different ages of curing with the compressive strength of the pastes.

In the research above, three nMt dispersions were compared, investigating their effectiveness in cementitious binders. In a recent publication, for the first time one organomodified dispersion (nC2) and the inorganic dispersion (nC3) were compared against an industrial product, of undispersed nanomontmorillonite in powder form (nC4) [12]. The reference formulation was a non-pozzolanic paste containing 60% PC, 40% LS, 3% PVA fibers and 2% superplasticizer. Furthermore, results on the effect of the undispersed nMt, nC4 in comparison with results on the effect of nC2 on flexural strength and crystallographic characteristics were presented in a pozzolanic reference paste containing 60%PC, 20%LS, 20%FA, 3% PVA fibres and 2% superplasticizer [13].

Further studies by other scientific teams have yielded promising results and have shed more light on the effect of nMts in cementitious matrices; for example it has been proven that cement pastes containing organomodified nanomontmorillonite possess damping properties, a result that can potentially alter the dynamic response of structures made by this material offering a more sustainable option for damping [14]. Moreover, it has been established that the cation exchange degree of nMts having the same modifier, affects the chemical reactivity of the nanoparticles and the lower it is the sooner the nanoparticles of montmorillonite can engage in pozzolanic reactions and the higher the mechanical properties measured [15]. In a subsequent study, four different nMts were synthesized with a modifier with and a modifier without aromatic substitute group and four different basal spacing (d_{001} by X-ray diffraction measurements) [16]. Cementitious nanocomposites were formulated with these four nMts additionally containing colloidal nanosilica with superplasticizing properties and tested. It was concluded that the aromatic substitute group lead to larger d_{001}, and this structural change

lead to enhanced hydration of the paste at earlier ages, signaling higher mechanical strength and considerably lower sorptivity, while strength development was almost unaffected by basal spacing. Very recently it was shown that another parameter that must be taken into consideration is the chain length of the surfactant, which was proven to affect the morphology of the cement nanocomposite and the mechanical strengths [17]. Only 0.5% addition of nMt lead to over 11% increase in compressive strength due to the filling and nanoreinforcement effect of the nMt. Furthermore, the pozzolanic activity of a bentonite clay, modified by silane was found superior even to calcined bentonite clay by quantifying portlandite consumption transforming into additional calcium silicate hydrates with the help of thermogravimetric and Rietveld analyses [18]. The additional advantage of this modification was that the swell index and hydrophilicity of the nanobentonite was considerably reduced. In a subsequent study the authors showed that silane treatment can successfully reduce the hydrophilicity of sodium montmorillonite up to 84% [19].

Following the strategy of previous research carried out by the authors, the carbon dioxide footprint of the formulations under consideration was limited in a twofold manner; (i) the amount of Portland cement was reduced beyond the acceptable by the Eurocodes limit and (ii) the amount of supplementary cementitious materials (SCM) was increased, again beyond the acceptable by the Eurocodes limit (Figure 1)[20]. To leverage possible delay in hydration reactions nanoparticles of montmorillonite have been added as SCM and nanoreinforcement in the resulting fibre cement nanohybrids. Therefore, the present study offers a complete overview of the microstructural and thermal changes the addition of similar nMt's can attribute to a pozzolanic reference paste, depending on their state (dispersed or in powder form).
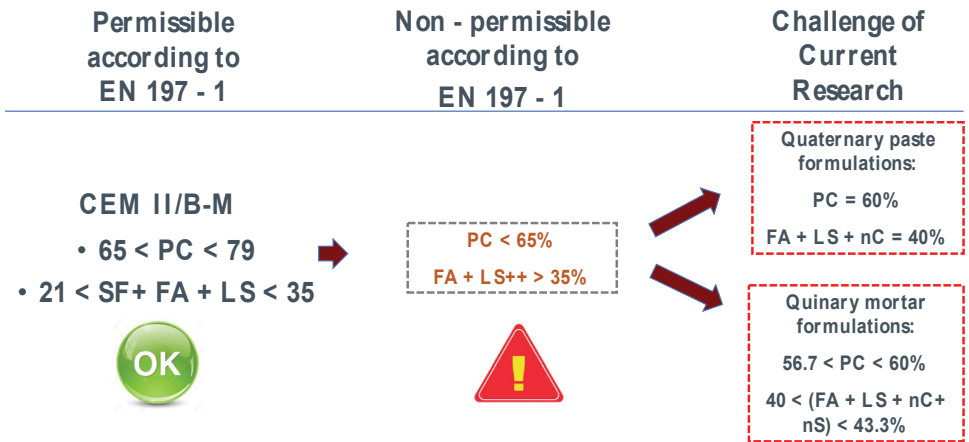
Figure 1 - Eurocode limits of clinker substitution and supplementary cementitious materials (SCM) addition and target of current research.

These new results on thermal properties, relative density and impermeability, that largely affect the microstructure and strength gain of cementitious nanocomposites are correlated with crystallographic results already presented [21]. Lastly, for the first time, compressive

strength and long term density of mortar cubes has also been tested in an effort to solidify the conclusions made with respect to pastes. In fact, the addition of nanomontmorillonite has been stretched by the additional inclusion of nanosilica, which has been found particularly effective in strength gain in previous research. This final paper of the extensive analysis of nanomodified pastes in ternary, quaternary or even quinary low Portland cement content formulations, contains the additional attempt for further activation of the nMt's by adding nanoparticles of silica (LnS) in the mortar mixes.

2. MATERIALS AND METHODS

2.1. Materials and Nanomaterials

The materials and nanomaterials used were:

- Portland limestone cement CEMII/A-L42.5 (containing 14% by mass of limestone). The supplier gave the following clinker composition: 70% C_3S, 4% C_2S, 9% C_3A, 12% C_4AF.

- Limestone (additional - LS), conforming to EN 197-1. The total LS content of each paste was the sum of that contained in the Portland limestone cement and this additional LS.

- Fly ash (FA), conforming to EN 450. The oxide composition provided by the material data sheet was: 53.5% SiO_2, 34.3% Al_2O_3, 3.6% Fe_2O_3, 4.4% CaO.

- Organomodified nanomontmorillonite (nMt), nC2 dispersed in water with the help of an alkyl aryl sulfonate surfactant, containing about 15% by mass of nMt particles.

- Organomodified nanomontmorillonite (nMt), nC4, a commercially available product by Sigma-Aldrich, undispersed – in powder form. It consists of Montmorillonite K-10 (70-75%) surface modified with 25-30WT% methyl dihydroxyethyl hydrogenated tallow ammonium (Nanomer® I.34MN). The supplier's data sheet gives the following additional information: 6.5<pH<7.0 and density = 1.7 g/cm^3. It should be noted that, the specific industrial product used has been discontinued recently.

- Commercially available colloidal amorphous nS containing 15% by mass of nanoparticles in an aqueous suspension (LnS).

- PVA fibers, kuralon H-1, 4 mm added at 3% by weight.

- Superplasticizer viscocrete 20HE, denoted as SP.

The levels of embodied CO_2 have been agreed in the UK and are evaluated in terms of kg CO_2 per tonne of binding material [22].

- PC = 930 kg CO_2/ tonne

- FA from coal burning power generation = 4 kg CO_2/ tonne

- LS = 32 kg CO_2/ tonne

It can be seen that in terms of CO_2 footprint, the use of FA as a supplementary cementitious material is beneficial. This is the reason for which it was used in the paste design despite of its shortage in the UK. The main goal of this research was to produce low carbon footprint cements. This was achieved by the following concept as also thoroughly explained utilizing Figure1: First of all PC, which is the most polluting material, was reduced below European Standard EN 197 -1 [23] acceptable limits and LS and FA were added above EN 197 -1 acceptable limits simultaneously. Moreover, of the available nanoparticles for cement scientists, the organomodified or inorganic nanoparticles have been produced by the naturally available material clay, by extracting the montmorillonite fraction and then a chemical (surfactant and/or modifier) is used. For the particular nMt's the platelets are not separated with calcination as with the calcined nanoclays [24] and therefore, nanohybrids of the above constituents present the lowest possible of embodied CO_2, even though the exact number of embodied CO_2 for the nanoparticles has not been assessed for the nMt nanoparticles.

2.2. Characterization of Constituent Materials and Nanomaterials

Particle size distribution analysis with optical system can provide the PSD of a wide range of scales of particles from 10 nm to 3 mm. Particle size distribution analysis was carried out at the MANIT laboratory, Bhopal, India, using a Laser Scattering Particle Size Distribution Analyzer Horiba LA950. Results are typical for this type of industrially available materials, as can be seen in Table 1 [20].

Table 1 - PSD results of materials [20].

	Mean size (µm)	Mode size (µm)	Median size (µm)	Diameter at 10% (µm)	Diameter at 90% (µm)
CEMII	11.38	2.74	3.25	1.40	22.16
LS	12.14	2.44	3.21	1.36	31.89
FA	9.09	2.14	2.53	1.46	10.13

The organomodified nanomontmorillonite nC2 was analyzed via X-ray diffraction (XRD), showing a d-spacing of 3.95 nm at 2.2°2θ and 2.0 nm at 4.4°2θ. Transmission electron microscopy (TEM) imaging revealed platelets ranging in size of 50-300 nm [25].

The commercial nanomontmorillonite had a particle size ≤ 20 micron but was also characterized before introduced to cement pastes. XRD analysis yielded a d-spacing of 1.8 nm which is more than expected for unmodified nanomontmorillonite. Transmission electron microscopy imaging showed platelets reaching the size of 100-300 nm [26].

The particles of nanosilica (nS) were characterized by means of TEM and SEM/EDX [13] and by Fourier transform infrared spectroscopy [27] by the authors in previously published research. They were found to be spherical with a diameter ranging from 8 nm to 50 nm. The LnS particles were homogenously dispersed in water and highly concentrated.

The characterization of the two organomodified nMt's via XRD, TEM, scanning electron microscopy coupled with X-ray energy dispersive spectroscopy and thermal gravimetric analyses (TGA) carried out in previously published research [12] has shown the following:

- TEM analyses showed that the production process for nC4 produced less crystalline structures.

- The XRD analysis of nC4 yielded a basal spacing (d-value) of 1.8 nm, which is more expected in unmodified nMt. nC2 seemed to have both intercalated (presence of higher order reflection which are typical of regular stackings) and exfoliated (disappearance of peak at 19.7 °2θ) platelets.

- Compared to nC2, the commercially available nC4 was better exfoliated, but showed marginally greater variation in Si/Al and more polycrystalline phases.

2.2. Methods

2.2.1. Formulation of nMt and Fibre Reinforced Cementitious Nanohybrids

Following previous research, the PC content was kept constant and the content of nMt solids was deducted from the LS content. By doing so, the $Ca(OH)_2$ production during PC hydration was comparable in all pastes, in order to detect potential additional pozzolanic activity due to the addition of nMt's [12]. The reference formulation comprised 60%PC, 20%LS, 20%FA, 3% PVA fibres and 2% superplasticizer, was denoted as F.PC60LS20FA20PVA3SP2 (F is for flexure) and was enhanced by the addition of nMt.

The formula for the nMt-fibre reinforced quaternary matrix was:

$$PC (60) + LS (20-x) + FA (20) + PVA (3) + SP (2) + xnMt \qquad (1)$$

Where x = % of nMt solids.

The different concentrations of the nMt dispersions are shown in Table 2. Only the 1% concentration was implemented, as it was found optimal in previous studies [8,12,28]. The amount of 2% superplasticizer was tested in previous research [12] and was found to be ideal in ternary formulations which also contained fibres and nMt, therefore the quaternary ones also started off with 2% superplasticizer. The water to solids ratio was kept constant for all formulations at 0.3.

Table 2 - Composition of quaternary fibre cement nanohybrids - proportions % by total mass of solids.

Sample Annotation	PC (%)	LS (%)	FA (%)	nMt (%solids)	SP (%)	PVA (%)	W/S
F.PC60LS20FA20PVA3SP2+0%nMt	60	20	20	0.0	2	3	0.3
F.PC60LS39PVA3SP2 +1%nC2	60	19	20	1.0	2	3	0.3
F.PC60LS39PVA3SP2 +1%nC4	60	19	20	1.0	2	3	0.3

A consistent mixing procedure has been followed for the entire project under which the current research is presented and has been already published by the authors [29]. The steps include:

- Dry mixing of all powder components was firstly carried out with a spatula by hand.
- For formulations containing nMt, the nC1 or nC2 nC3 dispersion was poured in a separate container together with water, stirred with the use of a magnetic stir bar for 1 min and then added to the mixed powders.
- The PVA fibres were added last after they had been manually further separated.
- With the addition of water (and nC2/nC4 where applicable), the paste was mixed employing a dual shaft mixer at 1150 rpm for a duration of up to four minutes.
- Slabs of 120 × 40 mm and 10 mm thickness were produced.

2.2.2. Formulation of nMt and nS Reinforced Mortars

A number of standard mortar cubes were also tested in compression in a final effort to explore any possible improvements within the new matrix (M.PC60LS20FA20), as shown in Table 3. The formulations were prepared in an automatic mixer complying with EN 196-1 mixing times. The w/b ratio was equal to 0.5, according to the standard and no superplasticizer was used. Distilled water and standard sand were used. The proportions by mass according to the standard were: one part of the cement, three parts of CEN Standard sand, and one half part of water (water/binder ratio 0.50). Each batch for three test specimens consisted of:

- (450 ± 2) g of powders (PC/LS/FA/nMt solids)
- (1 350 ± 5) g of sand and
- (225 ± 1) g of water

nC2 dispersion was diluted in the calculated amount of distilled water that was needed for every mortar combination.

nC4 being in powder form was dry mixed with other constituents in powder form (PC, LS and FA) and then water was added.

Table 3 - Composition of quaternary and quinary mortars - proportions % by total mass of solids.

Sample Annotation	PC (%)	LS (%)	FA (%)	nMt (%solids)	nS (%solids)	w/b
M.PC60LS20FA20+0%nMt	60	20	20	0.0	0.0	0.5
M.PC59LS20FA20+1%nC2	59	20	20	1.0	0.0	0.5
M.PC58LS20FA20+2%nC2	58	20	20	2.0	0.0	0.5
M.PC57.5LS20FA20+2%nC2+0.5%LnS	57.5	20	20	2.0	0.5	0.5
M.PC58.6LS20FA20+1.4%nC4	58.6	20	20	1.4	0.0	0.5
M.PC57.2LS20FA20+2.8%nC4	57.2	20	20	2.8	0.0	0.5
M.PC56.7LS20FA20+2.8%nC4+0.5%LnS	56.7	20	20	2.8	0.5	0.5

Each mortar formulation was cast into the standard moulds (160 x 40 x 40 mm), in three layers. It was vibrated and covered for 24 hours. Samples were demoulded and kept into water at 20±2ºC thereafter until the day of testing. On the day of testing (at day 7, 28, 56 and 90), cubes of 40 x 40 x 40 mm were cut from the prisms with a diamond saw at a very low speed to avoid cracking.

2.3. Characterization

2.3.1. Characterization of nMt and Fibre Reinforced Cementitious Nanohybrids and Mortars

The testing methodology comprised the following:

Flexural (three-point bending) strength tests were carried out in accordance with BS EN 12467. Flexural strength tests were carried out in accordance with BS EN 12467. Mean strength values of three specimens were calculated, as well as standard deviation at 7, 28, 56, and 90 days. All samples were tested at a loading speed of 0.5 MPa/s on a 100 kN servo hydraulic testing machine.

Thermogravimetric analysis (TGA) and derivative thermogravimetry (dTG) were carried out using Setaram TGA92. Each powder sample was placed in an alumina crucible and heated at a rate of 10 ºC/min from 20 to 1000 ºC in nitrogen atmosphere, as explained above for the characterization of nC4 at day 7, 28, 56, and 90. Buoyancy effects were taken into account, by correcting the curves using automatic blank curve subtraction. For the paste characterization, arrest of hydration was performed following two different methodologies: oven drying and solvent exchange. For TGA/dTG, the oven drying technique was adopted.

Three different areas were distinguished, as described in the literature, and correspond to the hydrates produced and consumed [29]:

i) The first area is related to the dehydration of C–S–H, ettringite, gehlenite and monosulfate, between 100◦C and 200◦C.

ii) The second area of interest is associated with the dehydration of $Ca(OH)_2$ between 440◦C and 510◦C.

iii) The third area of interest is the decomposition of $CaCO_3$ occurring between 700◦C and 810◦C.

For the late age relative density measurements, BS EN 12390-7:2009 [23], was selected as a basis and the exact procedure followed is covered in literature [29]. Mean density values of three specimens were calculated, as well as standard deviation.

Water impermeability tests were based on BS EN 492:2012 but the test was modified to account for the much smaller specimens used in this research (slabs 120 × 40 mm and 10 mm thickness). A transparent tube of 250 mm length was used as the water column with an internal bore of 29 mm diameter. A control water column was also adopted to ensure zero water evaporation in the laboratory testing environment. Tests were carried out at 7, 28 and 56 days.

2.3.2. Characterization of nMt and nS Reinforced Mortars

Compressive strength tests of mortars were carried out on three 40 mm cube specimens per mix [30]. All samples were tested at a loading speed of 0.5MPa/s. The compressive strength reported comprised the mean of the three results.

Long-term relative density of mortars was carried out in accordance with BS EN 12390-7:2009, which is designated for hardened concrete with limitations on the maximum coarse aggregate size, was selected as a basis for the long-term relative density measurements of the mortars. The volume of the specimen was obtained by water displacement because this method is suitable for specimens of irregular shape.

3. RESULTS & DISCUSSION

3.1. Results of nMt and Fibre Reinforced Cementitious Nanohybrids

3.1.1. Flexural Strength

As shown in Figure 2, nC4 provided marginal strength improvement at early ages, which, however, showed a reduction in strength at later ages (90 days). Although the standard deviation for the reference paste ranged was similar to the nC2 modified samples, for nC4 it was much lower and equal to about 0.8 MPa. This evidence of better distribution of nC4 in the mass of the paste did not offer strength improvements and therefore it has been postulated
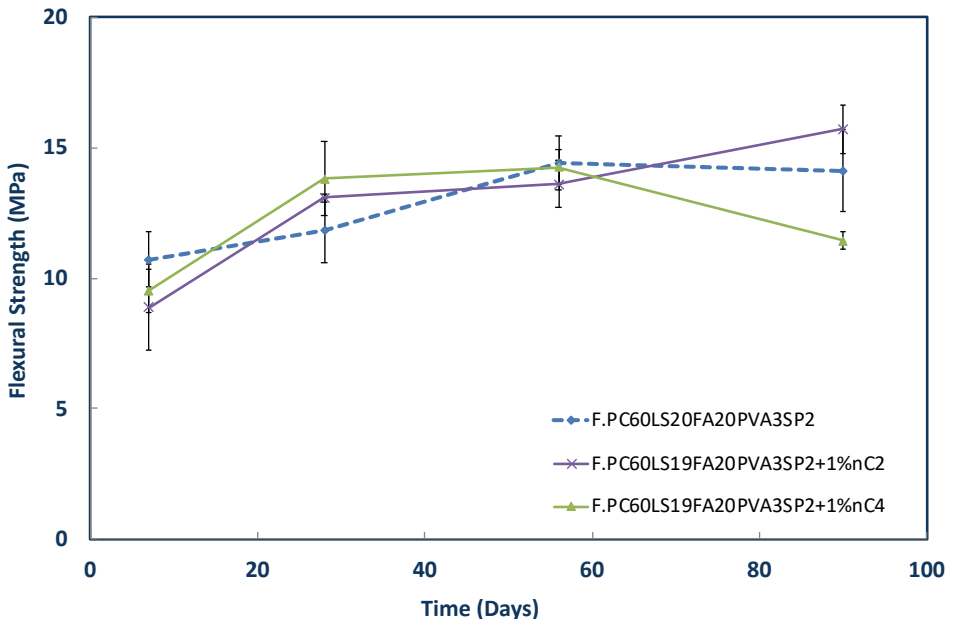
Figure 2 - Flexural strength of 1% nC2 and nC4 fibre-cement nanohybrids based on F.PC60LS20FA20PVA3SP2 [21].

that for cementitious nanohybrids it is best to disperse the nMt in water [21]. Moreover, with respect to nC4, the two events together; i.e. the significant error and the strength drop at later ages lead to the understanding that the specific commercial product is unstable in cement formulations. This conclusion is drawn by the fact that the reduced basal spacing of 1.8 nm, as discussed in section 2.1 above relates more to unmodified montmorillonite rather than modified one. It is possible, hence, that not all the platelets are individually available for reactions, as it should be the case. As a result, the commercial product is less reactive as a nanomaterial compared to nC2, that was produced for the scope of the FIBCEM project.

3.1.2. Thermal Gravimetric Analyses

For the fibre-cement nanohybrids based on F.PC60LS20FA20PVA3SP2, similar results to the ones based on F.PC60LS20FA20PVA3SP2 can be observed (Figure 3A and Figure 3B). Lastly, sample F.PC60LS19FA20PVA3SP2+1%nC4 seems to have carbonated, a condition that could be attributed to the fabrication process of the nMt and the properties this process yielded.
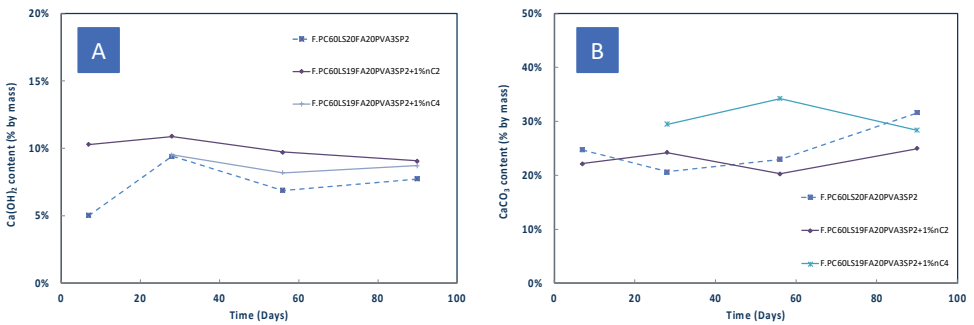
Figure 3 - Effect of nMt type on (A) Ca(OH)₂ and (B) CaCO₃ content of fibre-cement nanohybrids based on F.PC60LS20FA20PVA3SP2.

The pozzolanic performance was evaluated by TG analyses between approximately 100-180°C, at day 7, 28, 56 and at day 90 for the two different nMt types. As shown in Figure 4, at day 28 no additional C–S–H was produced neither by nC2 nor by nC4. By day 90 nC2 produced greater quantities of ettringite and C–S–H. However, sample F.PC60LS19FA20PVA3SP2+1%nC4 seems to have carbonated, therefore, the consumption of Ca(OH)₂ cannot be exclusively attributed to the production of ettringite and C–S–H. For this, X-ray diffraction analysis was also carried out at day 28 to assess the consumption of Ca(OH)₂ and monitor the amount of CaCO₃ present in the formulations, however no additional CaCO₃ was detected, whereas Ca(OH)₂ was indeed consumed [21].
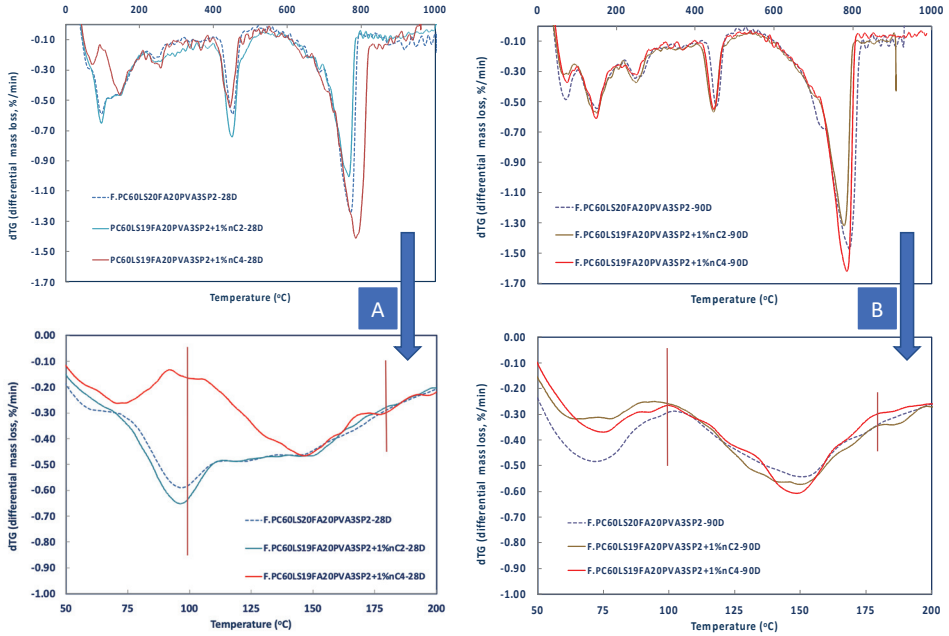
Figure 4 - Differential mass loss between 100-200°C of fibre-cement nanohybrids at (A) Day 28 [21] and (B) Day 90.

3.1.3. Relative Density Analyses

Late age (after month 3), relative density measurements were taken. All measurements showed a very low standard deviation (Figure 5) as in the case of the F.PC60LS40PVA3SP2 nanohybrids [12]. No significant difference between the reference paste and the nC2 or nC4 modified ones was observed and in fact, due to the very low nanoparticle addition no significant changes were expected either.

3.1.4. Water Permeability Analyses

Water impermeability tests were carried out for the fibre-cement nanohybrids based on F.PC60LS20FA20PVA3SP2, as before. As shown in Figure 6, the organoclays exhibited better performance than the reference nanohybrid at early ages. However, at later ages nC4 seemed to be less impermeable than the reference nanohybrid. These results are directly related to the flexural strength performance, as well, leading to the conclusion that the organomodification create clusters, increase porosity and in total, add localised weaknesses in the volume of fibre-cement nanohybrids.
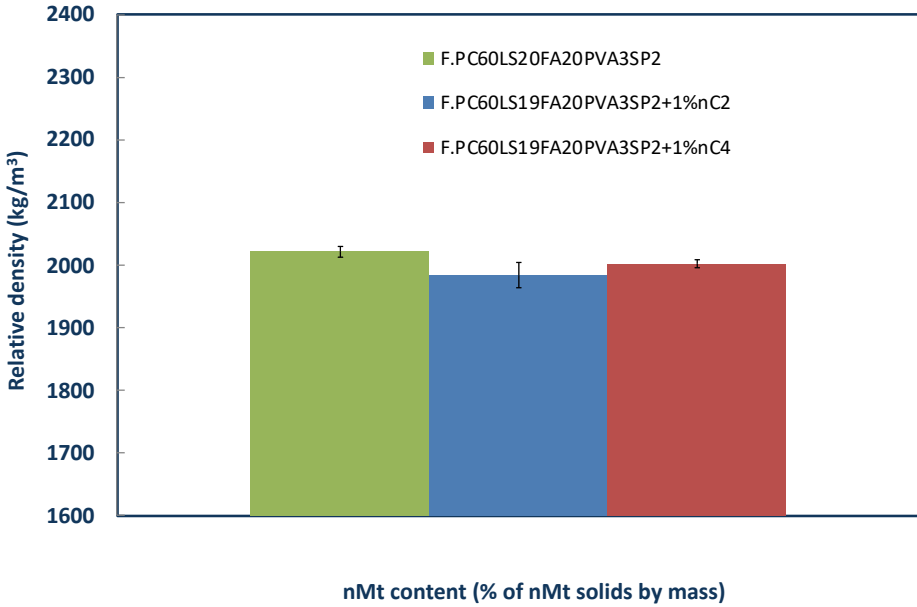
Figure 5 - Effect of nMt type on long term relative density of fibre-cement nanohybrids based on F.PC60LS20FA20PVA3SP2.
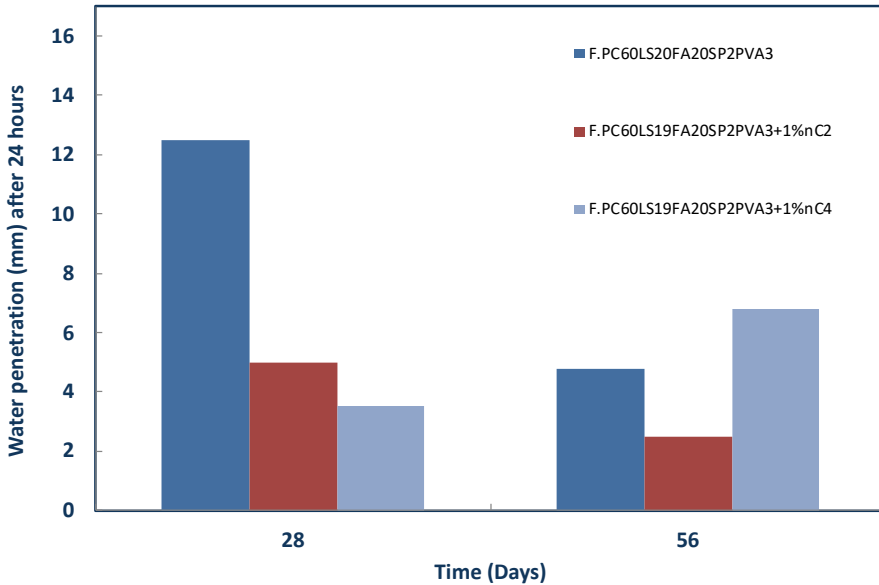
Figure 6 - Effect of nMt type on the impermeability of fibre-cement nanohybrids based on F.PC60LS20FA20PVA3SP2.

54

3.2. Results of nMt and nS Reinforced Mortars

3.2.1. Compressive Strength of Mortars Based on PC60LS20FA20

The compressive strength of mortar cubes based on PC60LS20FA20 and denoted as M.PC60LS20FA20 was measured (Figure 7). The standard deviation of the compressive strength remained within 0.5 and slightly increased for the higher nC2 concentrations, as expected since the dispersion was highly viscous. The best performance was achieved for the lower nC4 concentration, followed by the nC4 and nanosilica (nS) modified mortar. nC2 exhibited the lowest compressive strengths, however, best combination was given at 2% nC2 and 0.5% nS addition, as shown in Figure 7. It can also be deducted that nC4 could not be further optimized neither at greater concentrations nor with the addition of nS. The fact that nC4 absorbed water back into the paste could explain the drop of flexural strength at later ages.

It should be noted that the 28-day compressive strength of mortars containing 100% CEMII/A-L42.5 should be near 42.5 MPa. However, the mortar mixes tested contained 56.7 - 60% PC, hence the much lower 28-d compressive strength values. In addition, limestone content is very high 20% and fly ash content is equally very high, 20%, which has been found to delay strength gain beyond 56 days of curing. Although previous research on nanoreinforced pastes has shown that 0.5% addition of nanoparticles is optimum and in some mixes this addition can extend to 1.0%, the aim of this series of trial mortar mixes was to assess if the carbon footprint of the mix can be lowered by reducing the amount of PC and increasing the amount of nMt without compromising the strength. The experience gained by these results leads us to believe that the main difficulty in mortar mixes when using dispersed nMt rather than powder nMt, is to achieve homogeneous scattering of the nanoparticles throughout the matrix. For this, a step further would be to use sonicators for better dispersing nanoparticles within the mixes or nanofluidic droplets for more homogenous mixes [12]. Lastly, it could be argued that the compressive strength loss in the case of mortar application may be attributed to the effectiveness of surfactant in the presence of fine aggregate.

Interestingly, in a study published in 2021, on cementitious nanocomposites containing nMts and nanosilica the following mixing procedure yielded enhanced strength results; colloidal nanosilica with superplasticizing effects was used as dispersing medium. The nMt was poured into the nS suspension and part of the total required water and mixed with a magnetic hotplate stirrer at 1000 rpm for at least one hour. Then the nMt-nS-water suspension was mixed with cement and the residual water was added just before the mixing time was completed [16]. This procedure proved to be very efficient by providing highly dispersed suspensions, which eventually lead to higher observed compressive strength of the nanocomposites.

The issue with homogeneous dispersion of nMt in mortars has indeed attracted scientific attention. Another possible strategy for better dispersion of nMts in mortar matrices has been presented in 2022 [31]; wet grinding of raw montmorillonite in the presence of 1% of Polyethylene glycol for increased layer spacing through intercalation effect and enhancement of grinding efficiency, yielded an increase of 28.6% in one-day flexural strength for 2% nMT addition, although authors noted drawbacks to the later age strength development. More specifically the 28-day flexural strength of the nMt-mortars was similar to the reference mortar, whereas the 28-day compressive strength of the nMt-mortars was lower than the

reference mortar. The lower compressive strength at later age was attributed to the lower hydration degree of the higher (1% or 2%) nMt additions according to ^{29}Si NMR analyses. Also mercury intrusion porosimeter analyses showed that at 28 days the nMt enhanced mortars exhibited a larger harmful pore fraction than the reference mortar, a factor possibly contributing to the reduced compressive strength [31].
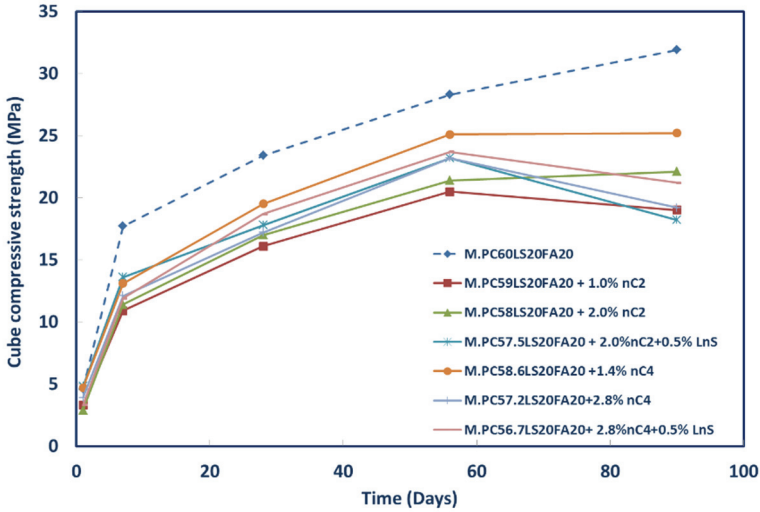
Figure 7 - Cube compressive strength of nC2 or nC4 and LnS modified mortars based on PC60LS20FA20.
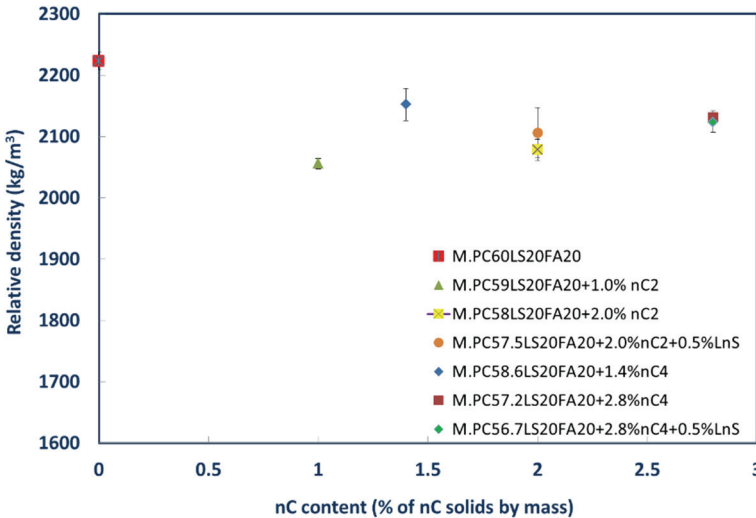
Figure 8 - Long term relative density of nC2 or nC4 and LnS modified mortars based on M.PC60LS20FA20.

3.2.2. Long Term Density of Mortars Based on PC60LS20FA20

The long term (after month 3) relative density measurements of the mortar cubes showed minor variation for nC2 and more significant for nC4 (Figure 8). The closest performance to the reference mortar was achieved by nC4. This is another indication as to why nC4 performed better in compression. The homogenous mixing and the compaction of the samples produced with nC4 was easier, due to the fact that it was added in powder form than in dispersion as nC2. This, possibly led to denser and more homogeneous mortars.

4. CONCLUSIONS

In the current paper, an exhaustive analysis of the addition of two different organomodified nMt's was presented. It was found that the one dispersed in water had better potential for improvement compared to the undispersed industrial product. Although $Ca(OH)_2$ was consumed, minimal amounts of additional C–S–H were identified, which could partially explain the limited strength enhancement. A hypothesis that nMt's act as nanofillers was rejected since there was practically no difference in the long-term density results. Moreover, results of impermeability tests were consistent with non-pozzolanic pastes, showing that nC2 can act as water barrier in pastes [12].

Lastly, the testing of various mortars led to the conclusion that nS can offer further improvements to nMt modified binders. Different compositions of nMt modified cements and mortars can yield significantly different mechanical performances. A possible advancement of the research on mortars could involve the production of samples with the use of nanofluidic droplets for the homogenous dispersion of nMt in the matrix and with lower w/b ratios containing superplasticizers, which are expected to yield interesting results as a number of limitations can be eradicated:

1. More coherent mortars can be delivered.
2. Nanoparticles mobility could be enhanced by avoiding clustering.
3. Minimization of total porosity would be expected.
4. Better pore size distribution should be maintained, since nanoparticles are better dispersed within the mass of mortars.

References

[1] R. Kalpokaitė-Dičkuvienė, I. Lukošiūtė, J. Čėsnienė, K. Brinkienė, A. Baltušnikas, Cement substitution by organoclay – The role of organoclay type, Cem. Concr. Compos. 62 (2015) 90–96. doi:10.1016/j.cemconcomp.2015.04.021.

[2] K. Brinkienė, J. Čėsnienė, I. Lukošiūtė, Baltušnikas, Arūnas, R. Kalpokaitė-Dičkuvienė, Effect of organoclay addition on durability related properties of cement pastes, Fresenius Environ. Bull. 24 (2015) 2624–2629.

[3] G. Habert, S.A. Miller, V.M. John, J.L. Provis, A. Favier, A. Horvath, et al., Environmental impacts and decarbonization strategies in the cement and concrete industries, Nat. Rev. Earth Environ. (2020). doi:10.1038/s43017-020-0093-3.

[4] E. Gartner, Industrially interesting approaches to "low-CO2" cements, Cem. Concr. Res. 34 (2004) 1489–1498. doi:10.1016/j.cemconres.2004.01.021.

[5] K.L. Scrivener, V.M. John, E.M. Gartner, Eco-efficient cements: Potential economically viable solutions for a low-CO2 cement-based materials industry, Cem. Concr. Res. 114 (2018) 2–26. doi:10.1016/j.cemconres.2018.03.015.

[6] X. He, X. Shi, Chloride permeability and microstructure of Portland cement mortars incorporating nanomaterials, Transp. Res. Rec. J. Transp. Res. Board. 2070 (2008) 13–21.

[7] N. Farzadnia, A.A. Abang Ali, R. Demirboga, M.P. Anwar, Effect of halloysite nanoclay on mechanical properties, thermal behavior and microstructure of cement mortars, Cem. Concr. Res. 48 (2013) 97–104. doi:http://dx.doi.org/10.1016/j.cemconres.2013.03.005.

[8] S. Papatzani, Effect of nanosilica and montmorillonite nanoclay particles on cement hydration and microstructure, Mater. Sci. Technol. 32 (2016) 138–153. doi:10.1179/1743284715Y.0000000067.

[9] M.C.G. Juenger, R. Siddique, Recent advances in understanding the role of supplementary cementitious materials in concrete, Cem. Concr. Res. 78 (2015) 71–80. doi:10.1016/j.cemconres.2015.03.018.

[10] D. Wang, C. Shi, Z. Wu, L. Wu, S. Xiang, X. Pan, Effects of nanomaterials on hardening of cement–silica fume–fly ash-based ultra-high-strength concrete, Adv. Cem. Res. 28 (2016) 555–566. doi:10.1680/jadcr.15.00080.

[11] Y. Reches, Nanoparticles as concrete additives: Review and perspectives, Constr. Build. Mater. 175 (2018) 483–495. doi:https://doi.org/10.1016/j.conbuildmat.2018.04.214.

[12] S. Papatzani, K. Paine, From Nanostructural Characterization of Nanoparticles to Performance Assessment of Low Clinker Fiber–Cement Nanohybrids, Appl. Sci. 9 (2019) 22. doi:10.3390/app9091938.

[13] S. Papatzani, K. Paine, Optimization of Low-Carbon Footprint Quaternary and Quinary (37 % Fly Ash) Cementitious Nanocomposites with Polycarboxylate or Aqueous Nanosilica Particles, Adv. Mater. Sci. Eng. 2019 (2019) 26. doi:10.1155/2019/5931306.

[14] P. Yu, Z. Wang, P. Lai, P. Zhang, J. Wang, Evaluation of mechanic damping properties of montmorillonite/organo-modified montmorillonite-reinforced cement paste, Constr. Build. Mater. 203 (2019) 356–365. doi:https://doi.org/10.1016/j.conbuildmat.2019.01.110.

[15] J. Čėsnienė, A. Baltušnikas, I. Lukošiūtė, K. Brinkienė, R. Kalpokaitė-Dičkuvienė, Influence of organoclay structural characteristics on properties and hydration of cement pastes, Constr. Build. Mater. 166 (2018) 59–71. doi:https://doi.org/10.1016/j.conbuildmat.2018.01.099.

[16] R. Kalpokaitė-Dičkuvienė, S.I. Lukošiūtė, A. Baltušnikas, J. Čėsnienė, Structural observation of cement paste modified with hydrophobic organoclay, Constr. Build. Mater. 272 (2021) 121931. doi:https://doi.org/10.1016/j.conbuildmat.2020.121931.

[17] J.-A. Oh, Y. Zhuge, S. Araby, R. Wang, H. Yu, W. Fan, et al., Cement nanocomposites containing montmorillonite nanosheets modified with surfactants of various chain lengths, Cem. Concr. Compos. 116 (2021) 103894. doi:https://doi.org/10.1016/j.cemconcomp.2020.103894.

[18] S. Khandelwal, K.Y. Rhee, Evaluation of pozzolanic activity, heterogeneous nucleation, and microstructure of cement composites with modified bentonite clays, Constr. Build. Mater. 323 (2022) 126617. doi:https://doi.org/10.1016/j.conbuildmat.2022.126617.

[19] S. Khandelwal, K.Y. Rhee, Effect of silane modified smectite clay on the hydration, intercalation of PCE superplasticizers, and mechanical strength of cement composites, Cem. Concr. Compos. 123 (2021) 104210. doi:https://doi.org/10.1016/j.cemconcomp.2021.104210.

[20] S. Papatzani, K. Paine, A Step by Step Methodology for Building Sustainable Cementitious Matrices, Appl. Sci. 10 (2020) 2955. doi:10.3390/app10082955.

[21] S. Papatzani, S. Grammatikos, K. Paine, Interesting remarks on the comparison of organomodified nanomontmorillonites in fibre-cement nanohybrids, IOP Conf. Ser. Mater. Sci. Eng. 842 (2020) 5. doi:https://doi.org/10.1088/1757-899X/842/1/012008.

[22] BCA, Fact Sheet 18 [Part 1] - Embodied CO2 of UK cement, additions and cementitious materials, (2009). www.cementindustry.co.uk.

[23] BSI, BS EN 197-1:2011: Cement. Part 1: Composition, specifications and conformity criteria for common cements, BSI, London, UK, 2011.

[24] S. Papatzani, E.G. Badogiannis, K. Paine, The pozzolanic properties of inorganic and organomodified nano-montmorillonite dispersions, Constr. Build. Mater. 167 (2018) 299–316. doi:10.1016/j.conbuildmat.2018.01.123.

[25] S. Papatzani, K. Paine, Inorganic and organomodified nano-montmorillonite dispersions for use as supplementary cementitious materials - A novel theory based on nanostructural studies, Nanocomposites. 3 (2017) 2–19. doi:10.1080/20550324.2017.1315210.

[26] S. Papatzani, Nanotechnologically modified cements: Effects on hydration, microstructure and physical properties, University of Bath, 2014.

[27] J. Calabria-Holley, K. Paine, S. Papatzani, Effects of nanosilica on the calcium silicate hydrates in Portland cement–fly ash systems, Adv. Cem. Res. 27 (2015) 187–200. doi:10.1680/adcr.13.00098.

[28] S. Papatzani, S. Grammatikos, K. Paine, Permeable Nanomontmorillonite and Fibre Reinforced Cementitious Binders, Materials (Basel). 12 (2019) 3245. doi:10.3390/ma12193245.

[29] S. Papatzani, K. Paine, Polycarboxylate/nanosilica-modified quaternary cement formulations – enhancements and limitations, Adv. Cem. Res. 30 (2018) 256–269. doi:10.1680/jadcr.17.00111.

[30] BSI, BS EN 196-1:2005: Methods of testing cement - determination of strength, BSI, London, UK, 2005.

[31] X. Gu, H. Tan, X. He, J. Zhang, X. Deng, Z. Zheng, et al., Improvement in flexural strength of Portland cement by lamellar structured montmorillonite, Constr. Build. Mater. 329 (2022) 127208. doi:https://doi.org/10.1016/j.conbuildmat.2022.127208.

Effect of Different Screen Types on Head Loss in Deep Wells Used for Irrigation

Nuri ORHAN[1]

ABSTRACT

This research was carried out with the help of a deep well simulator, which is commonly utilized for irrigation studies. In this study, flow types based on Reynolds number, well drawdown, head losses, and cost changes of these head losses were analyzed for four different sieve types used in wells. In addition, the flow types and head losses for the types of screen used were examined as per the theoretical calculations.

Theoretically, the turbulent head loss among types of screens was calculated at the highest (0.37 m) in the bridge slot screen (ST4) and at least (0.028 m) in the round slot (ST3). The drawdown is the sum of the head losses for deep wells. Among the well-types, the maximum drawdown (113.46 cm) was measured within the bridge slot well type (WT4), and the minimum drawdown (50.37 cm) was measured in the horizontal slot oblong well type (WT2). The least head loss per unit flow rate in the wells, which was formed with a horizontal oblong slot (WT2) screen, was measured in the well. Here, gravel and screen hole position affected the percentage of clogging in the screens. Over clogging of the screens caused the narrowing of the opening area, increased flow velocity and turbulent head loss, and increased drawdown.

It has been revealed that the use of a horizontal oblong slot screen, depending on the physical properties of the gravel used in this study, minimizes the head loss in the wells. One of the most important factors to be considered in well design is the compatibility of the screen type depending on the physical properties of the gravel. For example, changing the geometric shape among the screen types having similar apertures affected the blockage of the gravel, causing the head loss to change. The well-designers should pay attention to the selection of gravel depending on the screen type or the selection of the screen depending on the type of gravel used.

Keywords: Irrigation deep well, hydraulic conductivity, pumping, screen, head losses, drawdown.

1 University of Selcuk, Dep. of Agricultural Machinery and Technologies Engineering, Konya, Türkiye
nuriorhan@selcuk.edu.tr - https://orcid.org/0000-0002-9987-1695

1. INTRODUCTION

Water is globally used mainly for agricultural production. Irrigation accounts for 70% of the world's water usage, and about 17% of the cultivated land in the world is irrigated [1]. Approximately 96% of the unfrozen fresh water on Earth is stored as groundwater. Groundwater resources are one of the most reliable and healthy resources of freshwater found worldwide. Most of these underground water resources are used in agricultural irrigation activities. In Turkey, 32% of all agricultural irrigation activities are provided by underground water resources. This underground water is all brought to the surface by drilling different pumps with different diameters placed in deep wells. Even today, most wells are sized and created completely based on the drilling company's experience. Well designs may be more effective if geological and technological limitations on well geometry and its elements are understood. Prioritizing efficiency when designing a well would result in lower inlet losses and a slower rate of well-aging, thereby lowering expenses and extending the lifespan of the well [2]. The diameter of the well, gravel, and screen are the most important design parameters considered in deep wells for irrigation purposes. Among these, the most widely used design features are the screen velocity and the critical water inlet velocity (v_{critic}) to the screen [3, 4]. The water inlet rate to the screen varies according to the ratio of the aperture of the screen, the type and size of the screen slot, and the clogging of the screen with the gravel. The primary goal of the screen is to allow water to flow from the aquifer into the well while preventing loose dirt, silt, and rock from entering the well and reducing hydraulic resistance [5]. A good screen ensures the durability of the deep drilled well and its trouble-free operation [6]. Table 1 shows the screen types used in deep wells.

Table 1 - Typical open areas of screens [4]

Screen type	Open area (%)	Arrangement of slots
Louvered screens	<8	Horizontal
Slotted (bridge)	5–10	Vertical
Slotted (milled)	2–4	Horizontal or vertical
Wire wound	15–50	Horizontal

The drawdown is the total of the head losses brought on by aquifer loss, aquifer thickness, gravel pack, and screen during pumping from irrigation wells [7]. In other words, the main causes of the drawdown are the head losses brought on by the turbulent water flow around the filtered well. [8]. The head loss was also observed in some laboratory-scale pumping tests, affecting the pumping efficiency [9]. However, if the pumping rate is relatively small, the head loss when water flows through the pumping well would be relatively small [10]. In a study conducted to characterize the Konya region in Turkey, a total of 110 submersible irrigation pumping plants were tested, and it was determined that their flow rates varied between 20.4 and 60.5 L s^{-1} [11].

The porosity of the reduced well gravel pack increases the rate of flow of water. Some researchers generally recommend an inlet velocity of 0.03 m s^{-1} at the screen surface to avoid velocity losses and the aging of well [2-4]. Some researchers allow much higher speeds, such

as 0.6–1.2 ms^{-1} [12-14]. In the radial flow field around a well, a sharp increase in the velocities near its axis would potentially cause deviations from the laminar flow regime.

Reducing the open area in the screen region would further reduce the area made available for flow; thus, would further increase the velocity and triggers non-Darcy flow [15]. As a result, a quantitative link between the porosity of the gravel pack, the open sieve area, the effective casing diameter, and the linear laminar, nonlinear laminar, and turbulent head losses is developed [16]. Increasing the velocity in the screen zone affects the flow type and increases the head losses, and causes an additional drawdown [17].

As mentioned above, the screen, which is one of the important design parameters of irrigation wells, is used in different slot types and opening areas. The gravel, which is another design parameter, is used in different sizes and shapes. Well-designers in Turkey generally prefer vertical oblong slot screens as the screen type and 7–15 mm gravel as the gravel type. The fact that the experiments were carried out using a test tower designed by simulating an irrigation deep-well is the basis of the originality of this study. The main purpose of this study is to reveal the design parameters of the sheet-screen pipes having different slot shapes and opening ratios used in irrigation wells. Many researchers calculated the head losses and values of hydraulic conductivity in the screens by using different equations depending on the slot shape, slot area, opening ratio, and screen equipment pipe diameter. Similar calculations were made for other parameters that are important for the well design, such as aquifer, skin, and gravel pack. Through a thorough literature review on the design of deep-well screens, the question "whether the geometry of a screen slot showed a substantial influence on the performance of a screen" was not answered, properly. In the first part of this study, the drawdown levels occurring in the types of wells formed from different screens, including the specific flow rate of the wells and the specific drawdown values, were examined. In the second part, the flow type, head losses, hydraulic conductivity of the region in screen and gravel were determined by using the equations shown in the literature. In the third part of the study, head losses depending on the drawdown levels in deep wells were created by using different screen types. The cost of these head losses, the hydraulic conductivity, and their relations with the gravel package was examined.

2. MATERIALS AND METHODS

The Faculty of Agriculture, Agricultural Machinery and Technology Engineering at Selcuk University's Deep Well Testing Simulator was used to conduct the investigation.

In this study, a submersible pump with a 6" nominal diameter, a DN80 electromagnetic flowmeter, a digital display manometer with a 0-10 bar measurement range, and a level measurement sensor are used. The gravel casing pipes were filled with approximately 2 m^3 of clean, washed gravel shown in Figure 1.

The tank, which consisted of pipes having diameters of 6" and 3", supplied water to the deep well built for the tests. The deep well test tower used the compound containers method to establish these connections (Figure 1). The operational characteristics of the pump were determined as per EN ISO 9906 [18, 19].

In the experiments, an 8 m long-closed pipe with different screen types of length 2 m and diameter of 12" was used for all gravel types. Using pipes made specifically for gravel casing,

the gravel was poured around the screen pipe. Table 2 displays the average of some of the physical characteristics of the gravel as determined by measurements made on the 100 gravel samples taken from the pile [20, 21]. Table 2 shows that 76% of the gravel used in the studies lies between the sizes of 7 and 15 mm. Furthermore, the gravel used in the well had a porosity of 44%.

Four different screen types were tested, namely, the vertical oblong slot screen (ST1), the horizontal oblong slot screen (ST2), the round slot screen (ST3), and the bridged screen (ST4). The wells created by these screens were named WT1, WT2, WT3, and WT4, respectively. The technical specifications of the screens are provided in Table 3, and Figure 2 shows their pictures and slot sizes.
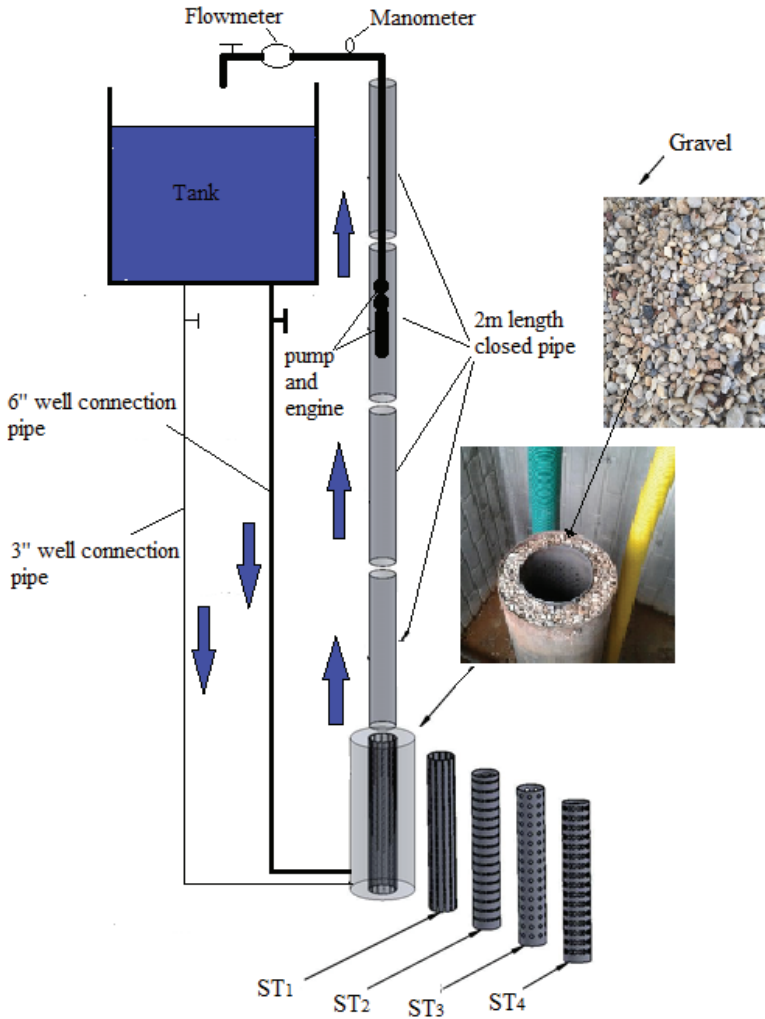
Figure 1 - Well equipment and the the operation of screens

Table 2 - Some of the physical characteristics of gravel utilized in tests [22]

Physical property	Average value
Bulk density (kg dm^{-3})	1.54
Density (kg dm^{-3})	2.75
Porosity (%)	44
Thickness (mm)	14.3
Length (mm)	19.6
Thickness (mm)	9.1
Geometric diameter (mm)	13.5
Globularness (%)	70
Natural agglomeration angle (°)	22.76
Metal-gravel static friction coefficient (-)	41.9
Frequency distribution of particles in terms of geometric diameter	
7.68 mm (min.) –10.00 mm (%)	8
10.01 mm –13.50 mm (%)	46
13.51 mm –15.00 mm (%)	22
15.01 mm –18.00 mm (%)	12
18.01 mm–21.94 mm (max.) (%)	12

Table 3 - Some dimensions and technical specifications of screen type equipment pipes

Inner diameter (mm)	Thickness (mm)	Material	Length (mm)	Unit weight (kg/m)	Screen type	Number (pcs)	Slot total area/Pipe surface area ratio (%)
302	5.00	Cast	2003	30.0	ST1 (vertical oblong)	1	9.3
303	5.00	Cast	2010	30.8	ST2 (horizontal oblong)	1	9.2
301	5.01	Cast	1950	23.1	ST3 (round)	1	19
302	4.75	Cast	1996	31.1	ST4 (bridged)	1	5.3

The drawdown (Δ) was measured for each of the wells having different screen types, the submersible pump (D) operating at the optimum speed, and for five different flow ranges (40, 45, 50, 55, 60 m^3 h^{-1}) (Figure 3). The first values were recorded when the pump was run at a specific flow rate, and the other flow rates were further tested. In addition, pump outlet pressure (P) and power (N) values were measured.

Software and automation systems were made to record the measured data. The information from the system sensors was wirelessly sent to the main computer using a data acquisition

card and a Bluetooth module. The central computer saved the necessary information, and the operator provided an appropriate name via the software interface. One measurement per second was chosen as the recording speed. Once the pump began to operate the recording procedure started and each sensor produced 50 data recordings. The tests were conducted at a depth of 188 cm (continuous hydraulic head). The level meter measured the drawdown (Δ) [23].
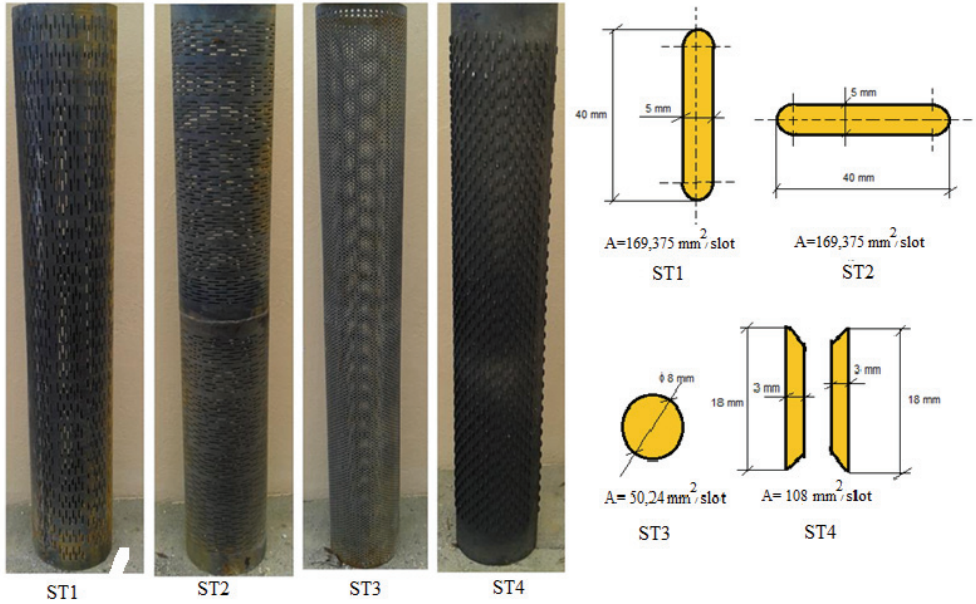
Figure 2 - Screen types and screen slot sizes
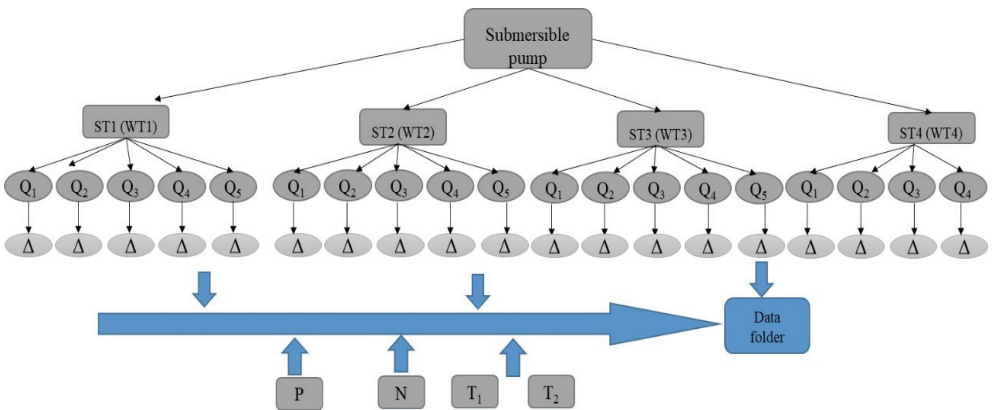
Figure 3 – Experimentation plan

3. RESULTS AND DISCUSSION

The findings will be presented in three stages. In the first part, the drawdown of the well consisting of different screen types, the specific flow rate, and the drawdown per unit flow rate are examined. The flow types, hydraulic conductivity, and head losses in different screen types are assessed in the second part. In the third part, the total head loss due to the drawdown, including the cost of the head loss and the hydraulic conductivity of the wells, are evaluated from the wells created by these screens. During experimentation, the average air and water temperatures were 15 °C and 12 °C, respectively. The constant hydraulic head of 188 cm and a level of 89 cm of static water level are the constant values maintained during the installation of the pump in the well and during all experiments.

3.1. Effect of the Well Types on the Drawdown

The drawdown values of the types of wells formed by vertical slot oblong (ST1), horizontal slot oblong (ST2), round slot (ST3), and the bridge (ST4) type screens are examined in this section. The wells created from these screens are named WT1, WT2, WT3, and WT4, respectively.
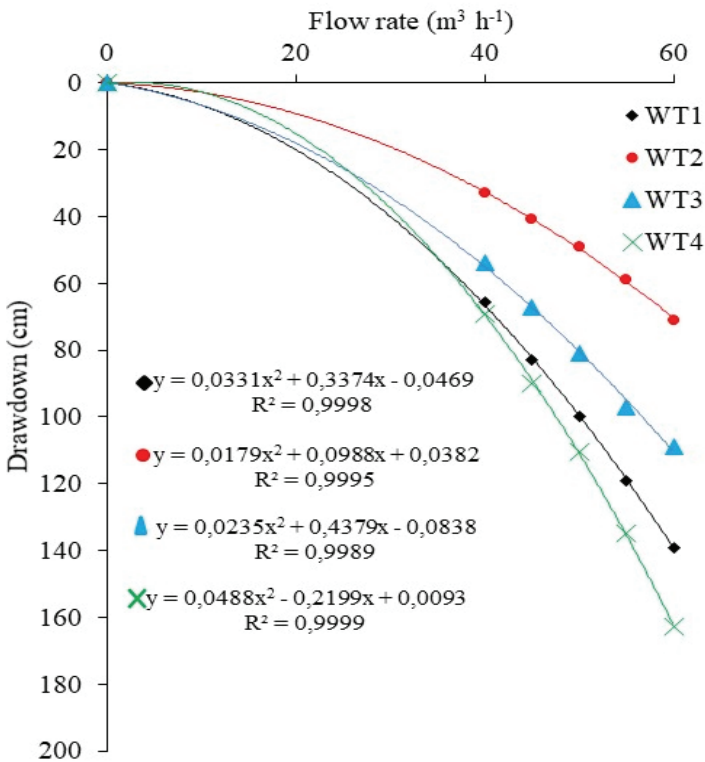
Figure 4 - The relationship between screen types and drawdown

In all well types, the drawdown increased as the flow rate increased. The highest decrease in fixed flow values of all well types was seen in WT4. The observed drawdowns in WT1, WT3, and WT2 well types were ranked in decreasing order.

When the well types are evaluated in terms of drawdown, it can be said that the most suitable sieve type is ST2, and the worst sieve type is ST4.

The increase in drawdown is an undesirable physical condition and is an indicator of well rig resistance. However, the drawdown is not the only criterion considered during the preference or selection of the screen types. Also, the filtration capacity of the screens serves as an important factor, since the screens have the task of preventing sediments (solid particles) such as sand and silt from entering the well from the aquifer during pumping. Therefore, the design or selection of the screens must be optimized in terms of drawdown and filtration efficiency. However, this issue was excluded from the scope of this study.

In the well-types, the maximum drawdown of 113.46 cm was measured in the WT4 well type, and the minimum decrease of 50.37 cm was measured in the WT2 well type. In the analysis of the variance applied to the drawdown values, it was found that the flow rate, well type, and the interaction of these two parameters were statistically different ($P<0.01$). The drawdown level in the wells increase with the increase in flow rate for all well types. Due to this increased value, the R^2 values were also very high (Figure 4).

The specific flow rate is the yield of a well corresponding to the unit drawdown. In this study, the values of the mean specific flow of the WT1, WT2, WT3, and WT4 wells formed from different screen types were calculated as 14.2, 28.4, 17.5, and 12.8 (L s^{-1}) m^{-1}, respectively. The specific flow decreased in the well-type that had the highest drawdown. Another parameter well-design is the drawdown value per unit of the pumping speed. The average specific drawdown values were 0.0715, 0.0357, 0.0577, 0.08 m (L s^{-1})$^{-1}$ for WT1, WT2, WT3, and WT4, respectively. Although the slot geometry and open area of the screens in the WT1 and WT2 wells were the same, a double difference between them existed in the drawdown, the average specific flow, and the specific drawdown. The slot position of the WT2 well-type screen caused the gravels not to close the screen openings. It is generally assumed that 50% of the aperture area of the screens can be clogged by gravel particles (Delleur 2010). Since the screen types were compared in this study, the openings of the gravel particles were not calculated according to 50% occlusion.

3.2. In the Screen Types Flow Velocity and Reynolds Number

In this section, the water inlet velocity, Reynolds number, hydraulic conductivity, and the head losses of the screen types and the gravel region used in this study are calculated based on the literature.

The rate of water entry into the well increases with the decrease in porosity or screen opening ratio. In the well-design, the screen water inlet velocity should not exceed 0.03 m s^{-1} [2, 24].

Exceeding this speed would cause increased head loss and aging of the well [16]. However, some researchers allow higher velocities [2, 12].

The water inlet velocity was calculated separately according to Equation 1, depending on the prosthesis of the gravel and the aperture ratio (Ap) of the screens.

$$V_a = \frac{Q}{2.\pi.r.b.Ap} \qquad (1)$$

where;

V_a = Average flow velocity (m s^{-1}),

Q   = Pumping rate (m^3 h^{-1}),

r   = Radius (The screens values in Table 3 and gravel in 100 mm have been used) (m)

b   = The height of the cylinder here (m)

Ap   = Porosity of a porous gravel medium or the open area of a screen

The determination of the flow regime is done by calculating the Reynolds number. The streamlines remain straight when the Reynolds number is less than 2, and the flow obeys Darcy's law. However, as the Re number increases eddies form intermittently. For Re numbers larger than 75 flow behaves more like turbulent. The increase in the flow velocity toward the well indicates that there may be deviations from Darcy's law, especially when very close to the well [2]. The Reynolds number at the screen inlet and the gravel region was calculated by using the following equation [5, 16, 25].

$$Re = \frac{\rho.v_a.d}{\mu} \qquad (2)$$

where;

ρ = Density of water (at 14 °C, it is 999.85 kg m^{-3}),

v_a = Water inlet velocity (m s^{-1}),

μ = Dynamic viscosity of water (at 14 °C, it is 0.0013097 kg m^{-1} s^{-1}),

d   = Characteristic length (m); For the gravel pack and the screen, the characteristic length equals the mean grain size d_{50} and the slot width W_{sl}.

In this study, the flow velocity of the gravel region was calculated between 0.04–0.06 m s^{-1} depending on the flow rate. Accordingly, the Reynolds number was also calculated within the range of $385 < Re < 575$. Bear [26] gives the range Re = 60–150 for the onset of turbulence in porous media, based on the literature review of experimental studies. During critical Reynolds numbers between Re = 100 [27] and 800 [28], the flow in the porous medium is considered to be purely turbulent. Based on these, occurrence of completely turbulent flow in the gravel region of the study was revealed.

In the screen types, the inlet flow velocities and Reynolds numbers depending on the aperture ratios are given in Figure 5. The decrease in the aperture ratios in the screen types increased the inlet velocity and caused turbulent flow. The flow rate and the Re number were the highest in the ST4 screen type, with the lowest aperture ratio. The highest drawdown values were also measured in the WT4 well-type created from this screen. However, the drawdown in the wells formed from these screens was different, although the aperture ratios, flow rates, and Re numbers in ST1 and ST2 screens were very close to each other. Although the ST3 screen had the highest aperture ratio and the lowest inlet velocity and Re number, it performed worse than the ST2 in the well-drawdown. Here, the position and shape of the screen slots affected the blockage of the pebbles in the well.
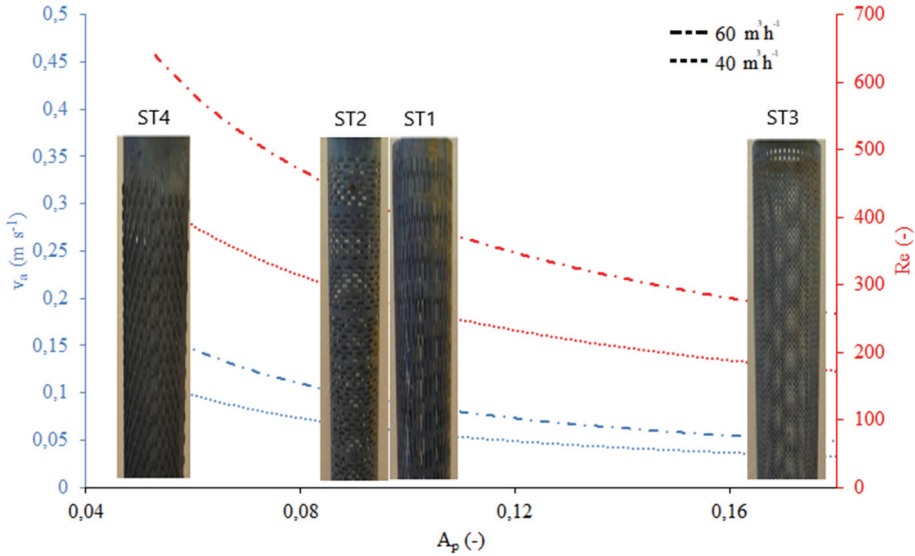
Figure 5 - Variation of Reynolds number (Re - red lines) and the velocity (Va- blue lines) depending on the screen opening ratio at flow rates of 40 (---) and 60 (– - –) m³ h⁻¹.

3.3. Head Loss and Hydraulic Conductivity of the Different Screen Types

Direct measurement of hydraulic conductivity is complicated, as the head losses in the screens are usually very small.

Various studies have been made based on the linear laminar flow assumption to calculate the head losses or hydraulic conductivity of the screens [29-33]

Barrash, et al. [29] suggested that the conductivity of a screen can be calculated according to Equation 3, based on Cubic's law [34] for linear laminar flow. Barrash, et al. [29] reported that screen conductivities obtained through laboratory experiments could be reconstructed by using Equation 3.

$$K_{sc} = n_s \frac{w_s^3 \cdot \rho \cdot g}{12 \cdot f_r \cdot \mu} \qquad (3)$$

where;

n_s	= Number of slots per length
w_s	= Screen slot width (m)
ρ	= Density of water (at 14 °C, it is 999.85 kg m⁻³)
g	= Gravitational acceleration (m s⁻²)
f_r	= Slot surface roughness (f≥1)
μ	= Dynamic viscosity of water (at 14 °C, it is 0.0013097 kg m⁻¹ s⁻¹),

The calculation of head loss based on linear flow can be made according to the Theim's equation (Equation 4) [7]. Some researchers suggested the turbulent flow in the screen region [13, 35-38]. As a result of their laboratory and field studies, Equation 5 for nonlinear flow was developed by Clark and Turner [37].

$$S_{sc} = \frac{Q}{2.\pi.K_{sc}.B} \ln\left(\frac{r_{s-in}}{r_{s-out}}\right) \qquad (4)$$

where;

S_{sc}	= Screen head losses (m)	
Q	= Flow rate (m^3 h^{-1})	
K_{sc}	= Screen hydraulic conductivity (ms^{-1})	
B	= Full aquifer thickness (m)	
r_{s-in}	= inner radius screen pipe (m)	
r_{s-out}	= inner radius screen pipe (m)	
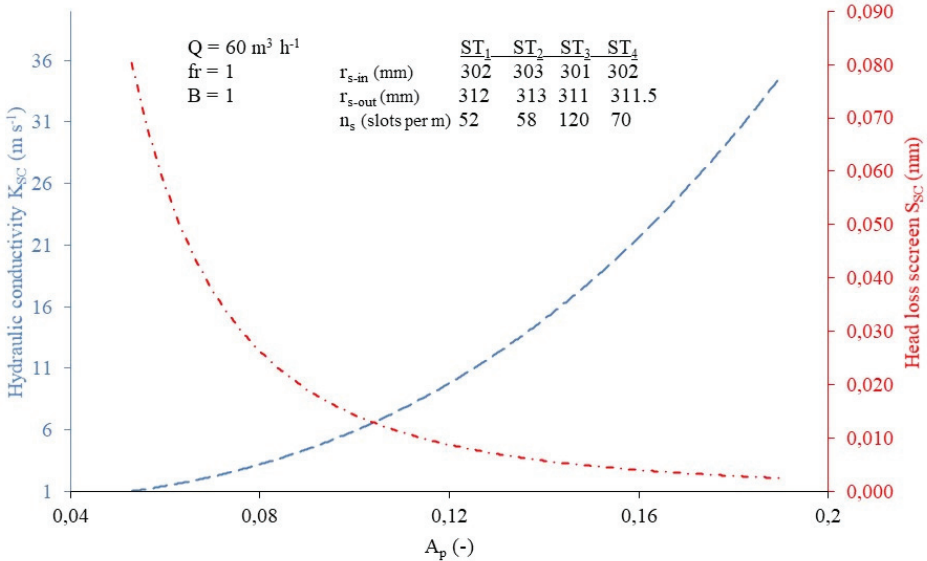
Figure 6 - Relationship between the hydraulic conductivity (blue lines) (according to Equation 3) and linear head loss (red lines) depending on the screen aperture ratios (according to Equation 4).

The value of hydraulic conductivity of the screen types used in the research was calculated according to Equation 3, and the linear head loss was calculated as per Equation 4, respectively. Figure 6 presents the calculated values based on the screen aperture ratio. Among the screen types, the highest value of hydraulic conductivity was calculated to be 38.34 ms^{-1} in ST3, and the least with 1.17 ms^{-1} in ST4. The highest head loss value of 0.069

mm was calculated in ST4 with, and the lowest value of 0.0022 mm in ST3. However, the ST2 screen type was the least drawdown (head loss) measured in the wells formed from the screens. Here, the state of blocking the screen slots of the gravel or the screen-gravel compatibility comes to the fore.

Houben [7] reported that the effect of the slot widths of the screen larger than 0.3 mm on the head loss could be neglected, according to Equation 3 (Cubic's law). In this study, the head loss values of the screens were found to be very low according to Cubic's rule (Figure 3). However, the fact that there was a difference only in the geometric shapes of ST1 and ST2 screens, which had the same slot widths affected the drawdown values in the wells created from these screens. In this case, it has been revealed that the slot shape positions are also an important factor in the designing of wells and the slot widths.

Houben and Hauschild [30] reported that screens having hydraulic conductivity lower than 0.0001 ms^{-1} for the linear laminar model would affect the total drawdown of the well. Thus, based on this, since the range of hydraulic conductivities observed in this work is larger than suggested limiting value, they do not affect the drawdown directly.

During the case of turbulent flow within the screen region, the head loss was calculated as per Equation 5 and is shown in Figure 7. The head loss increased with increasing of the screen inlet velocity. The head losses of the ST1-ST2-ST3 andST4 screen types at a flow rate of 60 m^3 h^{-1} were calculated as 0.12 m, 0.123 m, 0.028 m, and 0.37 m, respectively. The head losses occurring during the highest screen inlet velocities were low, which can be expressed in cm. The ST3 screen type was found to be especially very low. According to Equation 5, Houben [7] calculated the load losses at 0.03, 0.1, and 0.5 ms^{-1} as 0.12, 1.4, and 34.5 mm, respectively, and reported that it was small enough even in the worst case. According to both linear head loss and turbulent flow calculations, it can be said that the head loss increases when the ST4 type screen is used. This study observed the highest drawdown in the deep well-formed from the ST4 screen type.
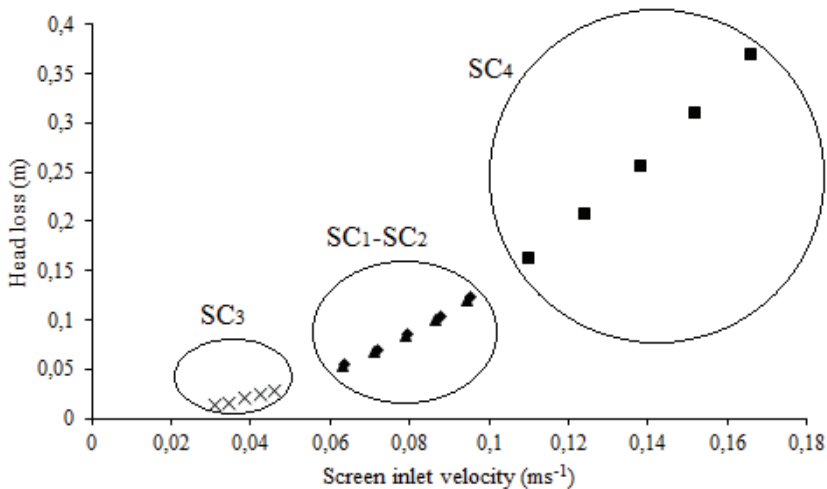
Figure 7 - Head loss according to Equation 5 in case of turbulent flow

$$S_{sc} = \frac{1}{2g} \left(\frac{Q}{2.\pi.L_s.C_v.C_c.A_p} \right)^2 \tag{5}$$

Where

Ssc   = Screen head losses (m)
Q   = Flow rate (m³ h⁻¹)
Ls   = Length of screen (m)
Cv   = Slot velocity coefficient (~0.98 (Houben, 2018)) (−)
Cc   = Contraction coefficient (~0.66 (Houben, 2018)) (−)
Ap   = Fractional open area (-)

3.4 Head loss and Hydraulic Conductivity of the Gravel

The hydraulic conductivities and the linear head losses for the gravel used in the study were determined. The hydraulic conductivity of the pack of gravel is related to its prosthesis. Houben, et al. [16] calculated the Kozeny-Carman equation for the calculation of the hydraulic conductivity [39] according to Bear [40] (Equation 6). The value of hydraulic conductivity was calculated according to Equation 6. The calculation of the linear head loss for the gravel package was made according to Equation 7. The hydraulic conductivity of the gravel was measured to be 1.9 ms⁻¹. This hydraulic conductivity and laminar head loss during a flow rate of 60 m³ h⁻¹ were calculated to be 0.39 mm.

$$K_{gp} = \left(\frac{\rho g}{\mu} \right) \left(\frac{d_{50}^2}{180} \right) \left(\frac{n^3}{(1-n)^2} \right) \tag{6}$$

where;

Kgp   = hydraulic conductivity of gravel pack (ms⁻¹)
n   = gravel zone prozite (-)
d₅₀   = mean grain size of gravel pack (m)
ρ   = Density of water (at 14 °C, it is 999.85 kg m⁻³)
μ   = dynamic viscosity of water (at 14 °C, it is 0.0013097 kg m⁻¹ s⁻¹)

$$S_{gp} = \frac{Q}{2.\pi.K_{gp}.B} \ln\left(\frac{r_{s-in}}{r_{s-out}} \right) \tag{7}$$

where;

Sgp   = head loss gravel pack (m)
rs-in   = inner radius screen pipe (m) (0.3 m)
rs-out = inner radius screen pipe (m) (0.4 m), gravel pack thickness 100 mm.

Differences were seen in the calculated head loss values for each screen type and the reductions of the wells created from these screens. For example, the least head loss was calculated in ST3 filter type in laminar and turbulent flow conditions, while the least decrease

in well types occurred in WT2. Depending on the calculated head losses in the filter types, the least reduction in the well types should have been in WT3, but it was not. Therefore, it would be more accurate to start from the reductions in the wells created from these screens while investigating the head losses of the screen types, because the clogging of each screen and the effect on the flow by the state of the gravel come to the fore. In the next part of the research, the drawdown values of the wells created from these screens are associated with hydraulic conductivity and head loss.

3.5. Cost of Head Losses in Well Types

The drawdown for well types studied in this work has been related to the head loss and is shown in Figure 8. Among the different well types, the highest head loss was found in WT4, which was created using a bridge-type screen, and the least value in WT2, which was formed by a vertical oblong-slot screen (Figure 8). The average head losses obtained during different flow rates were determined as 1.01 m, 0.50 m, 0.81 m, and 1.13 m in the WT1-WT2-WT3 and WT4 well types, respectively.
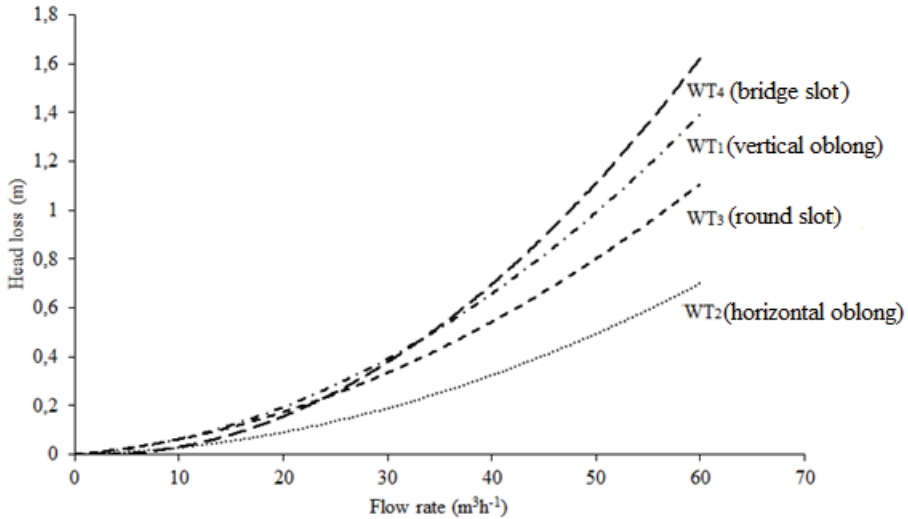
Figure 8 - Head losses in well types

The head losses of the bridged screen (ST4) were calculated as per Equations 4 and 5, and the head losses in the well (WT4) formed from this screen were higher than that of the other screens. Implementing these equations for this screen type could be a correct approach in terms of head loss. However, while the least value of the head loss was calculated in the ST3 screen type by using the same equations, the least head loss in the wells occurred in the head losses of the ST1 and ST2 screen types according to Equations 4 and 5 were very close to each other, the head loss was twice as high in WT1 while compared to that of WT2 among the well types formed from these screens. These two screens possess the same opening and slot shape, yet, with different slot directions, causes a two-fold difference in the load losses.

Differences were seen in the stack state of the gravels, clogging of the screen slots, and the blocking of the flow. To better demonstrate/observe this problem, it is considered that the next study would be simulated in a computerized environment, and the same would be carried out using CFD and Rocky Dem programs.

In the screens, the head loss calculated from equations and the head losses arising from the drawdown was not compared numerically because of the other parameters affecting the wells (head losses in the gravel and pipes).

The head losses per 1 m^3 h^{-1} of flow rate in the WT1, WT2, WT3, and WT4 well types were measured to be 0.036 m, 0.019 m, 0.027 m, and 0.047 m, respectively. The power required to overcome these head losses with a given flow rate could be calculated using Equation 8 [7].

$$Nnet = \frac{\rho.g.Q.H}{\eta} \tag{8}$$

where;

Nnet	= Power required (kW)
Q	= Flow rate (m^3 h^{-1})
H	= Head loss (m)
η_{pump}	= Submersible efficient (-)

In Germany, Hübner [41] found the average pump efficiency (η_{pump}) to be 0.41 during his study on 2500 submersible pumps. Çalışır [11] determined the average efficiency of all facilities to be 0.5 ±0.02 in his study conducted during 46 deep well irrigation facilities in the Konya region of Turkey. In this study, the calculation of the pumping system efficiency in different well types was made according to the following Equations [11]. Table 4 provides the pumping parameters measured in different well types.

$$\eta_{system} = \frac{Q.TDH.\Upsilon}{102. Nnet} \tag{9}$$

$$TDH = H_d + P + v^2/2 \ g \tag{10}$$

TDH	= Total dynamic head (m)
Hd	= Dynamic height (m)
γ	= Water density (kg L^{-1})
P	= Pressure outlet (bar)
v	= Water velocity of pump discharge pipe (m s^{-1})

The optimum flow range in all of the well types of the pumping plant was determined as 40–45-50-55-60 m^3 h^{-1} (Table 4). The system efficiencies of the pumping plant operated in the WT1-WT2-WT3 and WT4 well types were determined to be 42.6%-39.4%-39.8%-42.3%, respectively. These efficiency values were used for calculating the power required to overcome the head losses in the well types. In this context, the required power calculated according to Equation 8 for 1 m^3 h^{-1} flow rate in the WT1-WT2-WT3 and WT4 well types

was calculated as 2.4×10^{-4} kWh, 1.3×10^{-4} kWh, 1.9×10^{-4} kWh, and 3×10^{-4} kWh, respectively. As of 2020, 18 billion m^3 of usable underground water reserves were determined in Turkey, and 11,426 billion m^3 of this amount is used for irrigation purposes. The price of one kWh of electricity used for irrigation in Turkey is around € 0.0644. When one of these screen types is used to extract water from underground, the annual costs of these head losses are 174,000 € year^{-1}, 96.614 € year^{-1}, 138.637 € year^{-1} and 225.133 € year^{-1}, respectively. Assuming that these wells have been operating for 30 years, their total costs arrive at very high amounts, such as 5,220,000 €, 2,898,420 €, 4,159,110 €, and 6,753,990 €, respectively. Here, it appears that the costs of head loss resulting from the screen selection alone in designing the well are too high to be ignored.

Table 4 - Pumping parameters in different well-types

	Flow rate (m^3 h^{-1})	Power (kW)	Hd (m)	TDH (m)	η_{sistem} (%)
	40	4.41	1.55	16.43	41.17
	45	4.43	1.72	15.21	42.62
WT1	50	4.45	1.89	13.73	42.59
	55	4.45	2.08	12.28	41.69
	60	4.43	2.28	10.37	38.63
	40	4.41	1.22	15.71	39.28
	45	4.46	1.30	14.19	39.47
WT2	50	4.44	1.38	12.59	39.01
	55	4.41	1.48	10.63	36.55
	60	4.32	1.60	8.62	33.00
	40	4.41	1.43	15.92	39.10
	45	4.53	1.56	14.55	39.85
WT3	50	4.54	1.70	13.06	39.59
	55	4.54	1.86	11.33	37.76
	60	4.46	1.98	9.28	34.22
	40	4.32	1.58	16.36	41.45
	45	4.46	1.79	15.12	41.90
WT4	50	4.41	2.00	13.60	42.32
	55	4.44	2.24	12.19	41.46
	60	4.40	2.52	10.24	38.35

3.6. Hydraulic Conductivity in Well Types

In their study conducted in 2006, Barrash et al. experimentally calculated the screen drawdown depending on the specific flow change as per the Theim equation. This study calculates the hydraulic conductivity according to the Theim equation (Equation 4), depending upon the drawdown in different well types. The well having the highest hydraulic conductivity value was seen in the one possessing the lowest drawdown level, namely the WT2. As for the screen types, the highest value of hydraulic conductivity was calculated in the round slot screen (ST3). The relationship between the gravel package and the screen, which is seen in the head losses (drawdown) in the wells, was also seen during the hydraulic conductivity.

Table 5 - Hydraulic conductivity in well types

Flow rate ($m^3\ h^{-1}$)	K_{well} ($m\ s^{-1}$)			
	WT1	WT2	WT3	WT4
40	$8.7\ 10^{-5}$	$1.7\ 10^{-4}$	$1.0\ 10^{-4}$	$7.9\ 10^{-5}$
45	$7.8\ 10^{-5}$	$1.5\ 10^{-4}$	$9.7\ 10^{-5}$	$6.8\ 10^{-5}$
50	$7.2\ 10^{-5}$	$1.4\ 10^{-4}$	$8.8\ 10^{-5}$	$6.1\ 10^{-5}$
55	$6.6\ 10^{-5}$	$1.3\ 10^{-4}$	$8.1\ 10^{-5}$	$5.5\ 10^{-5}$
60	$6.2\ 10^{-5}$	$1.2\ 10^{-4}$	$7.9\ 10^{-5}$	$5.0\ 10^{-5}$
Average	$7.3\ 10^{-5}$	$1.4\ 10^{-4}$	$9.0\ 10^{-5}$	$6.3\ 10^{-5}$

4. CONCLUSION

In deep wells, the drawdown is an undesirable physical condition which is the sum of the head losses due to parameters such as the aquifer, aquifer thickness, gravel pack, and screen. It was observed that the WT4 well type, which was created with a drawdown bridge (ST4) screen, was the most common one among the different screen types. The high drawdown value for this well type was the fact that it caused the lowest specific flow rate and the highest specific drawdown value among the well types. Although the slot geometry and the aperture ratios of the screens in the vertically perforated oblong (WT1) and horizontally perforated oblong (WT2) wells were the same, approximately twice the difference in the drawdown, the average specific flow, and the specific drawdown were observed.

The flow type, which was calculated based on the Reynolds number in the gravel region for each screen type, was determined as turbulent. The highest Reynolds number among the screen types was calculated in the ST4 screen. The highest value of the head loss was measured in the well type (WT4) formed from this screen. However, the lowest head loss was not measured in the well (WT3) although the lowest Reynolds number was measured in the ST3 screen type. This can be explained by the increased screen blockage by the gravel, the narrowing of the open area, the increase in velocity and turbulent flow, and an increase in the head loss accordingly. The ranking of the head loss, which was calculated according

to the geometric properties of the screen types and the related equations, and the ranking of the same due to the well drawdown was different. The order of the turbulent head loss of the screens from most to least was calculated according to Equation 5 and was determined as ST4, ST2, ST1, and ST3, while the head loss calculated according to the well drawdown was determined as WT4, WT1, WT3, and WT2, respectively. In addition to the head loss of the gravel used in the experiments, the blockage of the screens affected the head loss within the wells as it differed from screen to screen.

The least value of the head loss per unit flow rate in the wells was measured in the well formed by a horizontal oblong slot (WT2) screen. According to the WT2 well type, the head loss per unit flow increased by 42% in WT3 (round slot), 89.4% in WT1 (vertical oblong slot), and 147% in WT4 (bridged). The cost required to overcome the head losses formed by the pump efficiency in the wells was determined to be the lowest in the WT2 well type. According to the WT2 well type, cost increases were seen due to the head loss of 43.5% in WT3, 80% in WT1, and 133% in WT4.

Based on the physical properties of the gravel used in this study, it has been revealed that using a horizontal oblong slot screen would minimize the head loss in the wells. One of the most important points to be considered in well designs is the compatibility of the screen type with the physical properties of the gravel. Even the change in the geometric shape of the screen types having similar apertures altered the blockage of the gravel, causing the head loss to change. Well designers should pay attention to the selection of gravel based on the screen type or the selection of the screen depending on the type of gravel used. It would be appropriate to use a horizontal oblong slot screen for the gravel, commonly used in Turkey and called 7–15 mm, since it would reduce well-head losses.

According to another result from this study, the evaluation of the screens by using theoretical head loss calculations could deviate the accuracy of the screen selections during well designs. It has been revealed that the relationship between the gravel and the screen should not be overlooked. At the same time, it is necessary to carry out similar studies with gravels having different physical properties. For researchers, this study result can guide the simulation of different filter types with flow software. The impact of the filter type on the well design and drawdown may be examined by well design companies and engineers, and the pumps can be chosen in accordance with the findings.

Acknowledgment

Notation

ρ	=	Water density (kg m^{-3})
μ	=	dynamic viscosity (kg m^{-1} s^{-1})
Δ	=	Drawdown (cm);

Hd	=	Dynamic head (mm);
ST1	=	Vertical oblong slot screen
ST2	=	Horizontal oblong slot screen
ST3	=	Round slot screen
ST4	=	Bridged slot screen
WT1	=	Vertical oblong slot well
WT2	=	Horizontal oblong slot well
WT3	=	Round slot well
WT4	=	Bridged slot well
K	=	Hydraulic conductivity (m s^{-1})
Re	=	Reynolds number (-)
Pb	=	Output pressure (kPa)
Q	=	Flow rate (m^3 h^{-1})
S	=	Submergence (mm)
V	=	water inlet velocity (m s^{-1})
TDH	=	Total dynamic head (kPa)
T1	=	Ambient temperature (°C)
T2	=	Water temperature (°C)

Declarations

The author declares no conflict of interest.

References

[1]   C. Gautier, *Oil, water, and climate: an introduction*. Cambridge University Press, 2008.

[2]   G. J. Houben, "Hydraulics of water wells—flow laws and influence of geometry," *Hydrogeology Journal,* vol. 23, no. 8, pp. 1633-1657, 2015.

[3]   F. G. Driscoll, "Groundwater and wells," *St. Paul,* 1986.

[4]   R. J. Sterrett, *Groundwater and wells*. Johnson Screens, 2007.

[5]   B. K. Wilk and A. Urbański, "The impact of the shape of screen openings on groundwater flow to a deep drilled well," *Czasopismo Techniczne,* vol. 2018, no. Volume 11, pp. 149-162, 2018.

[6] G. P. Karatzas, "Developments on modeling of groundwater flow and contaminant transport," *Water Resources Management,* vol. 31, no. 10, pp. 3235-3244, 2017.

[7] G. J. Houben, "Hydraulics of water wells—head losses of individual components," *Hydrogeology journal,* vol. 23, no. 8, pp. 1659-1675, 2015.

[8] V. Batu, *Aquifer hydraulics: a comprehensive guide to hydrogeologic data analysis.* John Wiley & Sons, 1998.

[9] C.-F. Zeng, W.-W. Song, X.-L. Xue, M.-K. Li, N. Bai, and G.-X. Mei, "Construction dewatering in a metro station incorporating buttress retaining wall to limit ground settlement: insights from experimental modelling," *Tunnelling and Underground Space Technology,* vol. 116, p. 104124, 2021.

[10] C.-F. Zeng, G. Zheng, and X.-L. Xue, "Responses of deep soil layers to combined recharge in a leaky aquifer," *Engineering Geology,* vol. 260, p. 105263, 2019.

[11] S. Çalışır, "The evaluation of performance and energy usage in submersible deep well irrigation pumping plants," *Agricultural Mechanization in Asia Africa And Latin America,* vol. 38, no. 1, p. 9, 2007.

[12] R. Moss and G. E. Moss, *Handbook of ground water development.* Wiley-Interscience New York, 1990.

[13] S. Parsons, "A re-evaluation of well design procedures," *Quarterly Journal of Engineering Geology,* vol. 27, no. Supplement, pp. S31-S40, 1994.

[14] D. E. Williams, "Modern techniques in well design," *Journal-American Water Works Association,* vol. 77, no. 9, pp. 68-74, 1985.

[15] J. H. van Lopik, R. Snoeijers, T. C. van Dooren, A. Raoof, and R. J. Schotting, "The effect of grain size distribution on nonlinear flow behavior in sandy porous media," *Transport in Porous Media,* vol. 120, no. 1, pp. 37-66, 2017.

[16] G. J. Houben, J. Wachenhausen, and C. R. G. Morel, "Effects of ageing on the hydraulics of water wells and the influence of non-Darcy flow," *Hydrogeology Journal,* vol. 26, no. 4, pp. 1285-1294, 2018.

[17] B. Boman, S. Shukla, and J. Hardin, "Design and construction of screened wells for agricultural irrigation systems," *EDIS,* vol. 2006, no. 17, 2006.

[18] *Rotodynamic Pumps-Hydraulic Performance Acceptance Tests, Class 1 and Class 2, TS EN ISO 9906*, Anonymous, Turkish Standards Institute, 2002.

[19] *For pumps-submersible-clean water, TS 11146*, Anonymous, Turkish Standards Institute, 2014.

[20] *Determination of Loose Agglomeration Density and Clearance Volume of Aggregates, TS EN 1097-3, Turkish Standardization Institute.*, Anonymous, Ankara, 1999.

[21] *Experiments for Geometric Properties of Aggregates. TS EN 933-3,Turkish Standardization Institute. Ankara.*, Anonymous, 2004.

[22] N. Orhan, O. Özbek, and A. Y. Şeflek, "Effect of the Gravel Zone Thickness Created in the Deep Well Test Simulation on the Operating Characteristics of the Pump and Head Loss," *Teknik Dergi,* vol. 32, no. 6, 2021.

[23] N. Orhan, "Determination of Vortex and Critical Submergence of Submersible Pumps," *Selcuk Journal of Agriculture and Food Sciences,* vol. 35, no. 2, pp. 161-169, 2021.

[24] T. Strickland and C. Korleski, "Pumping and Slug Tests, Technical Guidance Manual For Ground Water Investigations," *Ohio Environmental Protection Agency Division of Drinking and Ground Waters,* p. 45, 2006.

[25] F. Tügel, G. J. Houben, and T. Graf, "How appropriate is the Thiem equation for describing groundwater flow to actual wells?," *Hydrogeology Journal,* vol. 24, no. 8, pp. 2093-2101, 2016.

[26] J. Bear, "Dynamics of fluids in porous media Dover Publications," *INC, New York,* 1988.

[27] J. Bear, "Hydraulics of groundwater. Mineola," ed: New York: Dover Publications, 2007.

[28] R. R. Trussell and M. Chang, "Review of flow through porous media as applied to head loss in water filters," *Journal of Environmental Engineering,* vol. 125, no. 11, pp. 998-1006, 1999.

[29] W. Barrash, T. Clemo, J. J. Fox, and T. C. Johnson, "Field, laboratory, and modeling investigation of the skin effect at wells with slotted casing, Boise Hydrogeophysical Research Site," *Journal of Hydrology,* vol. 326, no. 1-4, pp. 181-198, 2006.

[30] G. J. Houben and S. Hauschild, "Numerical Modeling of the Near-Field Hydraulics of Water Wells," *Groundwater,* vol. 49, no. 4, pp. 570-575, 2011.

[31] H. Klammler, B. Nemer, and K. Hatfield, "Effect of injection screen slot geometry on hydraulic conductivity tests," *Journal of Hydrology,* vol. 511, pp. 190-198, 2014.

[32] D. Klotz, "Untersuchung von Grundwasserströmungen durch Modellversuche im Maßstab 1: 1," *Geologica Bavarica,* vol. 64, pp. 75-119, 1971.

[33] D. Klotz, *Berechnete Durchlässigkeiten handelsüblicher Brunnenfilterrohre und Kunststoff-Kiesbelagfilter (Stand 1990).* GSF-Forschungszentrum für Umwelt und Gesundheit, 1991.

[34] D. T. Snow, "Rock fracture spacings, openings, and porosities," *Journal of the Soil Mechanics and Foundations Division,* vol. 94, no. 1, pp. 73-91, 1968.

[35] J. Barker and R. Herbert, "Hydraulic tests on well screens," *Applied Hydrogeology,* pp. 7-19, 1992.

[36] J. Barker and R. Herbert, "A simple theory for estimating well losses: with application to test wells in Bangladesh," *Applied Hydrogeology,* pp. 20-31, 1992.

[37] L. Clark and P. Turner, "Experiments to assess the hydraulic efficiency of well screens," *Groundwater,* vol. 21, no. 3, pp. 270-281, 1983.

[38] S. R. Singh and S. K. Shakya, "A nonlinear equation for groundwater entry into well screens," *Journal of Hydrology,* vol. 109, no. 1-2, pp. 95-114, 1989.

[39] J. Kozeny, *Hydraulik: Ihre Grundlagen und praktische anwendung*. Springer-Verlag, 1953.

[40] J. Bear, *Dynamics of fluids in porous media*. Dove, New York.: Courier Corporation, 1972.

[41] M. Hübner, "Moderne Anlagentechnik für eine energieeffizientere Wasserversorgung (Modern installation engineering for energy efficient water supply)," *BBR Fachmagazine fur Brunnen und Leitungsbau,* vol. 62, no. 12, p. 72, 2011.

Car Fires in Multi-Story Parking Garages

Serdar SELAMET[1]
Burak AYVA[2]

ABSTRACT

Automated multi-story parking garages are modern alternatives to conventional parking structures to save space and volume in high demand parking spaces in urban areas. The design of such structures has significant knowledge gaps in terms of fire safety. The purpose of this study is to estimate the horizontal and vertical fire spread between passenger cars in automated multi-story parking garages and provide fire safety design to minimize fire spread and possible structural collapse. The fire spread between cars is established by estimating irradiance heat flux of each car component. An 8-floor automated multi-story parking garage with 56 passenger car capacity is designed in accordance with European standards. The results show that steel parking pallets underneath cars reach extreme temperatures about 1000 ℃ in early phases of fire for Category III vehicle fire with 8 MW maximum heat release rate, which could cause structural failure. Without any fire protection on the structure, the fire spreads to the car above in 23 minutes, to the neighboring car in 37 minutes and beyond the elevator shaft to the other cars in 82 minutes. The proposed sprinkler layout eliminates fire spread within 5 minutes. The most efficient way of passive fire protection is to seal steel pallet, its rail system and beams on the elevator shaft with 5 cm gypsum-based fire protection boards.

Keywords: Car fire, vehicle fire, parking garage, fire safety, fire resistance.

1. INTRODUCTION

The purpose of this study is to model and understand fire performance of an automated multi-story open parking garage including structural integrity, the energy content and heat release rate of passenger cars, horizontal and vertical fire spread and the effect of sprinkler locations. The goal is to provide additional active and passive fire safety measures in open car parks.

Fire safety design requirements for conventional open car parks are not strict. Automatic sprinkler systems, mechanical ventilation systems and passive fire protection on vertical

---

1 Bogazici University, Department of Civil Engineering, Istanbul, Türkiye
  serdar.selamet@boun.edu.tr - https://orcid.org/0000-0001-9444-470X

2 Bogazici University, Department of Civil Engineering, Istanbul, Türkiye
  burakayva@gmail.com - https://orcid.org/0000-0002-7329-1019

opening through floors are not part of NFPA 88A Standard [1]. According to NFPA 88A per Section 5.1.2, the height of an open car park is limited by 25 m for Type II (000) structures, whereas there is no limitation for Type I structures [1]. Such precautions may be valid for conventional open tall car parks; however, design of slabs and vertical openings are totally different in automated open tall car parks. Vertical opening area to total floor area is excessive in automated type car parks due to vertical lift openings. The vertical opening of lift system may act like an atrium rather than a simple vertical opening during a fire incident within an automated open tall car park; thereby changes vertical fire spread characteristics. Additionally, there is no slab fixed to the structural systems in automated open tall car parks. In such structures, car pallets docking and undocking between columns are utilized as carrying platforms of which structural fire response is unknown.

Passenger car fires in parking structures are not common, but such events can develop into large and uncontrollable fires [2]. Some cases of car park fires have involved hundreds of vehicles and caused structural collapses in the last two decades. A car park fire in Schiphol Airport in Amsterdam burned nearly 30 passenger cars and partly damaged around 101 passenger cars [3]. Another vital car park fire event is Kings Dock fire in Liverpool [4]. The fire led to a total loss of 1150 passenger cars. Firefighters have reported rapid lateral fire spread and vertical fire spread in both downward and upward directions. The most recent open car park fire has occurred in Stavanger, Norway [5]. With the effect of strong wind, flames engulfed the structure partially, a significant structural collapse has occurred, and around 300 passenger cars were destroyed. A few passenger car fire tests in full-size open car parks are carried out [6-9]. The general conclusion was that structural fire protection is not necessary for open deck car parking structures.

Fig. 1 - Automated multi-story parking garage with 4 units (Balıkesir, Turkey)

Automated multi-story parking garages are modern alternatives to conventional parking structures to save space and increase volume in high-demand parking regions in urban areas. They are generally constructed from steel. An 8-floor parking garage from Balıkesir, Turkey, is shown in Fig. 1. It is an externally braced steel structure with embedded elevator and car pallets to store and retrieve passenger cars. These structures may be constructed with either open or closed façade.

Fire characteristics of passenger cars depend on vehicle size, ignition source and location, environmental conditions and ventilation level. Peak HRR levels vary within a wide spectrum, from 1.9 MW to 10.8 MW [2]. The high level of heat release rate per unit area during car fires increases the collapse risk of parking garages. Most of fire spread tests are based on lateral fire spread scenarios in the literature [10,11]. Weisenpacker et al. [11] focused on temperature levels around and inside of burning cars and did not measure the heat release rates (HRR). On the contrary, Park et al. [10] measured HRR by using large-scale calorimeter and the maximum HRR for the single-car fire was estimated as 3.5 MW. Studies suggest that HRR curves of passenger cars show no clear correlation with vehicle age [2].
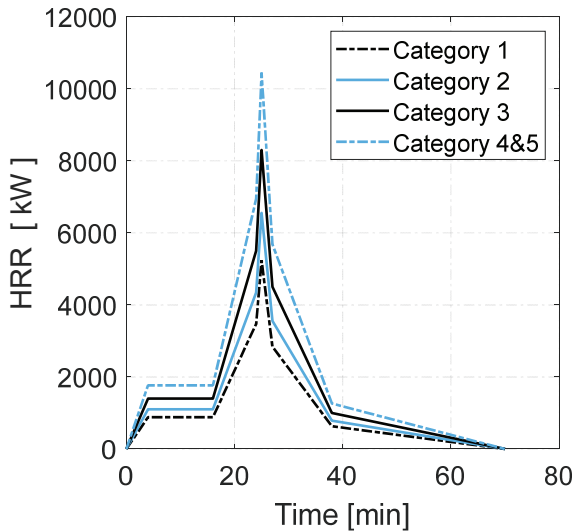
Fig. 2 - Equivalent HRR curves for classification of cars (adapted from Schleich et al. 1999 [12]).

The use of total combustion energy can classify passenger car fires during fire. The calorific potential classification that has five different categories is generally based on vehicle size and curb weight. Schleich et al. [12] have presented equivalent HRR curves for the potential calorific classifications of passenger cars in Fig. 2. The characteristics and trends of the HRR curves are identical. Schleich et al.'s [12] approach is based on the amplification of HRR values. In addition to the overall energy potential, ignition mechanism of individual components in vehicles are also essential to understand car fires. After the 1990s, the use of plastic components in passenger cars has increased from 5.1% in 1970s to 8.8% of car weight

in 2018 [2]. In addition to this, the average combustion energy per mass of plastic components within passenger cars has increased. Although the change in the mass of plastic materials is 72%, the total combustion energy has increased by 91% since the 1970s. The risk of fire spread from one car to another has risen with the increase in the use of plastic materials for exterior parts of passenger cars.

The occurrence of ignition can be forecast with a calculation of surface temperature if the substance is heated by convection and radiation. A set of test results of plastic vehicle components that used on outmost surfaces of passenger cars are given in Table 1 [13]. Ignition times under different irradiance levels and critical irradiance levels of plastic components are determined by tests [13]. All exterior plastic components excluding tires can be ignited by an irradiance level of 20 kW/m^2 in 7.5 minutes, whereas it takes less than 1 minute with an irradiance level of 30 kW/m^2. On the other hand, the ignition of tires takes much more time, but its critical irradiance level is not high.

Table 1 - Ignition times of plastic passenger car components [13] (NI: not ignited)

Component	Time to ignition (seconds) (NI=no ignition) Irradiance level				Critical irradiance level (kW/m^2)
	10 kW/m^2	20 kW/m^2	30 kW/m^2	40 kW/m^2	
Hub cap	NI	205	58	28	17.5
Mud flap	380	57	29	16	10
Wheel arch	NI	81	44	25	12
Bumper	NI	450	89	43	18.5
Bumper grill	NI	114	44	19	17.5
Bumper trim	415	83	30	16	11.5
Fuel tank	NI	354	114	59	16.5
	10 kW/m^2	12 kW/m^2	15 kW/m^2	20 kW/m^2	
Tire	NI	1100	597	240	11

Building Research Establishment (BRE) conducted a set of fire tests on fire spread modes between passenger cars [13]. All possible fire spread patterns between passenger cars are tested. These patterns are side-by-side fire spread, nose-to-nose fire spread and vertical fire spread at car stacker. Before and after photographs of tests are shown in Fig. 3. The gas temperature close to the ceiling has reached 1100 °C during side-by-side fire spread test. In the nose-to-nose fire spread test, the fire has spread to the next vehicle in approximately five minutes. In the case of car stackers, both cars in the stacker were engulfed in flames after 21 minutes.

Fig. 3 - Fire spread between passenger cars (BRE,2010 [13]).

One of the most critical knowledge gaps in suppression of passenger car fires is the effectivity of sprinkler systems in car stackers. Carpark fires are defined as ordinary hazard in most of national fire safety codes such as BS EN 12845:2015 [14], AS 2118:2017 [15], NZS 4541:2020[16] and the Turkish Regulation on Fire Protection [17]. BRE has conducted tests on the efficiency of sprinklers on passenger car fires for ordinary car parks and stacker systems [18]. The setup represents a closed car park, but ventilation is enough for a fuel-controlled fire. The fire started at the outermost passenger car. The first sprinkler was activated after 4 minutes, then all sprinklers were activated at the early stage of fire. The fire was not extinguished, and its thermal power reached around 7000 kW. However, the fire did not spread to the next vehicle. Cooling and transport effect of water droplets from sprinklers caused the smoke to drag down.

2. METHODOLOGY

In this study, an automated multi-story steel parking garage is designed based on an existing example shown in Fig. 1 and modelled in Fire Dynamics Simulator (FDS) [19] and SAP2000 [20]. A widely used design car fire HRR curve is modified to decrease computational demand of FDS and vertical and lateral fire spread criteria between passenger cars is defined via FDS simulations. Thermal response of structural members including the car pallets are obtained from FDS analyses.

2.1. Parking Garage

An 8-floor open-facade steel car park with 4 units and a capacity of 56 cars is designed according to Turkish Building Earthquake Code 2018 and Eurocode 3 [21,22]. Turkish Fire Regulation requires R15 rating for load-bearing structural elements for open parking structures with height 30.5 meters and below. Article 96c in the regulation mandates the use of sprinklers in garages, where more than 10 vehicles are taken into the garage through an elevator. However, the regulation does not specify sprinkler layout. The parking garage has a sprinkler system with a layout adopted by Australasian Fire and Emergency Service, which recommends placing the sprinklers on top of 4 vehicle corners. The reason behind this is merely an easy way of piping installation for sprinklers near four column-beam joints. Steel bracings are chosen as S235 grade. All remaining structural elements (i.e. beams and columns) are chosen as S275 grade. The structure is braced for lateral resistance. The structural system is designed in accordance to DD2 (10% - 50 year) design earthquake (TBDY 2018). The parameters used for the spectrum analysis are $S_S = 0.878$ s and $S_1 = 0.214$ s with ZA soil condition, $R = 5$, $\Omega_o = 2$. All column cross sections are TUBO 160x160x10. The beams for the car pallet are HEA100 sections. The beams connecting to columns as part of the structural system are HEA140. The beams and columns are connected via shear connections. The structural design is shown in Fig. 4. Member cross sections are tabulated in Table 2.

Table 2 - Member sections of parking garage (see Fig. 4).

Member	Section
Columns	TUBO160x160x10
Beams	HEA140
Bracing	TUBO80x80x8
Car pallet beams	HEA100

Car pallets stay on wheels, which are mounted on short cantilever beams fixed to the columns. The car pallet is illustrated in Fig. 5. The pallet contains 4 longitudinal beams and 4 cross beams (HEA100) with a 2mm thick sheet metal above to carry the vehicle load. For the loading condition, the vehicle weight is taken as 2000 kg, which is an average weight of ordinary size SUV. Considering the vehicle as a live load (i.e. 1.6 live load factor), the vehicle load is applied as 4 point-loads of 7.85 kN on each pallet, which are 2.7 m apart from each
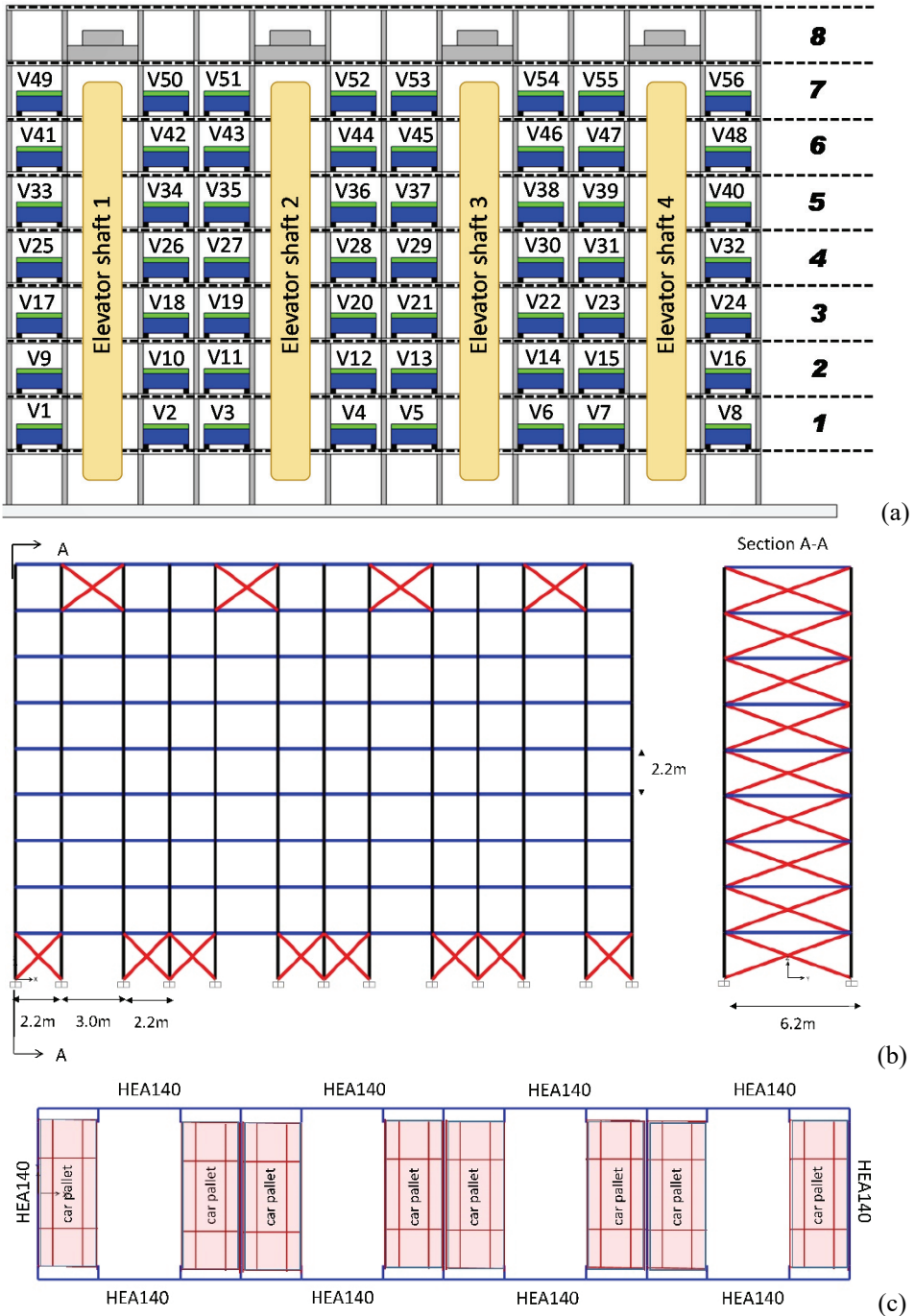
Fig. 4 - *Multi-story parking garage: (a) illustration, structural design (b) elevation view and (c) top view.*

other in accordance to the wheelbase of ordinary size SUV. Car pallet does not transfer moment or axial force to the cantilever beam supports. The elevator equipment on the top floor of each elevator shaft as seen in Fig. 4a is taken as 11 kN. The connection detail shown in Fig. 5 is commonly used in current parking garages and it does not transfer moment or axial force from the pallet to the main column.
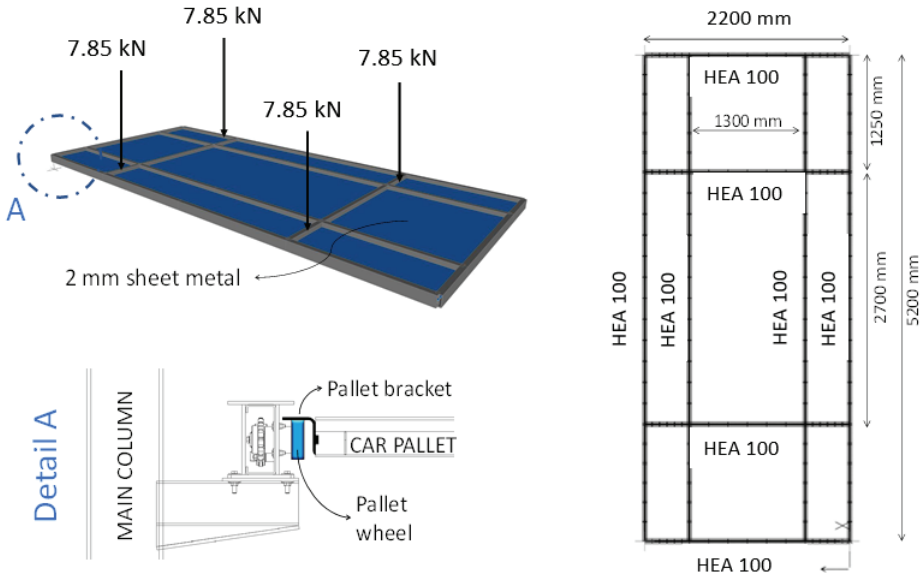
Fig. 5 - Car pallet design.
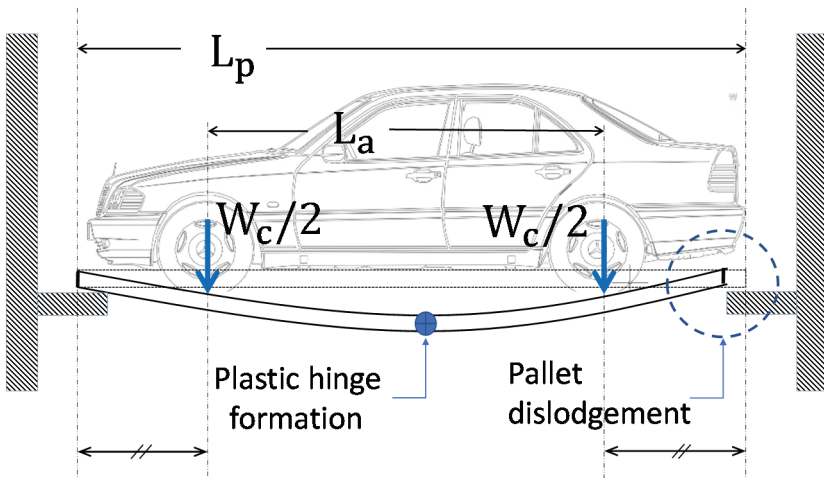
Fig. 6 - Car pallet collapse mechanism.

In this study, the thermo-mechanical analysis of the cark park structural system is not conducted because both columns and beams under low utilization ratios μ have significantly high critical temperatures T_{cr} even without any fire protection. TUBO160x160x10 columns with $\mu = 0.129$ have $T_{cr} = 809\ °C$. On the other hand, HEA100 beams underneath the car pallet carry a significant load and they are likely subjected to extreme temperatures from car fires just below. HEA100 beams with $\mu = 0.502$ have $T_{cr} = 590\ °C$. A possible collapse mechanism of the car pallet is illustrated in Fig. 6 where a plastic hinge at the mid-span forms during fire. Such failure indicates that the pallet could collapse before the fire spreads to other cars.

2.2. FDS Model

The Fire Dynamics Simulator (FDS) model is created in PyroSim [23]. FDS solves numerically a form of Navier-Stokes equations appropriate for low-speed, thermally driven flow with an emphasis on smoke and heat transport from fires [19]. The turbulence is solved by Large-Eddy Simulation (LES). For the building model dimension and mesh size of this study, LES is the most suitable simulation type. For wildfires and large open space, very large eddy simulation is generally preferred. Direct numerical solver (DNS) is not suitable for this problem type.

The fire initiates from the car labeled as V13 on the 2nd floor as illustrated in Fig. 4a. No smoke control system is installed on the model. The heat and radiation transport calculation is performed with polyurethane as the fuel load and with 20 cm mesh size [24]. HEA100 and TUBO160x160x10 structural member surface temperatures are calculated utilizing the 'exposed back condition' in the FDS model, i.e. assuming that the members conduct heat through the cross-sectional thickness.

To estimate this cell size in the FDS model, the characteristic length scale of fire is calculated using Equation 1, where D* is dimensionless diameter in m, Q is peak heat release rate (HRR) in kW, ρ_∞ is ambient air density in kg/m3, T_∞ is ambient temperature in °C, c_p heat capacity of air under constant pressure in J/kgK and g is gravitational acceleration in m/s2.

$$D^* = \left(\frac{Q}{\rho_\infty T_\infty c_p \sqrt{g}} \right)^{2/5} \tag{1}$$

The heat release rate curve of Category III car is with a peak HRR of 8.3 MW, hence D* is obtained as 2.235 m. It is suggested that for a reliable large eddy simulation (LES) at least 10 cells shall fit within the dimensionless diameter [25]. Therefore, 20 cm or smaller cell size with a simple chemistry model can be used. The cell size is chosen as 10 cm for all fire simulations in this study. Prandtl number, which relates the viscosity to the thermal conductivity is taken as 0.7 as recommended by FDS Technical Reference Guide [19] in case liquid droplets are simulated as water droplets from sprinklers. Radiative fraction is the fraction of energy released from the fire as thermal radiation. This number is set to 0.35. In FDS, the radiative fraction is defined between 0.3 and 0.4 for most combustibles and Table 16.1 in FDS Technical Reference Guide [19] takes 0.35 as default for all fuels other than liquid fuels such methane.

2.3. Passenger Car Design Fire

To reduce computational effort and shorten the run time on FDS simulations, both the heat release rate (HRR) curve and the vehicle model detail are modified without compromising the accuracy. For the passenger car design fire, Category III HRR curve with a peak HRR of 8.3 MW for maximum of 70-minute fire duration is modified as seen in Fig. 7. Schleich et al. [12] grouped the cars in five categories mainly due to their size (i.e. volume) and weight. Category III vehicle type (SUV) is defined to indicate the worst-case scenario. The modification mainly focuses on the ascent and descent parts around the peak point of the curve. Equations of ascent ($\dot{q}_{asc}$) and descent ($\dot{q}_{dec}$) heat flux of the Modified Category III fire curve are given in Eq. 2 and Eq. 3 where t is time in minutes and $\dot{q}$ is heat release rate in kW.

$$\dot{q}_{asc} = 11.8\, t^2 \qquad 11 \leq t \leq 25 \tag{2}$$

$$\dot{q}_{dec} = \dot{q}_{asc}(25) * e^{-(t-25)/6} \qquad 25 \leq t \leq 70 \tag{3}$$
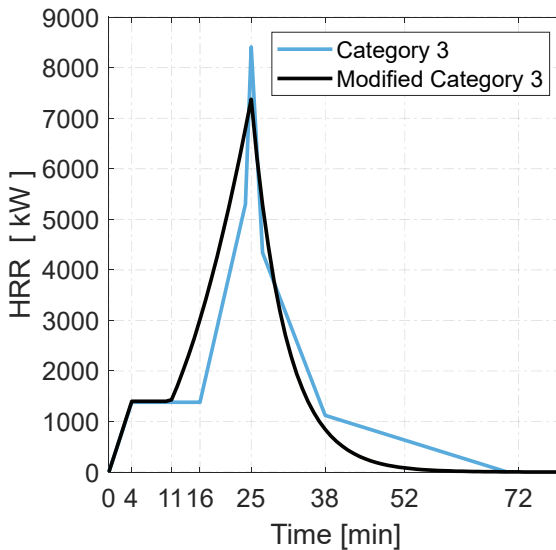
Fig. 7 - Category III design car fire [12] and Modified Category III fire.

As can be seen in Fig. 7, the cumulative thermal energy is shifted to the left in the Modified Category III fire with respect to the original curve. The decreasing phase is also faster so that the dying out of fire occurs quickly. This allows the flexibility to stop simulation earlier without compromising accuracy. The predefined termination of simulation is when the fire curve drops to 5% of its peak value at 43rd minute. The total energy release (i.e. area under HRR curve) is not violated by using the modified HRR curve. Differences between maximum gas temperatures are detected on a ceiling just above the fire pool as low as 50 °C, and maximum surface temperature levels are very similar in both cases [26]. High performance

computer used for the FDS analyses is 8-node Intel Xeon E5-2680 2.4 GHz with 128 Gb Ram per node. The case study FDS models consist of approximately 900,000 meshes and this modification in HRR curve results in 28% reduction of the computational time from 65 hours to 46 hours.
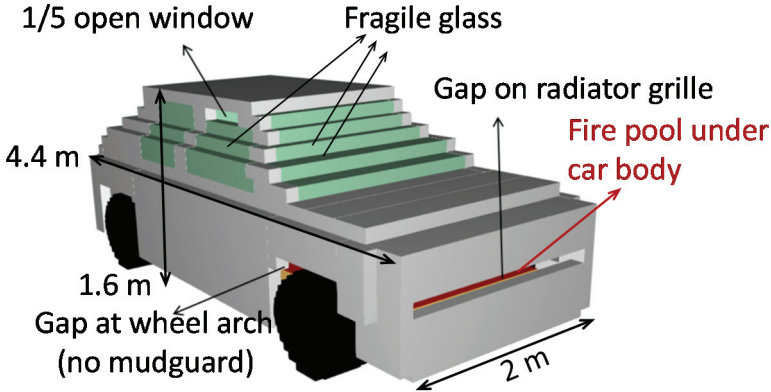
Fig. 8 - Car model in FDS.

A compact size car body encloses on a fire pool is designed in FDS with car body and window details as illustrated in Fig. 8. Metal parts in the body are defined as 1 mm steel sheet with 40 W/m.K of heat conduction coefficient. Windows are ordinary glass with 3 mm thickness and 1 W/m.K heat conduction coefficient. Glass breakage is simulated according to Weisenpacher et al. [11]. It is expected that windshield glass will break first followed by side and rear windows. The ground clearance of the passenger car is 20 cm.

2.4. Horizontal and Vertical Fire Spread Between Passenger Cars

'NFPA-1710: Standard for the Organization and Deployment of Fire Suppression Operations, Emergency Medical Operations, and Special Operations to the Public' by Career Fire Departments mandates 5:20 minutes response criterion for passenger car fires after the department is informed [27].

Joyeux [8] estimated the time duration needed for horizontal (lateral) fire spread between passenger cars as 12 minutes. In contrast, Li et al. [28] assessed the period as approximately 20 minutes, whereas Park et al. [10] reported the fire spread to an adjacent car at the 8th minute. Hence, the fire brigade must be alerted in a few minutes after the fire initiated.

Vertical fire spread between passenger cars is as important as lateral fire spread between passenger cars. However, the literature on this topic is very limited [13] [18]. To assess criteria for vertical fire spread; undercover, tires, and front bumper of the car given in Fig. 8 is modeled with combustible polymers. The undercover and bumper are chosen as polypropylene and the tires are selected as rubber. Thermal properties of materials used in the model are given in Table 3.

Table 3 - Thermal properties of materials in ignitable passenger car model

Material	Ignition Temp. [°C]	Specific Heat [kJ/kg.K]	Conductivity [W/m.K]	Heat of Combustion [kJ/kg]	Emissivity	Density [kg/m³]
	Thermal Properties					
Rubber [29]	350	1.88	0.13	50	0.90	910
Polypropylene [29]	388	1.75	0.15	46	0.90	946
Steel [19]	-	0.46	45.8	-	0.95	7850
Glass [19]	-	0.79	1.0	-	0.05	2500
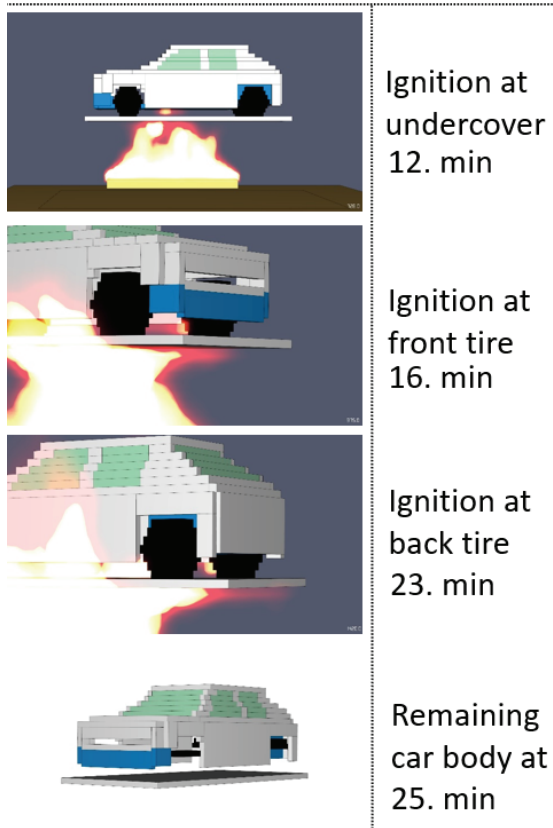
Fig. 9 - Vertical fire spread to a passenger car.
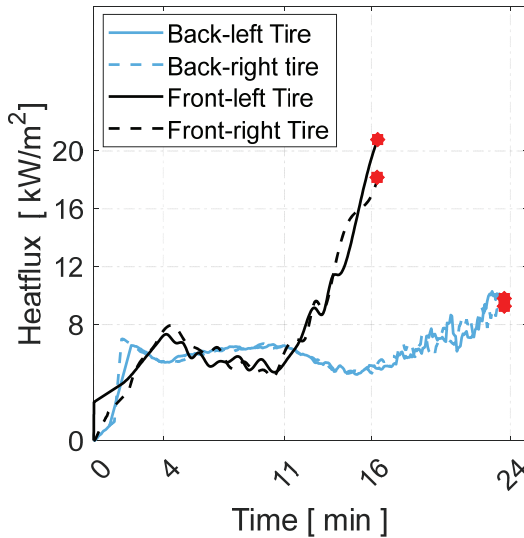
Fig. 10 - Incident surface heat flux on car tires (* : ignition time).

During the fire simulation, the first ignition occurred at the undercover of car, which is also observed in BRE tests [13]. The undercover in the simulation caught fire at t = 12 minutes . In BRE tests, the car above caught fire on the 5th minute and it was fully engulfed by t = 10 minutes where the peak HRR was measured as 8.5 MW on the 12th minute. BRE tests investigated the fire spread between cars directly stacked on top of each other without the steel pallet acting as a heat shield. The cars in the parking garage in this simulation are on different floors with 40 cm clear vertical distance from each other and 5 mm steel pallet as a heat shield. Hence, the fire spread times differ significantly. After the ignition of undercover, front tires ignite at 16th minute. The vertical fire spread is illustrated chronologically in Fig. 9. The result indicates that at approximately 10 kW/m^2 of incident surface heat flux is sufficent to start combustion on undercover. Incident surface heat flux curves for tires are shown in Fig. 10. The incident surface heat flux at ignition time nearly reaches to 20 kW/m^2 on front tires and 10 kW/m^2 on back tires.

With the aforementioned analysis, both vertical and lateral fire spread criteria are proposed. When the incident heat flux level is lower than 8 kW/m^2, there is no risk of ignition, whereas the level is higher than 16 kW/m^2, passenger cars start to burn and spread the fire. If the incident heat flux level is between 8 and 16 kW/m^2, the adiabatic surface temperature [30] should be observed closely. As long as the adiabatic surface temperature is lower than the ignition temperature of the material, the related component cannot catch fire.

3. CASE STUDIES

In order to provide fire safety to automated multi-story parking garages, it is imperative to eliminate or slow down the fire spread between passenger cars. In addition, the structural

integrity including the steel pallets should be maintained during fire. Fire spread risk levels are shown in Fig. 11. Fire starts at vehicle V13 as shown in Fig. 4a. The neighboring passenger cars are designated as 'R' (right side of the car), 'L' (left side of the car), and 'U' (upper side of the car).
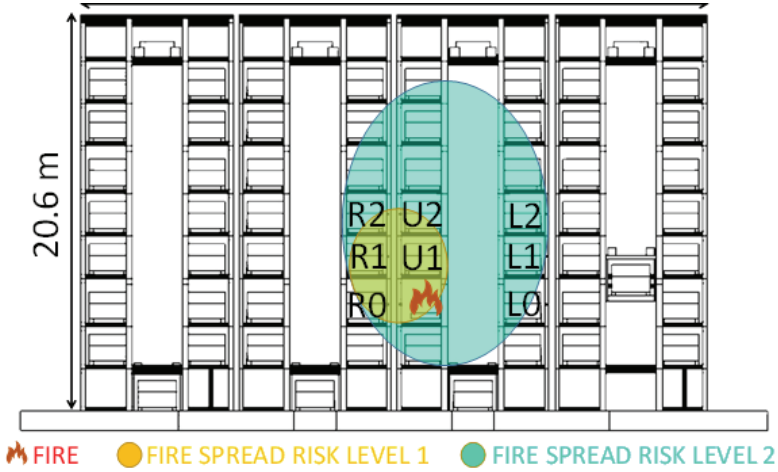
Fig. 11 - Automated tall car park: Fire origin at vehicle V13.
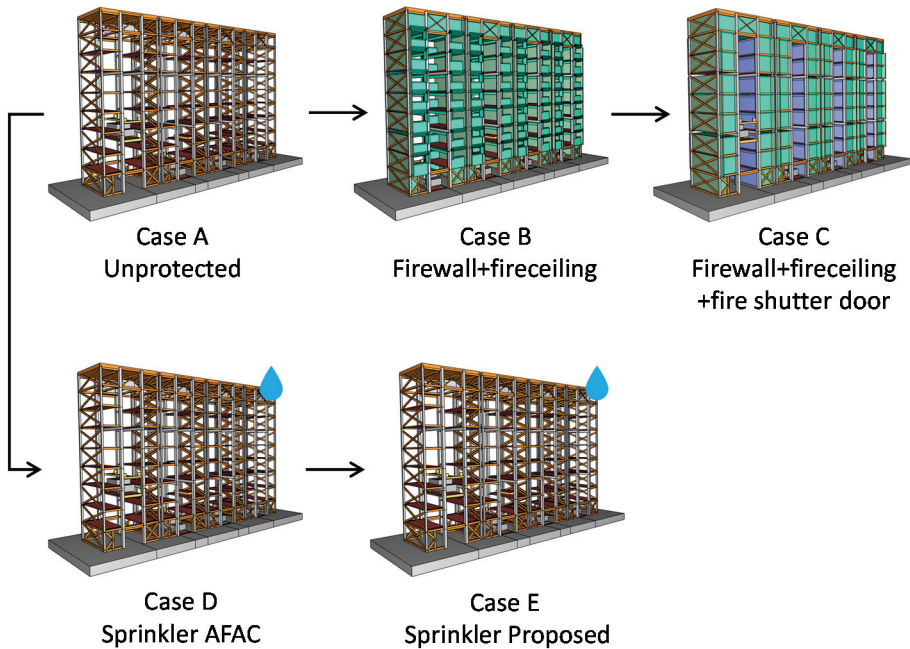
Fig. 12 - Case studies.

Case studies are illustrated in Fig. 12 with passive and active fire safety measures. In all case studies, Modified Category III HRR design curve is utilized. Unprotected car park is the base scenario without sprinklers (Case A). This study is conducted to understand the fire spread risks without any active and passive fire protection. The parking structure with partial firewalls and fireproof ceilings is shown in Case B. The structure with fire shutter doors is shown in Case C. Both Case B and C provide passible fire protection only. Finally, Case D utilizes the current (mandated) sprinkler active fire protection system in the parking garage and the sprinkler layout is adopted by [31]. Case E utilizes an improved sprinkler layout proposal.
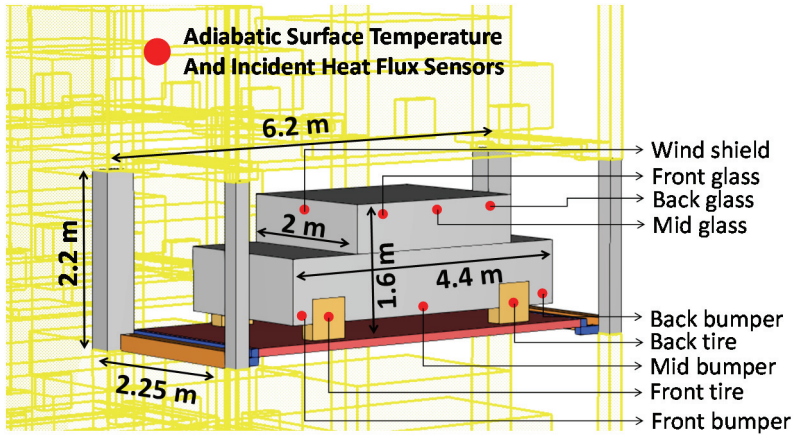
Fig. 13 - Sensor positions on passenger cars.

Fig. 14 - Nomenclature of structural elements around the fire zone

The passenger car model in Fig. 8 is used in FDS simulations. Adiabatic surface temperature and incident heat flux sensors shown in Fig. 13 are used as indicators for fire spread. The nomenclature of structural elements around the fire zone V13 over the car pallet P2E is shown in Fig. 14.

3.1. Case A: Car Park without Fire Protection

The fire safety level of an open façade unprotected car cark is examined. Fig. 15 shows the development of vehicle fire in the car park. After 15th minute, hot gases and flames start to pervade the entire parking slot and upper areas. The gas temperature reaches to 900 °C under the upper car pallet P3E. It causes the ignition on the undercover of car U1 at 20th minute. Hot gases with 600°C are dragged up with buoyancy force and reach car U2 and R2. At 25th minute, the hot gas temperatures around the neighboring vehicle U1 and R1 reached 1100 °C as illustrated in Fig. 15. Passenger cars L0, L1 and L2 are at a relatively far distance from the fire, where the gas temperature remains low. Incident heat flux levels over these cars are under 5 kW/m^2 which is deemed safe as previously stated. Incident heat flux levels for car U1, R0 and R1 are given in Fig. 16. Incident heat flux levels at mid bumpers of upper cars reach over 50 kW/m^2 that causes fire to spread. Fig. 16 also indicates that the fire can spread to all surrounding cars within 25 minutes.
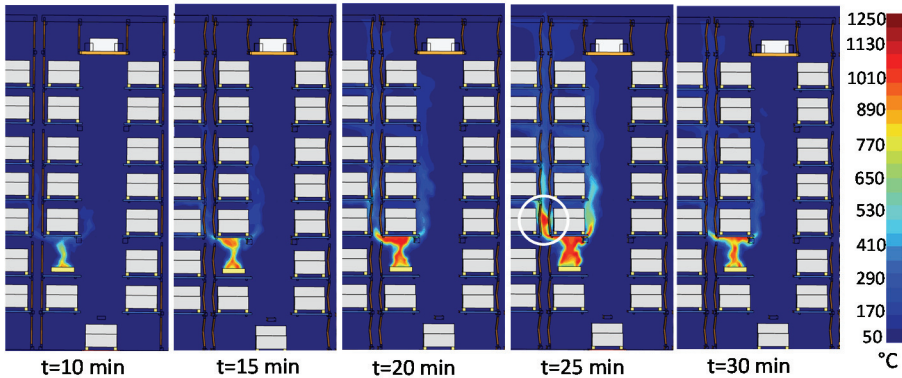
Fig. 15 - Gas temperature map (Case A)

The average temperatures of steel members are shown in Fig. 17. The average column temperatures (C2N1, C2N2, C3N1, C3N2) remain below 100 °C. The beam (B2E) near the elevator shaft (see Fig. 14) reaches as high as 800 °C, whereas the temperature level is much lower (i.e. 150 °C) in beams B2W and B3NE. This observation suggests that vehicle fire intensifies near the shaft where ventilation is expected to be at maximum levels. The beam underneath the car pallet P3E reaches temperatures as high as 1000 °C. It can be concluded that a possible dislodgement of the car pallet will occur at the early phase of fire because these beams have merely 590 °C critical temperature as calculated previously. Overall, the columns in the parking garage remain below critical temperatures and can be left without fire protection. The beams near the elevator shaft, however, go beyond the critical temperatures and exhibit a high risk of collapse and fire protection is necessary.
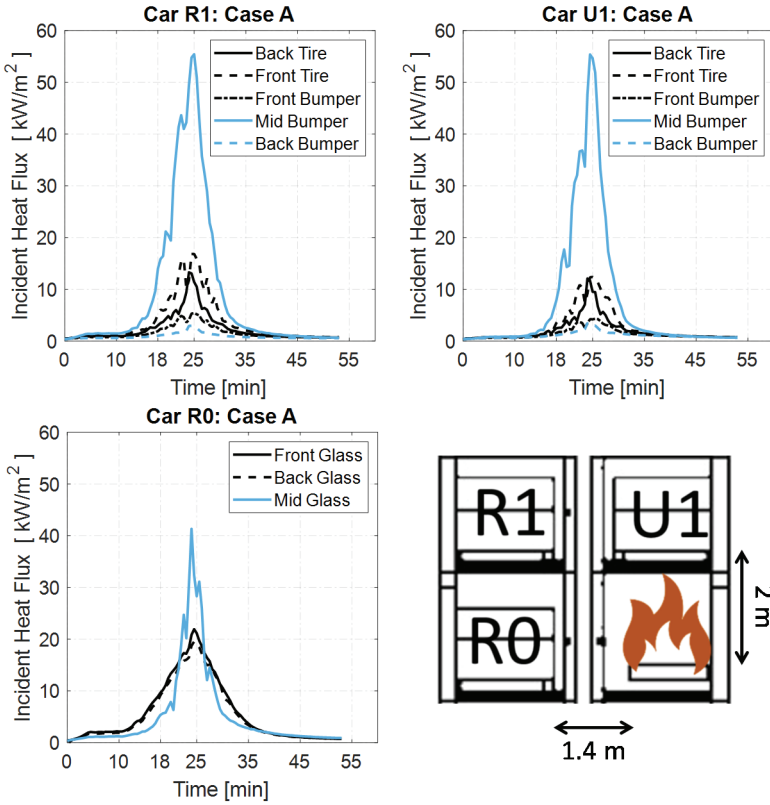
Fig. 16 - Incident heat flux levels on cars (Case A)
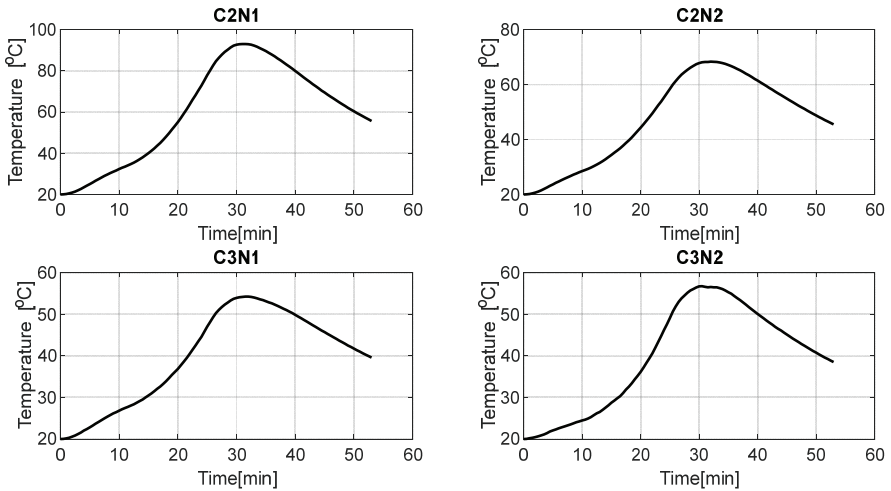
Fig. 17 - Average temperature levels of steel structural members (Case A). The steel pallet and beams near the elevator shafts reach critical temperatures.
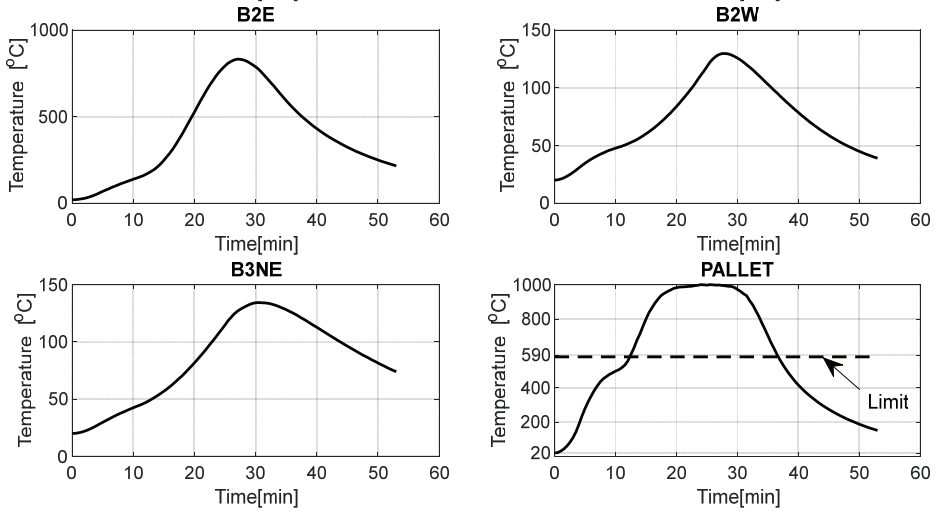
Fig. 17 - Average temperature levels of steel structural members (Case A). The steel pallet and beams near the elevator shafts reach critical temperatures. (continued)

3.2. Case B: Car Park with Firewalls

In order to minimize the fire spread, over 1800 m^2 of firewalls between passenger cars and outermost columns are placed throughout the structure. In addition, fire ceilings with 30 cm overhang are placed just underneath car pallets. The firewall configuration is seen in Fig. 18. By utilizing firewalls, hot gases are expected to channelize between the firewall and the overhang and exhausted through the façade. The firewalls are 5cm thick with 0.05 W/mK conductivity and 1 kJ/kgK specific heat. It is assumed that the thermal properties are temperature-independent and thereby stay constant throughout the fire.
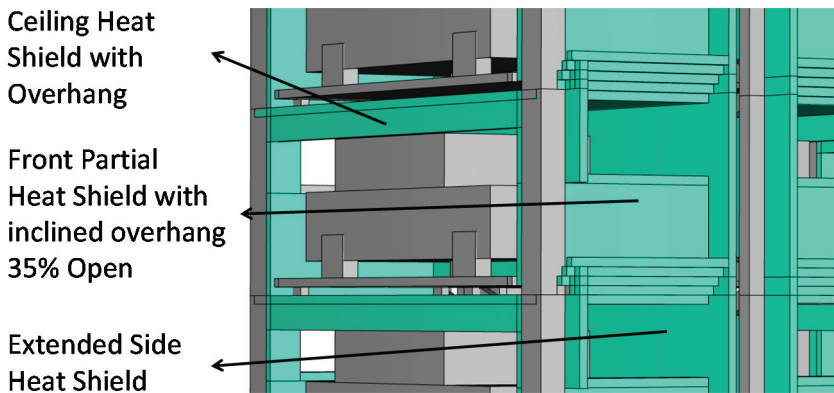
Fig. 18 - Fire wall configuration (Case B)
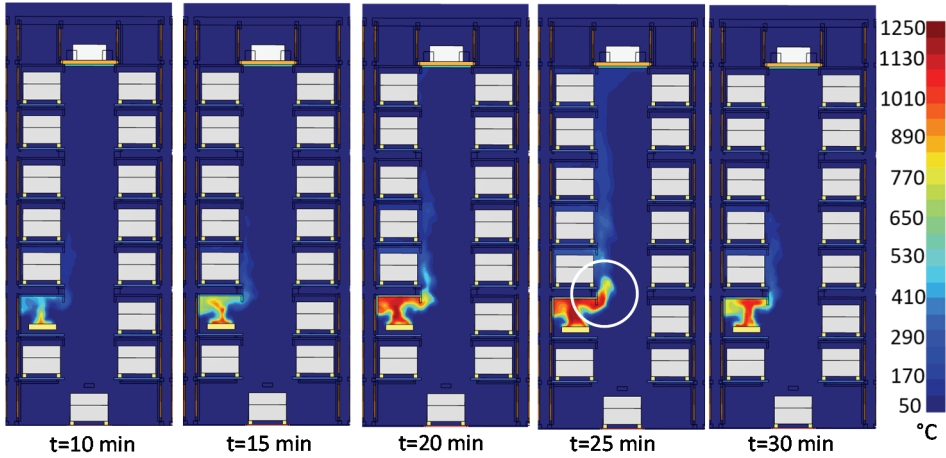
Fig. 19 - Gas temperature map (Case B)
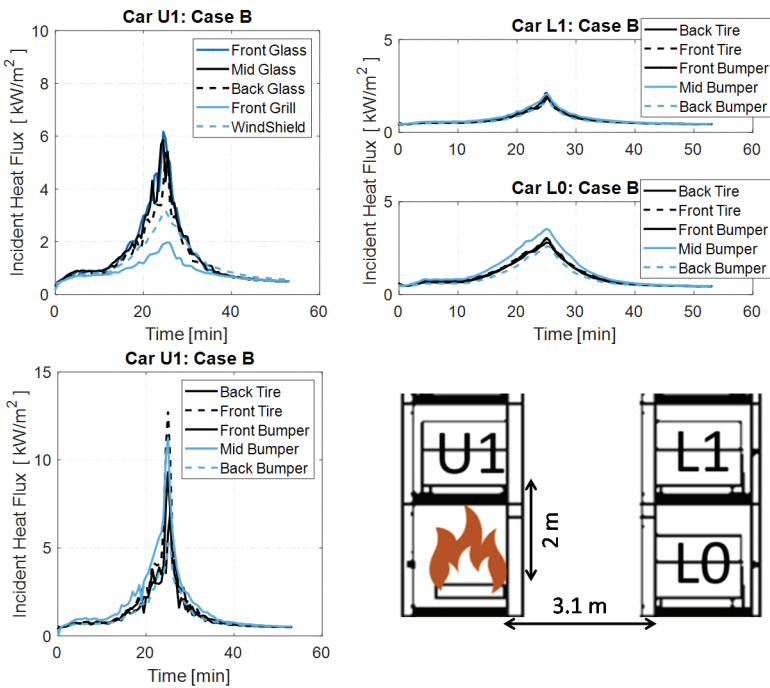
Fig. 20 - Incident heat flux levels on cars (Case B)

The gas temperatures in Case B show that the firewall and fire ceiling are mostly effective in preventing fire spread. The incident heat flux levels on neighboring passenger cars as given

in Fig. 20 are considerably lower compared to Case A. Car R0 and R1 are also totally protected by extended side heat shield as illustrated in Fig. 18. The vehicles on the opposite of the elevator shaft (i.e. L0, L1) are subjected to incident heat flux below 3 kW/m^2 and therefore the fire spread is eliminated in these vehicles. The mid bumper and the front tires of car U1 are exposed to an incident heat flux between 8 kW/m^2 and 16 kW/m^2. Ignition temperatures for bumpers and tires were previously defined as 388 °C and 350°C, respectively. As seen in Table 4, the temperature levels obtained from the fire simulation are 382°C for mid bumper and 392°C for the front tire at 25th minute. Thus, the car U1 is assumed to catch fire at front tires. Case B significantly minimizes the fire spread but it cannot prevent it completely.

Table 4 - Maximum adiabatic surface temperatures of the car U1 at 25th minute

	Bumper			Tire	
	Front	**Mid**	**Back**	**Front**	**Back**
U1	348°C	382°C	252°C	392°C	293°C

3.3. Case C: Car Park with Firewalls and Shutter Doors

In Case C, fire shutter doors are placed between the slots and elevator shaft. In addition, all firewall overhangs are improved as seen in Fig. 21. A total of 2100 m2 firewall is required for this design. This design approach aims to convert the fuel-controlled fire into the ventilation-controlled fire once the fire shutter doors are activated. The activation time or triggering mechanism of the fire shutter is essential. Fire shutters can be triggered not only electronically but also mechanically. If the triggering mechanism fails, and the electric motor is disabled, the fire shutter should be closed manually by security personnel or firefighters. The previous FDS results reveal that the activation time of 15 minutes to close the fire shutter is deemed to be satisfactory.
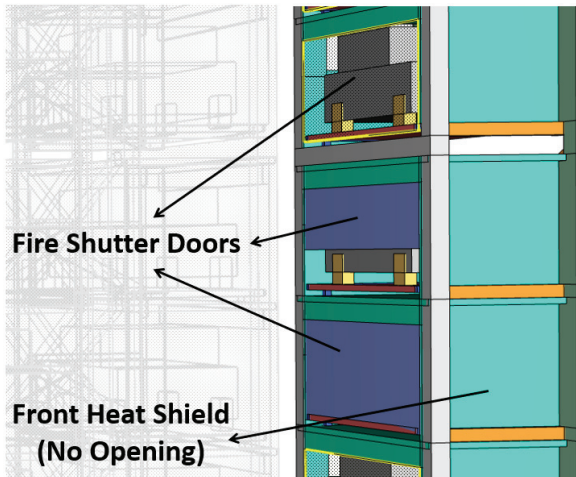
Fig. 21 - Improved fire wall configuration with fire shutter doors.
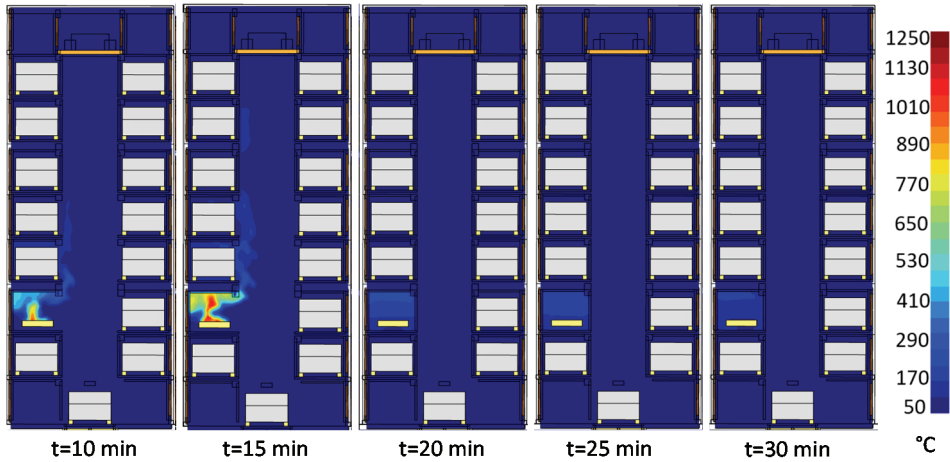
Fig. 22 - Gas temperature map (Case C)
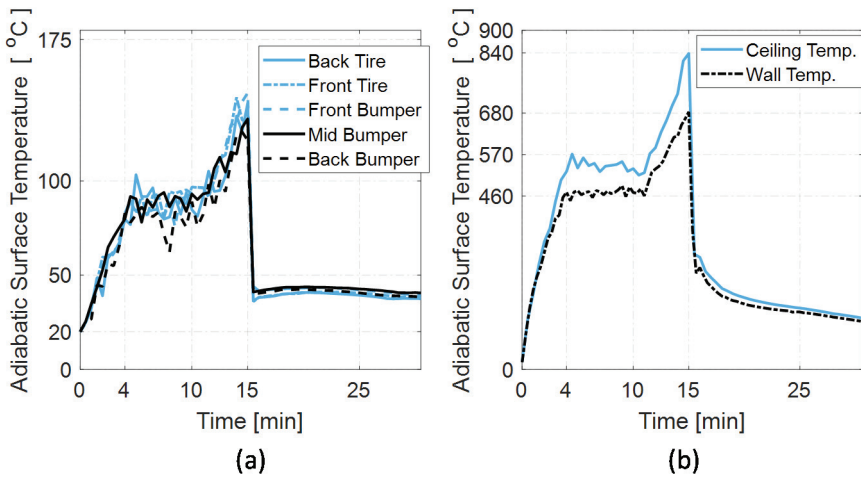
Fig. 23 - Temperature levels: (a) car U1, (b) shutter door and ceiling.

As seen in the gas temperature map Fig. 22, hot gases rising to car U1 are not able to cause an ignition before 15th minute, i.e. before the fire shutter doors are shut. After the fire shutter door is activated, the combustion reaction rapidly consumes oxygen in the compartment and the fire burns out. The maximum adiabatic surface temperature on car U1 is lower than 175 °C as seen in Fig. 23a. This level of adiabatic surface temperature does not cause ignition of any car component. Incident heat flux levels on all neighboring cars are also under 3 kW/m² as can be seen in Fig. 24. Temperature levels near the burning car reach to 850 °C, and the fire duration is limited to 30 minutes as seen in Fig. 23b. In conclusion, Case C has adequate fire safety with the combination of fire shutter doors and firewalls. However, the cost of such level of fire protection outweighs the benefit of complete elimination of the fire spread.
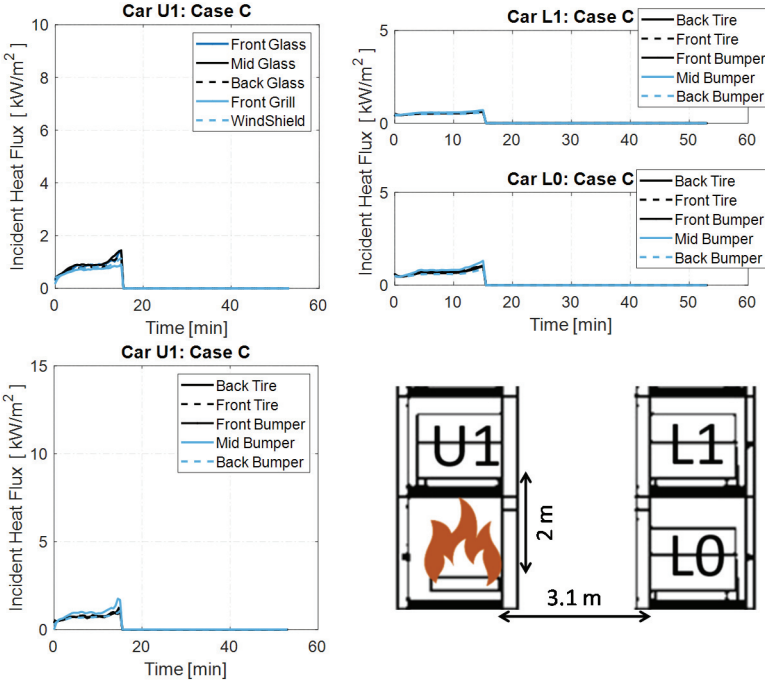
Fig. 24 - Incident heat flux levels for cars (Case C, fire shutter doors are closed after 15 minutes).

3.4. Case D and Case E: Car Park with Sprinklers

The main purpose of sprinkler water on a fire zone is to create a cooling effect by absorbing heat during phase change from liquid to vapor [32]. FDS is capable of modelling heating up and evaporation of water droplets engulfed by hot gases or over a hot surface. FDS is also adequate to model a reduction in HRR, while water droplets encounter the burning surface with predefined HRR curve. The main equation that governs the phenomena is given in Eq. 4 [19]. $\dot{q}_o''(t)$ is the predefined heat release rate per unit area in kW/m². The term may be obtained by dividing time dependent HRR to the area of the burning surface. The term k is calculated by Eq. 5, in where m_W'' is the local mass of water per unit area in kg/m². a is an empirical constant in m²/kg.s. The empirical constant is dependent on the water flux, material properties and global geometric features of the burning substance. Thus, it is strictly case-specific, and there is no study found that defines a coefficient for passenger car fires.

$$\dot{q}''(t) = \dot{q}_o''(t)\, e^{-\int k(t)dt} \tag{4}$$

$$k(t) = a\, m_W'' \tag{5}$$

The coefficient a is taken as 0.001 m²/kg.s. Same sprinkler nozzle is used in all cases. K factor is chosen as $160\ L/min\sqrt{atm}$. The activation temperature and operating pressure are

78 °C and 1 atm. Latitude angles of conical jet stream are defined as 60° and 75° in the sprinkler spray model in FDS. Jet stream velocity is chosen as 5 m/s. Two different sprinkler system layouts are examined. The layouts are given in Fig. 25. The first layout is marked as 'Case D', which is the current sprinkler application in car parks suggested by Australasian Fire and Emergency Service Authorities Council Limited [31]. It contains one sprinkler at corners of each passenger car. The second layout is proposed by [26], which contains four sprinklers per passenger car at corners.
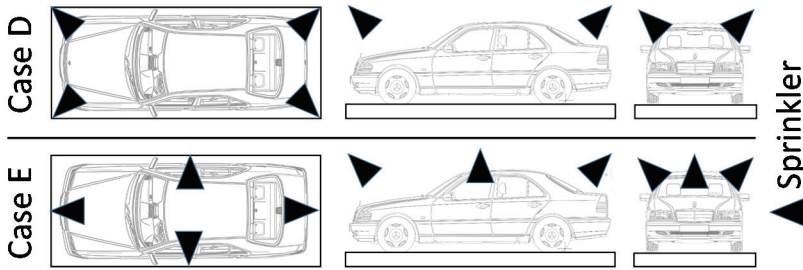
Fig. 25 - Sprinkler layouts: Case D proposed by AFAC [31] and Case E proposed by authors [26]
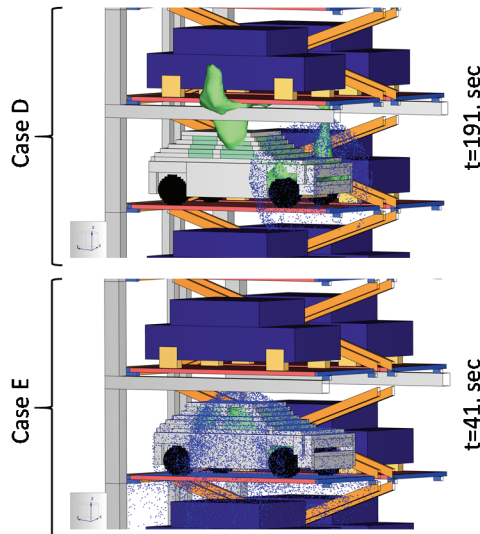
Fig. 26 - First sprinkler activation times.

Sprinkler activation is illustrated in Fig. 26. In the case D layout, the sprinkler at the southwest corner of the burning car is activated at 191st sec. Position of the sprinkler is not on the heat flow path from the gap on the front grill or the partially open window. It is the main reason for the relatively late sprinkler activation. In contrast, the sprinkler on the west of burning car is triggered at 41th sec. in the Case E because of its proper location. In the case, sprinkler water faces directly to the fire plume exhausted from side windows.
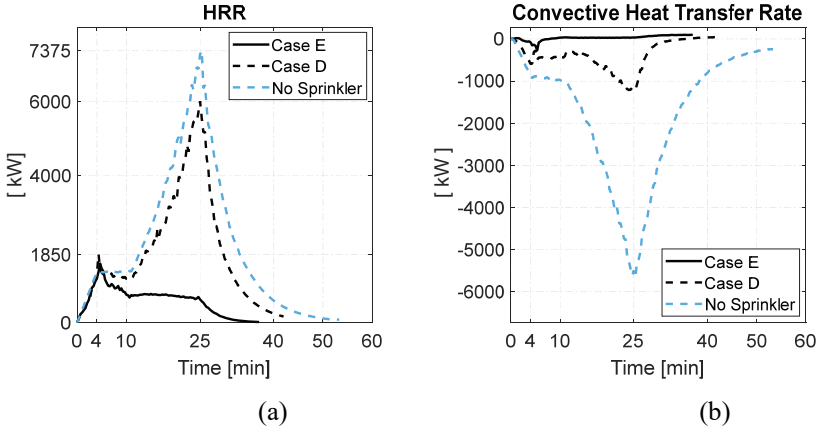
Fig. 27 - Effect of sprinklers: (a) on HRR, (b) on the convective heat transfer.
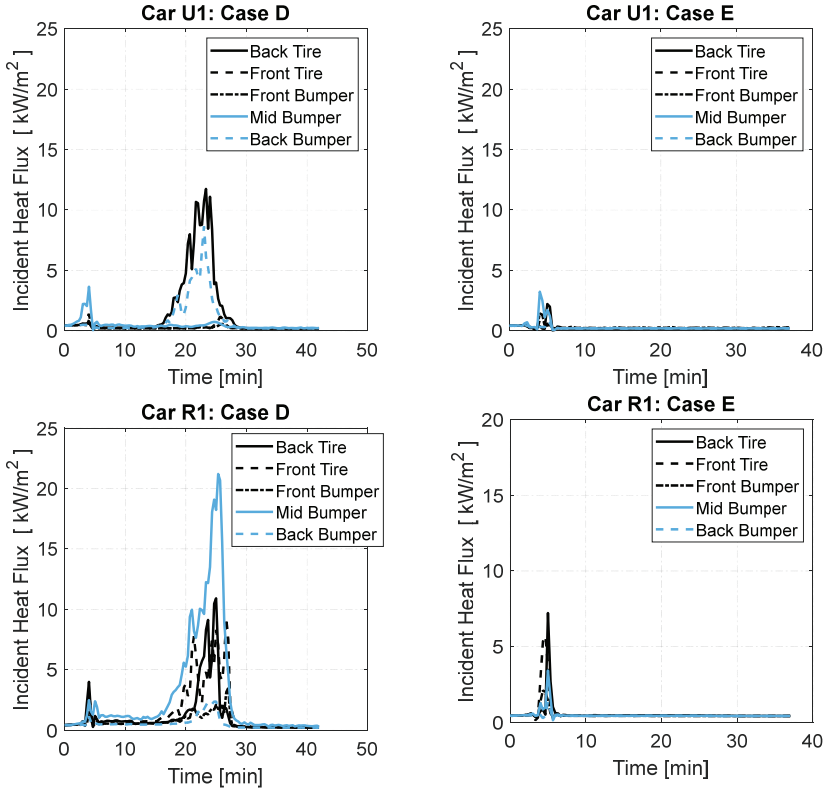
Fig. 28 - Incident heat flux on surrounding cars.
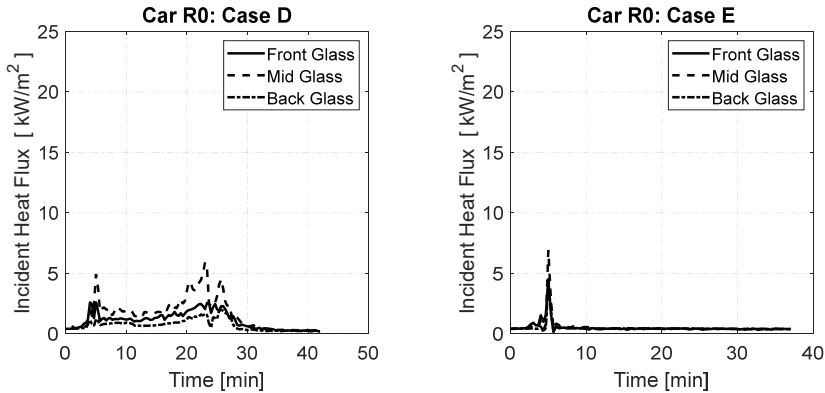
Fig. 28 - Incident heat flux on surrounding cars. (continued)

The reduction in HRR is directly related to the amount of water penetrating the fire surface. The sudden changes in HRR curves are shown in Fig. 27a. Sprinkler water also absorbs an important portion of total convective heat as shown in Fig. 27b. A similar phenomenon on convective heat transfer during a FDS simulation of a water mist spray on a propane burner has been observed in another study [32]. The incident heat flux levels on surrounding vehicles for both sprinkler layouts are shown in Fig. 28. The performance of the AFAC layout is satisfactory (Case D). Fire spread risk is eliminated for car U1 and R0 and, nearly 80% of convective heat is absorbed. However, the incident heat flux on the mid bumper of car R1 is still over 20 kW/m^2. On the other hand, the proposed sprinkler layout in Case E not only prevents the fire spread but also suppresses it completely. Incident heat flux levels on all surrounding cars remain below 8 kW/m^2.

4. CONCLUSIONS

In this study, the fire performance of an 8-story automated parking garage is investigated. The main goal is to find out the characteristics of vertical fire spread between passenger cars and add passive and active fire prevention measures to the structure to minimize the fire spread. Given the HRR of the passenger car, FDS model simulated the ignition times of nearby cars and realistically estimated the fire spread rate in multi-story parking garages. The study points out the most critical fire safety issues are (a) premature failure of steel car pallets and the rail system in automated parking garages, (b) fire spread risk to the cars above, adjacent and beyond the elevator shaft. Once the cars beyond the elevator shaft ignite at around 90 minutes, the structural system is considered as compromised.

These issues are addressed by firewalls and shutter door as passive fire safety measures. However, a complete fire spread elimination requires over 2000 m2 firewall with combination of shutter doors, which is not cost effective. Instead, the priority is to keep the fire spread risk minimized as Risk Level 1 as illustrated in Fig. 11. Fire protection underneath the steel pallets and beams on the side of elevator shafts is required. The proposed sprinkler layout as active fire safety measure extinguishes the fire from the motor (i.e. front) and

broken glasses on the sides and back more efficiently and eliminates fire spread completely. Sprinklers need to function properly, which depends on the correct installation, continuous inspection of sprinklers, water supply and assumption of no power outage for pumps. This layout, however, requires additional piping installation along the beams.

The following conclusions are drawn:

- Without any passive and active fire protection on the parking garage, the fire spreads to the car above in 23 minutes, to the neighboring car in 37 minutes and beyond the elevator shaft to the other cars in 82 minutes.

- FDS simulations determined the ignition times and the order of ignition in the surrounding passenger cars. The ignition will start with undercover and tires and at incident heat flux levels higher than 16 kW/m². FDS simulations show that car components do not ignite if the incident heat flux levels are below 8 kW/m². These upper and lower bounds for heat flux for ignition are important findings in vehicle fire CFD investigations.

- NFPA-1710 mandates 5:20 minutes response criteria for passenger car fires. In order to prevent collapse of the parking pallet above the burning car, the fire brigade must be alerted within 7 minutes.

- During a car fire, all columns of the unprotected multi-story parking garage remain below their critical temperatures. Maximum column temperatures in all cases are under 200 °C. These temperature levels are not considered as significant to comprise the structural integrity. The beam temperatures on the façade remain below 150°C. The beams next to the elevator shaft reach critical temperatures as high as 800°C if left unprotected against fire.

- Steel car pallets are not robust against a passenger car fire. The member temperature of car pallet beams reaches to 1000°C at around 20th minute of fire. Plastic hinge mechanism will likely form in the load-bearing beams underneath the car pallet in the very early phase of fire. This means that a car pallet just above a fire may collapse before the fire spreads vertically to a car on the car pallet.

- The proposed sprinkler layout is efficient and eliminates the fire spread within 5 minutes. When the sprinkler heads are placed at the rear, front and sides of the cars as opposed to placing at the corners of the cars.

- Placing firewalls on the sides of the cars and adopting shutter doors to deprive the fire from oxygen are effective in preventing the fire spread but both architectural and cost concerns likely outweigh their performance.

- The most efficient way of passive fire protection is to seal steel pallet, its rail system and beams on the elevator shaft with 5 cm gypsum-based fire protection boards.

References

[1]   NFPA 88A Standard for Parking Structures 2019 Edition, Quincy, MA.

[2]   Boehmer and Klassen, CSE Combustion Science & Engineering: Modern Vehicle Hazards in Parking Garages and Vehicle Carriers, 2020.

[3]   L. Noordijk, T. Lemaire, Modelling of fire spread in car parks, Heron. 50 (2005) 209–218.

[4]   BAFSA British Automatic Fire Sprinkler Association, Kings Dock Car Park Fire. https://www.bafsa.org.uk/wp-content/uploads/bsk-pdf-manager/2018/12/Merseyside-FRS-Car-Park-Report.pdf, 2018 (accessed 27 June 2020).

[5]   FESG Fire Engineered Solutions Ghent, FESG provides explanation on Stavanger car park fire. https://www.fesg.be/en/news/fesg-stavanger-car-park-fire, 2020 (Accessed 27 June 2020).

[6]   I. D. Bennetts, D. Proe, R. Lewins and I. R. Thomas, Open-vehicle park fire analyses, Proceedings of the Pacific Structural Steel Conference, 1986, Aukland, New Zealand.

[7]   T. Kitano, O. Sugawa, H. Masuda, T. Ave and H. Uesugi, Large Scale Fire Tests of 4-Story Type Car Park Part 1: The Behavior of Structural Frame Exposed to the Fire at the Deepest Part of the First Floor, in Proceedings of the 4th Asia-Oceania Symposium on Fire Science and Technology, Tokyo Japan, 2000, pp. 527-538.

[8]   D. Joyeux, J. Kruppa, L.G. Cajot, J.B. Schleich, P. Van de Leur, L. Twilt, Demonstration of real fire tests in car parks and high buildings, Technical Steel Research Report, European Commission, Brussels, Belgium, 2002.

[9]   B. Zhao, J. Kruppa, Structural Behaviour of an Open Car Park Under Real Fire Scenarios, Fire and Materials, 28 (2004) 269-280.

[10] Park, J. Ryu, H.S. Ryou, Experimental study on the fire-spreading characteristics and heat release rates of burning vehicles using a large-scale calorimeter, Energies. 12 (2019).

[11] P. Weisenpacher, J. Glasa, L. Halada, Automobile interior fire and its spread to an adjacent vehicle, J. Fire Sci. 34 (2016) 305–322.

[12] J.B. Schleich, L.G. Cajot, J.M. Franssen, J. Kruppa, D. Joyeux, L. Twilt, J. Van Oerle, G. Aurtenetxe. Development of design rules for steel structures subjected to natural fires in closed car parks, Technical Steel Research Report, European Commission, Brussels, Belgium, 1999.

[13] BRE British Research Establishment, Fire Spread in Car Parks. BRE Report, Department for Communities and Local Government, London, UK, 2010.

[14] British Standard Institution, BS EN 12845:2015 Fixed firefighting systems – Automatic sprinkler systems – Design, installation and maintenance.

[15] Standards Australia, AS 2118.1:2017 Automatic fire sprinkler systems-General Systems.

[16] Standards New Zealand, NZS 4541:2020 Automatic fire sprinkler systems.

[17] Republic of Turkey Ministry of Environment and Urbanization, Binaların Yangından Korunması Hakkında Yonetmelik, Turkish Official Journal, 27344, (2009) 45.

[18] BRE British Research Establishment, Sprinkler Protected Car Stacker Fire Test. BRE Technical Report, The British Automatic Fire Sprinkler Association, London, UK, 2009.

[19] K. McGrattan, S. Hostikka, R. McDermott, J. Floyd, C. Weinschenk, K. Overholt, Sixth edition fire dynamics simulator technical reference guide volume 1 : mathematical model, NIST Spec. Publ. 1018. 1 (2015).

[20] Computers and Structures Inc. SAP2000, Berkeley, California, USA, 2020.

[21] Afet ve Acil Durum Yönetimi Başkanlığı, TBDY-2018 Türkiye Bina Deprem Yönetmeliği, Ankara, 2018.

[22] EN 1993-1-2: Eurocode 3. Design of steel structures. Part 1–1: General rules – Structural Fire Design. European Committee for Standardization (CEN), Brussels, 2005.

[23] Thunderhead, PyroSim 2020, Manhattan, Kansas, USA, 2020.

[24] McGrattan K. B., McDermott R. J., Weinschenk C. G. and Forney G. P., Fire Dynamics Simulator User's Guide. NIST special publication 1019.6, National Institute of Standard and Technology, Maryland, USA, 2013.

[25] McGrattan K.B., Baum H.R., Rehm, R.G., Large eddy simulations of smoke movement, Fire Safety Journal 30:161–178, 1998.

[26] B. Ayva, Performance-Based Fire Safety Design For Automated Vehicle Parking Steel Structures, Master's Thesis, Bogazici University, 2020.

[27] NFPA 1710 Standard for the Organization and Deployment of Fire Suppression Operations, Emergency Medical Operations, and Special Operations to the Public by Career Fire Departments 2020 Edition, Quincy, MA.

[28] D. Li, G. Zhu, H. Zhu, Z. Yu, Y. Gao, X. Jiang, Flame spread and smoke temperature of full-scale fire test of car fire, Case Stud. Therm. Eng. 10 (2017) 315–324.

[29] E.M. Pearce, Polymer Flammability. Am. Chem. Soc. Polym. Prepr. Div. Polym. Chem. 26 (1985) 198.

[30] U. Wickström, A. Robbins, G. Baker, The use of adiabatic surface temperature to design structures for fire exposure, J. Struct. Fire Eng. 2 (2011) 21–28.

[31] Australiasian Fire and Emergency Service Authorities Council, Fire Safety Requirements for Automated Vehicle Parking Systems. AFAC Publication no 3044, East Melbourne, AU, 2020.

[32] B. Merci, M. Shipp, Smoke and heat control for fires in large car parks: Lessons learnt from research?, Fire Saf. J. 57 (2013) 3–10. https://doi.org/10.1016/j.firesaf.2012.05.001.

[33] S. Noda, B. Merci, F. Tanaka, T. Beji, Experimental and numerical study on the interaction of a water mist spray with a turbulent buoyant flame, Fire Saf. J. (2020) 103033.

Analysis of the Hydrodynamic Characteristics in a Rectangular Clarifier under Earthquake-Induced Sloshing

Murat AKSEL[1]

ABSTRACT

Wastewater treatment plants, which play a crucial role in protecting the hydrosphere, are earthquake-prone infrastructures with large tanks and sensitive equipment. Damage to the structures in such facilities during seismic activity on the lithosphere can cause environmental pollution and threaten public health. Since the units/tanks in the treatment plants are not of different geometries and sizes, they may exceed the freeboard of the wave height due to the sloshing event. In this study, the sloshing dynamics of a rectangular type of clarifier were investigated. First, numerical parameters, boundaries, and initial conditions were validated using the results of an experimental campaign. Secondly, model conditions were kept constant, and geometry was enlarged (i.e., scaled-up) to investigate the variation of hydrodynamic forces near vulnerable equipment (such as scrapers and weirs) in clarifier. The numerical model was run for characteristics of two different earthquakes (i.e., Chi Chi-1999 and Kocaeli-1999). The results showed that dynamic pressure values near vulnerable equipment increased up to 120 times higher than the operating conditions. The maximum sloshing wave heights were calculated as 1.2 m and 1.45 m for Chi Chi (1999) and Kocaeli (1999) earthquakes, respectively.

Keywords: Natural disasters, earthquake, treatment plant, sloshing, public and environment health.

1. INTRODUCTION

Seismic activities in the lithosphere, earthquakes, have devastating effects. Important past and recent earthquakes (e.g., Alaska 1964, Loma Prieta 1989, Kobe 1995, Kocaeli 1999, Tohoku 2011, Christchurch 2011) have damaged many civil and industrial infrastructures such as highways, airports, bridges, water transmission lines, and treatment systems, as well

---

1 Alanya Alaaddin Keykubat University, Department of Civil Engineering, Antalya, Türkiye
  murat.aksel@alanya.edu.tr - https://orcid.org/0000-0002-6456-4396

as residential buildings. Infrastructure facilities are critical facilities that must maintain their functionality even after an earthquake.

The earthquake has direct and indirect impacts on water treatment plants (WTPs) and wastewater treatment plants (WWTPs) [1]–[18]. Tsunami, floods, and prolonged power outages are the indirect effects of the earthquake on treatment facilities. Direct effects include deformation and fractures in structural elements (e.g., pipes, tank walls, pool screens, bearing components), various damages due to ground liquefaction (e.g., settlements, collapses, slope flow), and damage to non-structural elements (e.g., scrapers, mixers, aerators, separator panels and curtains, monitoring, and control equipment) [19]. The effects that may cause damage can be examined under three main headings; (1) strong ground motion, (2) soil failure, (3) inertial forces [14]. Inertial forces cause sloshing in treatment tanks, depending on the geometry and depth of the unit and the earthquake characteristics. In addition to the damage of non-structural elements caused by the displacement due to fault rupture on the lithosphere, the sloshing in the tanks can also cause damage to the non-structural elements [6], [10], [12], [14], [17], [20]–[22].

The sloshing problem is a comprehensive phenomenon that has been studied for a long time in fields such as maritime, aviation, space technology, construction, geology, machinery, transportation, fuel storage, chemistry with the help of experiments and numerical methods. Field investigations after major earthquakes revealed that non-structural element damage due to sloshing in treatment plant units frequently occurred in the primary and secondary clarifiers and floating type oil removers [12], [14], [19], [23]–[25]. Rectangular type clarifiers are generally designed with 15 – 40 m streamwise length (L), length/width ratio (L/W) of 3 – 5, and 3 – 4.5 m average water depth (D) due to environmental engineering process optimization [26], [27]. Liquid sloshing investigations are based on detecting natural frequencies/sloshing modes, sloshing wave height, hydrodynamic pressure distribution, forces, and damping methods to suppress sloshing.

The sloshing wave height in a rectangular tank is the vertical displacement of the liquid surface caused by an external disturbance, such as a change in the tank's orientation or the introduction of a fluid into the tank. The natural frequency of the tank is the frequency at which the tank will naturally oscillate if disturbed. The natural frequency of a rectangular tank is dependent on the tank's dimensions and the fluid's density and can be calculated using the eigenvalue equation for the system. The sloshing wave height can be determined experimentally by measuring the displacement of the liquid surface, or it can be calculated using numerical simulations or analytical models[28], [29].

During the sloshing phenomenon, energy dissipation occurs because of viscosity, boundary layer development induced vortices near the wall, viscous boundary layers due to air-liquid interaction [30]. This dissipation brings out a damping effect to absorb liquid sloshing. Ibrahim [30] summarized that the damping factor is controlled by the liquid depth, the kinematic viscosity of the liquid, and tank diameter or tank width for a rectangular cross-section. At excitation periods close to the first natural period for fluid motion in the tank, even small motion amplitudes result in violent sloshing. A motion of the tank normal to the undisturbed free surface may excite symmetric modes, but since the maximum sloshing period is of primary relevance, vertical tank excitation is of secondary significance. First mode natural sloshing period of a rectangular tank is controlled via tank length and the filling depth [31]. For a low filling water depth (i.e., (h/L < 0.2) shallow water sloshing), wave run-

up occurs sidewall of the tank when the excitation period differs from the initial natural period of the fluid in tank. The angle between the free surface and the wall is modest, and the upward velocity of the water at their contact is high. Period of the motion effects the sloshing wave height and wave height inside the tank increases with the motion of the movement [32].

To decrease the sloshing-induced destructive hydrodynamic forces on the structure and suppress the sloshing waves, the efficiency of various applications (e.g., ring and cruciform baffles, floating baffles, lids and mats, flexible baffles, surface roughness increasing methods) were investigated. Fixed type baffles alter the volume of the sloshing domain, cause vortex generating with their sharp edges, and block the bulk climbing of liquid over the side walls [33].

Sloshing in rectangular tanks can be examined as a two-dimensional fluid motion. This two-dimensional flow can be classified under two sloshing behavior types: (1) low liquid fill depth, and (2) high liquid fill depth. If the ratio of liquid depth to the cross-sectional width of the tank in the direction of motion ratio is higher than 0.2, this case is classified as 'high liquid fill depth' [30]. If the aforementioned ratio is smaller than 0.2, typical for rectangular type clarifiers, the sloshing is classified as 'low liquid fill depth' (i.e., shallow water tank, or shallow type sloshing). In a shallow type of sloshing, hydraulic jumps and traveling waves for excitation periods around resonance were reported by various researchers [34]–[37]. This strong sloshing, accompanying waves and hydraulic jumps cause extremely high impact pressures on all kinds of structural (e.g., baffles, feeding wells) and non-structural elements (e.g., scrapers, chains, measurement probes) placed inside the tank or on the tank walls. Ibrahim [30] also pointed out that these impact pressures cannot be determined theoretically and need experimental and numerical work to be estimated. Non-structural elements inside WTPs and WWTPs units must be investigated under sloshing dynamics for a proper design. Aksel (2021) numerically modelled circular type of clarifier under earthquake-induced sloshing conditions, and pointed that non-structural element (i.e., feeding well) inside the units significantly affected the dynamic of the sloshing [38].

Damage to the treatment system will cause the treatment facilities, which will have a critical role in public health after the earthquake, to lose their functionality. WTPs and WWTPs that cannot continue their activities due to damaged facilities will prevent public access to clean water and healthy sewage treatment after the earthquake and impair public health. As seen in previous earthquake cases, this state of affair may cause epidemics and even loss of life [39]–[43].

Determining the fragility and sensitivity of the units in the treatment plants against potential earthquakes and taking necessary precautions are essential for protecting the environment and public health, and reducing the potential economic losses experienced afterwards. There are some estimation methods in the literature about determining the fragility of treatment plant units and the earthquake sensitivity of facilities [23], [44]–[47]. However, these methods do not clearly define/suggest limits for the design. Instead, they only allow risk estimation according to the soil condition of the facilities, the year of construction, the nature of the building material used, and the earthquake impact zone. Reducing possible risks before a potential earthquake is disproportionally more cost-effective and time-efficient compared to post-earthquake surveys of treatment facilities, repairing the detected damages, and re-commissioning the facilities [25], [48].

Based on the process optimization from an environmental engineering perspective, regulations, standards, and specifications prepared for treatment plants in the literature were regulated. These facilities, which are planned and designed without considering the dynamic building performance, are located in low-elevation and generally alluvial areas of the city most of the time, considering water collection convenience. This situation results with weak soil conditions, and it further increases the risk of damage to the facilities, which should be included in the critical facilities class with high earthquake risk [24], [44]. There is a lack of knowledge about the behavior of such facilities under earthquake conditions and their performance in the current earthquake regulations and standards, especially for earthquake-induced sloshing.

With this motivation, experimental and numerical studies were undertaken in this study. First, the response of a simplified rectangular type of water tank geometry under the influence of periodical motion was investigated experimentally. The experimental results were analyzed, and the generated data constituted a reference for the numerical model. Then, during the numerical model study, the same problem was reproduced in a numerical domain. The model's initial and boundary conditions were prescribed, and model parameters (e.g., roughness coefficient, mesh aspect ratio, interaction coefficient between phases) were defined accordingly. This step is followed by the validation of the model. After calibrating the numerical model concept, a widely used geometry was selected as a rectangular clarifier, and the vulnerable equipment (i.e., scrapers) was integrated into the model. The sloshing behavior was examined under two different earthquake signals (i.e., Chi Chi (1999), Kocaeli (1999)). The main goal of this study is to examine the effect of earthquake-induced sloshing on hydrodynamic stability of a commonly used rectangular type clarifier and hydrodynamic pressure variations on non-structural equipment (i.e., scrapers) during the sloshing.

2. MATERIALS AND METHODS

Examination of the damage on treatment plant units caused by sloshing, especially those of the vulnerable equipment inside them, using the full-scale studies requires a challenging and expensive research process. In line with this fact, in this study, a two-stage analysis was applied. Firstly, physical model studies were conducted. Then, this stage is followed by a numerical model study in which Reynolds-Averaged Navier-Stokes (RANS) equations were solved. During the computer-aided computation of sloshing in model tanks, model parameters, boundaries, and initial conditions were calibrated with the results of the experimental research.

Computational Fluid Dynamics (CFD) based sloshing analysis was performed using RANS equations with the help of Flow-3D software, which is commonly used in various disciplines [49]–[57]. CFD tools are used by various researchers for the design and operation of WTPs & WWTPs [58]–[62]. In addition, this solver has also been used in sloshing analyses with confirmation by experimental studies and calculates results compatible with the experimental results [63]–[65].

2.1. Model Validation

2.1.1. Experimental Setup

Experimental studies were carried out in the laboratory of the Civil Engineering Department of Alanya Aladdin Keykubat University. The testing system consists of a water tank with uniaxial freedom of movement, built on a monorail driven by a computer-controlled step motor, a shaking table. The water tank was 28 cm in length and 10 cm in width, and it was filled with 5 cm depth of red-colored water. An accelerometer capable of recording 100 Hz data that sends measurements to the computer was mounted on the shaking table. A video camera synchronized with accelerometer measurements was also used (Figure 1). To conduct the experiments under identical controlled conditions, room temperature and humidity were kept constant at 22 °C and 55%, respectively.
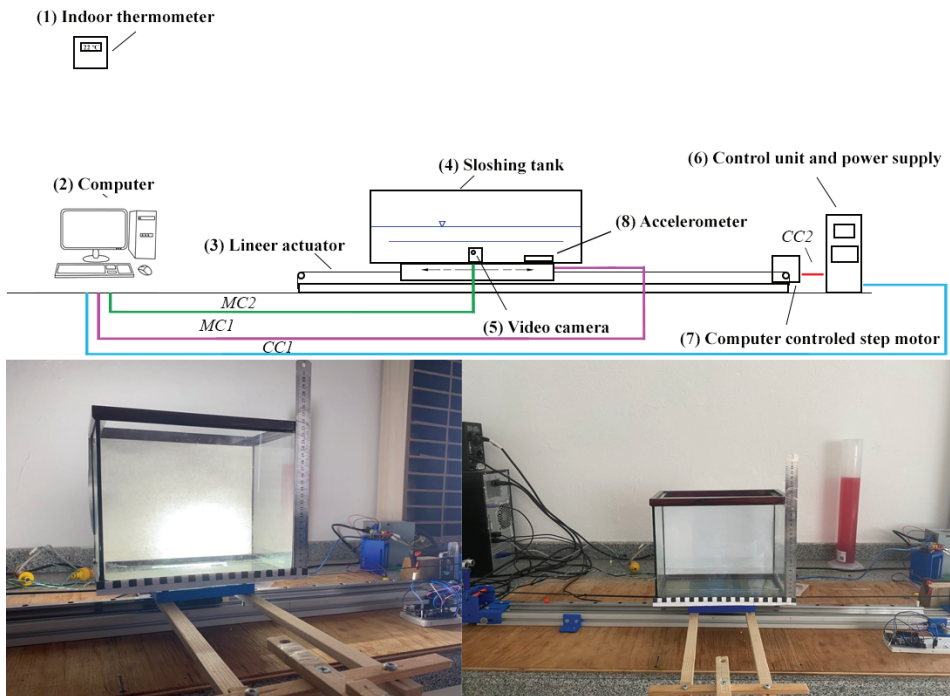
Figure 1 - Experimental setup (1) indoor thermometer, (2) computer, (3) linear actuator, (4) sloshing tank, (5) video camera, (6) control unit, (7) step type computer-controlled motor, (8) accelerometer. Green and red lines show control cables 1 and 2 (CC1), (CC2), and magenta and light blue colored lines present monitoring cables (MC1), (MC2), respectively.

In Figure 2a, the velocity vs. time signal used in the shake table and recorded velocity data from the accelerometer are presented with a dashed line and a solid red line, respectively. Input signal was sinusoidal, and the input signal period and amplitude were 2.81 sec and 4,62 m/sec, respectively. The incompatibility between the input signal and the speed data read on

the shake table stems from the errors originating from the entire system (e.g., measurement noise, motor response delay, belt system-induced oscillation). Nevertheless, the general behavior of the shaking table reflects the intended input signal. The main period of the tank motion, which is defined as the time for the moving tank to complete one full cycle in lateral direction (T_{ip}), was calculated via time differences between the successive local extrema in Figure 2a as 2.81 sec. In Figure 2b zero-crossing points for down/up are marked up the output signal. Mean period of the tank motion were calculated via MATLAB with an interpolation code for zero-up-crossing and zero-down-crossing as 2.76 sec and 2.68 sec, respectively.
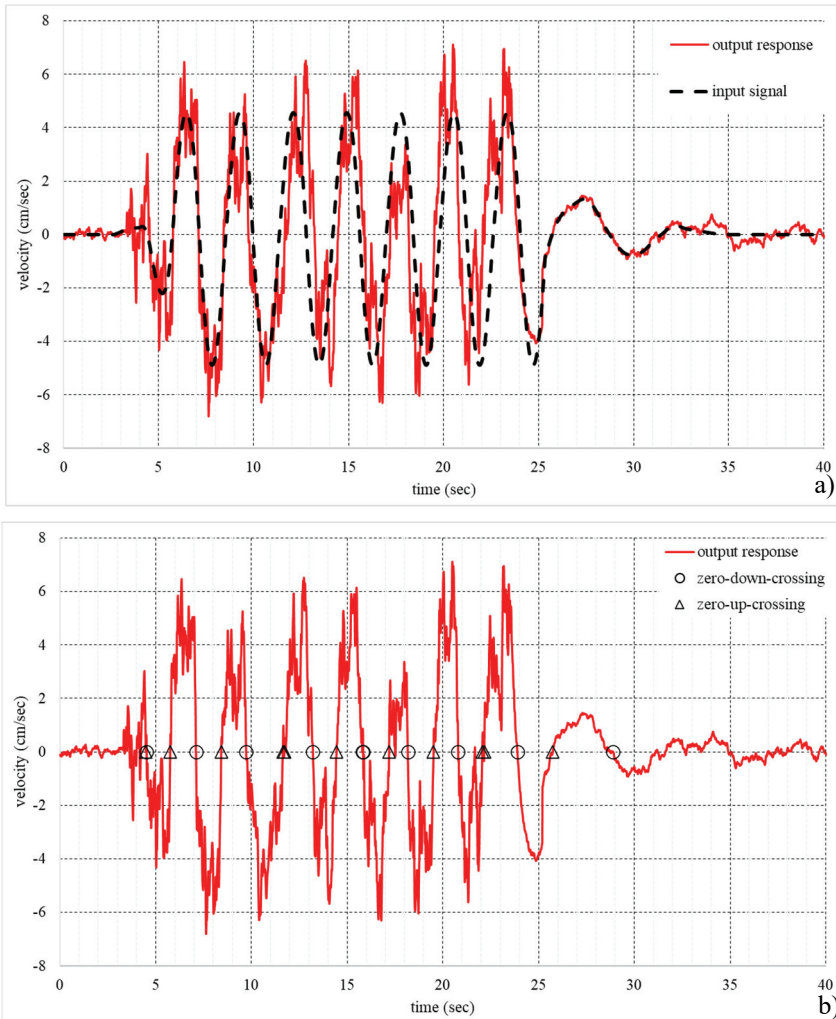
Figure 2 - a) Input velocity signal from the computer control unit (black dashed line) and recording from the accelerometer mounted on the shake-table (red line), b) output signal and zero down crossing (O)and zero down crossing (Δ) points

2.1.2. CFD Analysis for Validation

The basic equations of mass continuity and momentum balance was used in the numeric analysis, which are explained below.

$$V_F \frac{\partial \rho}{\partial t} + \frac{\partial}{\partial x}(\rho u A_x) + R \frac{\partial}{\partial y}(\rho v A_y) + \frac{\partial}{\partial z}(\rho w A_z) + \xi \frac{\rho u A_x}{x} = R_{DIF} + R_{SOR} \tag{1}$$

In Eq. 1, V_F is the fractional volume open to flow (i.e., flow domain), u, v, and w are velocity components, R is coordinate system conversion coefficient, ρ is the fluid density, ξ is the coordinate conversion parameter ($\xi = 0$ corresponds to cartesian geometry, while $\xi = 1$ corresponds to cylindrical geometry), R_{DIF} is a turbulent diffusion term, and R_{SOR} is a mass source term [66].

$$\frac{\partial u}{\partial t} + \frac{1}{V_F}\left\{ uA_x \frac{\partial u}{\partial x} + RvA_y \frac{\partial u}{\partial y} + wA_z \frac{\partial u}{\partial z} \right\} - \xi \frac{A_y v^2}{xV_F}$$

$$= -\frac{1}{\rho}\frac{\partial p}{\partial x} + G_x + f_x - b_x - \frac{R_{SOR}}{\rho V_F}(u - u_w - \delta u_s)$$

$$\frac{\partial v}{\partial t} + \frac{1}{V_F}\left\{ uA_x \frac{\partial v}{\partial x} + RvA_y \frac{\partial v}{\partial y} + wA_z \frac{\partial v}{\partial z} \right\} + \xi \frac{A_y uv}{xV_F}$$

$$= -\frac{1}{\rho}\left(R\frac{\partial p}{\partial y} \right) + G_y + f_y - b_y - \frac{R_{SOR}}{\rho V_F}(v - v_w - \delta v_s) \tag{2}$$

$$\frac{\partial w}{\partial t} + \frac{1}{V_F}\left\{ uA_x \frac{\partial w}{\partial x} + RvA_y \frac{\partial w}{\partial y} + wA_z \frac{\partial w}{\partial z} \right\} = -\frac{1}{\rho}\frac{\partial p}{\partial z} + G_z + f_z - b_z - \frac{R_{SOR}}{\rho V_F}(w - w_w - \delta w_s)$$

Here, in Eq. 2, G_x, G_y, G_z are body force components, A_x, A_y, A_z are the directional open area to flow, f is viscous force, b is flow losses in porous media/across porous baffle plates, and the final terms account for the injection of mass at a source represented by a geometry component. U_w (u_w, v_w, ω_w) is the velocity of the source component, U_S (u_S, v_S, ω_S) is the velocity of the fluid at the surface of the source relative to the source itself, and $\delta = 0.0$ in Eq. 2 the source is of the stagnation pressure type. If $\delta = 1.0$, the source is of the static pressure type. Thus, it is possible to define a linear acceleration or direction-based velocity using moving object physics in Flow-3D. The general moving object (GMO) mechanism that is either user-specified (prescribed motion) or dynamically connected with fluid flow (coupled motion). The motion of a rigid body can typically be described with six velocity components: three for translation and three for rotation. To accurately interpret the computational results and define the motion of a GMO, a user must comprehend the body-fixed reference system (body system), which is always fixed on the object and experiences the same motion [66].

Volume fraction change with time in Eq. 1 is replaced by $\vec{V}_{obj}.\vec{n}\, S_{obj}/V_{cell}$ for defining the mass conversation property of fluid, where S_{obj}, $\vec{n}$, and $\vec{V}_{obj}$ are surface area, surface normal direction and velocity of moving object boundary in a mesh cell, respectively [67].

The accelerometer record presented in Figure 2 was directly used to describe tank motion in the CFD verification analysis.

The fluid domain was divided into a quadratic type of mesh elements for calculations. Side and bottom walls were defined as wall type boundaries with no-slip conditions, and the top boundary was selected as relative pressure type boundary, which is equal to zero relative pressure magnitude. This boundary allows two-way fluid mass inlet-outlet, however in the model no water phase was defined nearby, it was set as stationary air phase. Compressibility was neglected for the fluids (both air and water) in model. Renormalized group (RNG) type of turbulent model was employed for turbulence closure. The water depth was set to 0.05 m, and physical water properties (e.g., density and viscosity of water, water-air interface entrainment, these parameters were taken as 22°C water temperature characteristics) were arranged identical with the experimental conditions. The water depth was selected to facilitate shallow water sloshing. The standards published by the American Society of Mechanical Engineers (ASME, 2009) were followed during the validation of the CFD model [68].
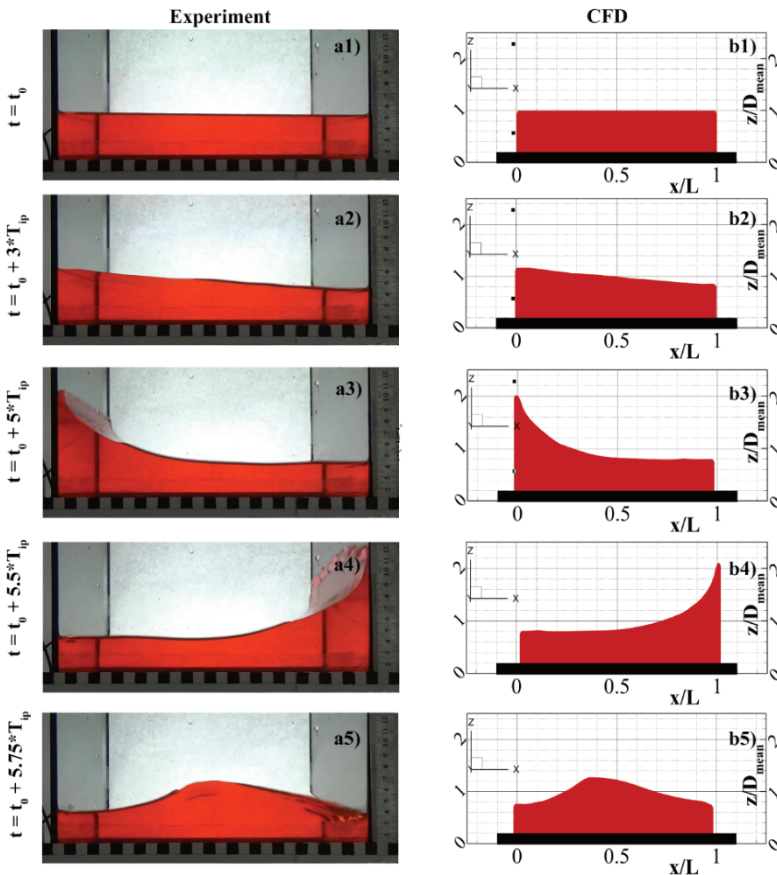
Figure 3 - Visual verification of the model outputs a1-a5) the pictures captured from the video and b1-b5) CFD model results for the water phase. The dimension of the ruler adjacent to sub-figures "a" is in cm. The squares located at the bottom of each sub-figures "a" are 1 cm x 1cm.

Images captured during the physical model tests of sloshing and CFD model results in the corresponding moment are given as couples in Figure 3. In addition, temporal information on which moment the results belong is presented on each figure's left side. Here, t is the instantaneous time, and t_0 is the initial time for both experimental and CFD analysis. The tank's sloshing period (T_{ip}) was calculated as 0.8 sec using Eq. 3 [69], in which L is the length of the tank in motion direction, g is gravitational acceleration, and D_{mean} is the depth of the fluid at rest inside the tank.

$$T_{ip} = 2 \frac{L}{\sqrt{g.D_{mean}}} \tag{3}$$

Visual comparison of the presented images belonging to the experiment and numerical model showed that the numerical model can simulate the sloshing process in the tank with acceptable accuracy. For a detailed quantitative analysis image processing tools were utilized to detect the left side wave height (i.e., instantaneous water level at the left edge of the tank) during the sloshing. Frames were exported from the video captured with a 60-fps rate. Firstly, masking was utilized to detect only red pixels. Secondly, the masked image was converted into a black-white image. Edge detection and corner detecting were applied on the frames to calculate the y coordinate of the top-left edge of the white-colored fluid domain (Figure 4). After all, pixels were counted automatically, and pixel coordinate was converted to water depth values. On the other hand, a probe was placed at the left side of the tank in the CFD model to calculate water depth during the analysis. The timeseries of water depth values from the image processing of experimental results and those from the CFD analysis are presented in Figure 5. As seen, a fair agreement between the experimental and numerical results is evident. In Figure 5b, relative errors of CFD results for minima and maxima extreme values due to image process results were given using bar and triangle, respectively. Extreme values (i.e., minima and maxima) were calculated using MATLAB signal processing tools for first 35 sec after the initial motion. This experimental setup and validation procedure were also used to model spherical particle behavior under sloshing event [70].
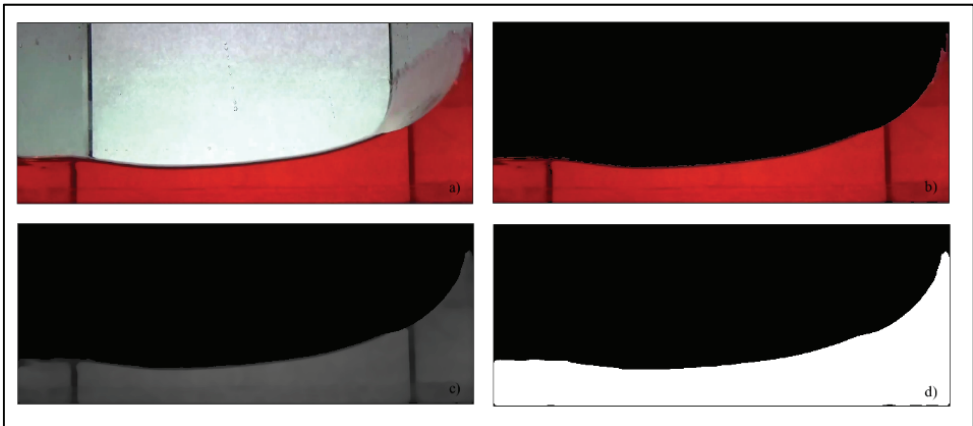
Figure 4 - Image processing procedure a) importing raw image, b) masking un-red pixels, c) converting grayscale and denoising, and d) converting black& white.
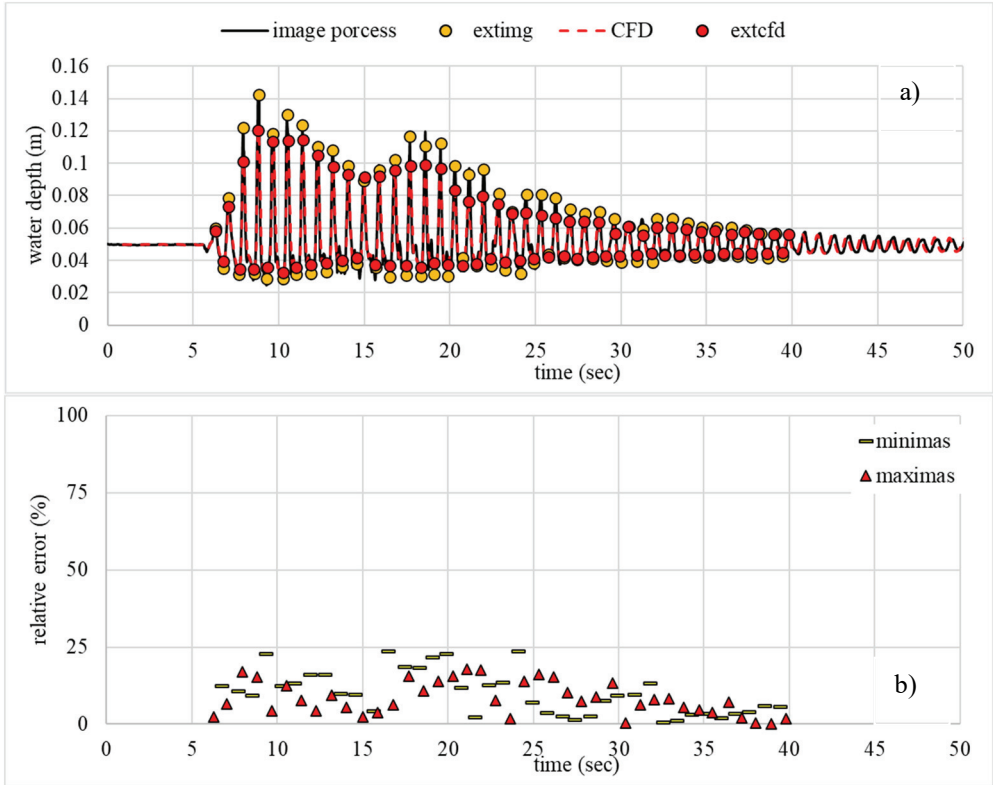
Figure 5 - a) Water depth at the left-hand side of the tank during the test 1 was calculated via image process and CFD. Image process and CFD results were presented with black and red lines, respectively. Yellow and red dots show minimum and maximum extremes for image process and CFD results, correspondingly. b) Relative errors of CFD results for minima and maxima extreme values due to image process results were given using bar and triangle, respectively.

2.2. CFD Model Analysis for Rectangular Type Clarifier

Rectangular type clarifiers include various pieces of equipment inside for process, sedimentation, and flow control (i.e., inlet baffles, flights, weirs, drive chains or belts, rails, monitoring probes, water, and sludge level sensors, scum collectors). This equipment is sensitive and vulnerable to hydrodynamic impacts. In the following sub-sections, first, the geometry of the operating conditions simulated by the numerical model is identified. Second, an earthquake-induced sloshing model is defined which was run using historical earthquake signal datasets.

Mesh and model characteristics are summarized in Table 1 for CFD models. Mesh quality effect on sloshing behavior calculation was performed by Gandara et. al. (2021) with an 800 mm tank and various mesh size. In their study, experimental tank volume / mesh number ratios were taken between $0.79 \times 10^{-6} - 2.26 \times 10^{-6} \text{ m}^3/\text{element}$. Improved mesh

quality (0.79×10^{-6} m³/element ratio) was sufficient to represent the sloshing behavior inside a rectangular tank [71]. During the modelling calculations in scope of this work experimental tank volume / mesh number ratio was employed as 1.56×10^{-8} m³/element.

Table 1 - Mesh and Model Characteristics

	Validation Model	**Real Scale Clarifier Model**
Mesh Type	Uniform Quadratic	Uniform Quadratic
Mesh Size (m)	0.0025	0.01
Number of Mesh	1002240	11648000
Dimension	3D	3D

2.2.1. Geometry Selection and Operating Conditions

To examine the earthquake-induced hydrodynamic pressure values acting on vulnerable equipment inside a rectangular clarifier, firstly, a characteristic tank geometry representing the average dimensions due to the standards was prepared. According to the average values of the ranges given by Metcalf & Eddy (2003), the prototype clarifier dimensions were chosen as L=30 m, W=6 m, and D_{mean}= 4 m. The sloshing period (T_P) for the selected clarifier dimensions was calculated as 9.58 s using Eq. 3. The average operation flow rate was taken as 0.125 m³/s to satisfy the typical value of overflow rate, which is approximately 60 m³/m² /day [27]. Water was assumed as clear water (i.e., no sludge inside the tank), and the temperature was chosen as 20 °C to configure physical parameters belonging to water.

A perspective view of the model domain with essential equipment inside and layout of numerical probes (shown as red dots) included in the model is presented in Figure 6. Still water level (SWL) was selected as 4.35 m from the tank bottom. The inlet boundary was pointed on the left-hand side, and the outlet weir was marked on the right side. The probes labeled as 1 and 2 are located in the front and back of the velocity reducing (pressure break) panel. Probes 3 and 4 are installed in front and behind of the outlet weir, respectively. The labeling of the monitoring probes for scrapers was based on the direction of the flow; the ones starting with the "u" code represent the near-surface location (z = 4.3 m), and the ones beginning with the "d" code represent the near-bottom (z = 0.8 m) points. The number sequence is given in the streamwise direction. Odd numbers indicate the upstream side of the obstacles, and even numbers indicate the downstream probes. The probes are shown as red dots in Figure 6.

The model representing operating conditions was run until the model's mass average kinetic energy value became stable. It took 6000 s (in the model time) to reach the steady-state conditions in the model environment. This value corresponds to four computer calculation days. When the model output stabilized, the earthquake analyses were initialized with the numerical model, using the steady-state operating conditions as an initial condition. In Figure 7, the flow pattern is plotted at the longitudinal centerline of the clarifier for stable (steady state) operating conditions. As seen in Figures 7a and 7b, representing t=3000 s and t=6000 s, respectively, the model became stable.
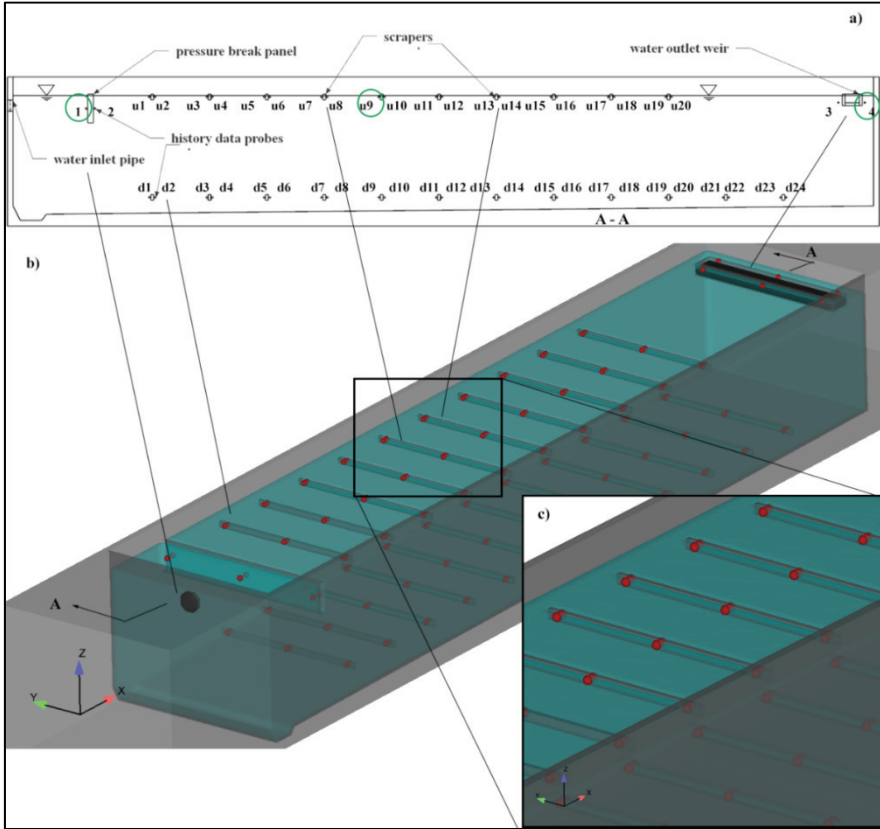
Figure 6 - The centerline of the longitudinal cross-section of the model includes fundamental elements and calculation probes. The red dots in subfigures b and c indicate the numerical probes. In subplot a, the green circles correspond to the locations where the analyses were carried out/presented in Fig 7.
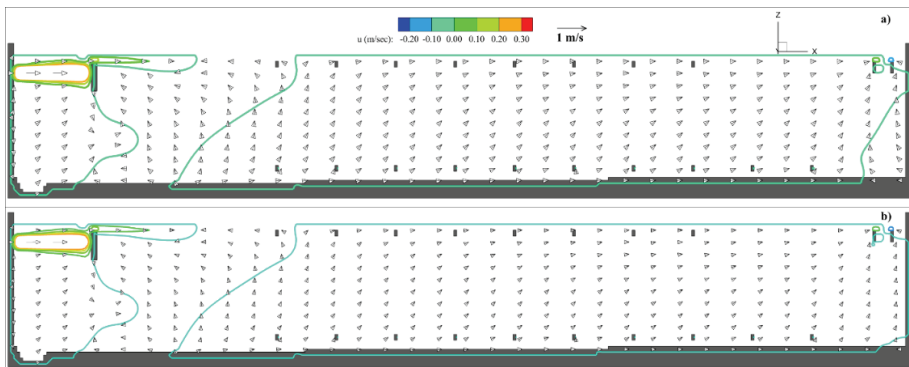
Figure 7 - Flow pattern inside clarifier under operating conditions a) t = 3000 s, b) t = 6000 s.

2.2.2. Earthquake Induced Sloshing Model

The general moving object model which is a rigid body with any kind of motion that is either user-prescribed or dynamically coupled with the fluid flow was selected to simulate clarifier response to the seismic motion. The hydrodynamic response of the rectangular type of clarifier under the earthquake-induced sloshing effect was investigated by accepting the model that has stabilized under the operating conditions as the initial condition. The clarifier was assumed to be a rigid moving element with equipment inside and would move simultaneously with the ground motion. The ground motion time series was created using velocity-time data from two well-known earthquakes, i.e., Chi Chi (1999) and Kocaeli (1999). Earthquake signals were downloaded from the Pacific Earthquake Engineering Research Center (PEER) Ground Motion Databases (PGMD).
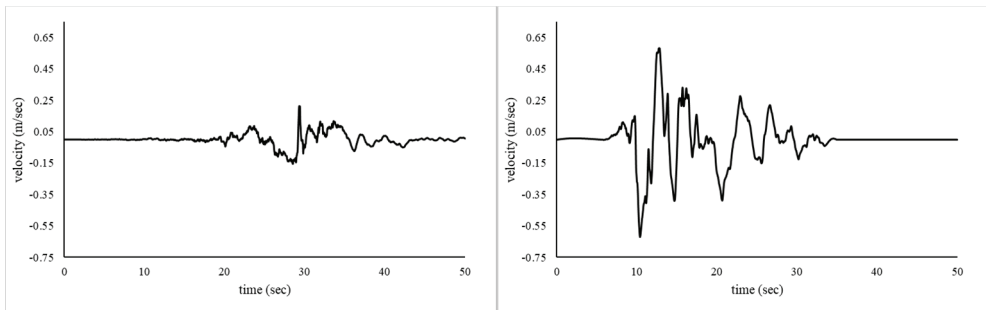
Figure 8 - Ground motion signals of a) Chi Chi (1999) and b) Kocaeli (1999) earthquakes.

In Figure 8, the time series of the ground motion velocities for Chi Chi (Figure 8a) and Kocaeli earthquakes (Figure 8b) were used directly (without any denoising or smoothing operation) in the model to define the prescribed one-directional motion to the clarifier. Although both Chi Chi and Kocaeli earthquakes have close maximum peak acceleration values (0.361 and 0.349 g, respectively), the specific energy density of the Kocaeli earthquake (1.0334 m^2/s) is approximately 12 times higher than that of the Chi Chi earthquake (0.08812 m^2/sec) (PEER-PGMD). During the earthquake-induced sloshing simulations, the operational flow rate input was stopped for the sake of simplification in the model, assuming a power outage during the earthquake.

3. ANALYSIS OF THE RESULTS

As stated above, the steady flow conditions were used as the initial condition. Then on top of the steady flow conditions, two different earthquake characteristics were applied. The hydrodynamic response of the clarifier was investigated under these two characteristic cases. The clarifier's center is represented by point u11, which was nearly located at the center of the scraper group (Figure 6). On the right-hand side, in the streamwise direction, point 4 was located near the outlet weir. Point 1 was located at the front side of the pressure break weir near the inflow.

In Figure 9, the temporal variations of water surface fluctuations at these three locations (i.e., points 1, u11, 4) under the effect of two characteristic earthquakes (i.e., Chi Chi and Kocaeli) are given. As seen from Figure 9, the sloshed wave heights, which are presented for points 1 and 4, were higher than the center point (i.e., u11). This result implies that the hydrodynamic forces acting on the clarifier at both edges are more critical than at the center zone, as also observed in the experiments. Second, the magnitude of extreme waves in Figure 9 is proportional to time variation of earthquake acceleration. Since the specific energy density belonging to Kocaeli earthquake is higher than the one in Chi Chi (Figure 8), the developed extreme sloshing waves do not attenuate rapidly, and the wave damping process takes markedly longer in the former case.
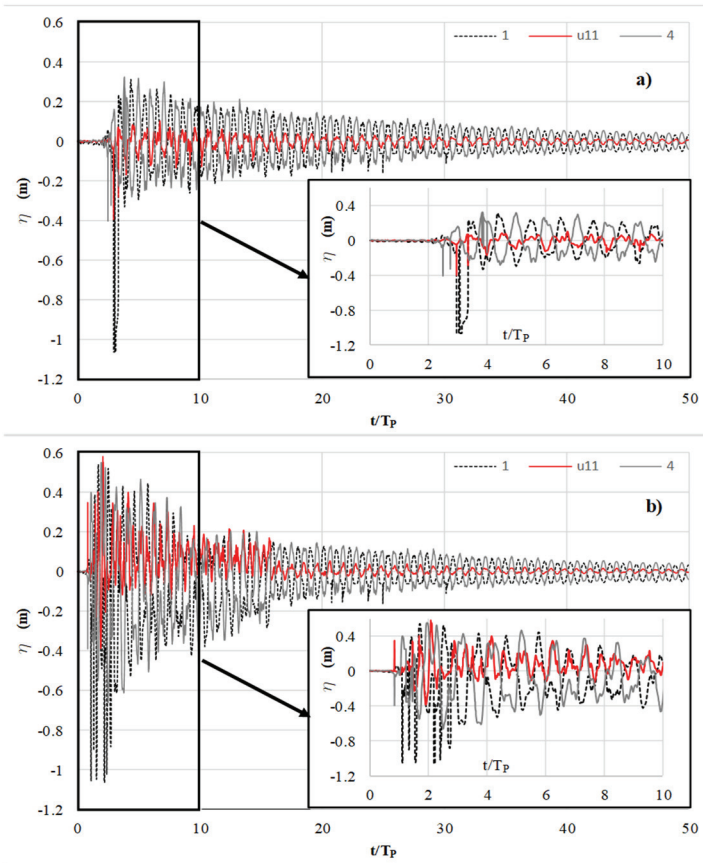
Figure 9 - Water surface displacement under a) Chi Chi earthquake b) Kocaeli earthquake for monitoring points left side (1 – dashed line), center (u11 – red line), and right side (4 – grey line) of the clarifier on cross sectional view. Points are marked with green circle on Fig. 6. The insets show the time-intervals where the analyses were given in Fig. 10 and 11.

In Figure 10, water surface displacement values which were presented in Figure 9a and b for Chi Chi and Kocaeli were analyzed using MATLAB signal processing tools and were plotted in frequency domain. Fast Fourier Transformation (FFT) was applied during this conversion. Natural frequencies for the first ten modes of the rectangular clarifier were calculated and marked up Figure 10 with blue circles.
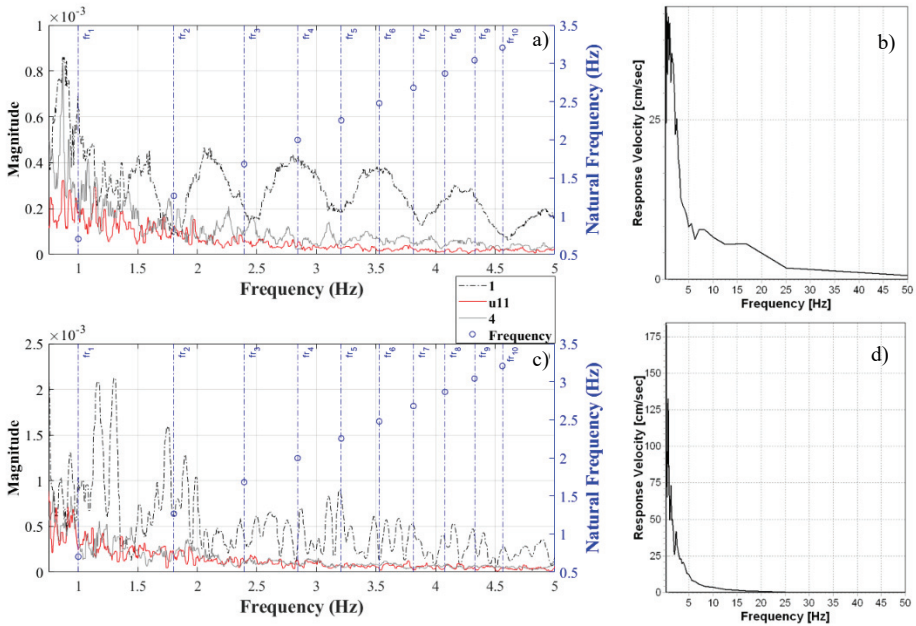
Figure 10 - Sloshing wave height magnitude in frequency domain a) Chi Chi earthquake c) Kocaeli earthquake for monitoring points left side (1 – dashed line), center (u11 – red line), and right side (4 – grey line) of the clarifier on cross sectional view. Points are marked with green circle on Fig. 6. Blue marks are the natural frequencies for the first 10 modes of the clarifier. Earthquake response velocities are in frequency domain for b) Chi Chi and d) Kocaeli.

In Figures 11 and 12, clarifier responses to Chi Chi and Kocaeli earthquakes are presented for the selected time intervals. On these charts, the normalized pressure distributions (P/P$_\infty$) were denoted by solid pink circles. Normalization was carried out based on the pressure value (P), which arises during the normal operation of the system (P$_\infty$), i.e., before the earthquake starts. It is evident from Figure 11 that for the case of Chi Chi earthquake, the individual instantaneous extreme pressure values were observed at the right and left-hand sides of the pressure break weir. In Kocaeli case, the instantaneous extreme pressure values in Figure 12 similarly concentrated around the pressure break weir. However, it is also worth mentioning that since the specific energy density of Kocaeli earthquake is significantly higher compared to Chi Chi, the same situation was observed in a more pronounced manner for this case.
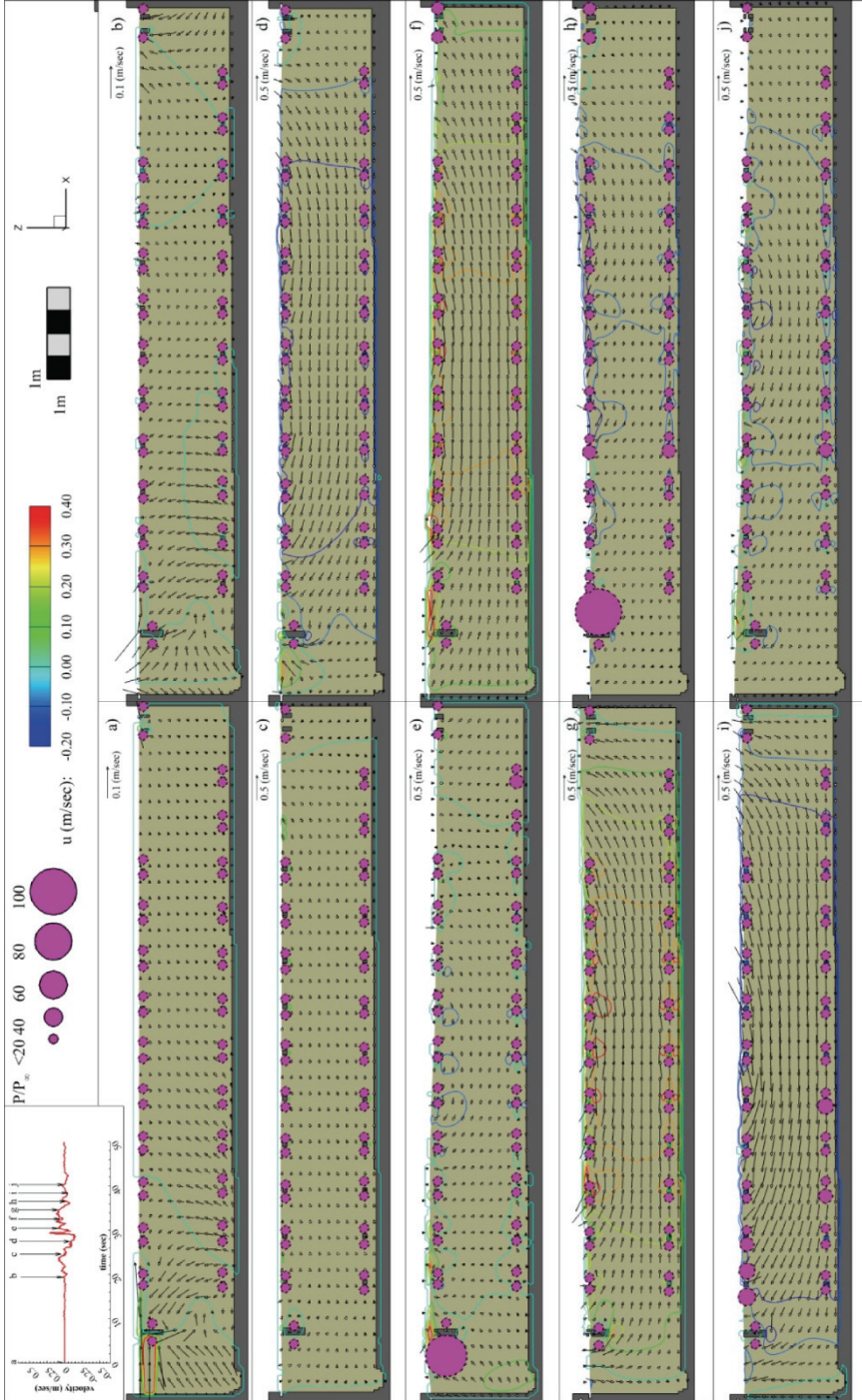
Figure 11 - Clarifier response to Chi Chi earthquake for selected time a) t_0, b) $t_0 + 2*T_P$, c) $t_0 + 2.5*T_P$, d) $t_0 + 3*T_P$, e) $t_0 + 3.2*T_P$, f) $t_0 + 3.4*T_P$, g) $t_0 + 3.6*T_P$, h) $t_0 + 3.8*T_P$, i) $t_0 + 4*T_P$, and j) $t_0 + 4.2*T_P$
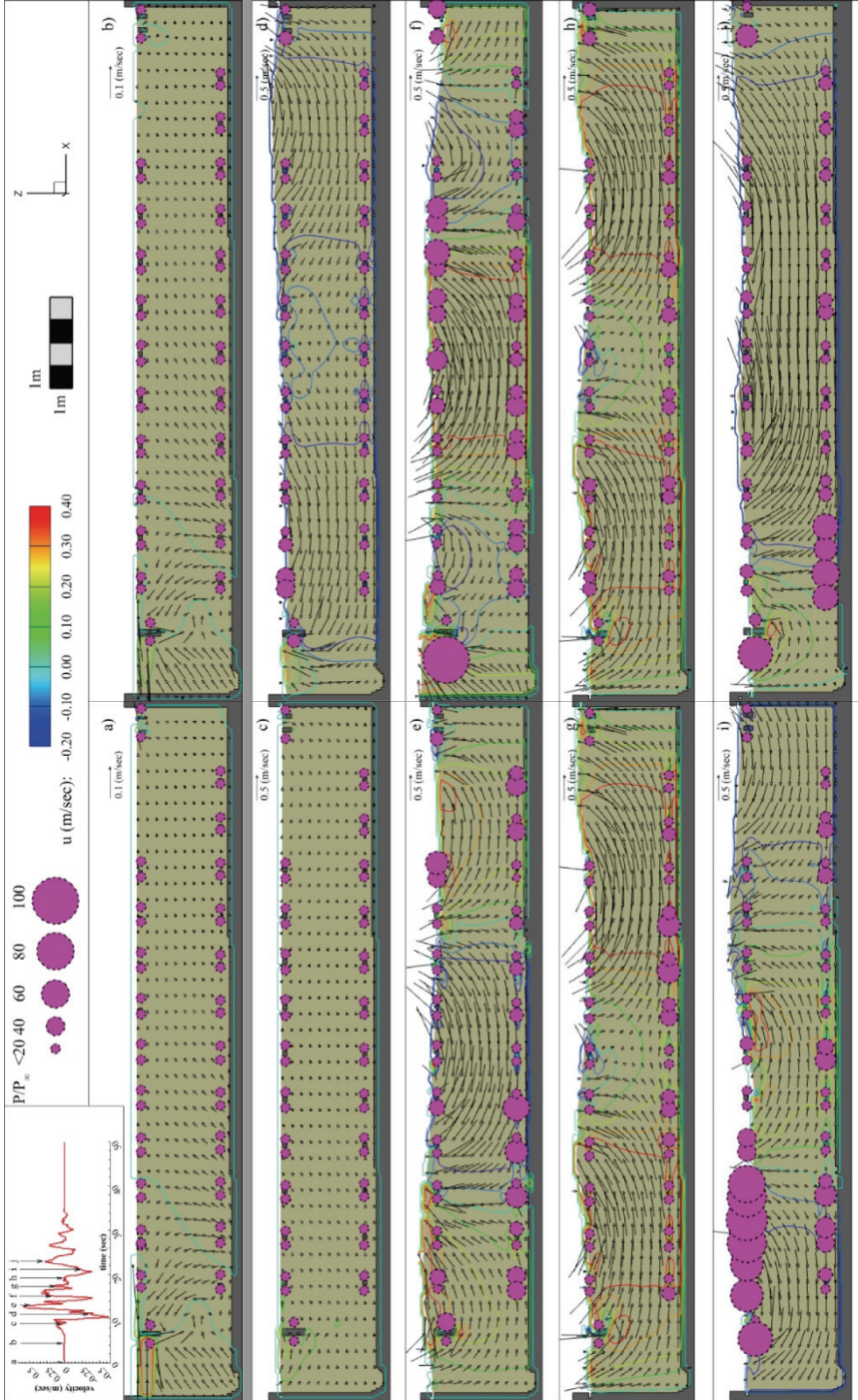
Figure 12 - Clarifier response to Kocaeli earthquake for selected time a) t_0, b) $t_0 + 0.5*T_P$, c) $t_0 + T_P$, d) $t_0 + 1.2*T_P$, e) $t_0 + 1.4*T_P$, f) $t_0 + 1.6*T_P$, g) $t_0 + 1.8*T_P$, h) $t_0 + 2*T_P$, i) $t_0 + 2.2*T_P$, and j) $t_0 + 2.4*T_P$
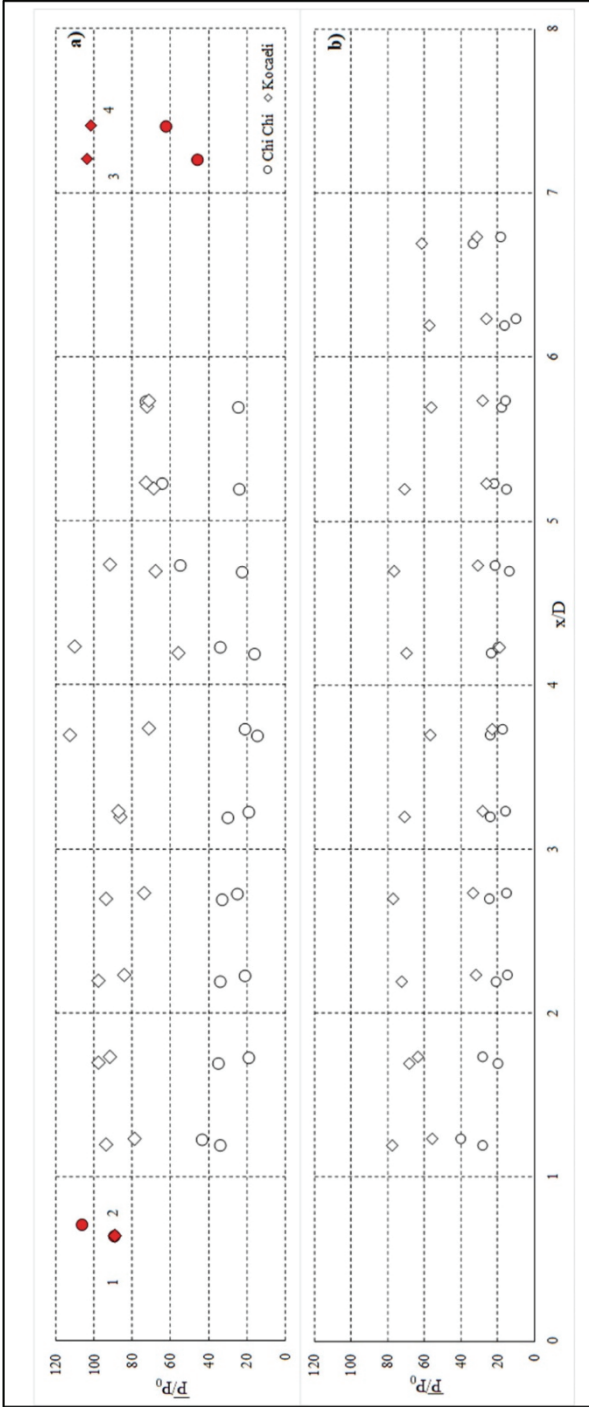
Figure 13 - Observed normalized maximum dynamic pressures at a) monitoring points near water surface (z=4.3 m) b) near bottom monitoring points (z=0.8 m). Red dots are named monitoring points belonging to inlet and outlet panel/weir. Diamonds and circles represent results of Kocaeli and Chi Chi earthquakes, respectively.

The instantaneous high-pressure values around scrappers are distributed unevenly under the sloshing condition of Kocaeli earthquake, differing from Chi Chi earthquake. When the relationship between velocity vectors and the emergence of extreme pressure zones are evaluated, it can be concluded that the extreme pressure values arise when two coherent flow domains converge to and diverge from each other.

In Figure 13, the average of maximum three normalized pressure values ($\bar{P}/P_0$) observed, occurring around each component (i.e., scraper and weirs), are presented; $\bar{P}$ is the time-averaged pressure value and P_0 is the hydrostatic pressure at calculation point. In line with Figures 11 and 12, the pressure values are quite high in the vicinity of the weirs. Besides, other extremes, which were not captured in flow domain analysis given for consecutive time steps (in Figures 11 and 12, only visualization was made for a certain time interval) presented in Figures 11 and 12, were calculated exactly at the center of the clarifier.

4. DISCUSSION AND RECOMMENDATION

Sloshing is a non-negligible governing factor in the design of wastewater treatment plants and the treatment capacity and efficiency, especially in high earthquake risk zones. Necessary measures should be taken to prevent/diminish any potential damages of equipment, which are vulnerable to earthquake-induced sloshing, inside the clarifiers. Limit situations should be determined considering earthquake-induced sloshing effects, and the standards should be formed according to these limit situations (e.g., freeboard, risk of damage for the sensitive equipment). This study was conducted to highlight the significance of the sloshing in clarifier. It was also aimed to present a fundamental knowledge which may aid in design of rectangular type clarifiers under earthquake conditions. The assumptions made in the model approach (RANS as turbulence model, surface tension, surface roughness) and mesh quality cause the model to calculate underestimated wave heights than the experiment, especially at peak values. In addition, the analysis of the test results with the image processing technique causes the splashes that occur during agitation to be detected as a continuous fluid phase. This causes a 13% relative error in the peak value at the 10th second of the analysis.

Previous studies on sloshing show that there is a relationship between natural frequency and sloshing wave. A similar relationship is also observed in this study as depicted in Figure 10. However, an important finding is that there is a delay caused by scrapers in the relationship between the sloshing and the natural frequencywhich becomes more evident as the earthquake intensity increases so that the correlation between the natural frequency and the sloshing wave decreases (Figure 10b. Kocaeli). This relationship reflects the facts that the natural frequency of the clarifier is related to the properties of the fluid and the tank and the sloshing wave height is related to the amplitude of the liquid surface displacement caused by an external excitation. However, the presence of scrapers in the tank can introduce a delay in between natural frequency and the sloshing frequency, particularly as the intensity of the disturbance (such as an earthquake) increases. The scrapers can cause additional damping in the system, which can affect the natural frequency and the sloshing wave height.

The effect of compressibility, adhesion interaction with wall surfaces, cohesion and air entertainment were neglected during the calculations. These parameters have effects on the sloshing behavior and on the model results. Air compressibility can affect the amount of air entrapped in the liquid, which can change the overall weight and volume of the liquid. Water

compressibility, on the other hand, can change the density of the liquid and affect the pressure on the container walls. These factors can affect the amplitude and frequency of the sloshing motion, as well as the stability of the liquid.

Adhesion and cohesion forces can affect the behavior of the liquid in several ways:

- Adhesion forces can increase the amplitude of the sloshing motion by creating a sticking effect between the liquid and the container walls. This can cause the liquid to cling to the walls and move with them, leading to larger sloshing motions. For the future studies it is recommended to examine this phenomenon more closely.

- Cohesion forces can decrease the amplitude of the sloshing motion by creating a resistance to motion within the liquid. This can bring about enhancement in temporal lag between tank motion and wave. However, further effort is needed to investigate this aspect of the phenomenon.

The effect of the neglecting adhesion can be clearly seen, especially in the differences between the results of image processing and CFD analysis. In video images the splashes and the water droplets could be identify as water domain during the calculations. Additionally, lack of air entrainment during the modelling was affected the phase changing, air entrapping and variation in fluid density.

During sloshing, the hydrodynamic pressure at the bottom of a tank can vary greatly depending on the amplitude and frequency of the sloshing motion. The pressure can fluctuate significantly as the fluid in the tank moves back and forth. The highest pressure occurs at the location of the bottom of the tank when the fluid surface is at its highest point. The pressure can also vary depending on the properties of the fluid, and the geometry of the tank. In addition, the frequency of the sloshing motion and the amplitude of the sloshing can also greatly affect the pressure distribution inside the calculation domain. When all of these governing parameters (flow domain, fluid properties, and sloshing characteristics) are adequately reproduced in the model domain, the resulting pressure values will always be within an acceptable error of the actual values. Image processing techniques are used here to capture sloshing wave height and fluid motion, as well as to investigate sloshing dynamics in the literature. In order to perform a more precise analysis and obtain accurate results, it is recommended that the scalar variables (e.g., pressure) and kinematic variables (e.g., velocity) must be measured with non-intrusive measurement devices in the future studies.

The primary objective of the experimental effort was to determine the capabilities of the turbulent model, initial and boundary conditions of the code. In the rectangular-type clarifier response under the seismic condition scenario, real-scale tank geometry was used, which was larger than the tank in the validation section. Geometric scale-up can have a significant effect on the results of a CFD model.

It is a standard practice to employ model tests to evaluate various types of tanks, while quantifying their efficiency in the field. 1/25 to 1/70 is the optimum scale for model testing [72]. Jeon et. al., (2008) disclosed that scales between 1/25 and 1/50 are reasonable scales in terms of keeping the governing forces reasonably proportional. Nevertheless, 1/100 can be regarded as too small [73]. Froude scaling is a commonly employed scaling law in a sloshing model test [72]–[74]. To compare the scaling effect in a more efficient manner, the CFD analysis of the experimental system was repeated by scaling up the model by a factor of 107

using Froude scaling (geometrical scale=1/107). The scaling was carried out according to the dimensions and time scale as stated in the sloshing model test procedure document [74]. The reason for choosing a scaling factor of 107 in Froude scaling is that the ratio of the length of the experimental tank (Lp=0.28 m) (and thus the validation model) to the tank length in the clarifier models (Lm=30 m) is Lm/Lp=107. Figure 14 presents the effect of scaling on the sloshing wave height (water depth at the left side of the tank) and pressure value in time. The values are compared for the point presented in Figure 5. Furthermore, maximum errors of 28% for wave height and 20% for pressure have been calculated. By conducting experimental studies in a larger tank environment and scaling up the experiments, these error rates can be further reduced.
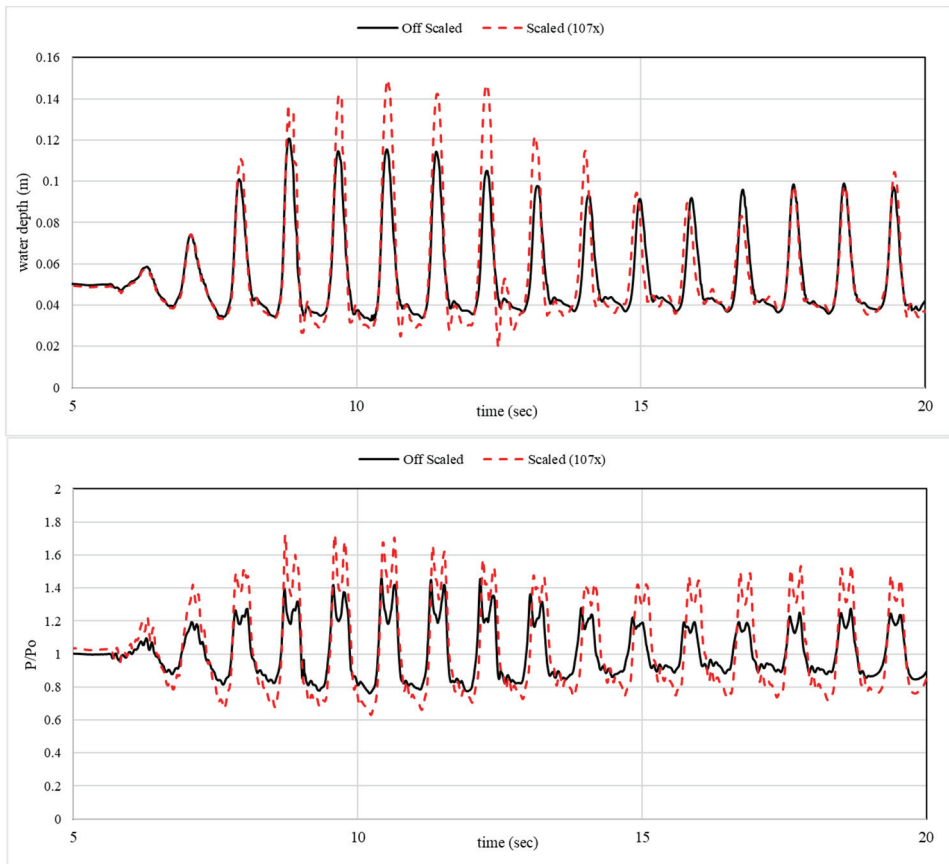
Figure 14 - Comparative graphics for off scaled (black solid line) and scaled (107x – red dashed line) a) water depth b) P/Po.

In this study, two historical earthquakes were considered as characteristic drivers to produce a sloshing effect in a typical clarifier. The characteristic earthquakes with similar periods were selected to make an efficient direct comparative analysis. It should be noted that the earthquake with various periods would results with different sloshing effects than the ones

presented here. The presented results should be evaluated within this perspective, as a realistic demonstration of the earthquake-induce sloshing process.

Sloshing waves are superimposed at the center of a clarifier. The resulting wave height and pressure can be affected by the amplitude, frequency, and phase difference of the individual waves (Figure 13). The superposition of waves can result in destructive interference, which can either amplify the total wave height and pressure at the units and causes failure of non-structural elements. The superposition of waves is a complex phenomenon, and it is influenced by many factors such as the properties of the fluid, the geometry of the tank, and the type of excitation (such as harmonic or random).

It is recommended that further parametric studies are performed to investigate the impact of the earthquake characteristics on the hydrodynamic pressures acting on the clarifiers. It is also suggested that the results of these parametric analyses are used to generate a set of non-dimensional empirical relationships between the earthquake parameters (such as the peak period, PGA, etc.) and the sloshing-induced loads on clarifier components. Besides, a characteristic clarifier with typical specific dimensions obtained from [27]was selected, and the modeling study was conducted for the clarifier with these dimensions. However, it should be noted that even under the identical period, different clarifier dimensions would lead to different loads on the equipment in the clarifier. Hence, it is recommended that the influence of clarifier dimensions on the emerging hydrodynamic loads under the sloshing effect are investigated.

5. CONCLUSION

In this study, a numerical model, which was validated against an experiment, was undertaken to simulate earthquake-induced sloshing in a clarifier. Once the model validation was accomplished, the following conclusions were drawn from the CFD analysis of a clarifier with typical full-scale dimensions, with which the hydrodynamic loads on equipment in the clarifier were analyzed under two historical earthquake signals.

1) From the spatial distribution of wave height within the clarifier obtained by the numerical model, it was seen that wave heights due to sloshing were higher near the edge sides of the tank compared to those in the center. This primary finding can be interpreted as the sloshing-induced forces acting on the clarifier and the equipment located at both edges being more severe than the center zone.

2) The simulations showed that the instantaneous extreme pressure values intensified around the pressure break weir. It was also seen that this situation becomes more pronounced as the enhanced specific energy density of the earthquake enhanced.

3) The findings revealed that the characteristics of the extreme waves (i.e., sloshing duration and wave heights) which were generated during the sloshing were well correlated with the time variation of earthquake accelerations. In other words, the higher waves generated under the high acceleration sloshes in the clarifier had relatively longer durations and damped significantly later. Once it is considered that the duration can be a significant factor in fatigue and causing damage to devices in the clarifier, the meaning of this finding is recognized better. This finding is in good harmony with the pertinent findings in the literature.

4) It was seen that under the influence of the sloshing, the extreme pressures are generated at the locations where two coherent flow domains with opposite flow directions meet each other within the clarifier.

5) The analysis of pressure domains indicated that the weirs are exposed to a higher-pressure effect compared to the scrapers. This finding shows that the weirs are more sensitive under the earthquake-induced sloshing event compared to other components. Hence, special attention should be given to these vulnerable units at the design stage for the clarifier. The results presented on pressure are based on the results of a numerical model that has only been validated against water level measurements and not some dynamic pressure measurements. As a result, these results contain some errors due to a variety of factors (numerical schemes, air entrapment, compressibility, etc.) and require additional investigation.

References

[1]   EERI, "Earthquake of January 17, 1995: Reconnaissance Report," Oakland, California, USA, 1995.

[2]   EERI, "The Nisqually Earthquake of 28 February 2001: Preliminary Reconnaissance Report," Oakland, California, USA, 2001.

[3]   C. Strand and J. Masek, "Sumatra-Andaman Islands Earthquake and Tsunami of December 26, 2004 Lifeline Performance," Reston, VA, USA, 2007.

[4]   R. Kayen *et al.*, "Investigation of the M6.6 Niigata-Chuetsu Oki, Japan, Earthquake of July 16, 2007, Report 2007-1365," 2007.

[5]   A. K. Tang and A. Schiff, "Kashiwazaki, Japan, Earthquake of July 16, 2007, Lifeline Performance," Reston VA, USA, 2010.

[6]   N. L. Evans and C. Mc Ghie, "The performance of lifeline utilities following the 27th February 2010 Maule Earthquake Chile," 2011.

[7]   A. K. Tang, P. Eng, C. Eng, and F. Asce, "Lifelines Performance of the Mw 8.8 off Shore Biobío, Chile Earthquake," *Procedia Eng.*, vol. 14, pp. 922–930, 2011, doi: 10.1016/j.proeng.2011.07.116.

[8]   EERI, "El Mayor Cucapah, Baja California Earthquake of April 4, 2010: Reconnaissance Report," Oakland, California, USA, 2010.

[9]   J. Eidinger and M. Yashinsky, "Oil and water system performance – Denali M 7.9 earthquake of November 3, 2002. In: Yashinsky, M. (Ed.), 2004. San Simeon Earthquake of December 22, 2003 and Denali, Alaska, Earthquake of November 3, 2002," Reston VA, USA, 2004.

[10]   D. G. Wareham and M. Bourke, "The 2010–2011 Canterbury earthquakes: impact on the liquid waste management system of Christchurch, New Zealand," *Civ. Eng. Environ. Syst.*, vol. 30, no. 1, pp. 1–14, Mar. 2013, doi: 10.1080/10286608.2012.709507.

[11] J. Eindinger, "Performance of water systems in the Mw 8.4 Atico (Perù) earthquake of June 23, 2001. In: Edwards, C.L. (Ed.), 2002. Atico, Peru, Mw 8.4 Earthquake of June 23, 2001: Lifeline Performance," 2001.

[12] J. Eindinger and A. K. Tang, "Christchurch, New Zealand Earthquake Sequence of Mw 7.1 September 04, 2010 Mw 6.3 February 22, 2011 Mw 6.0 June 13, 2011: Lifeline Performance," Reston, VA, USA, 2012.

[13] M. Erdik, "Report on 1999 Kocaeli and Düzce (Turkey) Earthquakes," 1999.

[14] A. Panico *et al.*, "Evaluating the structural priorities for the seismic vulnerability of civilian and industrial wastewater treatment plants," *Saf. Sci.*, vol. 97, pp. 51–57, Aug. 2017, doi: 10.1016/j.ssci.2015.12.030.

[15] S. Kuraoka and J. H. Rainer, "Damage to water distribution system caused by the 1995 Hyogo-ken Nanbu earthquake," *Can. J. Civ. Eng.*, vol. 23, no. 3, pp. 665–677, Jun. 1996, doi: 10.1139/l96-882.

[16] A. J. Schiff, "Hyogoken-Nanbu (Kobe), Earthquake of January 17, 1995, Lifeline Performance," 1998.

[17] A. Rodriguez-Marek, J. Williams, J. Wartman, and P. Repetto, "Ground motion and site response Southern Peru Earthquake of June 21, 2001 Reconnaissance Report," 2003.

[18] M. Yashinsky, "San Simeon Earthquake of December 22, 2003, and Denali, Alaska, Earthquake of November 3, 2002," Reston, VA, USA, 2004.

[19] NIST, "Disaster Resilience Framework (Draft)," 2014. [Online]. Available: https://www.nist.gov/system/files/documents/el/building_materials/resilience/Disaster _Resilience_Chapter_9_Water_and_Wastewater_50-Draft_102014.pdf.

[20] D. Ballantyne and C. Crouse, "Reliability and Restoration of Water Supply Systems for Fire Supression and Drinking Following Earthquakes," 1997.

[21] NIST, "The January 17, 1995 Hyogoken-Nanbu (kobe) Earthquake: Performance of Structures, Lifelines, and Fire Protection Systems," 1996.

[22] J. Meneses *et al.*, *The El Mayor Cucapah , Baja California Earthquake The El Mayor Cucapah , Exponent Failure Analysis Associates*. 2010.

[23] K. Kakderi and S. Argyroudis, "Fragility Functions of Water and Waste-Water Systems," in *Geotechnical, Geological and Earthquake Engineering*, vol. 27, 2014, pp. 221–258.

[24] A. Panico, G. Lanzano, E. Salzano, F. S. De Magistris, and G. Fabbrocino, "Seismic vulnerability of wastewater treatment plants," *Chem. Eng. Trans.*, vol. 32, no. January, pp. 13–18, 2013, doi: 10.3303/CET1332003.

[25] X. Y. Wang and A. M. Fu, "Earthquake Impact on the Sewage Treatment Plant and Emergency Measures," *Adv. Mater. Res.*, vol. 243–249, pp. 5076–5079, May 2011, doi: 10.4028/www.scientific.net/AMR.243-249.5076.

[26] M. N. Alpaslan, D. Dölgen, and H. Sarptaş, *Atıksu Arıtma Tesisleri Tasarım ve İşletme Esasları*. İzmir: Dokuz Eylül Üniversitesi Çevre Araştırma ve Uygulama Merkezi (ÇEVMER), 2004.

[27] I. Metcalf & Eddy, *Wastewater engineering : treatment and reuse*. Fourth edition / revised by George Tchobanoglous, Franklin L. Burton, H. David Stensel. Boston : McGraw-Hill, [2003] ©2003, 2003.

[28] J. H. Jung, H. S. Yoon, and C. Y. Lee, "Effect of natural frequency modes on sloshing phenomenon in a rectangular tank," *Int. J. Nav. Archit. Ocean Eng.*, vol. 7, no. 3, pp. 580–594, May 2015, doi: 10.1515/ijnaoe-2015-0041.

[29] A. VakilaadSarabi and M. Miyajima, "Study of the Sloshing of Water Reservoirs and Tanks due to Long Period and Long Duration Seismic Motions," 2012.

[30] R. Ibrahim, "LIQUID SLOSHING," S. B. T.-E. of V. Braun, Ed. Oxford: Elsevier, 2001, pp. 726–740.

[31] H. Olsen and K. R. Johnsen, "Nonlinear sloshing in rectangular tanks. A pilot study on the applicability of analytical models," 1975.

[32] O. F. Rognebakke, "Sloshing in rectangular tanks and interaction with ship motions," Norwegian University of Science and Technology, 2002.

[33] L. Ren, Y. Zou, J. Tang, X. Jin, D. Li, and M. Liu, "Numerical Modeling of Coupled Surge-Heave Sloshing in a Rectangular Tank with Baffles," *Shock Vib.*, vol. 2021, p. 5545635, 2021, doi: 10.1155/2021/5545635.

[34] P. Disimile, J. Pyles, and N. Toy, "Hydraulic Jump Formation in Water Sloshing Within an Oscillating Tank," *J. Aircr. - J Aircr.*, vol. 46, pp. 549–556, Mar. 2009, doi: 10.2514/1.38493.

[35] T. Lee, Z. Zhou, and Y. Cao, "Numerical Simulations of Hydraulic Jumps in Water Sloshing and Water Impacting ," *J. Fluids Eng.*, vol. 124, no. 1, pp. 215–226, 2001, doi: 10.1115/1.1436097.

[36] S. Gurusamy, V. S. Sanapala, D. Kumar, and B. S. V Patnaik, "Sloshing dynamics of shallow water tanks: Modal characteristics of hydraulic jumps," *J. Fluids Struct.*, vol. 104, p. 103322, 2021, doi: https://doi.org/10.1016/j.jfluidstructs.2021.103322.

[37] P. J. Disimile and N. Toy, "The imaging of fluid sloshing within a closed tank undergoing oscillations," *Results Eng.*, vol. 2, p. 100014, 2019, doi: https://doi.org/10.1016/j.rineng.2019.100014.

[38] M. Aksel, "Dairesel Tipteki Çöktürme Havuzunun Deprem Altındaki Çalkalanma Analizi," *Türk Deprem Araştırma Derg.*, vol. 3, no. 2, pp. 149–166, Dec. 2021, doi: 10.46464/tdad.1014192.

[39] P. Du *et al.*, "Environmental risk evaluation to minimize impacts within the area affected by the Wenchuan earthquake," *Sci. Total Environ.*, vol. 419, pp. 16–24, Mar. 2012, doi: 10.1016/j.scitotenv.2011.12.017.

[40] J. Lee, D. Perera, T. Glickman, and L. Taing, "Water-related disasters and their health impacts: A global review," *Prog. Disaster Sci.*, vol. 8, p. 100123, Dec. 2020, doi: 10.1016/j.pdisas.2020.100123.

[41] F. Maleki, S. Hemati, and R. Pourashraf, "Prevalence Waterborne Infections after Earthquakes Considered as Serious Threat to Increasing Victims in Disaster-Affected Areas," *Egypt. J. Vet. Sci.*, vol. 51, no. 1, pp. 111–117, Jun. 2020, doi: 10.21608/ejvs.2019.18629.1114.

[42] E. J. Nelson, J. R. Andrews, S. Maples, M. Barry, and J. D. Clemens, "Is a Cholera Outbreak Preventable in Post-earthquake Nepal?," *PLoS Negl. Trop. Dis.*, vol. 9, no. 8, p. e0003961, Aug. 2015, doi: 10.1371/journal.pntd.0003961.

[43] J. T. Watson, M. Gayer, and M. A. Connolly, "Epidemics after Natural Disasters," *Emerg. Infect. Dis.*, vol. 13, no. 1, pp. 1–5, Jan. 2007, doi: 10.3201/eid1301.060779.

[44] G. Yazici, A. K. Ö. Roglu, M. Aksel, and Y. H. Önen, "Seismic Vulnerability of Treatment Plants in Istanbul," no. May, 2015.

[45] M. R. Zare, S. Wilkinson, and R. Potangaroa, "Vulnerability of Wastewater Treatment Plants and Wastewater Pumping Stations to Earthquakes," *Int. J. Strateg. Prop. Manag.*, vol. 14, no. 4, pp. 408–420, Dec. 2010, doi: 10.3846/ijspm.2010.30.

[46] K. Pitilakis, A. Anastasiadis, K. Kakderi, S. Argyroudis, and M. Alexoudi, *Vulnerability Assessment and Risk Management of Lifelines, Infrastructures and Critical Facilities: The Case of Thessaloniki's Metropolitan Area*. 2007.

[47] FEMA, "Multi-hazard Loss Estimation Methodology (HAZUS)," 2003.

[48] M. Liu, S. Giovinazzi, R. MacGeorge, and P. Beukman, "Wastewater Network Restoration Following the Canterbury, NZ Earthquake Sequence: Turning Post-Earthquake Recovery into Resilience Enhancement," in *International Efforts in Lifeline Earthquake Engineering*, Dec. 2013, pp. 160–167, doi: 10.1061/9780784413234.021.

[49] J. E. Richardson and V. G. Panchang, "Three-Dimensional Simulation of Scour-Inducing Flow at Bridge Piers," *J. Hydraul. Eng.*, vol. 124, no. 5, pp. 530–540, May 1998, doi: 10.1061/(ASCE)0733-9429(1998)124:5(530).

[50] H. D. Smith and D. L. Foster, "Modeling of Flow Around a Cylinder Over a Scoured Bed," *J. Waterw. Port, Coastal, Ocean Eng.*, vol. 131, no. 1, pp. 14–24, Jan. 2005, doi: 10.1061/(ASCE)0733-950X(2005)131:1(14).

[51] M. Ghasemi and S. Soltani-Gerdefaramarzi, "The Scour Bridge Simulation around a Cylindrical Pier Using Flow-3D," *J. Hydrosci. Environ.*, vol. 1, no. 2, pp. 46–54, 2017, doi: 10.22111/JHE.2017.3357.

[52] S. C. Chen and S. S. Tfwala, "Performance assessment of FLOW-3D and X flow in the numerical modelling of fish-bone type fishway hydraulics," *7th IAHR Int. Symp. Hydraul. Struct. ISHS 2018*, pp. 272–282, 2018, doi: 10.15142/T3HH1J.

[53] J. Li, S. Alinaghian, D. Joksimovic, and L. Chen, "An Integrated Hydraulic and Hydrologic Modeling Approach for Roadside Bio-Retention Facilities," *Water*, vol. 12, no. 5, p. 1248, Apr. 2020, doi: 10.3390/w12051248.

[54] A. Bayon, D. Valero, R. García-Bartual, F. José Vallés-Morán, and P. A. López-Jiménez, "Performance assessment of OpenFOAM and FLOW-3D in the numerical modeling of a low Reynolds number hydraulic jump," *Environ. Model. Softw.*, vol. 80, pp. 322–335, Jun. 2016, doi: 10.1016/j.envsoft.2016.02.018.

[55] A. Najafi-Jilani, M. Z. Niri, and N. Naderi, "Simulating three dimensional wave run-up over breakwaters covered by antifer units," *Int. J. Nav. Archit. Ocean Eng.*, vol. 6, no. 2, pp. 297–306, Jun. 2014, doi: 10.2478/IJNAOE-2013-0180.

[56] A. Musa, Y. Maliki, M. Ahmad, wan sani wan nik, O. Yaakob, and K. Samo, "Numerical Simulation of Wave Flow Over the Overtopping Breakwater for Energy Conversion (OBREC) Device," *Procedia Eng.*, vol. 194, pp. 166–173, Dec. 2017, doi: 10.1016/j.proeng.2017.08.131.

[57] M. Aksel, O. Yagci, V. S. O. Kirca, E. Erdog, and N. Heidari, "A comparative analysis of coherent structures around a pile over rigid-bed and scoured-bottom," *Ocean Eng.*, vol. 226, p. 108759, Apr. 2021, doi: 10.1016/j.oceaneng.2021.108759.

[58] L. P. Martell, "Computational fluid dynamics techniques for fixed-bed biofilm systems modeling : numerical simulations and experimental characterization [en línea]," Universitat Internacional de Catalunya, 2018.

[59] M. Patziger, "Improving wastewater treatment plant performance by applying CFD models for design and operation: selected case studies," *Water Sci. Technol.*, vol. 84, no. 2, pp. 323–332, Jan. 2021, doi: 10.2166/wst.2021.019.

[60] Q. Plana, P. Lessard, and P. A. Vanrolleghem, "Dynamic grit chamber modelling: dealing with particle settling velocity distributions," *Water Sci. Technol.*, vol. 81, no. 8, pp. 1682–1699, Mar. 2020, doi: 10.2166/wst.2020.108.

[61] E. Wicklein *et al.*, "Good modelling practice in applying computational fluid dynamics for WWTP modelling.," *Water Sci. Technol. a J. Int. Assoc. Water Pollut. Res.*, vol. 73, no. 5, pp. 969–982, 2016, doi: 10.2166/wst.2015.565.

[62] C. J. Brouckaert and C. A. Buckley, "The Use of Computational Fluid Dynamics for Improving the Design and Operation of Water and Wastewater Treatment Plants," *Water Sci. Technol.*, vol. 40, no. 4–5, pp. 81–89, Aug. 1999, doi: 10.2166/wst.1999.0578.

[63] C. Ma and M. Oka, "Numerical Investigation on Sloshing Pressure for Moss-Type LNG Tank Based on Different SPH Models ." Oct. 11, 2020.

[64] S. Ransau and E. Hansen, "Numerical Simulations of Sloshing in Rectangular Tanks," Jan. 2006, doi: 10.1115/OMAE2006-92248.

[65] S. Brizzolara *et al.*, "Comparison of experimental and numerical sloshing loads in partially filled tanks," *Anal. Des. Mar. Struct. Incl. CD-ROM*, no. Lloyd 1989, pp. 13–26, 2009, doi: 10.1201/9780203874981.ch2.

[66] Flowscience, "Flow-3D User Manual." 2019.

[67] G. Wei, "A Fixed-Mesh Method for General Moving Objects in Fluid Flow," *Mod. Phys. Lett. B*, vol. 19, no. 28, pp. 1719–1722, Dec. 2005, doi: 10.1142/S021798490501030X.

[68] H. Coleman and C. Members, *ASME V&V 20-2009 Standard for Verification and Validation in Computational Fluid Dynamics and Heat Transfer (V&V20 Committee Chair and principal author)*. ASME, 2009.

[69] J. R. Merian, "Ueber die Bewegung tropfbarer Flüssigkeiten in Gefässen [On the motion of drippable liquids in containers]," 1828.

[70] O. Yagci, M. Aksel, F. Yorgun, and M. Valyrakis, "Analysis of oscillatory flow around a rigidly attached spherical particle to the bottom in a sloshing tank," in *EGU General Assembly 2022*, 2023, p. 10068, doi: 10.5194/egusphere-egu22-10068.

[71] T. Gándara, E. C. Del Barrio, M. Cruchaga, and J. Baiges, "Experimental and numerical modeling of a sloshing problem in a stepped based rectangular tank," *Phys. Fluids*, vol. 33, no. 3, p. 033111, Mar. 2021, doi: 10.1063/5.0044682.

[72] A. I. Yılmaz, "A Review of Studies on the Sloshing Effect of Liquid in Partially Filled Tank," *Journal*, no. 11, pp. 19–28, 2018.

[73] S. Jeon *et al.*, "Experimental investigation of scale effect in sloshing phenomenon," 2008.

[74] S. C. of the 28th ITTC, "Prosedure of Sloshing Model Tests," 2017.

Mineral Katkı İkamesinin Kalsiyum Alümina Çimentolu Harçların Taze Hal ve Zamana Bağlı Sertleşmiş Hal Özelliklerine Etkileri

Faruk EREN[1]
Muhammer KESKİNATEŞ[2]
Burak FELEKOĞLU[3]
Kamile TOSUN FELEKOĞLU[4]

ÖZ

Kalsiyum alüminat çimentoları (KAÇ) bir onarım malzemesinden beklenen; hızlı sertleşme, iyi yapışma, mevcut betonla uyumluluk, boyutsal kararlılık ve korozyon direnci gibi özellikleri sağlamaya aday bir alternatif bağlayıcıdır. Hidratasyon ürünleri arasında suda çözünür kireç olmaması da önemli bir avantaj olarak görülebilir. Ancak KAÇ'ın zaman içerisinde ortam koşullarına bağlı olarak faz yapısında meydana gelebilen dönüşüm reaksiyonları, bu çimento ile üretilen betonlarda dayanım kaybına neden olabilmektedir. Bu çalışmada KAÇ'ın hidratasyon sürecindeki dönüşüm reaksiyonlarından kaynaklanan problemlere çözüm sunmak, taze hal özelliklerini geliştirmek ve uzun dönemde dayanım gelişimini kararlı hale getirmek amaçlanmıştır. Buna bağlı olarak, farklı mineral katkı kaynaklarının (SiO_2 ve $CaSO_4$), KAÇ ile birlikte kullanımının harç kıvamı, priz süresi ve reolojik özelliklere etkileri incelenmiştir. Sertleşmiş halde aşınma dayanıklılığı ve zamana bağlı basınç ve eğilme dayanımı gelişimleri belirlenmiştir. Deneysel çalışmalar sonucunda, %16 SiO_2 katkılı ve %50 $CaSO_4$ katkılı KAÇ içeren harçların, taze hal özelliklerinde kullanım alanlarına uygun gelişmiş özellikler kazandırılabildiği ve hidratasyon sürecinde kararlı ürünler elde ederek zamana bağlı bir mukavemet kaybına uğramadan, 400 günlük periyot sonunda dayanım gelişimi gösterdiği sonucuna ulaşılmıştır.

Anahtar Kelimeler: Kalsiyum alüminat çimentosu, mineral katkı, taze hal özellikleri, reoloji, mekanik dayanım.

1 Dokuz Eylül Üniversitesi, Fen Bilimleri Enstitüsü, İnşaat Mühendisliği Bölümü Yapı Malzemesi Programı, İzmir, Türkiye
  farukeren.fe@gmail.com - https://orcid.org/0000-0003-4518-0669

2 Karamanoğlu Mehmetbey Üniversitesi, İnşaat Mühendisliği Bölümü, Karaman, Türkiye
  muhammerkeskinates@hotmail.com - https://orcid.org/0000-0001-8334-3073

1 Dokuz Eylül Üniversitesi, İnşaat Mühendisliği Bölümü, İzmir, Türkiye
  burak.felekoglu@deu.edu.tr - https://orcid.org/0000-0002-7426-1698

2 Dokuz Eylül Üniversitesi, İnşaat Mühendisliği Bölümü, İzmir, Türkiye
  kamile.tosun@deu.edu.tr - https://orcid.org/0000-0003-2191-7793

ABSTRACT

Effects of Mineral Additive Substitution on the Fresh State and Time-Dependent Hardened State Properties of Calcium Alumina Cement Mortars

Calcium aluminate cements (CAC) are a candidate alternative binder to provide the requirements of a repair material such as accelerated hardening, good adhesion, compatibility with existing concrete, dimensional stability and corrosion resistance. The absence of water-soluble hydrated lime among the hydration products can also be accepted as an important advantage. However, the transformation reactions that may occur in the phase structure of the CAC depending on the ambient conditions over time may cause a loss of strength in the concrete produced with this cement. In this study, it is aimed to provide solutions to the problems arising from the conversion reactions in the hydration process of CAC, to improve the fresh state properties and to stabilize the strength development in the long term. Consequently, the effects of using CAC blended with different mineral additives (SiO_2 and $CaSO_4$) on the mortar consistency, setting time and rheological properties were investigated. In the hardened state, abrasion resistance and time-dependent compressive and flexural strength developments were determined. As a result of the experimental studies, it was concluded that the CAC mortars containing 16% SiO_2 and 50% $CaSO_4$ additives can provide improved properties in their fresh state, and they also demonstrate an improvement in strength after 400 days by obtaining stable products during the hydration process without any time-related strength loss.

Keywords: Calcium aluminate cement, mineral additive, fresh state properties, rheology, mechanical strength.

1. GİRİŞ

Kalsiyum alüminat çimentosu (KAÇ) hızlı dayanım gelişimi (tünel kaplaması vb. yerlerde), yüksek sıcaklık direnci [1], karbonatlaşma direnci [2], [3], sülfat ve asit direnci sağlaması nedeniyle birçok endüstriyel uygulamada (refrakter malzeme üretimi, boru imalatı, kanalizasyon inşaatlarında, endüstriyel zeminlerde, atık su uygulamasında ve aşınmaya karşı direnci nedeniyle baraj dolu savakları vb.) yüksek maliyetine rağmen tercih edilmektedir [1], [3], [4]. KAÇ'ın belirli koşullarda basınç dayanımının 150 MPa'a kadar ulaşabildiği ve yüksek dayanımlı malzeme olarak kullanılabileceği rapor edilmiştir [3], [5]. Ayrıca 0°C'den daha düşük sıcaklıklarda bile hızlı dayanım kazanma yeteneği, soğuk havada beton dökümünü de mümkün kılmaktadır [6].

Yukarıda bahsedilen birçok avantaja rağmen, sıcak ve nemli koşullar, ilerleyen yaşlardaki faz dönüşümüne bağlı olarak gözenek hacminde artış [3] ve dolayısıyla basınç dayanımında düşüşlere neden olabilmektedir [1], [7]–[9]. 20 °C'nin altındaki sıcaklıklarda KAÇ'ın ana hidratasyon ürünü CAH_{10}'dur. 20 °C'nin üzerindeki sıcaklıklarda ana hidratasyon ürünleri ise C_2AH_8 ve AH_3'dür. KAÇ'ın yüksek erken dayanımı, baskın hidratasyon ürünleri olan altıgen hidratların (CAH_{10} ve C_2AH_8) oluşumuna bağlanmaktadır [8]. Bununla birlikte, CAH_{10} ve C_2AH_8'in yarı kararlı olduğu ve aşağıdaki Denklem 1 ve 2'ye göre zamana bağlı olarak daha kararlı C_3AH_6 ve AH_3'e [8]–[10] dönüştüğü bilinmektedir (Denklemlerdeki kısaltmaların çimento terminolojisindeki karşılıkları şu şekildedir; C:CaO, A:Al_2O_3, H:H_2O).

$$3CAH_{10} \rightarrow C_3AH_6 + 2AH_3 + 18H \qquad (1)$$

$$3C_2AH_8 \rightarrow 2C_3AH_6 + AH_3 + 9H \qquad (2)$$

Kararsız CAH_{10} ve C_2AH_8'in kararlı C_3AH_6'ya dönüşümüyle, gözeneklilikte bir artış ve dolayısıyla dayanımda bir azalma meydana gelir [9], [11]. C_3AH_6 ve AH_3 bağlarının, eşit gözeneklilikte bile CAH_{10} ve C_2AH_8'den daha zayıf olduğu diğer araştırmacılar tarafından da belirtilmiştir [12], [13]. Dönüşüm reaksiyonları sonucu oluşan basınç dayanımındaki kararsızlık nedeniyle, KAÇ'ın taşıyıcı sistem yapı elemanı olarak kullanımı bazı ülkelerde kısıtlanmıştır [3], [7].

S/Ç oranı 0.4'ün altında olması durumunda, yukarıda belirtilen dönüşüm reaksiyonlarının önemli ölçüde azaldığı ve gözeneklilikteki artışın daha düşük seviyelerde kaldığı bildirilmiş [14], [15] olmasına rağmen; düşük S/Ç oranı da, işlenebilirlik problemlerine yol açabilmektedir. Bu bağlamda KAÇ'ın taze hal davranışlarını inceleyen çalışma sayısı oldukça sınırlıdır [16], [17]. KAÇ'ın, suya ilk temastan sonra yaklaşık 15 dakikada içinde belirgin bir işlenebilirlik kaybına uğradığı rapor edilmiştir [18].

KAÇ'ın dönüşüm reaksiyonları nedeniyle, literatürdeki çalışmalar çoğunlukla sertleşmiş hal davranışlarına yoğunlaşmıştır. KAÇ faz dönüşümünün engellenmesi üzerine yapılan önceki çalışmalar, kürleme sıcaklığını kontrol ederek C_3AH_6 oluşumunu arttırmayı ve silikat kaynağı dahil ederek doğrudan C_2ASH_8 oluşumunu teşvik etmeyi amaçlamaktadırlar [19], [20]. Zaman içinde mekanik performansa ilişkin bu kaygının üstesinden gelmek için kimyasal ve mineral katkılar kullanılarak yarı kararlı hidratların dönüşümünün ortadan kaldırılması için bazı önlemler alınmaya çalışılmıştır [1], [19], [21]–[24].

KAÇ'a cüruf ilavesinin 40 °C'de su altında kürlenen hamurlarda dayanım kaybını önlediği belirlenmiştir. Cürufun dönüşüm reaksiyonlarını önleme yeteneği, camsı faz içeriği ve bazik çözeltilerdeki çözünme yeteneğine bağlı olan hidrolik aktivitesi ile ilişkilendirilmiştir [1], [25], [26]. Literatürdeki çalışmalarda [27], [28], C_2ASH_8 hidrat oluşumunun, 20°C ve 40°C'de, %50 oranında cüruf ikamesi ile iki tip ticari KAÇ (Ciment Fondu ve Secar 71) için dayanım gelişimini iyileştirdiği rapor edilmiştir. Kalsiyum alüminatların, nem varlığında, stratlingite olarak bilinen C_2ASH_8'i oluşturmak üzere cürufun amorf silisi ile reaksiyona girerek yarı kararlı hidrat dönüşümünü engellediği bildirilmiştir [25], [29]. KAÇ'a doğrudan silis dumanı veya nanosilika eklendiğinde, birkaç dakikada çözelti içinde büyük miktarda silikat iyonu çözündüğü belirtilmiştir [30]. İlerleyen aşamada C_2ASH_8 kararlı fazının oluşumu ile basınç dayanımındaki azalmanın büyük ölçüde önüne geçildiği değerlendirilmiştir [19], [20], [24]. Majumdar ve Singh [31] benzer şekilde KAÇ ile silisli malzemelerin ikamesinin, bağlayıcı türlerine ve ikame oranlarına bağlı olarak dayanım gelişimini arttırdığı sonucuna varmışlardır. Silikat iyonlarının, uçucu kül veya silis dumanından oluşan KAÇ tabanlı ikili sistemde stratlingite oluşturma yeteneği, başka çalışmalarda da rapor edilmiştir [20], [32], [33].

KAÇ'a $CaSO_4$ eklenmesi ile ilgili, literatürde sınırlı sayıda çalışma bulunmaktadır [3]. KAÇ'a eklenen $CaSO_4$ miktarının, hidrat fazlarında farklılıklara yol açmamasına rağmen etrenjit üretim miktarlarını değiştirerek KAÇ bazlı çimentolu malzemelerin mekanik ve mikroyapısal özelliklerinde farklılaşmaya neden olduğu vurgulanmıştır [34]. Son ve diğerleri [3] KAÇ'a $CaSO_4$'ün eklenmesinin, etrenjitin doğrudan oluşumu ile kararsız CAH_{10} dönüşümünü engellediğini bildirmişlerdir.

Bu çalışmada KAÇ harcına iki tür mineral katkının (SiO_2 ve $CaSO_4$) farklı oranlarda ikame edilmesinin; taze hal, kısa ve uzun dönemli sertleşmiş hal özelliklerine etkileri araştırılmıştır. Bu bağlamda üretilen harçların çeşitli uygulama alanlarında kullanılabilirlikleri kıvam,

reolojik parametreler, priz süresi parametreleri dikkate alınarak değerlendirilmiş olup, sertleşmiş hal özelliklerini incelemek üzere 400 gün boyunca basınç ve eğilme dayanımı gelişimi analiz edilerek eklenen katkı türü ve oranının KAÇ üzerindeki etkisi tartışılmıştır.

2. DENEYSEL ÇALIŞMALAR

2.1. Amaç ve Kapsam

Çalışmada, katkısız, SiO_2 ve $CaSO_4$ katkılı KAÇ harçların taze hal özellikleri ve uzun dönem mekanik etkilerinin araştırılması ile KAÇ'ın günümüzdeki kullanımını sınırlayan sebeplerin önüne geçilmesi amaçlanmıştır. KAÇ'a iki farklı mineral katkının iki farklı oranda eklenmesi ile taze hal özelliklerinin geliştirilmesi, buna bağlı olarak sahadaki uygulama alanlarının arttırılmasına yönelik çalışmalar yapılması; aynı zamanda uzun dönemde dayanımda belirsizliğe neden olan hidratasyon sürecinin, iki farklı mineral katkının kullanımıyla yeni stabil fazlar oluşturup bloke edilmesi ve katkı miktarının arttırılmasına bağlı olarak uzun dönemli dayanım gelişiminin sağlanması hedeflenmiştir. Bu kapsamda mevcut literatür bilgileri kullanılarak; stratlingite faz oluşumunun en yüksek seviyeye ulaştığı aralık olan %8 ve %16 oranında mikro silis [6], [35]; etrenjit fazının en yoğun hacimde gözlemlendiği %30 ve %50 oranında anhidrit alçı [3], [36]–[38] eklenmesi ile harçlar hazırlanmıştır.

2.2. Kullanılan Malzemeler, Karışım Oranları, Karışımların Hazırlanması ve Kür İşlemi

Deneysel çalışmalarda yaklaşık %40 Al_2O_3 içeriğine sahip KAÇ kullanılmıştır. Tablo 1'de çimentonun fiziksel ve mekanik özellikleri sunulmuştur. Silika kaynağı olarak; 15 mikron boyutunda, %99 saflık oranına sahip silisyum dioksit (SiO_2) katkısı kullanılmıştır. Özgül yüzey alanı ve gerçek yoğunluk değerleri sırasıyla 400-1000 m^2/g, 2400 kg/m^3 olduğu üretici firma tarafından beyan edilmiştir. 136.14 g/mol ağırlığında, 2960 kg/m^3 yoğunluğunda, 1460 ºC erime noktası ve %99 saflık oranına sahip anhidrit kalsiyum sülfat katkısı ($CaSO_4$) toz halinde temin edilmiştir. Çimento harçlarında en büyük tane boyutu 4 mm olan ince agrega kullanılmıştır. Agrega elek analizi sonuçlarına göre; 4 mm'den %100, 2 mm'den %64, 1 mm'den %32, 0.5 mm'den %16, 0.25 mm'den %12, 0.125 mm'den %8 oranlarında agrega geçişleri belirlenmiştir. Agreganın özgül ağırlık, su emme ve incelik modülü değerleri sırasıyla 2.7, %1.7 (ağırlıkça) ve 3.9'dur.

KAÇ harçlarının karışım oranları Tablo 2'de sunulmuştur. "KAÇ" kodlu karışımda mineral katkı kullanılmazken, SiO_2 katkısı bağlayıcı oranın %8 ve %16'sı oranında, $CaSO_4$ katkısı ise bağlayıcı oranın %30 ve %50'si oranında kullanılmıştır. Tüm harçlarda KAÇ hidratlarının dönüşüm oranının orta seviyede olmasını sağlamak için su/bağlayıcı oranı 0.5'de [39] ve ince agrega/bağlayıcı oranı 3.0'de sabit tutulmuştur.

Harç karışımları EN 196-1 standardına göre hazırlanmıştır. Harçların taze hal deneyleri bir sonraki bölümde açıklanmıştır. Eğilme ve eğilme sonrası basınç deneyleri için her seriden EN 196-1 standardına göre 105 adet 40*40*160 mm^3 prizmatik numune ve aşınma deneyi için 71×71×71 mm^3 boyutlarında 15 adet küp numune hazırlanmıştır. Numuneler dökümden bir gün sonra kalıptan çıkarılarak, deney gününe kadar 20±5 °C (%60±20 BN) koşulunda bekletilmiştir.

Tablo 1 - KAÇ'ın kimyasal ve fiziksel/mekanik özellikleri

Kimyasal Özellikler		Fiziksel ve Mekanik Özellikler	
CaO (%)	36.20	Özgül ağırlık	3.25
Al_2O_3 (%)	39.80	Özgül yüzey (Blaine) m^2/kg	300
Fe_2O_3 (%)	17.05	Priz başlangıcı (dk)	280
SiO_2 (%)	3.60	Priz sonu (dk)	295
MgO (%)	0.65	Hacim sabitliği (mm)	1
SO_3 (%)	0.04	0.045 mm elek bakiyesi (%)	23
Kızdırma kaybı (%)	0.30	6 saatteki basınç dayanımı (MPa)	47
Cl^- (%)	0.009	24 saatteki basınç dayanımı (MPa)	70
S^2 (%)	0.01		

Tablo 2 - Karışım oranları (kg/m^3)

Karışım kodları	Çimento (kg)	Mineral katkı (kg)	Bağlayıcı (kg)	Kum (kg)	Su (kg)	Su/Bağlayıcı **	Kum/Bağlayıcı **
KAÇ	521	0	521	1563	261	0.5	3.0
%8 SiO_2	477	42	519	1556	259	0.5	3.0
%16 SiO_2	434	83	517	1549	258	0.5	3.0
%30 $CaSO_4$	363	156	519	1556	259	0.5	3.0
%50 $CaSO_4$	259	259	518	1551	259	0.5	3.0

*Bağlayıcı= Çimento + Mineral katkı

**Su/Bağlayıcı ve Kum/Bağlayıcı değerleri ağırlıkça oran değerleridir.

2.3. Deney Yöntemleri

Harç karışımlarının işlenebilirliği, ASTM C1437 [40] standardına göre mini çökme konisi ile ölçülmüş olup, detayları yazarların önceki çalışmasında [44] bulunabilir. Harçların kıvam değerleri ve belirlenen kıvamdaki priz süreleri 20ºC'de TS EN 196-3'e [41] uygun Vicat sondası ve iğnesi yardımıyla belirlenmiştir.

Reolojik ölçümlerde 8 mm çapında bilyeli ölçüm düzeneğine sahip (Ball measuring system – BMS) Physica MCR 51 reometresi kullanılmış olup, detaylı bilgiler Felekoğlu (2009)'da [42] bulunabilir. Çalışma kapsamındaki taze harçların akma eğrilerini çıkartmak için "Rheoplus" yazılımı ile Şekil 1b'de gösterilen kayma hızı makrosu hazırlanmıştır. Hazırlanan harçlar içinde bilye, 1. aşamada 5 s^1'lik sabit bir kayma hızında döndürülerek elde edilen akma eğrilerinden, statik (durgun halden ilk harekete geçiş) eşik kayma gerilmeleri ($\tau_{0, statik}$) belirlenmiştir. Bu makrodaki 4. ve 5. aşamalara kıyasla, 2. ve 3. aşamalardaki akış eğrilerindeki değişkenlik daha fazladır. İleride yapılan histerezis alanı hesabında söz konusu değişkenliğin kaynağı değerlendirilecektir. Söz konusu değişkenlik nedeniyle dinamik eşik

kayma gerilmesi (EKG) ve viskozite değerleri 2. ve 3. aşamalar yerine, 4. ve 5. aşamalardan elde edilmiştir. Bunun sebebi, taze harçların başlangıç ölçümlerinde oluşabilecek değişkenliği azaltmaktır [43]. 4. ve 5. aşamadaki akma eğrisi verileri Herschel Bulkley (HB) modeli yardımıyla analiz edilerek, bir sonraki paragrafta verilen reolojik parametreler hesaplanmıştır. HB bağıntısı Denklem 3'de sunulmuştur.

$$\tau = \tau_{0,\text{dinamik}} + b\,\dot{\gamma}^{p} \tag{3}$$

burada τ: herhangi bir kayma hızında (Şekil 6'daki y ekseni değişkeni) kayma gerilmesi (Pa), $\tau_{0,\text{dinamik}}$: Dinamik eşik kayma gerilmesi (Pa), γ: Kayma hızı (1/s) (Şekil 6'daki x ekseni değişkeni), b ve p, HB modelinin katsayıları olup detaylı bilgiler Keskinateş ve Felekoğlu (2018)'de [44] bulunabilir. Dinamik eşik kayma gerilmesi ($\tau_{0,\text{dinamik}}$), sıfır kayma hızında model denkleminin değeridir ve HB modeli analiz sonucu elde edilen eğrinin y-eksenini (τ) kestiği nokta olarak tanımlanmıştır. Bu değer ($\tau_{0,\text{dinamik}}$), statik eşik kayma gerilmesi ($\tau_{0,\text{statik}}$) değerinden farklı olup, doğrudan verilerden değil, modelden alınan bir büyüklüktür.
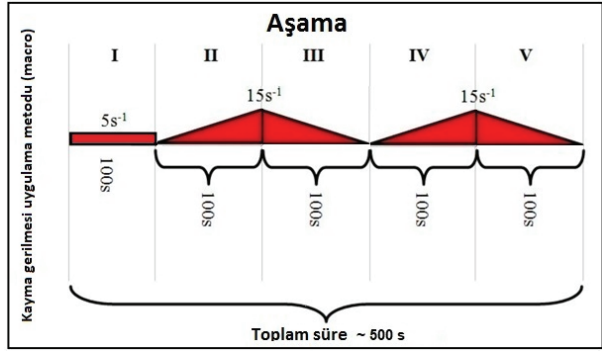
(a)   (b)

Şekil 1 - a) BMS ile donatılmış reometre, b) Uygulanan kayma hızı makrosu ve akış eğrilerini elde etmek için kullanılan adımlar [49].
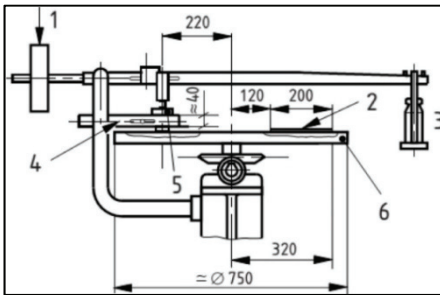
(a)   (b)

Şekil 2 - (a) Böhme cihazı çizimi (1: Karşı ağırlık, 2: Test hattı, 3: Yükleme ağırlığı, 4: Numune tutucu, 5: Numune, 6: Döner disk, boyutlar mm'dir), (b) Aşınma deneyi için kullanılan Böhme cihazı

40x40x160 mm^3 boyutlu prizma numuneler üzerinde eğilme ve eğilme sonrası basınç deneyleri; 1, 3, 7, 28, 90, 180 ve 400 günlerin her birinde eğilme deneyi için 3 ve basınç deneyi için 6 numune sonucunun ortalaması alınarak belirlenmiştir. Eğilme dayanımının tespiti 3 noktalı deney ile mesnet açıklığı 100 mm ve yükleme hızı 5 mm/dk olacak şekilde yapılmıştır. Eğilme deneyi sonucu iki parçaya ayrılan numuneler üzerinde 40x40 mm^2'lik yüzey alanı ve 244 kgf/s yükleme hızında basınç deneyleri gerçekleştirilmiştir.

Çalışmadaki harçlardan 71×71×71 mm^3 boyutlarında oluşturulan küp numuneler, dökümden 28 gün sonra aşınma deneyine tabi tutulmuştur. Yüzeysel aşınma deneyi için Böhme yüzeysel aşınma cihazı kullanılmıştır (Şekil 2). TS EN 14157 (2017)'ye [45] uygun gerçekleştirilen aşınma deneyin detayları literatürde [46]–[48] bulunabilir.

3. BULGULAR VE TARTIŞMA

3.1. Taze Hal Sonuçları

3.1.1. Yayılma Deneyi Sonuçları

Taze harçların yayılma değerleri, hem katkı türünden hem de dozajdan etkilenmiştir (Şekil 3). Sabit su/bağlayıcı oranında, SiO$_2$ katkılı harçların yayılma çapı değeri referans harç olan %100 KAÇ bağlayıcılı harçtan daha yüksek iken (%5-18), CaSO$_4$ katkılı harçların yayılma çapı değerleri daha düşüktür (%19-21). Ayrıca katkı oranı arttıkça yayılma çapı değerlerinin bir miktar düştüğü, dolayısıyla işlenebilirliğin azaldığı belirlenmiştir. Özet olarak; SiO$_2$ katkısının düşük kullanım oranlarında işlenebilirlik üzerinde olumlu etkisi görülmüştür. CaSO$_4$ katkısının ise daha az yayılma davranışı gerektiren onarım uygulamalarına daha uygun olduğu gözlemlenmiştir.

3.1.2. Kıvam Deneyi Sonuçları

Harçların kıvam tayinlerinde Vicat aleti sondasının harç içine batma seviyeleri Şekil 4'de gösterilmiştir. Kesik koni kalıp içinde bulunan harcın toplam yüksekliği 36 mm'dir. Gerek yayılma deneyi gerekse Vicat kıvam deneyi, benzer işlenebilirlik ölçüm teknikleri olduğundan, Şekil 3'deki harçların yayılma çapı değerleri ile Şekil 4'deki batma seviyesi değerleri benzer eğilim göstermektedir. Referans "KAÇ" harcına kıyasla SiO$_2$ katkılı harçlarda, Vicat sondasının batma seviyesi daha yüksek iken, CaSO$_4$ katkılı harçlarda sonda batma seviyesi azalmıştır (Şekil 4). Her iki mineral katkı ilavesinde de, katkı oranı arttıkça Vicat sondasının batma seviyesinin düştüğü belirlenmiştir.

3.1.3. Priz Deneyi Sonuçları

20 °C'de ölçülen priz başlangıç ve bitiş süreleri Şekil 5'de gösterilmiştir. Referans KAÇ harcına kıyasla; SiO$_2$ katkı ilavesi harçların priz başlangıç ve bitiş sürelerini arttırırken, CaSO$_4$ katkısı harçların priz başlangıç sürelerini azaltmıştır. Ancak priz bitiş süreleri için CaSO$_4$ katkı dozajının etkili olduğu görülmüştür. KAÇ bazlı çimentolu malzemelere eklenen nanosilikanın, KAÇ klinkerinin hidratasyonunu bir miktar geciktirebildiği önceki çalışmalarda da rapor edilmiştir [19], [50]. Deneysel bulgularda, SiO$_2$ katkısı ilavesi benzer şekilde priz sürelerini arttırmıştır. Referans KAÇ harcına kıyasla, %30 CaSO$_4$ ikamesi priz bitiş süresini arttırırken, %50 CaSO$_4$ ikamesi ile priz başlangıç süresi kısalmıştır.

Literatürdeki bir çalışmada [51], KAÇ-CaSO$_4$'lı sistemlerde normal dönüşüm reaksiyonlarının oluşmadığı ve genellikle oluşan ilk ürünün etrenjit olduğu belirtilmiştir. Bu açıdan düşünüldüğünde etrenjitin büyük miktarlarda suyu bağlama yeteneği, hızlı kuruyan ve hızlı sertleşen betonlar üretmek için avantajlı olabilir. Yapılan başka bir çalışmada ise [52], KAÇ-CaSO$_4$ ikili sisteminde CaSO$_4$ miktarı arttıkça, priz süresinin arttığı bildirilmiştir.
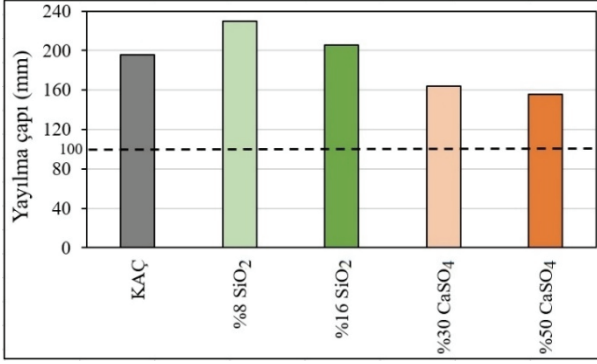
Şekil 3 - KAÇ ve mineral katkılı harçların yayılma değerleri
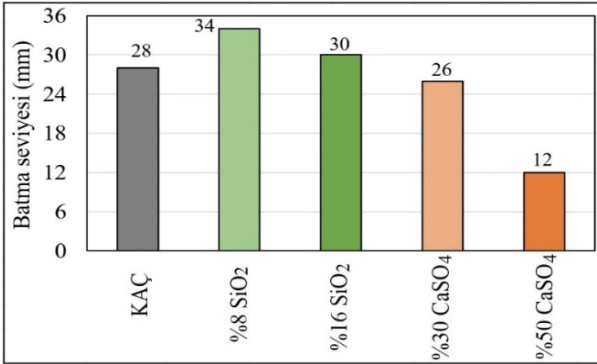
Şekil 4 - KAÇ ve mineral katkılı harçların kıvam değerler
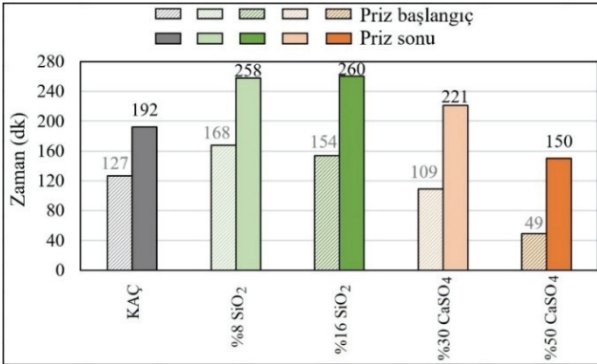
Şekil 5 - KAÇ ve mineral katkılı harçların priz başlangıç ve bitiş süreleri

CaSO$_4$, etrenjit oluşumuna bağlı ani prizi önlemek için genellikle Portland çimentosuna eklenir. Birçok yazar [6], [8], [53] CaSO$_4$ ilavesi ile bir bariyer, yani bir "etrenjit tabakası" oluştuğunu iddia etmektedir. Portland çimentosunda miktarı görece olarak az olan C$_3$A'nın yüzeyinde su ve iyonların taşınmasını sınırlayan yarı geçirgen bir etrenjit tabakası oluştururlar. Etrenjit oluşumu, katkılı harçların hidratasyonu ve dolayısıyla priz başlangıç ve bitiş süreleri ile yakından ilişkilidir [36]. Bu açıdan bakıldığında, KAÇ'lı sistemlerde yüksek alüminat içeriği de dikkate alınarak erken yaşlarda CaSO$_4$ katkılı harçlarda etrenjit oluşum potansiyelinin çok daha fazla olacağı değerlendirilmiştir. CaSO$_4$ katkılı harçların priz başlangıç ve bitiş sürelerinin diğer harçlardan (katkısız KAÇ ve SiO$_2$ katkılı harçlar) daha kısa olmasının bu mekanizma ile ilişkili olduğu düşünülmektedir. Yang ve diğerleri (2019) [21] KAÇ'daki hidratasyon sürecinin, çözeltideki Ca^{+2} ve Al(OH)$^{-4}$ iyonlarının konsantrasyonu tarafından yönetildiğini bildirmiştir. Bu nedenle söz konusu iyonların konsantrasyonu SiO$_2$ katkılı harçlarda düşerken, CaSO$_4$ katkılı harçlarda artış göstermektedir. Dolayısıyla bu iyonlardaki konsantrasyonların düşmesi priz sürelerinin uzamasına neden olurken, iyonların konsantrasyonun artması priz sürelerinin daha kısa olması şeklinde yorumlanabilir. Sonuç olarak KAÇ harcına kıyasla, SiO$_2$ katkılı harçlardaki daha uzun priz süreleri ve CaSO$_4$ katkılı harçlarda daha kısa olan priz süreleri, Ca^{+2} ve Al(OH)$^{-4}$ iyonlarının konsantrasyonunun priz süreleriyle ters orantılı olması ile açıklanabilir.

3.1.4. Reometre Deney Sonuçları

KAÇ, SiO$_2$ ve CaSO$_4$ katkılı harçların Herschel-Bulkley (HB) eğrileri ve model katsayıları sırasıyla Şekil 6 ve Tablo 3'de sunulmuştur. Sadece %50 CaSO$_4$ katkılı harcın düşük işlenebilirliği nedeniyle (Şekil 4), bu karışıma ait kayma gerilmesi değerleri reometrenin gerilme kapasitesi olan 2850 Pa'ı aşmıştır. Söz konusu harç için akma eğrileri elde edilememiştir (Şekil 6 c ve d). Hem kayma hızı artışının görüldüğü çıkış eğrisi bölümü (Şekil 1b 4. aşama) hem de kayma hızı azalışının görüldüğü iniş eğrisi bölümü (Şekil 1b 5. aşama) HB modeli ile analiz edilmiştir. Tablo 3'de görüldüğü üzere genel olarak 5. aşamaya kıyasla 4. aşamaya ait dinamik eşik kayma gerilmesi ve nihai viskozite değerleri daha yüksektir. Ancak 4. aşamadaki "KAÇ katkısı" ve "KAÇ-%30 CaSO$_4$" harçları için R katsayıları oldukça düşüktür (sırasıyla 0.29 ve 0.16). Bu nedenle reolojik parametrelerin kararlı rejime ulaştığı 5. aşamadaki verilerin HB ile modellenmesi daha anlamlı görünmektedir. Tablo 3'deki diğer tüm serilerin 5. aşamadaki HB modeli korelasyon katsayıları (R) 0.85'den büyük olduğundan, HB yönteminin modelleme için uygun bir yöntem olduğu söylenebilir. 5. aşamadaki HB analiz sonuçlarına göre; referans KAÇ harcı ile SiO$_2$ katkılı harçların dinamik eşik kayma gerilmesi ve nihai viskozite değerleri birbirine oldukça benzer iken, %30 CaSO$_4$ katkılı harcın dinamik eşik kayma gerilmesi ve nihai viskozite değerleri KAÇ harcına kıyasla oldukça yüksektir. Diğer taraftan, SiO$_2$ katkısı ikame oranın %8'den %16'ya arttırılması, dinamik eşik kayma gerilmesi ve nihai viskozite değerlerinin bir miktar yükselmesine neden olmuştur. %16 SiO$_2$ katkılı harç için p<1 olduğundan psödoplastik davranış sergileme eğiliminde iken, diğer tüm harçlar için p>1 olduğundan dilatant davranış gösterme eğilimindedir.

Statik eşik kayma gerilmesi (durgun halden akışı başlatmak için gerekli olan minimum kayma gerilmesi), genellikle dinamik kayma gerilmesinden (tiksotropik yapı bozulduktan sonra akışı korumak için gerekli olan minimum kayma gerilmesi) daha yüksek değerdedir.

Bunun nedeni, statik kayma gerilmesinin bozulmamış, iyi bağlanmış bir mikro yapıya, dinamik kayma gerilmesinin ise örselenmiş taze harç yapısına karşılık gelmesindendir.

Referans KAÇ harcına kıyasla; SiO_2 katkılı harçların hem statik EKG hem de dinamik EKG değerleri daha düşük iken, $CaSO_4$ katkılı harçlara ait değerler daha yüksektir. Ayrıca SiO_2 katkı oranı artışı (%8'den %16'ya) statik EKG değerini düşürürken, dinamik EKG değerinin artmasına neden olmuştur. %50 $CaSO_4$ katkılı harçta reometrenin kayma gerilmesi sınır değerini aştığı için veri alınamaması, %30 $CaSO_4$ katkılı harçtan daha yüksek statik ve dinamik EKG değerlerine sahip olduğu şeklinde yorumlanabilir. Bu nedenle $CaSO_4$ katkı oranının artışıyla, hem statik hem de EKG değerlerinde artışlar olduğu değerlendirilmiştir.

Tablo 3 - KAÇ ve katkılı harçların Herschel Bulkley Modeli ile hesaplanan reolojik parametreleri

Karışımlar ve analiz aşamaları*	Statik eşik kayma gerilmesi (Pa) ($\tau_{0, statik}$)	Dinamik eşik kayma gerilmesi (Pa) ($\tau_{0, dinamik}$)	b	p	R	viskozite (Pa.s) ($\eta_{15s^{-1}}$)
KAÇ katkısı (4. aşama)	2193	81.5	0.33	1.92	0.29	9.4
KAÇ katkısı (5. aşama)		59.2	3.30	1.15	0.87	8.9
KAÇ-%8 SiO_2 (4. aşama)	1853	66.6	2.49	1.27	0.96	9.7
KAÇ-%8 SiO_2 (5. aşama)		48.3	3.17	1.27	0.98	9.8
KAÇ-%16 SiO_2 (4. aşama)	832	90.6	3.25	1.19	0.97	11.4
KAÇ-%16 SiO_2 (5. aşama)		61.8	16.25	0.67	0.98	10.8
KAÇ-%30 $CaSO_4$ (4. aşama)	2850	-3960.6**	4344.10	0.01	0.16	33.2
KAÇ-%30 $CaSO_4$ (5. aşama)		272.1	6.34	1.32	0.89	33.2
KAÇ-%50 CaSO4 (4. aşama)	x	x	x	x	x	x
KAÇ-%50 CaSO4 (5. aşama)		x	x	x	x	x

* 4. ve 5. aşamalar Şekil 1'den görülebilir.   ** Fiziksel olarak anlamsız veri.   ***x: Cihaz kapasitesi aşıldığından veri alınamamıştır.

Akma eğrisinin çıkış ve iniş eğrileri arasında kalan alan "histerezis alanı" olarak tanımlanabilir. Histerezis alanı, malzemelerin kayma hızı değişimi karşısında yapısal olarak yumuşama (structural breakdown) veya toparlanma (structural recovery) özelliklerinin belirlenmesinde kullanılmaktadır. Çalışma kapsamındaki harçların histerezis alanları için kayma gerilmesi-kayma hızı eğrileri Şekil 7'de gösterilmektedir. Verilen grafiklerde kırmızı çizgiler 2. ve 3. aşamalardaki kayma hızı artışı ve azalışını, mavi çizgiler ise 4. ve 5. aşamalardaki kayma hızı artışı ve azalışının görüldüğü çıkış ve iniş eğrilerini göstermektedir. Tüm harçlarda kırmızı çizgi daha yukarıda olduğundan pozitif histerezis alanları yani yapısal yumuşama (structural breakdown) davranışı hakimdir. Bu durum, harçların reometre sondasının ucundaki bilyeye uyguladıkları kayma gerilmelerinin düşmesiyle açıklanabilir ve harçların tiksotropik özellik gösterdiği söylenebilir. Pozitif histerezis alanları, bu harçların kayma hızı artış ve sonrasında azalışı ile bilyeye uyguladıkları kayma gerilmesinin azaldığını göstermektedir.
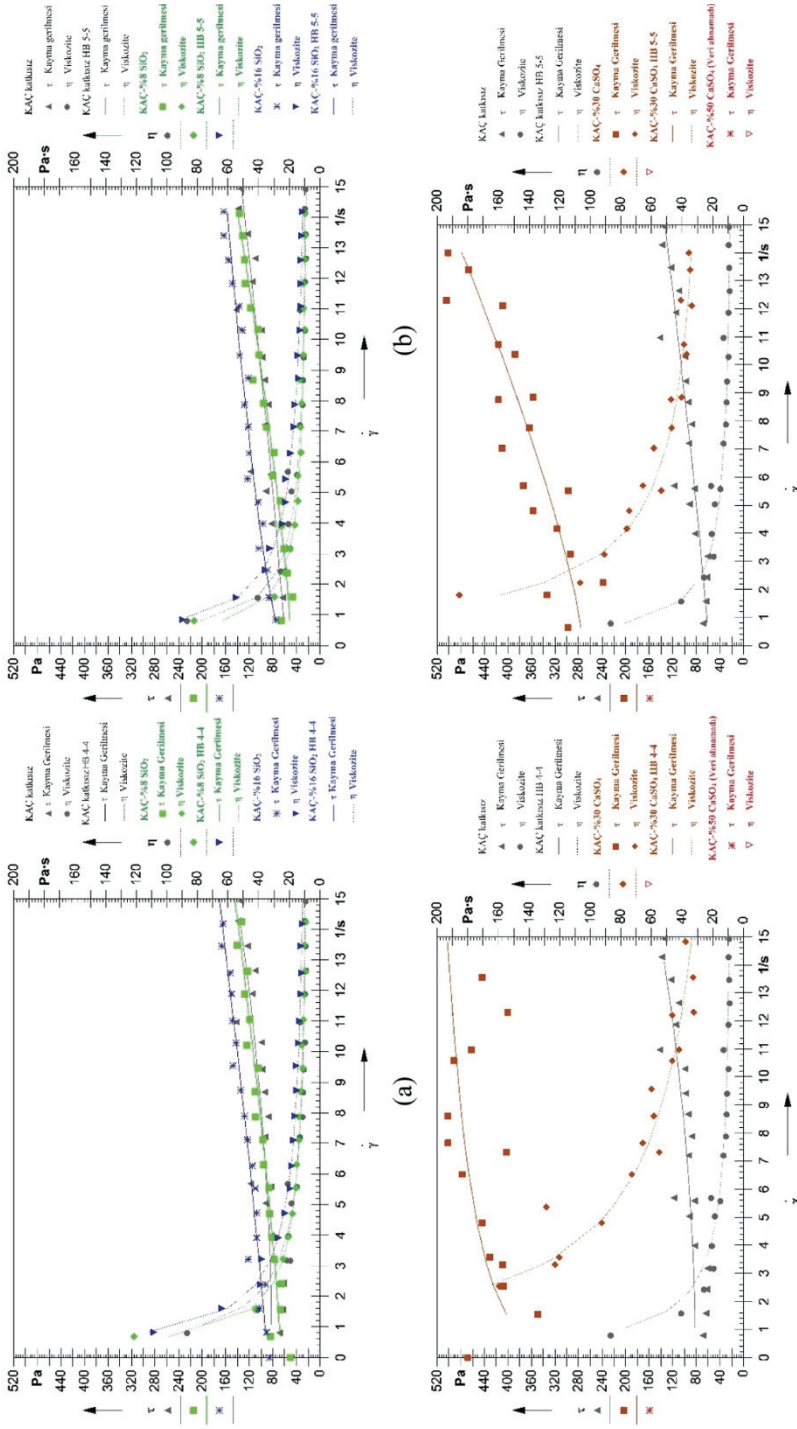
Şekil 6 - KAÇ ve mineral katkılı harçların akma ve viskozite eğrileri (a) 4-4 aşama KAÇ, %8 SiO₂ ve %16 SiO₂
(b) 5-5 aşama KAÇ, %8 SiO₂ ve %16 SiO₂ (c) 4-4 aşama KAÇ, %30 CaSO₄ ve %50 CaSO₄
(d) 5-5 aşama KAÇ, %30 CaSO₄ ve %50 CaSO₄

* τ: Kayma gerilmesi (Pa), γ̇: Kayma hızı (1/s), η: viskozite (Pa.s)

Tiksotropi ile ilişkilendirilebilecek artan ve azalan eğriler arasındaki histerezis alanları hem 2-3 hem de 4-5 aşamaları (Şekil 1) için hesaplanarak Tablo 4'de verilmiştir. KAÇ harcına kıyasla SiO_2 katkılı harcın histerezis alanı daha küçük iken, %30 $CaSO_4$ katkılı harçta daha büyüktür. Söz konusu durumun, katkıların kullanım oranları arttıkça daha belirgin hale geldiği tespit edilmiştir. Şekil 4'deki kıvam performansları göz önüne alındığında, kıvam performansı ile histerezis alanları arasında doğru orantılı bir ilişki olduğu gözlenmektedir.

Tablo 4'deki ilk gidiş dönüş hareketlerindeki (2. ve 3. aşamalar) histerezis alanları, ikinci gidiş-dönüş hareketinden (4. ve 5. aşamalar) daha büyüktür. Bu durum sürekli kayma hızı etkisi altında kalan harçlarda, gidiş ve dönüş sırasında davranışın birbirine yakınlaşması ile açıklanabilir. İlk iniş çıkış aşamaları olan 2-3 aşamalarında, bilye hareketlendikten sonra kum taneciklerinin çimento hamurundaki taneler arası elektrostatik etkileşimi kırdığı düşünülmektedir. Böylece ikinci iniş ve çıkış aşamaları olan 4-5 aşamalarında elde edilen histerezis alanı, 2-3. aşamada elde edilene kıyasla daha küçük olmaktadır.

(a)　　　　　　　　　　　　(b)

(c)　　　　　　　　　　　　(d)
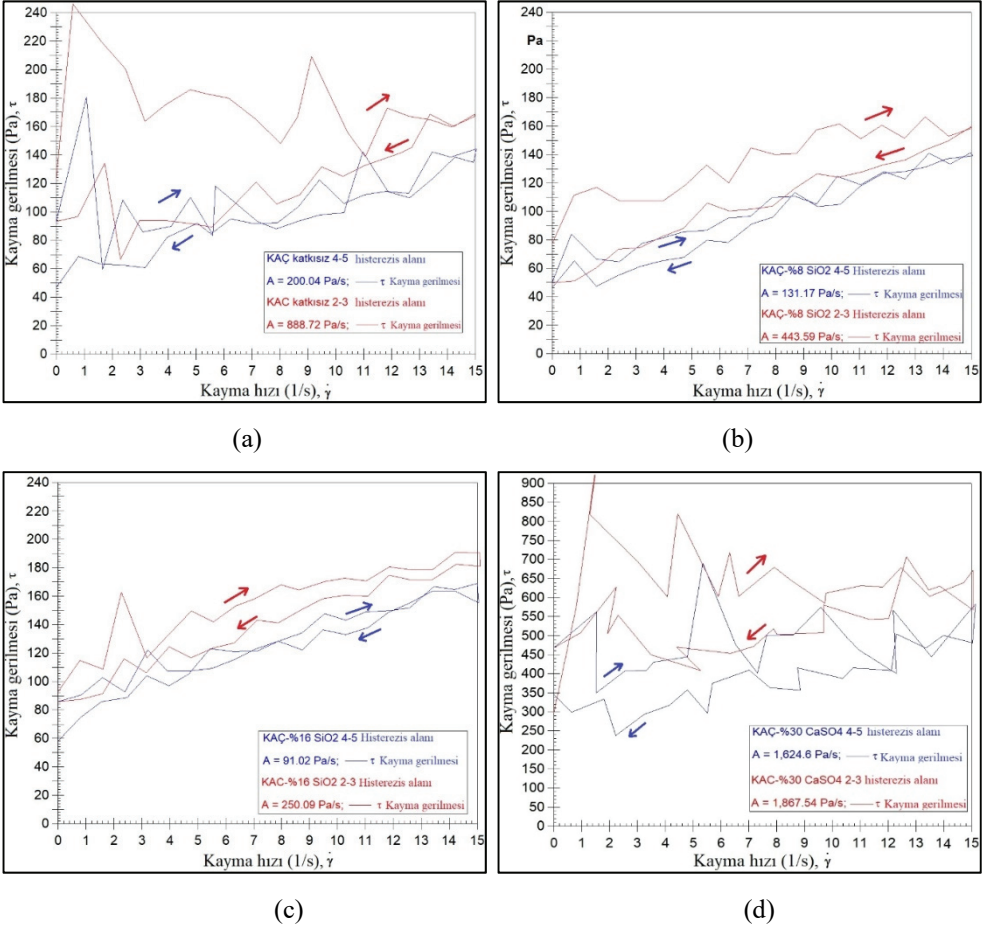
Şekil 7 - KAÇ ve mineral katkılı harçların histerezis alanları (a) KAÇ, (b) %8 SiO_2, (c) %16 SiO_2 ve (d) %30 $CaSO_4$ (kırmızı çizgi 2-3 ve mavi çizgi 4-5 aşama verilerini ifade etmektedir)

Tablo 4 - Taze harçların histerezis alanları (Pa/s)

Karışım kodu	2. ve 3. aşamalar arasındaki Histerezis alanı (Pa/s)	4. ve 5. aşamalar arasındaki Histerezis alanı (Pa/s)
KAÇ katkısız	889	200
KAÇ-%8 SiO$_2$	444	131
KAÇ-%16 SiO$_2$	250	91
KAÇ-%30 CaSO$_4$	1868	1625
KAÇ-%50 CaSO$_4$	*	*

* Veri alınamamıştır.

Tüm taze hal sonuçları için genel bir değerlendirilme yapıldığında, işlenebilirlik özelliği (yayılma ve kıvam) yüksekten düşüğe doğru harçlar sırasıyla; %8 SiO$_2$, %16 SiO$_2$, KAÇ, %30 CaSO$_4$ ve %50 CaSO$_4$ şeklindedir. Eklenen katkı türü ve oranına bağlı olarak, pratikte kullanılan katkısız kalsiyum alüminat çimentosuna kıyasla, hızlı sertleşmesi istenen veya akıcı kıvam gerektiren tamir ve onarım harcı uygulamalarına uygun malzemeler geliştirilmesi açısından farklı alternatif çözümler kazandırılabildiği görülmektedir.

3.2. Sertleşmiş Hal Sonuçları

3.2.1. Basınç Deneyi Sonuçları

Katkısız ve katkılı KAÇ harçlarının zamana göre basınç dayanımı gelişimleri Şekil 8'de gösterilmiştir. Referans KAÇ harcının basınç dayanımı 3. günde en yüksek değere ulaşmış ve sonrasında 180. güne kadar zamanla kademeli olarak azalarak sabitlenmiştir. Referans KAÇ harcının 400. gündeki basınç dayanımı, 3. gündeki değerine göre %47 oranında düşüktür. Diğer katkılı harçların basınç dayanımları, 28 güne kadar sürekli artış göstererek 62-73 MPa seviyelerine çıkmıştır. Ancak bekleme süresi uzadıkça "%8 SiO$_2$", "%16 SiO$_2$" ve "%30 CaSO$_4$" katkılı harçların basınç dayanımlarında sırasıyla %27, %12 ve %9 mertebelerinde düşüşler görülmüştür. Diğer taraftan, %50 CaSO$_4$ katkılı harçların 28 gündeki basınç dayanımı 62 MPa seviyesine ulaşmış ve bekleme süresinin daha da artmasıyla düşüş olmadığı tespit edilmiştir. 400. gündeki katkılı harçların basınç dayanımları dikkate alındığında, yüksek oranda mineral katkı kullanılan harçların (%16 SiO$_2$ ve %50 CaSO$_4$) düşük oranda mineral katkı kullanılan harçlara (%8 SiO$_2$ ve %30 CaSO$_4$) kıyasla, basınç dayanımı değerlerinin %8-9 seviyesinde daha yüksek olduğu belirlenmiştir. Katkısız referans KAÇ ve katkılı harçların (%8 SiO$_2$, %16 SiO$_2$, %30 CaSO$_4$ ve %50 CaSO$_4$) 400. gündeki basınç dayanımı kıyaslandığında, katkısız harca göre katkılı harçların sırasıyla %35, %46, %44 ve %57 mertebelerinde daha yüksek değerlere sahip olduğu belirlenmiştir.

Yukarıdaki paragrafta ayrıntılı şekilde incelenen basınç dayanım gelişim verilerinden şu genel sonucun çıkartılması mümkündür: Mineral katkı türünden bağımsız olarak erken dönemde (28. güne kadar) düşük katkı oranlı harçların basınç dayanımları daha yüksek iken, uzun dönemde (180. gün ve sonrası) yüksek katkı oranlı harçların basınç dayanımları daha yüksektir. Literatürdeki bir çalışmada KAÇ'a %2, %4, %6 ve %8 oranlarında CaSO$_4$ eklenmesiyle ve oranın artışıyla, 3. ve 7. gündeki basınç dayanımlarının azaldığı rapor edilmiştir [3]. KAÇ ile yapılan başka bir çalışmada ise [54], 28. gün sonuçlarına göre,

kalsiyum sülfat içeriği arttıkça gözenekliliğin düşmesiyle basınç dayanımlarında artış gözlenmiştir.

KAÇ'ın SiO_2 ve $CaSO_4$ eklenmesinin, yarı kararlı fazlardan (CAH_{10} ve C_2AH_8) kararlı fazlara (C_3AH_6 ve AH_3) dönüşüm oranını azalttığı değerlendirilmiştir. Ayrıca sırasıyla strätlingite (C_2ASH_8) ve etrenjit fazlarını oluşturarak KAÇ'ın uzun vadeli dayanımını ve yapısal bütünlüğünü koruması açısından etkili olduğu söylenebilir. Bu konuda yapılan ayrıntılı mikroyapı incelemeleri yazarların önceki çalışmasında [55] sunulmuştur. Sonuç olarak, uzun dönemde (400. gün) özellikle %8 SiO_2 ve %50 $CaSO_4$ ilavesi ile oluşturulan katkılı harçlarda, strätlingite ve etrenjit oluşumuyla basınç dayanımı kaybının mertebesini önemli ölçüde azalttığı düşünülmektedir. Bir başka deneysel çalışmada, KAÇ bazlı çimentolu malzemelere eklenen nanosilikanın, C_2ASH_8 oluşmasına neden olarak C_3AH_6'ya faz geçişini engellemede önemli bir rol oynadığı rapor edilmiştir [19], [50]. C_2ASH_8'in, C_3AH_6'dan daha düşük bir yoğunluğa sahip olduğu ve iç gözenekleri doldurduğu belirtilmiştir. Bu da nanosilikanın KAÇ bazlı çimentolu malzemelere dahil edilmesinin yüksek dayanıma katkıda bulunacağı şeklinde yorumlanmıştır [52].

3.2.2. Eğilme Deneyi Sonuçları

KAÇ harçlarının eğilme dayanımları, 3. güne kadar zamanla artmış ve sonrasında 28. günde azalarak sonraki yaşlar için yaklaşık olarak sabitlenmiştir (Şekil 9). KAÇ harçlarının 400. gündeki eğilme dayanımı, 3. gündeki değerinden %33 oranında daha düşüktür.

Katkılı harçların eğilme dayanımları, 28 güne kadar artış göstererek maksimum seviyelerine ulaşmıştır (9.2-10.3 MPa). Ancak bekleme süresi uzadıkça (28. günden 400. güne) "%8 SiO_2", "%30 $CaSO_4$" ve "%50 $CaSO_4$" katkılı harçların eğilme dayanımlarında sırasıyla %11, %8 ve %18 mertebelerinde düşüşler görülmüştür. Diğer taraftan, %16 SiO_2 katkılı harcın 28 gündeki eğilme dayanımı 8.7 MPa seviyesine ulaşmış ve bekleme süresinin daha da artmasıyla (400. günde) düşüş olmadığı tespit edilmiştir.

400. gündeki sonuçlarda katkı dozajının etkisi incelendiğinde; SiO_2 katkı oranı arttıkça (%8'den %16'ya) eğilme dayanımı %8 oranında artarken, $CaSO_4$ katkı oranı arttıkça (%30'dan %50'ye) eğilme dayanımı %11 oranında düştüğü belirlenmiştir. Katkısız (KAÇ) ve katkılı harçların (%8 SiO_2, %16 SiO_2, %30 $CaSO_4$ ve %50 $CaSO_4$) 400. gündeki eğilme dayanımları kıyaslandığında, katkısız harca göre katkılı harçların sırasıyla %14, %23, %32 ve %17 mertebelerinde daha yüksek değerlere sahip olduğu belirlenmiştir. Ayrıca, 90. güne kadar düşük katkılı SiO_2 harçların (%8 SiO_2) eğilme dayanımı daha yüksek iken, 180. gün ve sonrasında yüksek oranda SiO_2 katkılı harçların (%16 SiO_2) eğilme dayanımının daha yüksek olduğu tespit edilmiştir. Öte yandan, genel olarak düşük oranda $CaSO_4$ katkılı harçların (%30 $CaSO_4$) eğilme dayanımlarının, yüksek oranda $CaSO_4$ katkılı harçlara (%50 $CaSO_4$) kıyasla daha yüksek olduğu görülmüştür.

Bir malzemenin mekanik özellikleri, gözenekliliği ile doğrudan ilişkilidir. Gözeneklilik arttığında basınç dayanımı azalır [56]. Şekil 8 ve 9'da görüldüğü gibi KAÇ harçların basınç ve eğilme dayanımlarını azaltan en önemli etkenin, gerçekte engellenemeyen dönüşüm reaksiyonları sonucu gözeneklilik artışı olduğu değerlendirilmiştir. Bu çalışmadaki karışımlara ait porozite analizi ile ilgili detaylı bilgiler yazarların önceki çalışmasından [55] bulunabilir.
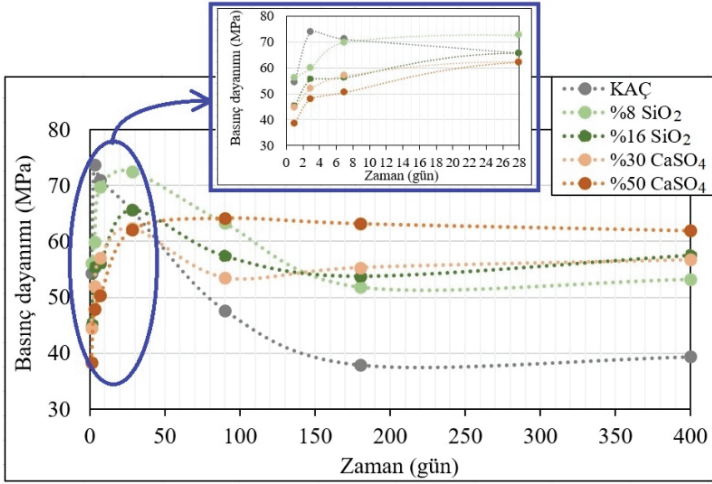
Şekil 8 - KAÇ ve mineral katkılı harçların zamana bağlı basınç dayanımı gelişimleri
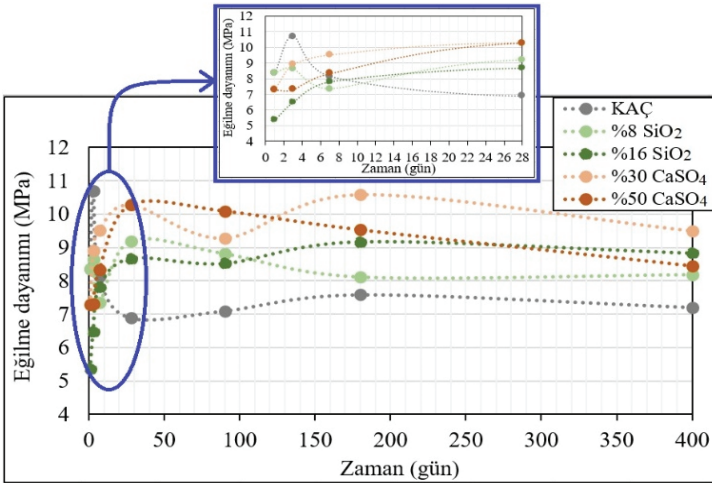
Şekil 9 - KAÇ ve mineral katkılı harçların zamana bağlı eğilme dayanımı gelişimleri

KAÇ harcında mekanik dayanımların düşmesine neden olan bu yüksek gözenekliliğin nedeninin; KAÇ'ın iki ana hidratasyon ürünü, altıgen faz olan CAH_{10} ve C_2AH_8'in uzun süreler boyunca kübik hidrogarnet fazına (C_3AH_6) [57] dönüşüm reaksiyonlarının olabileceği düşünülmektedir. Ding, Fu ve Beaudoin [58], fazların göreli hacimlerindeki farklılıklarından yola çıkarak gözeneklilikteki artışı açıklamıştır. Buna göre; CAH_{10}'un C_3AH_6'ya dönüştürülmesi, hacmin yaklaşık %50'ye düşmesiyle sonuçlanırken, C_2AH_8'in kübik faza dönüştürülmesi, reaksiyona giren ürünlerin orijinal hacminin yaklaşık %65 oranında azalması ile sonuçlanmıştır. Bu nedenle, dönüşüm olayının en büyük etkisi, gözeneklilikteki

artış ve bunun sonucu olarak dayanımdaki azalmadır. Silika (SiO_2), yarı kararlı hidrat fazlarla (CAH_{10} & C_2AH_8) aşağıdaki Denklem 4 ve 5'de gösterildiği gibi strätlingite bileşimi (C_2ASH_8) oluşturma potansiyeline sahiptir:

$$2CAH_{10} + S \rightarrow C_2ASH_8 + AH_3 + 9H \tag{4}$$

$$C_2AH_8 + S \rightarrow C_2ASH_8 \tag{5}$$
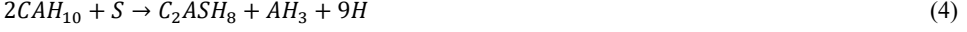
Bu çalışmadaki SiO_2 katkısı, uzun dönemde referans KAÇ harcında meydana gelen dönüşüm reaksiyonlarını strätlingite oluşumu ile engellediği için gözeneklilik artışının meydana gelmediği ve böylece SiO_2 katkılı harçlarda dayanım kayıplarının referans KAÇ harcına kıyasla daha düşük seviyelerde kaldığı değerlendirilmiştir.

3.2.3. Aşınma Deneyi Sonuçları

28 günlük katkısız ve katkılı KAÇ harçlarının aşınma kaybı değerleri Şekil 10'da sunulmuştur. Mineral katkı türü ve oranlarının sonuçlar üzerinde etkisi şu şekilde değerlendirilmiştir: %30 ve %50 oranlarında $CaSO_4$ katkısı içeren harçlar, %8 ve %16 SiO_2 kullanılarak oluşturulan harçlardan daha düşük aşınma kaybı değerlerine sahiptir. Katkı dozajı etkisinin aşınma üzerindeki etkisi incelendiğinde; SiO_2 katkı oranının %8'den %16'ya artışıyla aşınma artarken, $CaSO_4$ katkı oranının %30'dan %50'ye artışıyla aşınma miktarı azalmıştır. KAÇ harcına kıyasla, %8 SiO_2 ve %50 $CaSO_4$ katkılı harçların aşınma kaybı değerlerinin sırasıyla, %9 ve %32 daha düşük olduğu tespit edilmiştir.

Yukarıdaki sonuçlar iki mekanizma ile açıklanabilir: 1) Atiş [59], mineral katkı kullanımı ile çimento matrisi-agrega geçiş bölgesinin güçlendiğini ve böylece daha iyi aşınma direncinin oluştuğunu bildirmiştir. Buna göre, bu çalışmadaki referans KAÇ harcına kıyasla katkılı harçların, daha iyi agrega-bağlayıcı ara yüzey özellikleri oluşmasını sağlayarak aşınma direncini geliştirdiği söylenebilir. 2) Literatürde [60] geçirimlilikteki düşüşle aşınma direncinde artış olduğu belirtilmiştir. KAÇ'a kıyasla, SiO_2 ve $CaSO_4$ katkılarının daha küçük tane boyutlu olmasının (daha yüksek özgül yüzey alanı (Bölüm 2.2)), boşluklar için dolgu etkisi oluşturduğu ve böylece gözenekliliği düşürerek katkılı harçların aşınma direncinin arttığı düşünülmektedir.

Bu çalışmadaki ile aynı aşınma deneyi standardı (TS 699 [61], TS 2824 [62], TS EN 1338 [63]) ve Portland çimentosu (PÇ) kullanılarak aynı karışım oranları ile gerçekleştirilen çalışmalarda; aşınma kaybı değerlerinin 23 g/50 cm^2 (basınç dayanımı 49 MPa) [64] ve 35 g/50 cm^2 (basınç dayanımı 61 MPa) [65] aralığında olduğu bildirilmiştir. Ayrıca Felekoğlu ve diğerleri [66] tarafından benzer karışım oranlarında PÇ ve %2 çelik lifli kendiliğinden yerleşen harcın (basınç dayanımı 48 MPa) aşınma kaybı değeri 37 g/50 cm^2 olarak bildirilmiştir. PÇ ve iri agrega kullanılarak beton karışımlarda aşınma kaybı 27 g/50 cm^2 (basınç dayanımı 37 MPa) [67] ve 57 g/50 cm^2 (basınç dayanımı 65 MPa) [68] olarak raporlanmıştır. Bu çalışmadaki aşınma kaybı değerlerinin 32-47 g/50 cm^2 aralığında olduğu dikkate alınırsa, bu sonuçların literatürdeki değerlere yakın, hatta bazılarından daha iyi olduğu söylenebilir. Ayrıca aşınma direncinin; su/çimento oranı, agrega tipi ve özellikleri, hava sürüklenme, kür yöntemi gibi faktörlerden etkilendiği [60] ve bu nedenlerle sonuçlarda farklılıklar olabileceği düşünülmektedir.
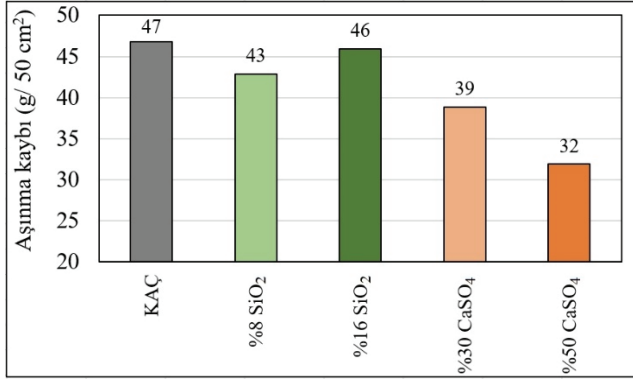
Şekil 10 - KAÇ ve mineral katkılı harçların aşınma kaybı değerleri

3.2.4. Basınç - Eğilme - Aşınma Dayanımları Arasındaki İlişkiler

KAÇ, %8 SiO₂, %16 SiO₂, %30 CaSO₄ ve %50 CaSO₄ harçlarına ait eğilme dayanımı/basınç dayanımı oranları sırasıyla; 0.10-0.20, 0.11-0.16, 0.12-0.17, 0.16-0.19, 0.14-0.19 aralığındadır. Bu sonuçlar mineral katkı ikamesinin eğilme dayanımı/basınç dayanımı oranlarındaki değişkenliği azalttığını göstermektedir. Portland çimentosu ile üretilen beton için eğilme dayanımı/basınç dayanımı oranının yaklaşık 0.11-0.23 arasında değiştiği bilinmektedir [69]. Çalışma kapsamındaki KAÇ ve mineral katkılı harçların tüm eğilme dayanımı/basınç dayanımı oranlarının 0.10-0.20 arasında kaldığı ve Portland çimentosu ile üretilen betonlarla benzerlik gösterdiği tespit edilmiştir. Aşınma kaybı ile basınç ve eğilme dayanımları arasındaki 28. gün sonuçlarına göre elde edilen ilişkiler Şekil 11'de verilmiştir. Beklendiği üzere aşınma kaybı ile eğilme dayanımı arasında güçlü negatif bir korelasyon söz konusudur. Ancak bazı araştırmacılar [59], [70], [71] basınç dayanımı yüksek olan Portland çimentolu beton karışımlarının aşınma dayanımının da yüksek olduğunu bildirmelerine rağmen, bu çalışmada aşınma kaybı ile basınç dayanımı arasında herhangi bir ilişki tespit edilememiştir. Bu sonuç, ilk 28 günde KAÇ'da meydana gelen faz değişimlerinin eğilme dayanımından ziyade basınç dayanımında daha etkili olduğunu göstermektedir. Basınç dayanımı numunenin tüm kesitine etki eden gerilme üzerinden belirlenirken, eğilme dayanımı numunede tek bir noktada oluşan gerilme üzerinden hesaplanmakta (üç noktalı eğilme deneyi için) ve bu nedenle faz dönüşümlerinin basınç dayanımı üzerindeki etkisinin daha baskın olabileceği düşünülmektedir. Ayrıca numunelerdeki oluşabilecek mikro çatlaklar; basınç gerilmeleri etkisinde kapanma eğiliminde olduğundan, basınç dayanımı üzerindeki etkisinin, eğilme dayanımı ve aşınma kaybına kıyasla daha az olduğu değerlendirilebilir. Diğer bir ifadeyle; mikro çatlakların eğilme dayanımında oluşacak çekme gerilmesinin büyüklüğüne ve aşınmada oluşacak parça kopmalarına etkileri nedeniyle, basınç dayanımına kıyasla eğilme dayanımı ve aşınma kaybı üzerinde daha etkili olduğu şeklinde yorumlanabilir.

Bir başka çalışmada yukarıdaki hipotezi güçlendirecek bulgular şu şekilde sunulmuştur: Aşınma-eğilme dayanımı ilişkisinin, eğilme-basınç dayanımı ilişkisinden daha kuvvetli olduğu bildirilmiştir [65]. Bu sonuç yazarlar tarafından şu şekilde açıklanmıştır: Malzemede oluşan parça kopmalarının (aşınma) genellikle çekme dayanımının ya da çekme birim uzama

kapasitesinin aşılmasından dolayı olduğu, ancak basınç durumunda ise böyle bir durum söz konusu olmadığı ve bu durumun aşınma ile eğilme dayanımı arasında daha kuvvetli bir ilişkinin elde edilmesini sağladığı değerlendirilmiştir.

Özet olarak, eğilme dayanımı ve aşınma kaybı benzer davranış gösterirken basınç dayanımı ile aşınma kaybı arasında net bir ilişki elde edilememiştir. Ancak söz konusu hipotezleri güçlendirmek için daha geniş kapsamlı çalışmalara ihtiyaç vardır.
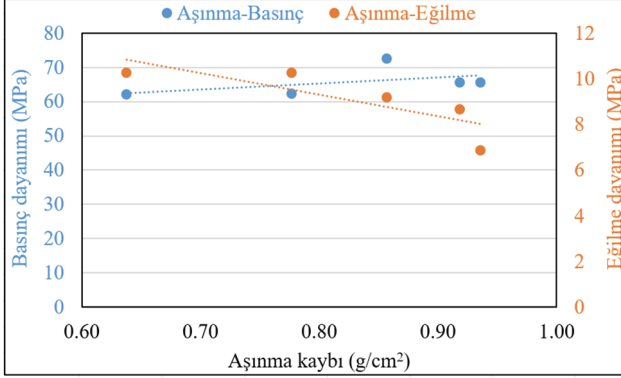
Şekil 11 - KAÇ ve mineral katkılı harçların aşınma kaybı ile basınç ve eğilme dayanımları arasındaki ilişki

4. SONUÇLAR

1) Taze hal deneylerinin sonuçları değerlendirildiğinde;

- SiO_2 katkılı harçların diğer harçlara kıyasla daha fazla yayılma davranışı gösterdiği, daha akıcı kıvama sahip olduğu ve prize daha geç başlayıp daha geç bitirdiği belirlenmiştir. Bu bulgular dikkate alındığında, SiO_2 katkılı kalsiyum alüminat çimentolu harçların saha uygulamalarında, zemin tesviye betonu olarak kullanımı bağlamında diğer harçlara kıyasla en elverişli yapıda olduğu düşünülmektedir.

- $CaSO_4$ katkılı harçların ise daha yoğun ve viskoz yapıya sahip olması, aynı zamanda prize daha erken başlayıp daha erken bitirmesi göz önüne alındığında; tamir, onarım harcı, yapıştırıcı gibi hızlı servise sokulması gereken uygulamalarda en etkili seçenek olduğu sonucuna varılmıştır.

2) Katkı türü, katkı dozajı ve zaman etkileri altında basınç dayanımlarında aşağıdaki gibi sonuçlar elde edilmiştir.

- Referans KAÇ harcının basınç dayanımı 3. günde en yüksek değere ulaşmıştır, ancak 400. gündeki basınç dayanımı, 3. gündeki değerine göre %47 oranında düşüktür.

- Katkılı harçların basınç dayanımları, 28 güne kadar sürekli artış göstererek 62-73 MPa seviyelerine ulaşmasına rağmen, bekleme süresi uzadıkça "%8 SiO_2", "%16 SiO_2" ve "%30 $CaSO_4$" katkılı harçların basınç dayanımlarında sırasıyla %27, %12 ve %9 mertebelerinde azalma meydana gelmiştir. Ancak %50 $CaSO_4$ içeren harcın basınç dayanımında bekleme süresinin daha da artmasıyla düşüş olmadığı tespit edilmiştir (62 MPa).

- 400. günde yüksek mineral katkılı harçların (%16 SiO_2 ve %50 $CaSO_4$) düşük mineral katkılı harçlara (%8 SiO_2 ve %30 $CaSO_4$) kıyasla, basınç dayanımı değerleri %8-9 daha yüksektir. Katkılı harçların (%8 SiO_2, %16 SiO_2, %30 $CaSO_4$ ve %50 $CaSO_4$) 400. gündeki basınç dayanımları, katkısız referans KAÇ harcına göre sırasıyla %35, %46, %44 ve %57 mertebelerinde daha yüksektir. Her iki katkının da uzun vadeli basınç dayanımında (bu çalışma için 400 güne kadar) dönüşüm kaynaklı basınç dayanımı kaybını önlemede etkili olduğu sonucu elde edilmiştir.

3) Aşınma deneyi sonuçlarına göre; referans KAÇ harcına kıyasla, %8 SiO_2 ve %50 $CaSO_4$ katkılı harçların aşınma kaybı değerlerinin sırasıyla, %9 ve %32 daha düşük olduğu tespit edilmiştir. $CaSO_4$ katkılı harçlar, SiO_2 katkılı harçlardan daha düşük aşınma kaybı değerlerine sahiptir. Öte yandan katkı dozajı artışıyla; SiO_2 katkılı harçlarda aşınma kaybı artarken, $CaSO_4$ katkılı harçlarda azalmaktadır.

4) Aşınma kaybı ile eğilme dayanımı arasında güçlü negatif korelasyon tespit edilmiş, ancak aşınma kaybı ile basınç dayanımı arasında belirgin bir ilişki gözlenmemiştir.

Teşekkür

Kaynaklar

[1]   N. Y. Mostafa, Z. I. Zaki, and O. H. Abd Elkader, "Chemical activation of calcium aluminate cement composites cured at elevated temperature," *Cem. Concr. Compos.*, vol. 34, no. 10, pp. 1187–1193, 2012, doi: 10.1016/j.cemconcomp.2012.08.002.

[2]   A. Macias, A. Kindness, and F. P. Glasser, "Corrosion behaviour of steel in high alumina cement mortar cured at 5, 25 and 55°C: Chemical and physical factors," *J. Mater. Sci.*, vol. 31, no. 9, pp. 2279–2289, 1996, doi: 10.1007/BF01152936.

[3]   H. M. Son, S. Park, H. Y. Kim, J. H. Seo, and H. K. Lee, "Effect of CaSO4 on hydration and phase conversion of calcium aluminate cement," *Constr. Build. Mater.*, vol. 224, pp. 40–47, 2019, doi: 10.1016/j.conbuildmat.2019.07.004.

[4]   S. Moehmel, W. Gessner, T. A. Bier, and C. Parr, "The influence of microsilica on the course of hydration of monocalcium aluminate," in *In International conference on calcium aluminate cements*, 2001, pp. 319–330.

[5]   J. D. Birchall, A. J. Howard, and K. Kendall, "Flexural strength and porosity of cements," *Nature*, vol. 289, no. 5796, pp. 388–390, 1981, doi: 10.1038/289388a0.

[6]   K. L. Scrivener and A. Capmas, *Calcium Aluminate Cements BT - Lea's Chemistry of Cement and Concrete (Fourth Edition)*. 2003.

[7] K. L. Scrivener, J. L. Cabiron, and R. Letourneux, "High-performance concretes from calcium aluminate cements," *Cem. Concr. Res.*, vol. 29, no. 8, pp. 1215–1223, 1999, doi: 10.1016/S0008-8846(99)00103-9.

[8] H. F. Taylor, *Cement chemistry*. London: Thomas Telford, 1997.

[9] J. Matusinovic, T., Vrbos, N., and Sipusic, "Rapid setting and hardening calcium aluminate cement materials," *Zement-Kalk-Gips İnternational*, vol. 58, no. 5, pp. 72–79, 2005.

[10] E. Sakai, T. Sugiyama, T. Saito, and M. Daimon, "Mechanical properties and micro-structures of calcium aluminate based ultra high strength cement," *Cem. Concr. Res.*, vol. 40, no. 6, pp. 966–970, 2010, doi: 10.1016/j.cemconres.2010.01.001.

[11] H. Fryda, K. L. Scrivener, G. Chanvillard, and C. Feron, "Relevance of laboratory tests to field applications of calcium aluminate cement concretes," in *In International conference on calcium aluminate cements*, 2001, pp. 227–246.

[12] L. G. Andión, P. Garcés, F. Cases, C. García-Andreu, and J. L. Vazquez, "Metallic corrosion of steels embedded in calcium aluminate cement mortars," *Cem. Concr. Res.*, vol. 31, no. 9, pp. 1263–1269, 2001, doi: 10.1016/S0008-8846(01)00572-5.

[13] H. Lamour, V. H. R., Monteiro, P. J. M., Scrivener, K. L., and Fryda, "Mechanical properties of calcium aluminate cement concretes," in *In International conference on calcium aluminate cements*, 2001, pp. 199–213.

[14] L. Scheinherrová and A. Trník, "Hydration of calcium aluminate cement determined by thermal analysis," in *AIP Conference Proceedings*, 2017, doi: 10.1063/1.4994514.

[15] M. D. M. Alonso, M. Palacios, and F. Puertas, "Effect of polycarboxylate-ether admixtures on calcium aluminate cement pastes. Part 2: Hydration studies," *Ind. Eng. Chem. Res.*, vol. 52, no. 49, pp. 17330–1734, 2013, doi: 10.1021/ie401616f.

[16] Ş. Alpaslan and K. Tosun-Felekoğlu, "Polikarboksilat Bazlı Süperakışkanlaştırıcıların Kalsiyum Alüminat Çimentosunun Kıvam Koruma Performansı Üzerine Karşılaştırmalı Bir Çalışma," *Afyon Kocatepe Üniversitesi Fen ve Mühendislik Bilim. Derg.*, pp. 140–154, 2019.

[17] G. Türedi, Ö. Kasap Keskin, and S. B. Keskin, "Self-compacting mortar production by using calcium aluminate cement," *Mugla J. Sci. Technol.*, vol. 6, no. 2, pp. 18–27, 2020, doi: 10.22531/muglajsci.686144.

[18] O. Akhlaghi, Y. Z. Menceloglu, and O. Akbulut, "Poly(carboxylate ether)-based superplasticizer achieves workability retention in calcium aluminate cement," *Sci. Rep.*, vol. 7, no. 1, pp. 1–7, 2017, doi: 10.1038/srep41743.

[19] H. M. Son, S. M. Park, J. G. Jang, and H. K. Lee, "Effect of nano-silica on hydration and conversion of calcium aluminate cement," *Constr. Build. Mater.*, vol. 169, pp. 819–825, 2018, doi: 10.1016/j.conbuildmat.2018.03.011.

[20] J. Ding, Y. Fu, and J. J. Beaudoin, "Strätlingite formation in high alumina cement - silica fume systems: Significance of sodium ions," *Cem. Concr. Res.*, vol. 25, no. 6, pp. 1311–1319, 1995, doi: 10.1016/0008-8846(95)00124-U.

[21] H. J. Yang, K. Y. Ann, and M. S. Jung, "Development of strength for calcium aluminate cement mortars blended with GGBS," *Adv. Mater. Sci. Eng.*, 2019, doi: 10.1155/2019/9896012.

[22] B. Majumdar, A. J., Edmonds, R. N., ve Singh, "Hydration of calcium aluminates in presence of granulated blast furnace slag," in *Calcium Aluminate Cements*, 1990, pp. 259–271.

[23] Ö. Kirca, I. Özgür Yaman, and M. Tokyay, "Compressive strength development of calcium aluminate cement-GGBFS blends," *Cem. Concr. Compos.*, vol. 35, no. 1, pp. 163–170, 2013, doi: 10.1016/j.cemconcomp.2012.08.016.

[24] J. F. Zapata, H. A. Colorado, and M. A. Gomez, "Effect of high temperature and additions of silica on the microstructure and properties of calcium aluminate cement pastes," *J. Sustain. Cem. Mater.*, vol. 9, no. 6, pp. 323–349, 2020, doi: 10.1080/21650373.2020.1737593.

[25] M. Heikal, M. S. Morsy, and M. M. Radwan, "Electrical conductivity and phase composition of calcium aluminate cement containing air-cooled and water-cooled slag at 20, 40 and 60 °c," *Cem. Concr. Res.*, vol. 35, no. 7, pp. 1438–1446, 2005, doi: 10.1016/j.cemconres.2004.09.027.

[26] M. Heikal and M. M. Radwan, "Physico-chemical properties and microstructure of some blended systems," *Silic. Ind.*, vol. 71, no. 9, pp. 161–166, 2006.

[27] A. J. Majumdar, R. N. Edmonds, and B. Singh, "Hydration of Secar 71 aluminous cement in presence of granulated blast furnace slag," *Cem. Concr. Res.*, vol. 20, no. 1, pp. 7–14, 1990, doi: 10.1016/0008-8846(90)90111-A.

[28] A. J. Majumdar, B. Singh, and R. N. Edmonds, "Hydration of mixtures of 'Ciment Fondu' aluminous cement and granulated blast furnace slag," *Cem. Concr. Res.*, vol. 20, no. 2, pp. 197–208, 1990, doi: 10.1016/0008-8846(90)90072-6.

[29] M. Heikal, M. M. Radwan, and M. S. Morsy, "Influence of curing temperature on the physicomechanical, characteristics of calcium aluminate cement with air-cooled slag or water-cooled slag," *Ceram. - Silikaty*, vol. 48, no. 4, pp. 185–196, 2004.

[30] N. Y. Mostafa and P. W. Brown, "Heat of hydration of high reactive pozzolans in blended cements: Isothermal conduction calorimetry," *Thermochim. Acta*, vol. 435, no. 12, pp. 162–167, 2005, doi: 10.1016/j.tca.2005.05.014.

[31] A. J. Majumdar and B. Singh, "Properties of some blended high-alumina cements," *Cem. Concr. Res.*, vol. 22, no. 6, pp. 1101–1114, 1992, doi: 10.1016/0008-8846(92)90040-3.

[32] M. Collepardi, S. Monosi, and P. Piccioli, "The influence of pozzolanic materials on the mechanical stability of aluminous cement," *Cem. Concr. Res.*, vol. 25, no. 5, pp. 961–968, 1995, doi: 10.1016/0008-8846(95)00091-P.

[33] C. Gosselin, E. Gallucci, and K. Scrivener, "Influence of self heating and Li2SO4 addition on the microstructural development of calcium aluminate cement," *Cem. Concr. Res.*, vol. 40, no. 10, pp. 1555–1570, 2010, doi: 10.1016/j.cemconres.2010.06.012.

[34] D. Torréns-Martín, L. Fernández-Carrasco, and M. T. Blanco-Varela, "Conduction calorimetric studies of ternary binders based on Portland cement, calcium aluminate cement and calcium sulphate," *J. Therm. Anal. Calorim.*, vol. 114, no. 2, pp. 799–807, 2013, doi: 10.1007/s10973-013-3003-9.

[35] I. Santacruz *et al.*, "Structure of stratlingite and effect of hydration methodology on microstructure," *Adv. Cem. Res.*, vol. 28, no. 1, pp. 13–22, 2016, doi: 10.1680/adcr.14.00104.

[36] L. Xu, P. Wang, and G. Zhang, "Formation of ettringite in Portland cement/calcium aluminate cement/calcium sulfate ternary system hydrates at lower temperatures," *Constr. Build. Mater.*, vol. 31, pp. 347–352, 2012, doi: 10.1016/j.conbuildmat.2011.12.078.

[37] F. Song, Z. Yu, F. Yang, Y. Liu, and Y. Lu, "Strätlingite and calcium hemicarboaluminate hydrate in belite-calcium sulphoaluminate cement," *Ceram. - Silikaty*, vol. 58, pp. 269–274, 2014.

[38] J. F. Georgin and E. Prud'Homme, "Hydration modelling of an ettringite-based binder," *Cem. Concr. Res.*, vol. 76, pp. 51–61, 2015, doi: 10.1016/j.cemconres.2015.05.009.

[39] M. P. Adams, R. D. Lute, E. G. Moffatt, and J. H. Ideker, "Evaluation of a procedure for determining the converted strength of calcium aluminate cement concrete," *J. Test. Eval.*, vol. 46, no. 4, pp. 1659–1672, 2018, doi: 10.1520/JTE20160277.

[40] ASTM, "ASTM C1437 - Standard test method for flow of hydraulic cement mortar," 2013.

[41] "TS EN 196-3 : Çimento deney yöntemleri - Bölüm 3: Priz süreleri ve genleşme tayini," Ankara, 2017.

[42] B. Felekoğlu, "Yüksek performanslı mikro beton tasarımı," Dokuz eylül üniversitesi, 2009.

[43] M. Westerholm, B. Lagerblad, and E. Forssberg, "Rheological properties of micromortars containing fines from manufactured aggregates," *Mater. Struct. Constr.*, vol. 40, no. 6, pp. 615–625, 2007, doi: 10.1617/s11527-006-9173-1.

[44] M. Keskinateş and B. Felekoğlu, "The influence of mineral additive type and water/binder ratio on matrix phase rheology and multiple cracking potential of HTPP-ECC," *Constr. Build. Mater.*, vol. 173, pp. 508–519, 2018, doi: 10.1016/j.conbuildmat.2018.04.038.

[45] TS EN14157, "TS EN 14157. Doğal taşlar - Deney yöntemleri - Aşınma direncinin tayini," Ankara, 2017.

[46] F. Eren, "Kalsiyum alüminat çimentolu harçların reolojik davranışlarının ve uzun dönemli dayanım-dayanıklılık özelliklerinin incelenmesi," Dokuz Eylül Üniversitesi, 2022.

[47] C. Atiş, "Yüksek oranda uçucu kül kullanımı ile üretilen betonun aşınma direnci," *Tek. Dergi*, vol. 11, no. 4, pp. 2217–2230, 2000.

[48] C. Atiş, "Uçucu kül içeren beton için aşınma-boşluk oranı-dayanım modeli," *Tek. Dergi*, vol. 14, no. 4, pp. 3035–3040, 2003.

[49] M. Keskinateş, "Çoklu çatlak davranışı gösteren farklı polimerik lifli çimento esaslı kompozitlerin mikromekanik tabanlı tasarımları ve kıyaslanması," Dokuz Eylül Üniversitesi, 2022.

[50] G. Land and D. Stephan, "The influence of nano-silica on the hydration of ordinary Portland cement," *J. Mater. Sci.*, vol. 47, no. 2, pp. 1011–1017, 2012, doi: 10.1007/s10853-011-5881-1.

[51] J. H. Ideker, "Early-Age Behavior of Calcium Aluminate Cement Systems," The University of Texas at Austin, 2008.

[52] H. Kim, H. M. Son, and H. K. Lee, "Review on recent advances in securing the long-term durability of calcium aluminate cement (cac)-based systems," *Functional Composites and Structures*. 2021, doi: 10.1088/2631-6331/ac1913.

[53] J. Skalny, I. Jawed, and H. F. W. Taylor, "Studies on hydration of cement-recent developments," *World Cem Technol*, vol. 9, no. 6, pp. 183–6, 1978.

[54] J. Bizzozero and K. L. Scrivener, "Limestone reaction in calcium aluminate cement-calcium sulfate systems," *Cem. Concr. Res.*, vol. 76, pp. 159–169, 2015, doi: 10.1016/j.cemconres.2015.05.019.

[55] F. Eren, M. Keskinateş, B. Felekoğlu, and K. Tosun-Felekoğlu, "The role of Pre-Heating and mineral additive modification on Long-Term strength development of calcium aluminate cement mortars," *Constr. Build. Mater.*, vol. 340, no. 127720, 2022.

[56] M. Rößler and I. Odler, "Investigations on the relationship between porosity, structure and strength of hydrated portland cement pastes I. Effect of porosity," *Cem. Concr. Res.*, vol. 15, no. 2, pp. 320–330, 1985, doi: 10.1016/0008-8846(85)90044-4.

[57] N. Ukrainczyk, T. Matusinovic, S. Kurajica, B. Zimmermann, and J. Sipusic, "Dehydration of a layered double hydroxide-C2AH8," *Thermochim. Acta*, vol. 464, no. 1–2, pp. 7–15, 2007, doi: 10.1016/j.tca.2007.07.022.

[58] J. Ding, Y. Fu, and J. J. Beaudoin, "Study of hydration mechanisms in the high alumina cement - Sodium silicate system," *Cem. Concr. Res.*, vol. 26, no. 5, pp. 799–804, 1996, doi: 10.1016/S0008-8846(96)85017-4.

[59] C. D. Atiş, "High Volume Fly Ash Abrasion Resistant Concrete," *J. Mater. Civ. Eng.*, vol. 14, no. 3, pp. 274–277, 2002, doi: 10.1061/(asce)0899-1561(2002)14:3(274).

[60] G. K. Febin *et al.*, "Strength and durability properties of quarry dust powder incorporated concrete blocks," *Constr. Build. Mater.*, vol. 228, no. 116793, 2019, doi: 10.1016/j.conbuildmat.2019.116793.

[61] "TS 699: Doğal yapı taşları - İnceleme ve laboratuvar deney yöntemleri," Ankara, 2009.

[62] "TS 2824 EN 1338/AC: Zemin döşemesi için beton kaplama blokları - Gerekli şartlar ve deney metotları," Ankara, 2009.

[63] "TS EN 1338/AC: Zemin döşemesi için beton kaplama blokları - Gerekli şartlar ve deney metotları," Ankara, 2006.

[64] O. Karahan, C. D. Atiş, and K. Arı, "Metakaolin ve silis dumanı içeren harçların aşınma direncinin karşılaştırılması," Kayseri, 2011.

[65] C. D. Atiş, O. Karahan, and K. Arı, "Alkali ile aktifleştirilmiş cüruf harcının aşınma direncinin araştırılması," Kayseri, 2010.

[66] B. Felekoğlu, S. Türkel, and Y. Altuntaş, "Effects of steel fiber reinforcement on surface wear resistance of self-compacting repair mortars," *Cem. Concr. Compos.*, vol. 25, no. 9, pp. 391–396, 2007, doi: 10.1016/j.cemconcomp.2006.12.010.

[67] A. Kandemir, "Kendiliğinden yerleşen betonun kalıcılık özelliklerinin incelenmesi," Dokuz Eylül Üniversitesi, 2005.

[68] O. Karpuz and M. V. Akpınar, "İnce Agrega Türünün Kaplama Betonunun Aşınma Direncine Etkisi," *Yapı Teknol. Elektron. Derg.*, vol. 5, no. 2, pp. 1–8, 2009.

[69] D. Mindess, S., Young, F. J., & Darwin, *Concrete 2nd Editio*. 2003.

[70] Ş. E. Güldür, "Mikronize kalsit katkısının beton özelliklerine etkisinin araştırılması," Niğde Üniversitesi, 2013.

[71] A. Mardani-Aghabaglou, H. Hosseinnezhad, O. C. Boyacı, Ö. Arıöz, İ. Ö. Yaman, and K. Ramyar, "Abrasion resistance and transport properties of road concrete," in *12th International Symposium on Concrete Roads*, 2014, pp. 23–26.

Türkiye Bina Deprem Yönetmeliğindeki Performans Düzeylerinin Betonarme Kolonlar için Karşılaştırmalı Değerlendirilmesi

Kaan TÜRKER[1]
Cengiz GÜLTEKİN[2]

ÖZ

Çalışmada, 2018 Türkiye Bina Deprem Yönetmeliği'nde (TBDY) plastik dönme açısını esas alan performans düzeyleri, ASCE/SEI 41-17'deki aşılma olasılığı esaslı kolon hasar sınırları ile karşılaştırılarak değerlendirilmiştir. Bunun için enkesit boyutu, eksenel kuvvet düzeyi, kesme etkisi, sargı/boyuna donatı oranı ve beton dayanımı bakımından farklı özelliklerde 4725 kolon örneğine ait karakteristik plastik dönme açıları için sayısal karşılaştırmalar yapılmıştır. Enkesit boyutu, eksenel kuvvet düzeyi ve sargı oranı, TBDY ve ASCE yaklaşımları arasında önemli farkların oluşmasına sebep olan parametreler olmuştur. TBDY'ye göre elde edilen performans düzeyleri, incelenen elemanların büyük bölümü için ASCE'de öngörülen olasılıksal risk düzeylerini sağlamıştır. Ancak, özellikle TBDY-2018 koşullarını sağlamayan elemanlar için ASCE'deki sınırların çok aşılabildiği ve belirli özellikteki elemanlarda aşırı güvenli sonuçlar elde edilebildiği belirlenmiştir.

Anahtar Kelimeler: Betonarme kolon, deprem performans düzeyi, plastik dönme açısı, olasılık esaslı hasar sınırı.

ABTRACT

Comparetively Evaluation of Performance Levels at Building Earthquake Code of Turkey for Columns

In the study, the performance levels based on the plastic rotation angle in the 2018 Building Earthquake Code of Turkey (BECT) were evaluated in comparison with the ASCE/SEI 41-17 column damage limits based on the probability of exceedance concept. For this purpose, numerical comparisions were carried out for the characteristic plastic rotation angles of 4725 column samples in terms of cross-section size, axial force level, shear force level confinement

1 Balıkesir Üniversitesi, İnşaat Mühendisliği Bölümü, Balıkesir, Türkiye
kturker@balikesir.edu.tr - https://orcid.org/0000-0002-3106-4627

2 FAB Teknik Mühendislik Yazılım Tic. A.Ş., Balıkesir, Türkiye
cengizgultekin0@gmail.com - https://orcid.org/0000-0002-0396-7562

ratio, longitudinal reinforcement ratio and concrete strength. Cross-section size, axial load ratio and confinement ratio were the parameters that caused significant differences between the BECT and the ASCE approaches. The performance levels obtained from the BECT fulfilled the probabilistic risk levels stipulated in the ASCE for the majority of the investigated elements. However, it has been determined that the risk limits in the ASCE can be exceeded especially for the elements non-compliant with the BECT-2018 and extremely safe results can be obtained for certain elements.

1. GİRİŞ

Yaklaşık 25 yıl önce geliştirilmeye başlanan performans esaslı deprem mühendisliği yaklaşımı günümüzde oldukça yaygınlaşmış ve birçok ülkenin deprem yönetmeliklerinde geniş yer bulmaya başlamıştır. İlk dönemlerde mevcut binaların deprem güvenliklerinin belirlenmesi ve güçlendirme ihtiyaçlarının değerlendirilmesi amacıyla kullanılan bu yaklaşım bugün tasarım amacıyla da kullanılmaktadır. Özellikle Türkiye'de yüksek binaların ve deprem riski yüksek bölgelerdeki özel öneme sahip binaların tasarımında performans esaslı yaklaşımların kullanılması zorunlu hale gelmiştir [1]. Performans esaslı yaklaşımlar temel olarak belirli bir deprem etkisi altındaki binada şekildeğiştirme taleplerinin belirlenmesine ve bunların çeşitli hasar düzeylerini temsil eden sınır değerleri ile karşılaştırılmasına dayanmaktadır [2-4]. Bu yaklaşımda, deprem taleplerinin ve performans düzeyinin değerlendirilmesinde kullanılacak ve hasar düzeyini temsil edecek şekildeğiştirme parametresi çok büyük önem arz etmektedir. Bugün bu konuda yürürlükte olan standartlarda hasar düzeylerini değerlendirmede eleman uçlarındaki beton/donatı birim şekildeğiştirmeleri, teğet-kiriş (chord) dönme açısı ve plastik dönme açısı gibi büyüklüklerin kullanıldığı görülmektedir [1,5,6]. Bu büyüklükler genel olarak birbiriyle ilişkili ve temel mekanik prensipleri çerçevesinde belirlenebilen büyüklüklerdir. Ancak betonarme elemanların deprem davranışının çok sayıda parametreye göre değişkenlik göstermesi nedeniyle söz konusu büyüklüklerin deneysel çalışmalarla desteklenmesi gerekmektedir. Eurocode 8 [5]'de esas alınan teğet-kiriş açısı ve ASCE standartlarında [6-8] esas alınan plastik dönme açısı, deneysel çalışmalardan elde edilebilen büyüklükler olduğu için bunlar oldukça geniş kapsamlı deneysel veri tabanlarına dayandırılmıştır. Buna karşılık, beton ve donatı birim şekildeğiştirmelerinin deneysel çalışmalardan elde edilmesindeki zorluklar nedeniyle, bu parametrelere ait kriterler yeterli deneysel veritabanı ile doğrulanması yapılamadan daha çok mekanik prensiplerine dayandırılmaktadır.

Türkiye'de ilk olarak 2007 deprem yönetmeliğinde (TDY-2007 [9]), mevcut betonarme binaların değerlendirilmesi ve güçlendirilmesi amacıyla yer verilen performans esaslı yöntemlerde, hasar düzeyi kontrol parametresi olarak beton ve çelik(donatı) birim şekildeğiştirme değerlerinin kullanılması öngörülmüştür. Hasar düzeylerinin birim şekildeğiştirme talepleri üzerinden değerlendirilmesi yaklaşımı için Priestley ve Calvi [10] ile Priestley ve Kowalsky [11] tarafından direkt deplasman esaslı tasarım çerçevesinde önerilen sınır durumlarından yararlanılmıştır. TDY-2007'deki yaklaşımda, yığılı plastisite (plastik mafsal veya doğrusal olmayan yay gibi) kabulü ile yapılan analizlerden elde edilen plastik dönme talepleri, enkesit moment-eğrilik ilişkilerinden yararlanarak birim

şekildeğiştirme taleplerine dönüştürülmektedir. Bu aşamada enkesit analizleri için detaylı malzeme (sargılı/sargısız beton ve pekleşmeli donatı modeli) modelleri ve belirli bir plastik mafsal boyu kabulü kullanılmaktadır [9]. Esasen birim şekildeğiştirme talepleri yayılı plastisite yaklaşımları ile enkesit analizine gerek kalmadan doğrudan belirlenebilse de bu analizlerin zorluğu ve ilgili araçların yetersizliği nedeniyle TDY'de yığılı plastisite yaklaşımı öne çıkarılmıştır. Öngörülen prosedürde eksenel kuvvet ve sargılama durumunun hasar sınırları üzerindeki etkileri moment-eğrilik ilişkileri ile büyük ölçüde gözönüne alınmakla birlikte, donatı burkulması ve histeretik etkiler (dayanım ve rijitlik azalması vb.) birim şekildeğiştirme kapasitelerinde getirilen kısıtlamalar ile dolaylı olarak dikkate alınmaya çalışılmıştır [11]. Ancak kesme kuvvetinin ve donatı detaylarındaki çeşitli yetersizliklerin hasar düzeylerine etkileri ihmal edilmiştir. Sucuoğlu ve Acun [12], TDY-2007'de öngörülen hasar sınırlarını, düşük eksenel kuvvet ve kesme kuvveti etkisindeki betonarme kolonlar üzerinde gerçekleştirilen deneysel gözlemlerle karşılaştırarak değerlendirmiştir. Sargı donatısı bakımından yönetmelik ile uyumlu ve yetersiz iki grup üzerinde yapılan karşılaştırmalar sonucu, yönetmelikte öngörülen hasar sınırlarının güvenli tarafta kaldığı ve deney sonuçları ile uyumlu olduğu gösterilmiştir [12]. Kazaz ve Gülkan [13], sünek perde elemanlar için gerçekleştirdiği çalışmada, deneysel sonuçlara göre kalibre edilen sonlu eleman modelleri kullanarak belirlenen birim şekildeğiştirme talepleri ile enkesit analizinden elde edilen birim şekildeğiştirme kapasitelerini karşılaştırmıştır. Donatı birim şekildeğiştirmelerinde benzer sonuçlar elde edilirken, beton birim şekildeğiştirmelerinde sonuçların çok değişebildiği gösterilmiştir. Aynı çalışmada, incelenen perde elemanlarda yönetmelikteki sargı koşulları sağlanmasına rağmen TDY-2007'deki birim şekil değiştirme kapasitelerinin özellikle kesme kuvveti düzeyi arttıkça oldukça güvensiz tarafta kalan sonuçlar verdiği rapor edilmiş ve birim şekildeğiştirme sınırlarının kesme kuvveti düzeyine bağlı olarak güncellemesi önerilmiştir [13]. Sonlu eleman modelleri ile enkesit analizi sonuçlarının benzer çerçevede karşılaştırıldığı bir diğer çalışma Özdemir vd. [14] tarafından kolonlar üzerinde yapılmıştır. Çalışmada, plastik mafsal bölgelerindeki ortalama beton ve donatı birim şekildeğiştirmelerinin belirlenmesinde iki yaklaşımın biribiriyle oldukça uyumlu sonuçlar verdiği gösterilmiştir. Ancak özellikle yüksek eksenel kuvvet etkisindeki kolonlarda TDY-2007'deki beton birim şekildeğiştirme sınırlarının güvensiz sonuçlar verebildiği rapor edilmiştir [14].

2018 yılında yürürlüğe giren Türkiye Bina Deprem Yönetmeliğinde (TBDY-2018 [1]) önemli bir değişikliğe gidilerek hasar kontrol parametresi ile ilgili büyüklük, taleplerin belirlenmesinde kullanılan analiz yaklaşımına bağlanmıştır. Buna göre, hasar sınırlarının birim şekildeğiştirmelerle ölçülebilmesi için taleplerin de fiber model veya sonlu eleman modeli analizi gibi doğrudan birim şekildeğiştirmelerin belirlenebildiği yayılı plastisite yaklaşımlarının kullanılması zorunlu hale getirilmiştir. Buna alternatif olarak da enkesit analizine dayalı yığılı plastisite yaklaşımları (plastik mafsal vb.) ile hasar değerlendirmelerinin plastik dönme açısı üzerinden yapılması öngörülmüştür. Her iki durumda da performans düzeylerine ait hasar sınırları için TDY-2007'de olduğu gibi beton ve donatı birim şekildeğiştirme sınırları referans alınmıştır. Yeni getirilen plastik dönme açısı ile değerlendirmede, plastik mafsal hipotezi ve kesit moment-eğrilik ilişkilerinin kullanıldığı mekanik prensiplerine dayanan yaklaşım benimsenmiştir. Ancak plastik dönme kapasitelerinin hesabında donatı sıyrılmasından kaynaklanan dönme değerlerini de gözönüne almak amacıyla Biskinis [15] ve Fardis [16]'de önerilen amprik ifadelerden yararlanılmıştır. TBDY-2018'de ayrıca, mevcut binalarda karşılaşılabilecek donatı detayı yetersizliklerinin

ve yüksek kesme kuvvetinin hasar düzeyleri üzerindeki etkileri de basitleştirilmiş şekilde gözönüne alınmaya başlanmıştır [1]. Cansız vd.[17] kolonlar üzerinde gerçekleştirilen deneysel bir çalışma kapsamında, TBDY-2018'de plastik dönme kapasitesi için öngörülen yaklaşımı değerlendirmiştir. Donatı burkulması ve sargılı beton ezilmesi gibi dayanım azalmasına sebep olan hasarlar referans alınarak yapılan değerlendirmelerde, TBDY-2018'de öngörülen plastik dönme kapasitelerinin genel olarak güvenli olduğu, ancak eksenel yük düzeyi yönetmelik üst sınırına yaklaştığında güvensiz durum oluşabildiği rapor edilmiştir [17]. Değer ve Başdoğan [18], TBDY-2018'deki yığılı plastisite yaklaşımının belirli özellikteki betonarme perde elemanlarda kullanımına yönelik olarak, geniş kapsamlı deneysel veri tabanına dayanan bir çalışma gerçekleştirmiştir. Perdelerin deneysel iç kuvvet-şekildeğiştirme bağıntılarının istatistiksel olarak değerlendirildiği çalışmada, eksenel yük ve kesme kuvveti düzeyine bağlı olarak karakteristik modeleme parametreleri ve performans düzeyleri için hasar sınırları önerilmiştir [18].

ABD sismik değerlendirme standartlarında diğer standartlardan farklı olarak, yapısal eleman türleri (kolon, kiriş vb.) için tersinir tekrarlı yükler altındaki iç kuvvet-şekildeğiştirme davranışını temsil eden karakteristik modelleme parametreleri önerilmekte ve performans düzeylerini temsil eden hasar sınırları bu parametreler üzerinden tanımlanmaktadır [6-8]. Kolonlar için Şekil 1'de şematik olarak gösterildiği gibi, eğilme ve eksenel kuvvet taşıma kapasitelerine ait karakteristik sınırlar esas alınarak tanımlanan moment-dönme (M-θ) bağıntıları kullanılmakta ve bu sınırlar mevcut deneysel veri tabanlarından istatistiksel olarak belirlenmektedir. ABD standartlarının 2017'den önceki versiyonlarında [7,8], M-θ bağıntılarına ait karakteristik dönme açıları için deneysel sonuçlara ait dağılımlardan elde edilen alt sınır değerlerinin esas alınması benimsenmiştir (Şekil 1a). Böylece medyan değerlere göre oluşabilecek en büyük sapmaların göz önüne alınması ve güvenli tarafta kalınması amaçlanmıştır. Çeşitli deneysel ve sayısal çalışmalarda, ASCE 41-06 [7] ve ASCE 41-13[8] versiyonlarına göre elde edilen kolon modelleme parametrelerinin oldukça güvenli sonuçlar verdiği gösterilmiştir [12,14,19]. Ancak, söz konusu parametrelere göre belirlenen performans düzeylerinin gerçekleşme olasılıklarının çok değişken olması ve birçok durumda aşırı güvenli sonuçlar vererek olumsuz güçlendirme kararlarına sebep olması nedeniyle, ASCE 41-17'deki yaklaşım geliştirilerek kolonlar için belirli aşılma olasılıklarının esas alındığı modelleme parametreleri ve performans düzeylerinin kullanımına geçilmiştir [6,20-22]. Yeni yaklaşımda, modelleme parametreleri için deneysel verilere dayanan regresyon bağıntıları geliştirilmiş ve bu bağıntı değerleri ile deneysel sonuçlar arasında oluşan hataların (farkların) kümülatif dağılımları esas alınarak, hedeflenen aşılma olasılıklarına bağlı modelleme parametreleri ve performans düzeyleri geliştirilmiştir (Şekil 1b). Pratikte, deneysel sonuçlara göre güvensiz durum oluşma olasılığını ifade eden aşılma olasılıklarının kullanımı ile hem performans değerlendirmelerinde aşırı güvenli sonuçlardan kaçınılması hem de sınırlı sayıda test sonuçlarına dayanan durumlar için riskin kontrol altında tutulması hedeflenmiştir. Eyitayo ve Elwood [23]'da, ASCE'deki eski ve yeni yaklaşım, ACI 369 [24] veri tabanındaki sünekliği yetersiz kolonlar için karşılaştırmalı olarak değerlendirilmiştir. Söz konusu çalışmada [23], ASCE 41-17'de önerilen yeni yaklaşım ile önceki versiyonlarda özellikle yüksek kesme kuvveti etkisindeki elemanlarda karşılaşılan aşırı güvenli sonuçların daha makul düzeye geldiği ve modelleme parametrelerinin beklendiği gibi, test sonuçlarının medyan değerleri ile oldukça uyumlu olduğu gösterilmiştir.

Yapısal elemanlarla ilgili deneysel veri tabanlarının zenginleşmesiyle, hasar kontrolü amacıyla kullanılan büyüklükler için çok parametreli regresyon bağıntılarının kullanımı

yaygınlaşmaktadır. Bununla birlikte önerilen bağıntıların halen deneysel sonuçlarla korelasyonlarının çok düşük olduğu ve bu nedenle bazı durumlarda güvensiz sonuçlar elde etme olasılığının yüksek olabildiği görülmektedir [15,22,25]. Bu bağlamda, TBDY 2018'de yer alan ve diğer standartlardan önemli ölçüde farklılıklar içeren yeni yaklaşımların da doğrudan deneysel veri tabanları ile veya veri tabanlarına dayanan sayısal yaklaşımlarla değerlendirilmesi büyük önem arzetmektedir.
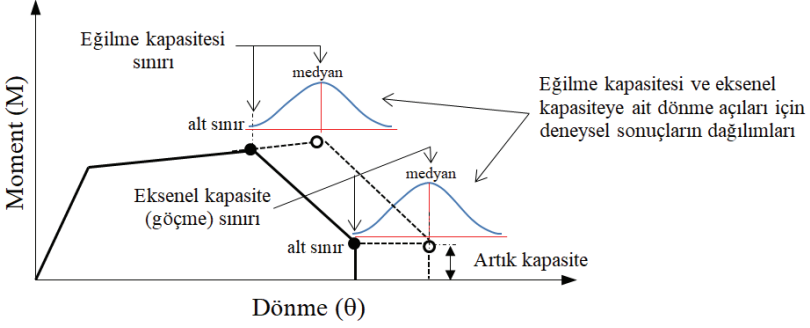
(a) ASCE 41-17 öncesi versiyonlarda esas alınan yaklaşım
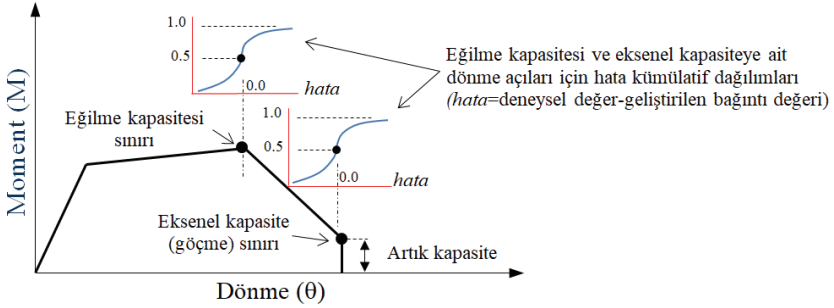
(b) ASCE 41-17 versiyonunda esas alınan yaklaşım

Şekil 1 - ASCE'de kolonlar için kullanılan karakteristik modelleme parametreleri

Bu çalışmada, TBDY-2018'de plastik dönme açısını referans alan performans düzeylerinin (hasar sınırlarının), ASCE/SEI 41-17'de kolonlar için önerilen aşılma olasılığı esaslı performans kriterleri ile karşılaştırılarak değerlendirilmesi amaçlanmıştır. Bunun için, enkesit boyutları, eksenel kuvvet düzeyi, kesme etkisi, sargı donatısı oranı, boyuna donatı oranı ve beton dayanımı bakımından farklı özelliklerdeki kolon örnekleri üzerinde TBDY ve ASCE yaklaşımlarından elde edilen karakteristik plastik dönme açıları karşılaştırılmıştır. İki standarttan elde edilen sonuçlar arasında önemli farklılıklara yol açan parametreler ortaya konmuştur. Ayrıca, deneysel verilere dayanan ASCE yaklaşımında, çeşitli hasar düzeyleri için verilen olasılıksal sınırlar referans alınarak, TBDY'deki performans kriterlerinin risk düzeyleri değerlendirilmiştir.

2. TBDY-2018 PERFORMANS DÜZEYLERİ

TBDY-2018'e göre mevcut ve yeni yapılacak yapıların performans değerlendirmesinde önemli farklılıklar bulunmakla birlikte, genel olarak üç temel performans düzeyi tanımlanmıştır. Bunlar *Sınırlı Hasar* (SH), *Kontrollü Hasar* (KH) ve *Göçmenin Önlenmesi* (GÖ) performans düzeyleridir. Bu performans düzeyleri, taleplerin belirlenmesinde kullanılan analiz yöntemine bağlı olarak doğrudan beton ve donatı birim şekildeğiştirmelerine göre veya eleman ucundaki plastik dönme açılarına göre belirlenebilmektedir. Bu büyüklükler için yönetmelikte öngörülen performans düzeyi sınırları Tablo 1'de verilmiştir. Bu çalışmada, plastik dönme açılarına ait sınırların değerlendirilmesi amaçlandığından sadece onlara ait açıklamalara yer verilmiştir.

Tablo 1 - TBDY performans düzeylerine ait birim şekildeğiştirme ve plastik dönme sınırları

Hasar kontrol parametresi		Performans düzeyleri		
		Sınırlı Hasar (SH) P. düzeyi (ε_c^{SH} / ε_s^{SH} / θ_p^{SH})	*Kontrollü Hasar* (KH) P. düzeyi (ε_c^{KH} / ε_s^{KH} / θ_p^{KH})	*Göçmenin Önlenmesi* (GÖ) P. düzeyi ($\varepsilon_c^{GÖ}$ / $\varepsilon_s^{GÖ}$ / $\theta_p^{GÖ}$)
Birim şekildeğiştirme	Beton (ε_c)	0.0025	$0.75*\varepsilon_c^{GÖ}$	$0.0035 + 0.04\sqrt{\omega_{we}} \leq 0.018$ (Dikdörtgen kesit) $0.0035 + 0.07\sqrt{\omega_{we}} \leq 0.018$ (Dairesel kesit)
	Donatı (ε_s)	0.0075	$0.75*\varepsilon_s^{GÖ}$	$0.40*\varepsilon_{su}$
Plastik dönme (θ_p) (rad)		0	$0.75*\theta_p^{GÖ}$	$\frac{2}{3}\left[(\phi_u - \phi_y)L_p\left(1 - 0.5\frac{L_p}{L_s}\right) + 4.5\phi_u d_b\right]$

Tablo 1'de; ε_{su} boyuna donatı kopma birim uzamasını, L_p enkesitin eğilmeye çalışan yüksekliğinin yarısı olarak alınan plastik mafsal boyunu, L_s kesme açıklığını, d_b kesitteki ortalama donatı çapını, ϕ_y kesitin akma eğriliğini, ϕ_u GÖ sınır durumuna ait beton veya donatı sınır birim şekildeğiştirmesine göre belirlenen maksimum eğriliği ifade etmektedir. ω_{we} betondaki sargı etkisini ifade eden katsayıdır ve (1) bağıntısı ile belirlenmektedir.

$$\omega_{we} = \alpha_{se}\rho_{sh,min}\frac{f_{yw}}{f_c} \tag{1}$$

Burada, α_{se} (2) bağıntısı ile belirlenen sargı donatısı etkinlik katsayısını, $\rho_{sh,min}$ dikdörtgen enkesit için (3) bağıntısı ile belirlenen iki yatay doğrultudaki hacimsel enine donatı oranının küçük olanını, f_{yw} enine donatının akma dayanımını, f_c sargısız beton basınç dayanımını göstermektedir.

$$\alpha_{se} = \left(1 - \frac{\sum a_i^2}{6b_0 h_0}\right)\left(1 - \frac{s}{2b_0}\right)\left(1 - \frac{s}{2h_0}\right) \tag{2}$$

$$\rho_{sh} = \frac{A_{sh}}{b_k s} \tag{3}$$

(2) ve (3) bağıntılarında; s enine donatı aralığını, b_o ve h_o sargı donatısı eksenlerinden ölçülen sargılı beton boyutlarını, a_i etriye kolu veya çiroz tarafından mesnetlenen boyuna donatıların eksenleri arasındaki uzaklığı, A_{sh} enine donatı alanını ve b_k enine donatıya dik doğrultudaki çekirdek boyutunu (en dıştaki enine donatı eksenleri arasındaki uzaklık) göstermektedir.

TBDY'ye göre SH performans düzeyinin sağlanabilmesi için eleman ucunda plastik dönme oluşmaması şartı bulunmaktadır. KH performans düzeyi, GÖ performans düzeyine ait plastik dönmenin ¾'ü alınarak belirlenmekte, böylece ileri plastik şekildeğiştirmelerin sınırlanması ve elemanların onarılabilir kalması amaçlanmaktadır. GÖ performans düzeyi ise elemanın eğilme kapasitesinde önemli bir azalmanın oluşmasını engellemek amacıyla kesiti oluşturan malzemelerin birim şekildeğiştirme kapasitelerine göre belirlenen bir sınırı ifade etmektedir. Bu sınır plastik dönme değeri, detaylı malzeme modelleri ile hazırlanmış kesit moment-eğrilik bağıntısı üzerinden sınır birim şekildeğiştirme değerlerine ($\varepsilon_c^{GÖ}, \varepsilon_s^{GÖ}$) bağlı olarak belirlenir. Beton ve donatı birim şekildeğiştirmelerinden GÖ sınırını tanımlayan ϕ_u eğriliğine geçiş Şekil 2'de şematik olarak gösterilmiştir.
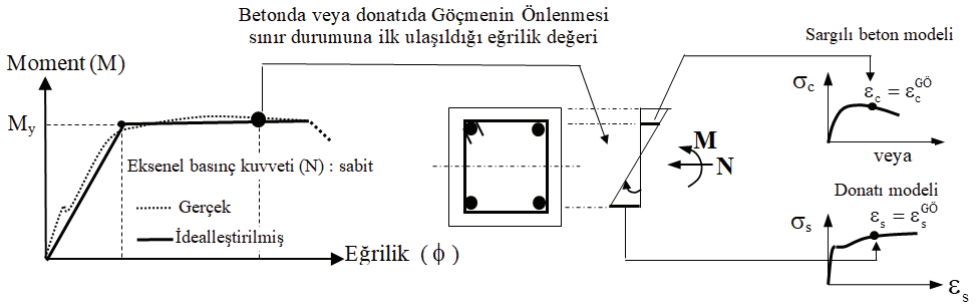
Şekil 2 - TBDY-2018'de Göçmenin Önlenmesi (GÖ) sınırına ait eğriliğin belirlenmesi

Şekil 2'de M_y enkesit akma momentini, N kolondaki eksenel basınç yükünü, σ_c ve σ_s sırasıyla beton ve donatıdaki gerilmeleri ifade etmektedir. M_y akma momenti için TBDY'deki tanım esas alınmıştır. Buna göre 0.0035'lik beton birim kısalması veya 0.01'lik donatı uzamasına karşılık gelen moment değeri kullanılmıştır. (ϕ_u) eğriliğinden plastik dönme açısına ($\theta_p^{GÖ}$) geçiş için plastik mafsal hipotezi çerçevesinde temel mekanik prensipleri kullanılmaktadır. Ancak tersinir tekrarlı yüklerden kaynaklanan donatı sıyrılmasının etkisi de amprik bir ifade ile plastik dönme açısına eklenmektedir (Tablo 1). TBDY-2018'de, mevcut yapıların performans değerlendirmesinde yeni yapılacak yapılardan farklı olarak, kesme kuvvetinin belirli düzeyi aştığı durumlarda Tablo 1'de verilen plastik dönme açısı sınırlarında belirli oranda azaltma uygulanmaktadır.

3. ASCE/SEI 41-17 KOLON MODELLEME PARAMETRELERİ VE PERFORMANS DÜZEYLERİ

ASCE'de kolonların tersinir tekrarlı yükler etkisindeki davranışı için Şekil 3'deki karakteristik θ_p^a, θ_p^b ve c modelleme parametreleri ile tanımlanan moment-dönme bağıntıları kullanılmakta ve performans düzeylerine ait sınırlar bu bağıntı esas alınarak verilmektedir

[6]. Bu bağıntıda, θ_p^a elemanın eğilme (yatay yük) kapasitesinde önemli azalmaların başladığı plastik dönme açısını, θ_p^b elemanın düşey yük taşıma kapasitesini kaybettiği (eksenel göçme) plastik dönme açısını, c ise eksenel göçme kapasitesine ulaşmış elemandaki kalan (artık) eğilme kapasitesi oranını ifade etmektedir. ASCE'deki bu parametreler, eksenel kuvvet düzeyi, kesme kuvveti düzeyi, sargı donatısı oranı ve malzeme özellikleri bakımından farklılık gösteren dikdörtgen ve dairesel enkesitli kolonlara ait deneysel veri tabanına dayanarak belirlenmiştir [20,21,24,26]. İlgili çalışmada, deneysel yatay yük-yatay yerdeğiştirme verilerinden plastik dönme açısına geçmek için plastik mafsal yaklaşımı esas alınmıştır [20]. θ_p^a açısı için kolonun maksimum eğilme (yatay yük) dayanımı sonrası %20 azalmaya karşılık gelen plastik dönme değeri ve θ_p^b açısı için ise kolonun eksenel kuvvet (yük) taşıma kapasitesinin sonlandığı plastik dönme değeri esas alınmıştır. Mevcut test verileri içinde eksenel kuvvet taşıma kapasitesinin rapor edilmediği veya deneyin daha erken sonlandırıldığı durumlarda, maksimum eğilme dayanımı sonrası %75 azalmaya karşılık gelen plastik dönme açıları eksenel göçmenin başlangıcı olarak kabul edilmiştir [20].
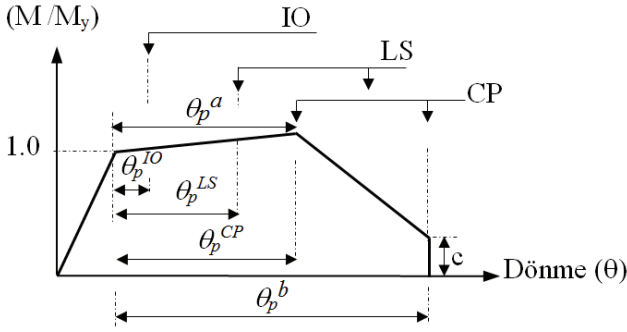
Şekil 3 - ASCE 41-17 kolon moment-dönme bağıntısı için modelleme parametreleri ve performans düzeylerine ait plastik dönme açıları [6]

Tablo 2 - ASCE 41-17 modelleme parametreleri ve performans düzeyi sınırları [2]

Moment-Dönme bağıntısına ait karakteristik değerler (modelleme parametreleri) (Aderans yetersizliği bulunmayan dikdörtgen enkesitli elemanlar için)		Performans düzeylerine ait plastik dönme açıları (rad)		
		Hemen Kullanım p. düzeyi (θ_p^{IO})	*Can Güvenliği* p. düzeyi (θ_p^{LS})	*Göçme Önleme* p. düzeyi (θ_p^{CP})
θ_p^a (rad)	$0.042 - 0.043\frac{N}{A_c f_c} + 0.63\rho_t - 0.023\frac{V_y}{V_r} \geq 0.0$	$0.15*\theta_p^a$ ≤ 0.005	$0.5*\theta_p^b$	$0.7*\theta_p^b$
θ_p^b (rad)	$\frac{N}{A_c f_c} \leq 0.5$ ise $0.5/(5+\frac{N}{0.8A_c f_c}\frac{1}{\rho_t}\frac{f_c}{f_{yw}}) - 0.01$			
	$0.5 < \frac{N}{A_c f_c} < 0.7$ ise lineer interpolasyon			
	$\frac{N}{A_c f_c} = 0.7$ ise 0			
c	$0.24 - 0.40\frac{N}{A_c f_c} \geq 0.0$			
$\frac{V_y}{V_r} \geq 0.2$; $\frac{N}{A_c f_c} \geq 0.1$; $0.0005 \leq \rho_t \leq 0.0175$ ve $\theta_p^b \geq \theta_p^a$ olmalıdır				

İlgili çalışmada [20], testlerden elde edilen θ_p^a ve θ_p^b değerleri için sargı, eksenel kuvvet, kesme kuvveti oranı ve malzeme özelliklerini içeren lineer regresyon bağıntıları elde edilmiştir. Regresyon bağıntıları ile deneysel sonuçların farkı için hazırlanan kümülatif dağılımlar esas alınarak, θ_p^a ve θ_p^b parametrelerinin deneysel değerlere göre aşılma (güvensiz durum oluşma) olasılıkları %50 ile sınırlandırılmıştır (Şekil 1b). ASCE 41-17'de dikdörtgen enkesitler için öngörülen modelleme parametreleri ve performans düzeylerine ait plastik dönme açıları Tablo 2'de verilmiştir. Bu bağıntılar donatı detayları nedeniyle aderans yetersizliği bulunmayan elemanlara ait olup, aderans yetersizlikleri bulunan elemanlar ve dairesel olan enkesitler için farklı bağıntılar öngörülmüştür [6].

Tablo 2'de; A_c brüt enkesit alanını, V_y akma (plastikleşme) momentine karşılık gelen kesme kuvvetini göstermekte ve kesit akma momentinin (M_y) kesme açıklığı L_s'ye bölünmesi ile belirlenmektedir. Akma momenti için TBDY-2018'deki tanım kullanılmıştır. ρ_t gözönüne alınan doğrultudaki enine donatı oranını göstermekte ve b enkesit genişliği olmak üzere (4) bağıntısı ile belirlenmektedir.

$$\rho_t = A_{sh}/bs \tag{4}$$

V_r kesitin kesme kuvveti taşıma kapasitesini göstermekte ve (5) bağıntısı ile belirlenmektedir.

$$V_r = k_{nl}\left[\alpha_{col}\left(\frac{A_{sh}f_yd}{s}\right) + \lambda\left(\frac{0.5\sqrt{f_c}}{M/Vd}\sqrt{1+\frac{N}{0.5A_c\sqrt{f_c}}}\right)0.8A_c\right] \tag{5}$$

Burada k_{nl} deplasman sünekliği talebine bağlı katsayıdır, çalışmada 1.0 alınmıştır. d enkesit faydalı yüksekliğini, α_{col} enine donatının etkinliğini ifade eden katsayıdır ($s/d \leq 0.75$ ise $1.0, s/d \geq 1.0$ ise 0 alınır, ara değerler için doğrusal interpolasyon uygulanır). λ beton özelliğini ifade eden katsayıdır, hafif beton için 0.75, normal beton için 1.0 alınmaktadır. M/Vd, kesite etkiyen momentin, kesme kuvveti faydalı yükseklik çarpımına oranını göstermektedir (ASCE'ye göre $2 \leq M/Vd \leq 4$ olmalıdır) [6].

Eğilme dayanımında önemli azalmanın başladığı karakteristik sınırı ifade eden θ_p^a açısının, malzeme özellikleri ile birlikte eksenel kuvvet düzeyi, sargı oranı ve kesme kuvveti düzeyine bağlı olduğu, eksenel göçmeye karşılık gelen θ_p^b açısının ise malzeme özellikleri ile birlikte eksenel kuvvet düzeyi ve sargı oranına bağlı olduğu görülmektedir (Tablo 2). ASCE'de %50'lik aşılma olasılığına karşılık gelen modelleme parametlerinin yanı sıra θ_p^a ve θ_p^b dönme açılarının %10, %25 ve %40'lık aşılma olasılıklarını sağlamaları için bu parametrelere uygulanması gereken katsayılar da verilmiştir (Tablo 3)[6]. Bu katsayılar ile farklı risk düzeyleri için değerlendirmeler yapılmasına olanak sağlanmıştır.

Tablo 3 - Farklı aşılma olasılıkları için modelleme parametresi katsayıları

| Modelleme parametresi	Aşılma olasılığı katsayısı		
	% 40 aşılma olasılığı	%25 aşılma olasılığı	%10 aşılma olasılığı
θ_p^a (rad)	0.80	0.62	0.47
θ_p^b (rad)	0.80	0.70	0.50

ASCE 41-17'de, *Hemen Kullanım* (*Immediate Occupancy*-IO), *Can Güvenliği* (*Life Safety*-LS) ve *Göçme Önleme* (*Collapse Prevention*-CP) olmak üzere üç performans düzeyi tanımlanmıştır (Şekil 3) [6]. IO ile deprem sonrası yapının kullanımını engellemeyecek düzeydeki hasar düzeyi ifade edilmektedir. Bu sınır plastik dönme açısı θ_p^a değerinin %15'i alınarak belirlenmekte ve 0.005 rad ile sınırlanmaktadır. LS ile kısmi veya toptan göçmenin başlangıcına göre belirli bir güvenliği içeren hasar düzeyi öngörülmektedir. CP ile ise düşey yüklerin taşınmaya devam ettiği ancak göçmeye karşı güvenliğin kalmadığı hasar düzeyi ifade edilmektedir. LS ve CP düzeylerine ait sınırlar, kolonun eksenel göçme sınırını ifade eden θ_p^b değerinin sırasıyla % 50'si ve % 70'i alınarak belirlenmektedir. LS düzeyine ait oran, θ_p^b açısının %10'luk, CP düzeyine ait oran θ_p^b açısının %25'lik aşılma olasılığı esas alınarak belirlenmiştir [6]. Bu aşılma olasılıkları ile tüm elemanlarda eksenel göçmeye karşı risklerin kontrol altında tutulması hedeflenmiştir. Yüksek eksenel kuvvet/kesme kuvveti, çok düşük sargı düzeyi vb. durumlarda eksenel kapasite ve eğilme kapasitesi birlikte sonlanabilmekte, bu durumda söz konusu aşılma olasılıkları aynı zamanda eğilme kapasitesi için de geçerli olmaktadır.

4. PARAMETRİK SAYISAL İNCELEME

Çalışmada, kolon hasar düzeyleri üzerinde etkili olması beklenen enkesit boyutu, eksenel kuvvet (yük) düzeyi, boyuna ve enine donatı (sargı) oranı, kesme etkisi ve beton dayanımı için parametrik incelemeler yapılmıştır. Parametrelere ait değişkenler hem mevcut yapılarda karşılaşılan bazı yetersizlikleri hem de TBDY-2018'e uygun tasarımları temsil edecek şekilde seçilmiştir. Enkesit boyutlarının etkisini gözlemek için alanları yaklaşık aynı, boyutları 1/1, 1/2 ve 1/3 oranında olan enkesitler seçilmiş ve dikdörtgen kesitlerin hem zayıf ve hem güçlü eksendeki eğilmelerini içerecek şekilde beş farklı enkesit boyutu incelenmiştir (Şekil 4). Beton basınç dayanımı için 14, 20 ve 30 MPa olmak üzere üç farklı beton kalitesi gözönüne alınmıştır. Boyuna donatı için kolon minimum ve maksimum donatı oranlarının arasını temsil edecek şekilde ρ_1=0.011, ρ_2=0.023, ρ_3=0.039 olmak üzere üç farklı alternatif incelenmiştir (Şekil 4, Tablo 4). Sargı etkisinin incelenmesi amacıyla, 3 farklı enine donatı uygulaması yapılmıştır. Uygulamaların birincisinde, sadece seyrek yerleştirilmiş dış etriye kullanılarak düşük düzeyde sargı durumu temsil edilmiş, diğer iki uygulamada ise çiroz kullanımı ve etriye özellikleri değiştirilerek orta ve yüksek düzeyde sargılama oluşturulmuştur (Şekil 4, Tablo 4).

Düşük ve orta düzeyde sargı durumları TBDY-2018'e göre yetersiz kalırken, yüksek düzeyde sargı tüm yönetmelik koşullarını sağlamaktadır. (N/f_cA_c) oranının 0.10-0.70 arasında değişen yedi farklı değeri için eksenel kuvvet etkisi incelenmiştir. Kesme kuvveti etkisinin incelenmesi amacıyla kesme açıklığı/faydalı yükseklik (a/d) oranı 3.5 ile 11.5 arasında değişen beş farklı durum gözönüne alınmıştır. Bunun için kolonların tekil yük etkisinde konsol sistem olduğu kabul edilerek her bir enkesit boyutu için sabit birer a/d değeri elde edilecek şekilde kolon boyları kullanılmıştır. S(40/40)'lık enkesit için kullanılan kolon boyları Şekil 4'de gösterilmiştir. Böylece her bir eleman boyutu için farklı düzeyde kesme etkinliklerinin incelenmesine ve farklı özelliklerdeki elemanların aynı düzeyde kesme etkisi altında karşılaştırılabilmesine olanak sağlanmıştır.

a) Düşük düzeyde sargı durumu (ρ_{t1}) için donatı detayları

b) Orta ve yüksek düzeyde sargı durumu (ρ_{t2}, ρ_{t3}) için donatı detayları

c) S(40/40)'lık enkesitte farklı a/d değerleri için kullanılan kolon boyları

Şekil 4. *Enkesit boyutları, donatı detayları ve S(40/40)'lık enkesit için kolon boyları*

Tablo 4 - Kullanılan boyuna ve enine donatılar

Kesitler	Boyuna donatı			Enine donatı					
	1	2	3	1		2		3	
				Etriye	Çiroz	Etriye	Çiroz	Etriye	Çiroz
S(25/75)/S(75/25)	*14ϕ14*	*14ϕ20*	*14ϕ26*				*5ϕ8*		*5ϕ10*
S(30/60)/S(60/30)	*12ϕ14*	*12ϕ20*	*12ϕ26*	*ϕ8/200*	-	*ϕ8/120*	*4ϕ8*	*ϕ10/60*	*4ϕ10*
S(40/40)	*12ϕ14*	*12ϕ20*	*12ϕ26*				*4ϕ8*		*4ϕ10*
Donatı oranı (%)	ρ_1	ρ_2	ρ_3	ρ_{t1}		ρ_{t2}		ρ_{t3}	
($\rho=A_s$/bh) ($\rho_t=A_{sh}$/bs)	1.10	2.30	3.90	0.07-0.20		0.33-0.50		0.98-1.57	

TBDY-2018'e göre kesme kuvvetinin hasar sınırına etkisi sadece mevcut yapıların değerlendirilmesinde gözönüne alınmakta, yeni yapılacak yapılarda bu konuda bir madde bulunmamaktadır. Mevcut yapılarda (6) bağıntısı ile tanımlanan elemandaki kesme kuvveti oranı %65'i aştığında plastik dönme açılarına ait sınırlar bir kesme katsayısı ile azaltılmaktadır.

$$V_e/bdf_{ct} \tag{6}$$

Burada V_e elemanın kesme tasarım dayanımını, f_{ct} betonun çekme dayanımını ifade etmektedir. Çalışmada V_e elemanın moment taşıma kapasitesinin (M_u) kesme açıklığına (L_s) oranı alınarak hesaplanmış, çekme dayanımı f_{ct} ise karakteristik basınç dayanımına bağlı olarak TS500 [27]'den belirlenmiştir. Elemandaki kesme kuvveti oranına göre hesaplanan kesme katsayısı Şekil 5'de gösterildiği gibi 0.5 ile 1.0 arasında lineer olarak değişmektedir. Çalışmada incelenen elemanlardaki kesme kuvveti oranları (a/d)'ye bağlı olarak Şekil 5'de verilmiştir. Grafikten görüldüğü gibi, a/d oranının küçülmesiyle TBDY'deki kesme katsayısının etkinliği ve uygulandığı eleman sayısı önemli ölçüde artmıştır (Şekil 5). Yeni yapılacak yapılarda kesme katsayısı uygulaması bulunmaması nedeniyle TBDY-2018 tasarım koşullarını sağlayan elemanlarda, kesme katsayısı içermeyen hasar sınırları da belirlenerek ASCE ile ayrıca karşılaştırılmıştır.
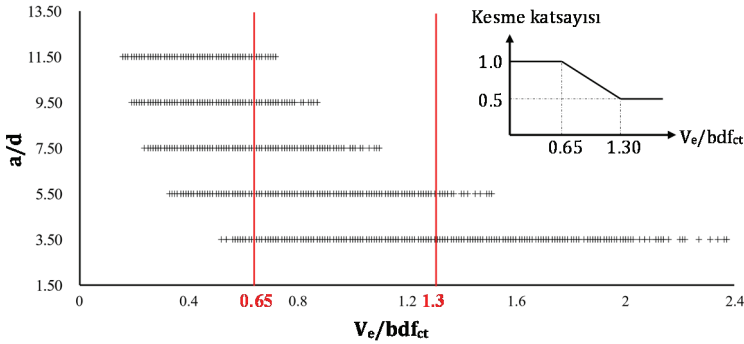
Şekil 5 - İncelenen elemanlarda TBDY-2018'e göre kesme kuvveti düzeyinin ve kesme katsayısının değişimi

TBDY-2018'e göre hasar sınırlarının hesabı için gerekli moment-eğrilik analizlerinde beton ve donatı için yönetmelikte önerilen modeller kullanılmıştır [1]. Çalışmada incelenen üç farklı sargı durumu için S(40/40) enkesitinde elde edilen sargılı beton hesap modelleri ile sargısız beton modeli ve boyuna donatı modeli Şekil 6'da örnek olarak gösterilmiştir.

a) Beton (S40/40, f_c=20MPa) b) Betonarme donatı çeliği (B420C)
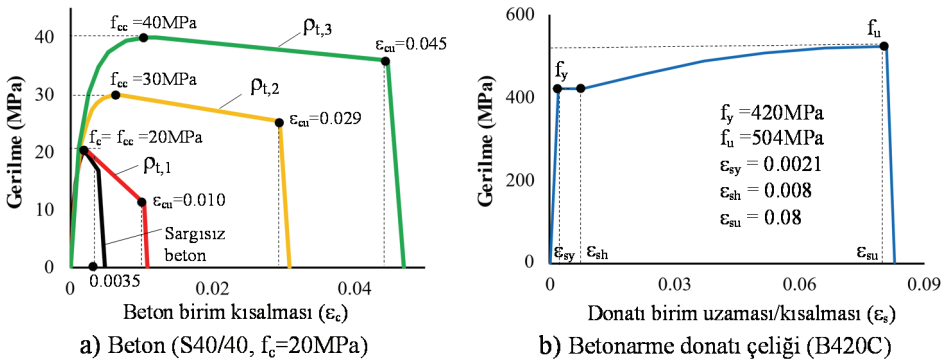
Şekil 6 - S(40/40) enkesiti için kullanılan beton ve boyuna donatı hesap modelleri

Çalışma kapsamında 5 farklı enkesit, 7 eksenel kuvvet düzeyi, 5 kesme kuvveti düzeyi, 3 sargı oranı, 3 boyuna donatı oranı ve 3 farklı beton dayanımı için yapılan kombinasyonlar sonucunda 4725 kolon elemanı oluşturulmuş ve ilgili beton/donatı modelleri kullanılarak moment-eğrilik analizleri gerçekleştirilmiştir. Kesit analizleri için çalışma kapsamında geliştirilen excel tabanlı yazılım kullanılmıştır. ρ_2=0.023'lük boyuna donatı oranına sahip S(40/40) kesiti üzerinde üç farklı sargı durumu ve üç farklı eksenel kuvvet düzeyi için elde edilen moment-eğrilik bağıntıları Şekil 7'de verilmiştir. Ayrıca beş farklı enkesit boyutu için N/f_cA_c=0.40'lık eksenel kuvvet düzeyinde elde edilen moment-eğrilik bağıntıları Şekil 7'de karşılaştırılmıştır. Her bir grafikte TBDY'deki *Göçmenin Önlenmesi* (GÖ) sınırına ait eğrilik değeri (ϕ_u) işaretlenmiş ve söz konusu eğriliğin belirlenmesinde etkili olan malzeme birim şekildeğiştirmesi ($\varepsilon_c^{GÖ}$ veya $\varepsilon_s^{GÖ}$) de belirtilmiştir.

a) $\rho_{t,1}$ için farklı eksenel yük düzeyleri

b) $\rho_{t,2}$ için farklı eksenel yük düzeyleri

c) $\rho_{t,3}$ için farklı eksenel yük düzeyleri

d) Farklı kesit boyutları için
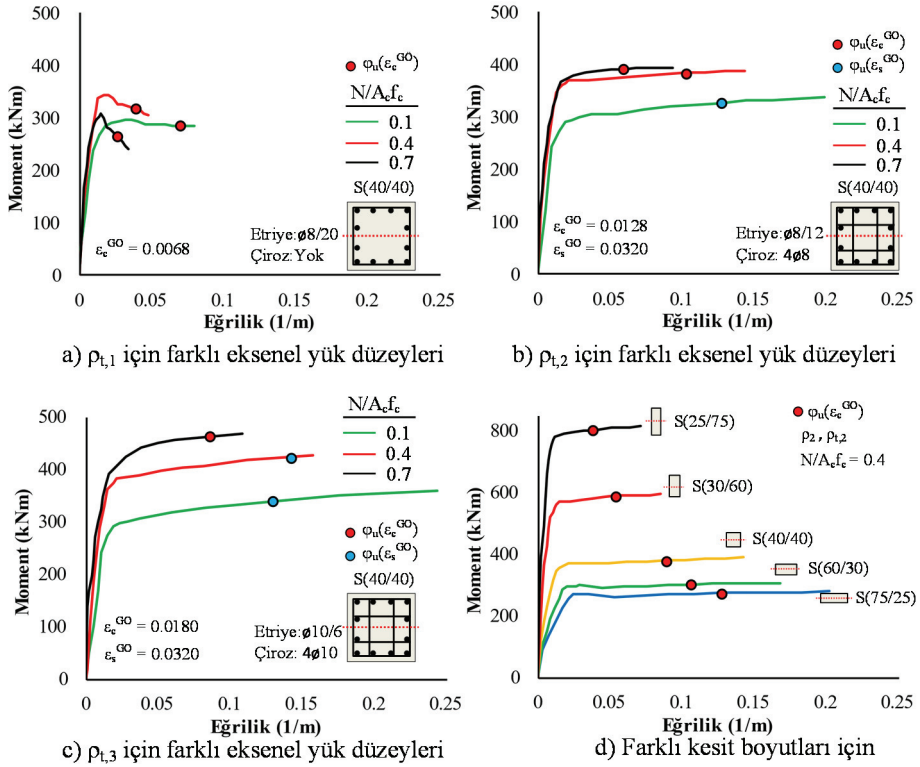
Şekil 7 - Farklı sargı düzeyi, eksenel kuvvet düzeyi ve enkesit boyutları için moment-eğrilik bağıntıları ve TBDY-2018'e göre Göçmenin Önlenmesi sınır eğrilikleri (f_c=20 MPa, a/s=7.5, ρ_2 için)

ASCE modelleme parametreleri kullanılarak çeşitli kolon elemanları için moment-plastik dönme bağıntıları (ideal-plastik kabulü ile) oluşturulmuş ve bunlar üzerinde TBDY'den elde edilen KH ve GÖ performans düzeyi sınırları işaretlenerek Şekil 8-10'da gösterilmiştir. Bu grafiklerde, her bir parametrenin (enkesit boyutu, eksenel kuvvet düzeyi vb.) ve parametreler

a) a/d=11.5 için   b) a/d=3.5 için
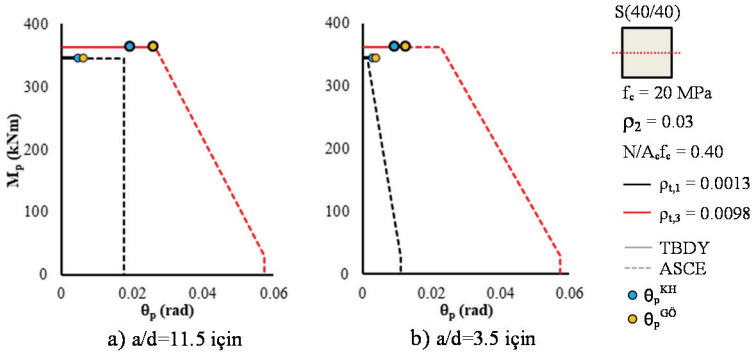
Şekil 8 - Kesme kuvveti düzeyi (a/d) ve sargı oranının ASCE modelleme parametreleri ve TBDY θ_p^{KH}, $\theta_p^{GÖ}$ değerleri üzerindeki etkisi

a) Farklı malzeme dayanımları için   b) Farklı eksenel yük düzeyleri için

c) Farklı donatı oranları için   d) Farklı kesit tipleri için
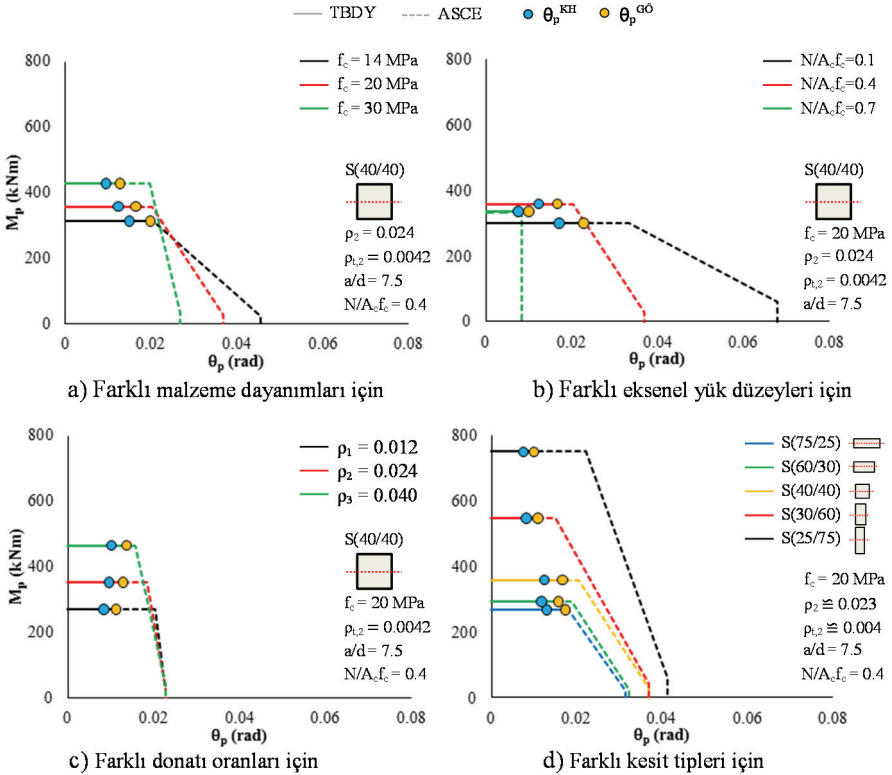
Şekil 9 - Beton dayanımı, eksenel kuvvet düzeyi, boyuna donatı oranı ve kesit boyutunun ASCE modelleme parametreleri ve TBDY θ_p^{KH}, $\theta_p^{GÖ}$ değerleri üzerindeki etkisi

için seçilen değişkenlerin moment-plastik dönme davranışına etkileri gözlenebilmektedir. ASCE'de eksenel göçmeye karşılık gelen karakteristik sınırın referans alınması nedeniyle, yeterli sargı donatısı bulunan ve düşük eksenel kuvvete maruz elemanlarda, dayanım azalmalarına rağmen eğilme kapasitesi sınırının ötesinde önemli bir dönme kapasitesi artışı sağlandığı, buna karşılık düşük düzeyde sargılı ve yüksek eksenel kuvvete maruz elemanlarda eğilme kapasitesi ile birlikte eksenel kapasitenin de sonlandığı görülmektedir (Şekil 8-10).
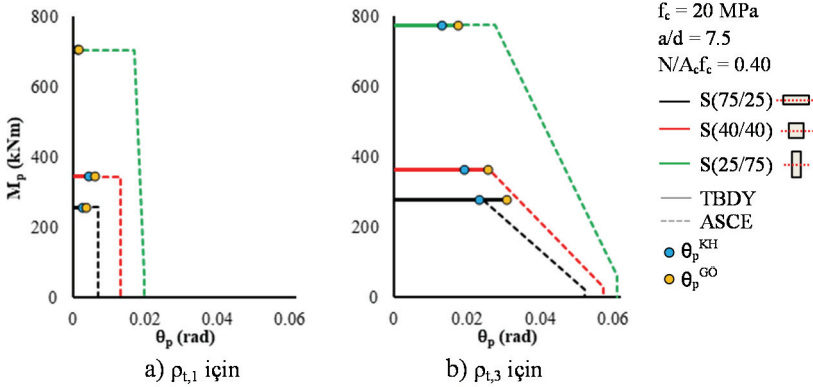

Şekil 10 - Sargı oranı ve kesit boyutunun ASCE modelleme parametreleri ve TBDY θ_p^{KH}, $\theta_p^{GÖ}$ değerleri üzerindeki etkisi

4.1. TBDY $\theta_p^{GÖ}$ ve ASCE θ_p^{a} Dönme Açılarının Karşılaştırılması

Bu bölümde, gözönüne alınan parametrelerin ASCE ve TBDY'den elde edilen dönme açıları üzerindeki etkileri karşılaştırmalı olarak değerlendirilmiş ve iki yaklaşım arasında önemli farklılığa sebep olan parametreler ortaya konmuştur. ASCE ve TBDY'de esas alınan performans düzeyi (hasar sınırı) tanımlarında önemli farklılıklar bulunması nedeniyle karşılaştırmalar, her iki yaklaşımda da benzer karakteristik sınırı ifade eden TBDY $\theta_p^{GÖ}$ ve ASCE θ_p^{a} dönme açıları için yapılmıştır.

4.1.1. Eksenel Kuvvet Etkisi

TBDY $\theta_p^{GÖ}$ ve ASCE θ_p^{a} dönme açılarının eksenel kuvvet düzeyine göre değişimleri, f_c=20MPa, a/d =7.5 ve S(40/40) özelliklerindeki kolon elemanları için Şekil 11'de karşılaştırılmıştır. Grafiklerde her bir eksenel kuvvet düzeyi için üç farklı enine donatı (sargı) ve boyuna donatı oranına ait sonuçlar gösterilmiştir. Genel olarak eksenel kuvvet değişiminin plastik dönme açıları üzerindeki etkisi ASCE'de TBDY'ye göre çok daha belirgin olmuştur. ASCE θ_p^{a} dönme açısı eksenel kuvvet etkisi ile hemen hemen lineer değişim göstermiş ve beklendiği gibi eksenel kuvvet oranı arttıkça azalmıştır (Şekil 11). Kesit boyutu ve diğer parametreler bu eğilimi değiştirmemiştir.
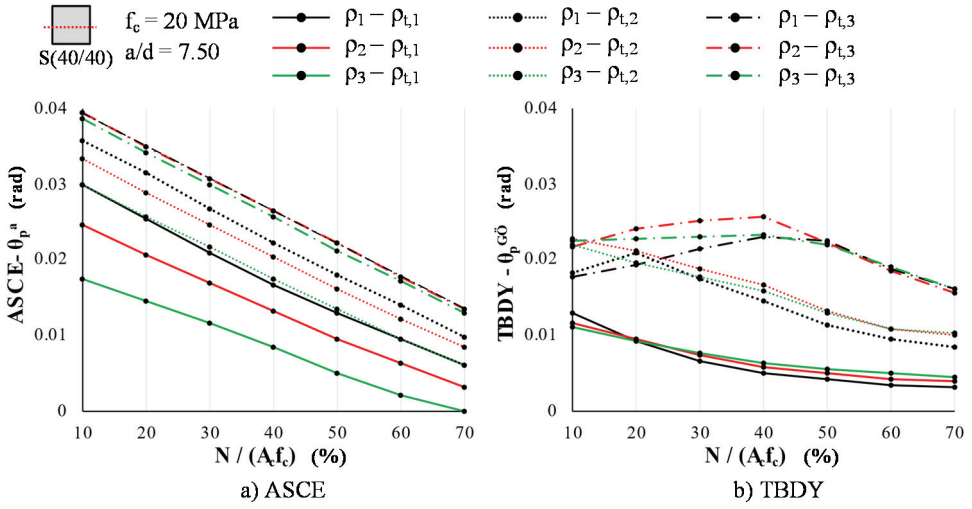
Şekil 11 - Eksenel kuvvet düzeyinin θ_p^a ve $\theta_p^{GÖ}$ üzerindeki etkisinin karşılaştırılması

TBDY $\theta_p^{GÖ}$ açısının eksenel kuvvet düzeyi ile değişimi ise, orta ve düşük düzeyde sargı durumunda ASCE ile benzer eğilim göstermiştir. Ancak yüksek sargı durumunda ve 0.40'lık eksenel kuvvet düzeyinin altında eğilim önemli ölçüde değişmiştir (Şekil 11b). Düşük eksenel kuvvet düzeylerinde *Göçmenin Önlenmesi* sınırına ait eğrilikte, yüksek sargı nedeniyle beton yerine donatı birim şekildeğiştirme sınırı ($\varepsilon_s^{GÖ}$) belirleyici olmuş, bu da TBDY $\theta_p^{GÖ}$ açısını azaltmıştır. Bu nedenle bu özellikteki elemanlarda TBDY ve ASCE dönme açıları arasındaki fark önemli ölçüde artmıştır.

Boyuna donatı oranının dönme açıları üzerindeki etkisi değerlendirildiğinde; her iki yaklaşımda da sargı düzeyi belirleyici olmuş, ancak ASCE'de sargı oranı artıkça boyuna donatının dönme açıları üzerindeki etkinliği önemli ölçüde azalırken, TBDY'de genel olarak bunun tersi eğilim gerçekleşmiştir (Şekil 11). Bu eğilim farkı diğer tüm parametrelere ait sonuçlarda da benzer şekilde gözlenmiştir.

4.1.2. Enkesit Boyutunun Etkisi

TBDY $\theta_p^{GÖ}$ ve ASCE θ_p^a dönme açılarının enkesit boyutlarına göre değişimleri, f_c=20MPa, a/d=7.5 ve N/A_cF_c=0.40 özelliklerindeki kolonlar için Şekil 12'de karşılaştırılmıştır. Grafiklerde her bir enkesit boyutu için üç farklı boyuna donatı ve enine donatı (sargı) oranına ait sonuçlar gösterilmiştir. ASCE ve TBDY arasındaki önemli farklardan birisi enkesit değişiminde görülmektedir. Eğilme doğrultusundaki enkesit yüksekliğinin artması ASCE'de θ_p^a açısını genel olarak arttırırken, TBDY'deki $\theta_p^{GÖ}$ açısında azalışa sebep olmuştur. Ancak bu eğilimler üzerinde sargı düzeyi oldukça etkili olmuştur (Şekil 12).
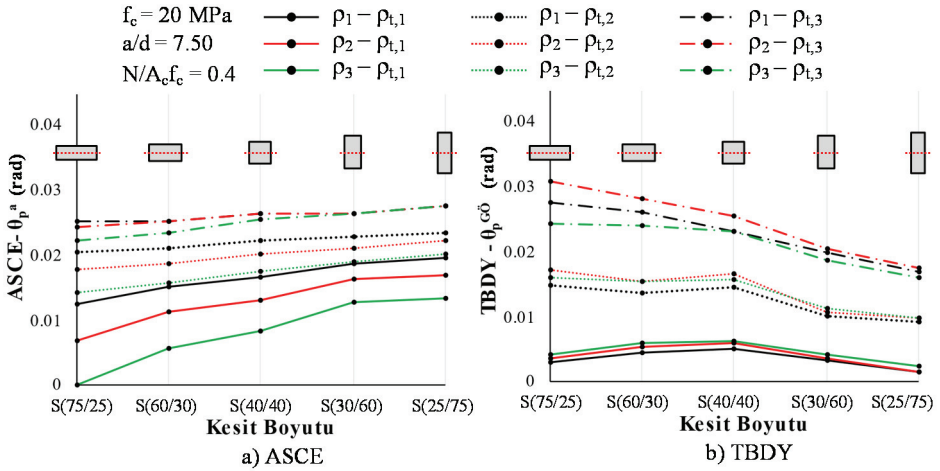
Şekil 12 - Enkesit boyutlarının θ_p^a ve $\theta_p^{G\ddot{O}}$ üzerindeki etkisinin karşılaştırılması

ASCE'de sargı düzeyinin artması enkesit değişiminin etkisini azaltmış, hatta en yüksek sargı durumunda hemen hemen değişim olmamıştır (Şekil 12a). ASCE yaklaşımında bu eğilimin oluşmasında kesme düzeyini temsil eden (V_y/V_r) oranı belirleyici olmuştur. TBDY'de ise kesit yüksekliği ile $\theta_p^{G\ddot{O}}$ değerindeki değişim, özellikle en düşük sargı durumunda farklılık göstermiştir (Şekil 12b). TBDY yaklaşımındaki eğilimin oluşmasında donatı sıyrılması nedeniyle ilave edilen dönme açısı belirleyici olmuştur. Bu amaçla kullanılan amprik bağıntıdaki enkesit eğriliği (ϕ_u), kesit yüksekliği artışına bağlı olarak azalmış, bu da plastik dönme açısını özellikle yüksek sargılı durumda önemli ölçüde azaltmıştır.

4.1.3. Kesme Kuvveti Etkisi

Kesme kuvveti düzeyinin etkisini gözlemek amacıyla, f_c=20MPa, N/A_cf_c=0.40, S(40/40) özelliklerindeki elemanlarda TBDY $\theta_p^{G\ddot{O}}$ ve ASCE θ_p^a açılarının a/d oranına göre değişimleri Şekil 13'de karşılaştırılmıştır. $\theta_p^{G\ddot{O}}$ değerleri, TBDY'de mevcut yapılar için öngörülen kesme katsayısı uygulanarak elde edilmiştir. ASCE'deki θ_p^a dönme açısı kesme kuvveti düzeyini içeren bir denklem ile belirlendiğinden, a/d değeri büyüdükçe genel olarak θ_p^a değeri de artmaktadır (Şekil 13a). Ancak bu değişimin önemli ölçüde sargı düzeyine bağlı olduğu görülmektedir. Yüksek düzeyde sargı durumunda kesmenin daha az etkili olduğu, sargı düzeyi azaldıkça kesmenin θ_p^a üzerindeki etkisinin önemli ölçüde arttığı gözlenmektedir. TBDY'deki kesme katsayısı, a/d oranının 9.5'dan küçük değerleri için etkili olarak $\theta_p^{G\ddot{O}}$ değerini azaltmış, ancak ASCE'dekinin tersine, sargı düzeyi yüksek olan kesitlerde dönme açısı kesme katsayısı ile daha fazla azalırken, sargı düzeyi azaldıkça dönme kapasitesindeki değişim oranı düşmüştür.

TBDY-2018'e göre tasarlanan yeni bina elemanlarında kesme katsayısı uygulaması bulunmaması nedeniyle, çalışma kapsamında incelenen kolon elemanlarda beton dayanımı,
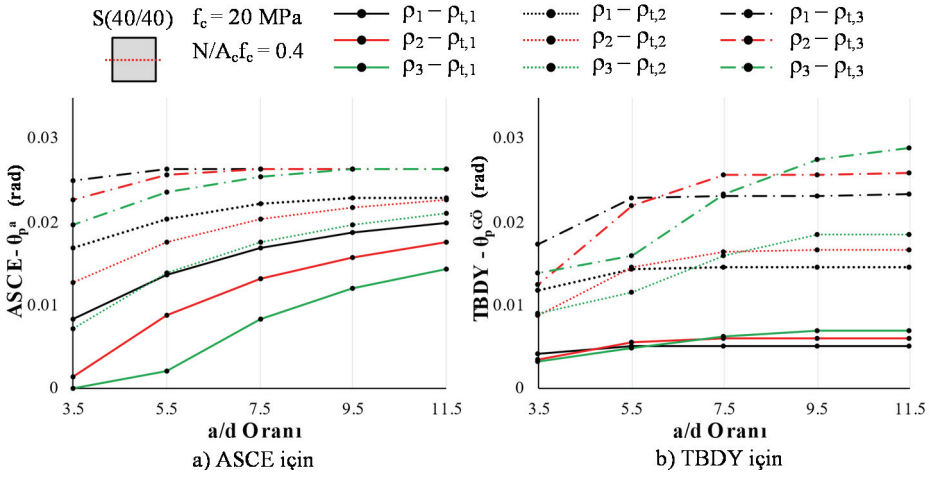
Şekil 13 - Kesme kuvveti düzeyinin $\theta_p^{G\ddot{O}}$ ve θ_p^a üzerindeki etkisinin karşılaştırılması
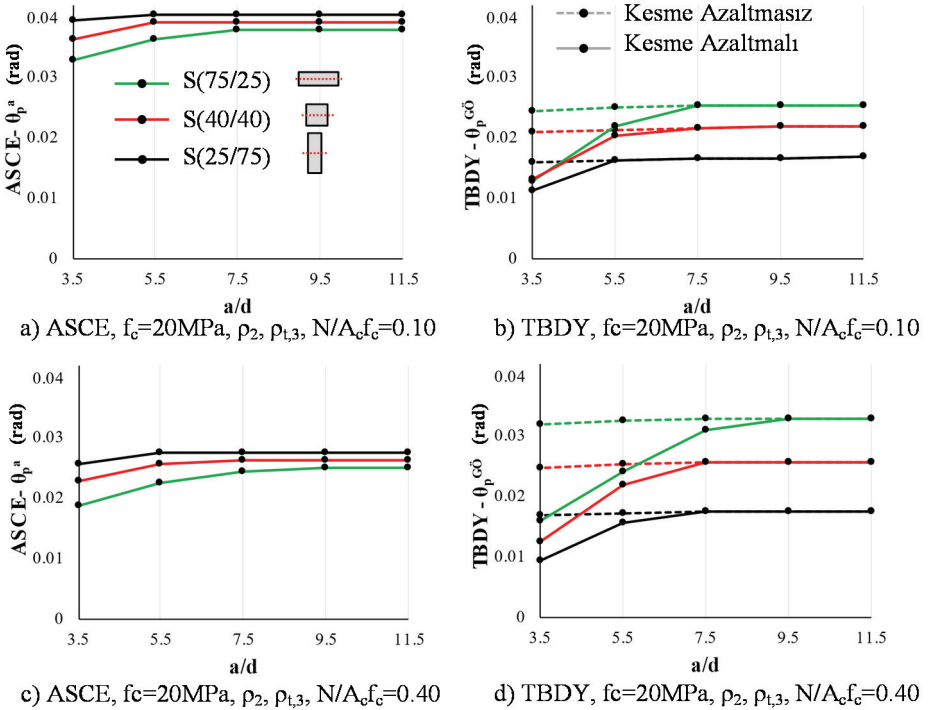
Şekil 14 - TBDY-2018 tasarım koşullarını sağlayan elemanlarda kesmenin $\theta_p^{G\ddot{O}}$ ve θ_p^a üzerindeki etkisinin karşılaştırılması

sargı oranı ve eksenel yük düzeyi bakımından TBDY-2018 tasarım koşullarını sağlayan elemanlar için kesme etkisi ayrıca değerlendirilmiştir. Bunun için örnek olarak üç farklı enkesit boyutu ve iki farklı eksenel yük düzeyi için kesme katsayısı uygulanarak ve uygulanmaksızın elde edilen $\theta_p^{GÖ}$ değerleri ASCE ile karşılaştırılmıştır (Şekil 14). TBDY-2018 ile uyumlu elemanlarda dahi yüksek kesme kuvveti oranları için (a/d≤5.5) ASCE plastik dönme açılarında azalma olduğu ve eksenel kuvvet düzeyine bağlı olarak kesmenin etkinliğinin arttığı gözlenmektedir (Şekil 14). TBDY'de mevcut binalar için kullanılan kesme katsayısının tasarım koşullarını sağlayan elemanlarda uygulanması durumunda ise dönme açılarındaki azalmanın ASCE'dekine oranla çok daha fazla olduğu görülmektedir (Şekil 14).

4.1.4. Beton Dayanımının Etkisi

Çalışmada göz önüne alınan üç farklı beton dayanımı için elde edilen sonuçlar, S(40/40) N/A$_c$f$_c$=0.40 ve a/d=7.5 özelliklerindeki elemanlar için Şekil 15'de karşılaştırılmıştır. Beton dayanımı değişiminin ASCE θ_p^a plastik dönme açısı üzerinde önemli bir etki yapmadığı, buna karşılık TBDY $\theta_p^{GÖ}$ dönme açısı üzerinde sargı düzeyine de bağlı olarak etkili olabildiği görülmektedir (Şekil 15). Özellikle orta düzeyli sargı durumunda, beton dayanımı artışına bağlı olarak TBDY $\theta_p^{GÖ}$ dönme açılarında önemli azalma gerçekleşmiştir.
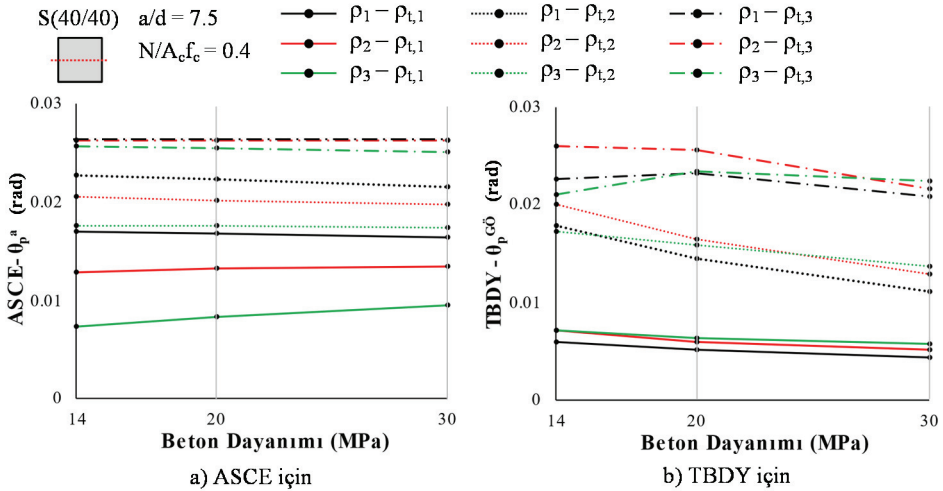
Şekil 15 - Beton dayanımının $\theta_p^{GÖ}$ ve θ_p^a üzerindeki etkisinin karşılaştırılması

4.2. ASCE41-17 Referans Alınarak TBDY Performans Düzeylerinin Değerlendirilmesi

Bu bölümde, farklı özelliklerdeki 4725 kolon elemanı için elde edilen TBDY $\theta_p^{GÖ}$ ve θ_p^{KH} değerleri, ASCE'de karakteristik dönme açıları için verilen aşılma olasılığı sınırları ile karşılaştırılarak değerlendirilmiştir. Değerlendirmelerde, ASCE'ye göre %50'lik aşılma olasılığı için verilen modelleme parametrelerinin (θ_p^a ve θ_p^b) yanı sıra Tablo 3'deki katsayılar

kullanılarak belirlenen %10, %25 ve %40'lık aşılma olasılıklarına karşılık gelen sınırlar ($\theta_p^{a,\%10}, \theta_p^{a,\%25}, \theta_p^{a,\%40}$ ve $\theta_p^{b,\%10}, \theta_p^{b,\%25}, \theta_p^{b,\%40}$) ve ASCE'de en düşük hasar düzeyini temsil eden *Hemen Kullanım* (IO) performans düzeyine karşılık gelen sınır da gözönüne alınmıştır.

ASCE'de eğilme kapasitesine ait karakteristik sınırı ifade eden plastik dönme açısı θ_p^a ile TBDY'deki $\theta_p^{G\ddot{O}}$ ve θ_p^{KH} dönme açılarının karşılaştırılması Şekil 16'da verilmiştir. Bu grafiğe göre, %50'lik sınırın (siyah çizgi) üzerindeki noktaların temsil ettiği elemanlarda TBDY ve ASCE değerlerinin eşit olduğu, bu sınırın altında kalan elemanlarda ise TBDY $\theta_p^{G\ddot{O}}$ değerlerinin, ASCE'de öngörülen %50'lik aşılma olasılığı düzeyini sağlayamacağı ifade edilebilmektedir. TBDY'ye göre hesaplanan $\theta_p^{G\ddot{O}}$ değerlerinin %83'ü ve θ_p^{KH} değerlerinin %93'ü, % 50'lik aşılma olasılığını sağlamıştır (Şekil 16a,b). TBDY ile belirlenen her iki dönme açısı için de %50'lik olasılığı sağlamayan elemanların çok büyük bir bölümünü eksenel yük düzeyi N/A$_c$f$_c$ =0.60-0.70 olan ve zayıf ekseninde eğilmeye maruz dikdörtgen enkesitli (60/30 ve 75/25) elemanlar oluşturmuştur (Şekil 16a,b). İncelenen elemanların, $\theta_p^{G\ddot{O}}$ değerleri için %33'ünde ve θ_p^{KH} değerleri için %53'ünde, ASCE'deki %10'luk aşılma olasılığı sınırının da altında kaldığı görülmektedir. Hatta sınırlı sayıda (%4) elemanda, TBDY'ye göre ileri hasar düzeylerini tanımlayan $\theta_p^{G\ddot{O}}$ ve θ_p^{KH} dönme açılarının, ASCE'deki en düşük hasar düzeyi olan *Hemen Kullanım* sınırının (θ_p^{IO}) da altında olduğu görülmektedir (Şekil 16a,b). Bu elemanların da büyük bölümünü düşük eksenel yüke ve güçlü eksende eğilmeye maruz elemanlar oluşturmuştur (Şekil 16a,b).


a) TBDY - $\theta_p^{G\ddot{O}}$ için

b) TBDY - θ_p^{KH} için
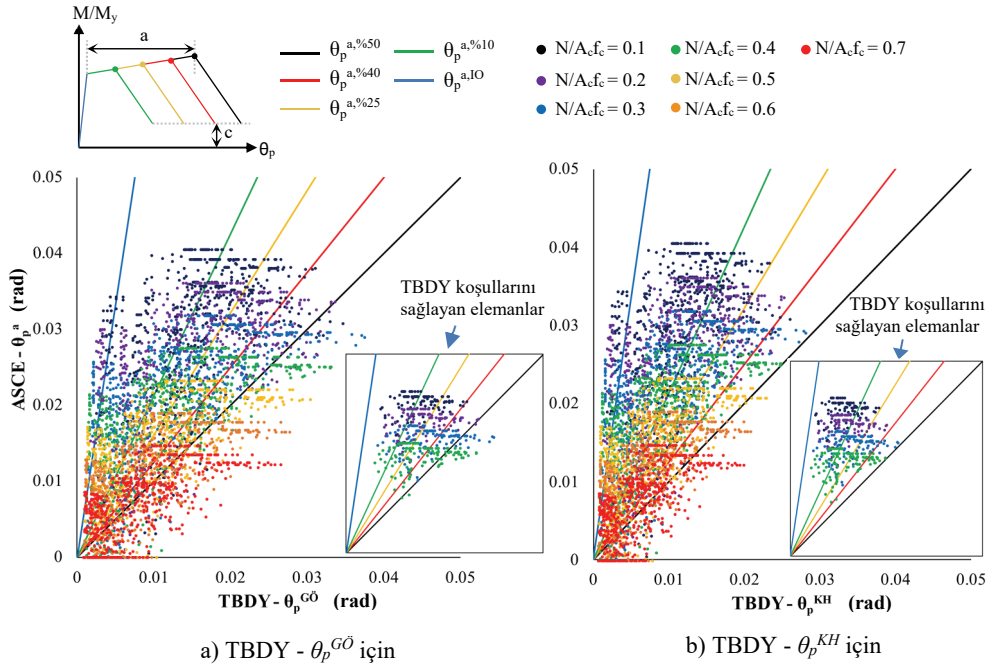
Şekil 16 - Tüm kesitler için TBDY $\theta_p^{G\ddot{O}}$ ve θ_p^{KH} ile ASCE θ_p^a değerlerinin karşılaştırılması

Tüm elemanların karşılaştırıldığı grafiklerde, eksenel yük düzeyi, sargı donatısı detayları ve beton dayanımı bakımından TBDY-2018'e uygun olmayan elemanlar çıkarılarak, sadece güncel tasarım koşullarını sağlayan 600 elemanın karşılaştırması grafik içinde ayrıca gösterilmiştir (Şekil 16). Bu tür elemanlar için TBDY'deki $\theta_p^{G\ddot{O}}$ dönme açısının genel olarak, ASCE θ_p^a plastik dönme açısına göre daha düşük elde edildiği, sadece zayıf ekseninde eğilmeye maruz S(75/25) ve S(60/30) boyutlarındaki 51(%8) elemanda %50'lik aşılma olasılığının sağlanamadığı görülmektedir. TBDY'deki θ_p^{KH} dönme açısı için ise 35(%6) elemanda %40'lık sınırın aşıldığı görülmektedir. $\theta_p^{G\ddot{O}}$ açısı için incelenen elemanların yaklaşık yarısında, θ_p^{KH} açısı için yaklaşık ¾'ünde ASCE'deki % 25'lik aşılma olasılığı sınırının sağlandığı görülmektedir (Şekil 16).

ASCE olasılıksal sınırlarına göre risk düzeyi yüksek ve aşırı güvenli elemanların özelliklerini ortaya koymak amacıyla her bir parametreye ait değişkenler için ASCE'deki $\theta_p^{a,\%40}$ sınırını aşan ve $\theta_p^{a,\%10}$ sınırının altında kalan eleman sayıları ($n^{\theta_p^{G\ddot{O}}>\theta_p^{a,\%40}}, n^{\theta_p^{G\ddot{O}}<\theta_p^{a,\%10}}$) ilgili parametreye/değişkene ait toplam eleman sayılarına (n^T) oranlanarak Şekil 17-18'de gösterilmiştir. Örneğin, N/A$_c$f$_c$=0.10'luk eksenel yük düzeyine maruz toplam 675 eleman içinde %40'lık aşılma olasılığını sağlamayan eleman oranı %13 (88/675) elde edilirken, 0.70'lik eksenel yük düzeyi için bu oran %70 (473/675) olarak elde edilmiştir. Bu grafiklerden, her bir parametrenin birbirine göre etkinlikleri ve gözönüne alınan değişkenlerin etkisi gözlenebilmektedir. Buna göre, tüm parametrelerdeki değişimin etkili olduğu görülmekle birlikte, enkesit boyutu ve eksenel yük düzeyi en belirleyici parametreler olmuştur (Şekil 17-18).

Eğilme doğrultusundaki enkesit yüksekliği azaldıkça %40'lık aşılma olasılığını sağlamayan eleman sayısının arttığı, buna paralel olarak %10'luk olasılığı aşmayan aşırı güvenli eleman sayısının azaldığı görülmektedir. Benzer şekilde eksenel yük düzeyi arttıkça %40'lık aşılma olasılığını sağlamayan eleman sayısı artmış, %10'luk olasılığı aşmayan eleman sayısı azalmıştır (Şekil 17-18). Kesme kuvveti düzeyi artışı, beton dayanımının azalışı ve boyuna donatı oranının artışı da yüksek riskli eleman sayısını belirli ölçüde artırıcı etki yapmıştır. Sargı oranı bakımından ise düşük düzeyli sargının belirgin olarak aşırı güvenli eleman sayısında artışa sebep olduğu görülmüştür (Şekil 17-18).
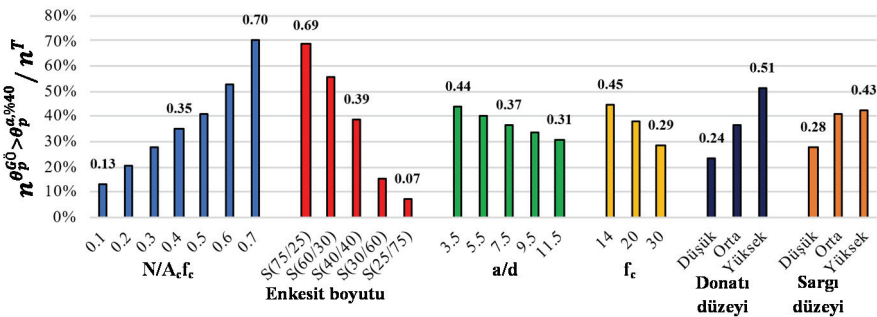
Şekil 17 - ASCE olasılıksal sınırlarına göre yüksek riskli ($\theta_p^{G\ddot{O}} > \theta_p^{a,\%40}$) eleman sayılarının oransal karşılaştırılması
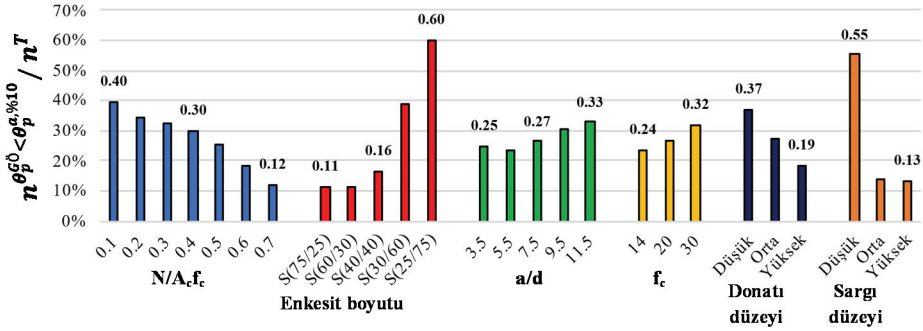
Şekil 18 - ASCE olasılıksal sınırlarına göre aşırı güvenli ($\theta_p^{GÖ} < \theta_p^{a,\%10}$) eleman sayılarının oransal karşılaştırılması

a) TBDY - $\theta_p^{GÖ}$ için   b) TBDY - θ_p^{KH} için
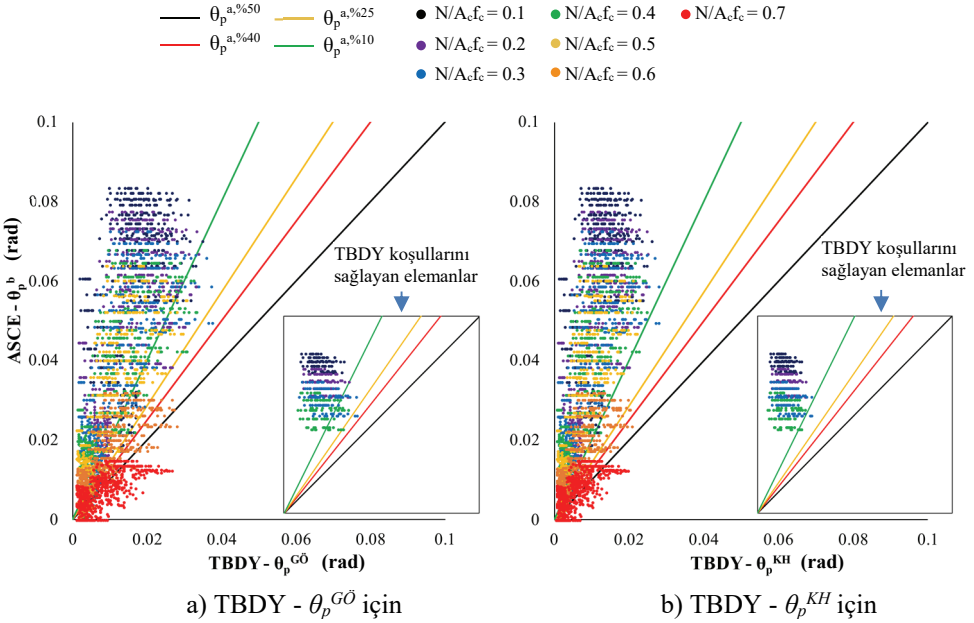
Şekil 19 - Tüm kesitler için TBDY $\theta_p^{GÖ}$ve θ_p^{KH} ile ASCE θ_p^b değerlerinin karşılaştırılması

ASCE'de eksenel yük taşıma kapasitesinin sonlandığı (eksenel göçme) sınırı ifade eden θ_p^b değerleri ile TBDY'deki $\theta_p^{GÖ}$ ve θ_p^{KH} sınırları tüm kesitler için Şekil 19'da karşılaştırılmıştır. Bu karşılaştırma ile ASCE sınırları referans alınarak TBDY'deki *Kontrollü Hasar* (KH) ve *Göçmenin Önlenmesi* (GÖ) sınırlarının eksenel göçmeye göre güvenilirlikleri

değerlendirilmiştir. TBDY $\theta_p^{GÖ}$ ve θ_p^{KH} dönme açıları için %50'lik aşılma olasılığının sağlanamadığı elemanların sayısı sırasıyla 378 ve 204 olarak belirlenmiştir. Bu elemanların hemen hemen tamamının N/A$_c$f$_c$=0.70'lik eksenel yük düzeyinde olduğu görülmektedir (Şekil 19). $\theta_p^{GÖ}$ açısı için elde edilen değerlerin %85'i, %25'lik aşılma olasılığını sağlamıştır. Bu sınırın aynı zamanda ASCE'deki *Göçme Önlenme* (CP) performans düzeyini ifade ettiği gözönünde bulundurulduğunda, TBDY'deki GÖ sınırının büyük ölçüde olasılıksal ASCE CP şartını da sağladığı ifade edilebilmektedir. Bununla birlikte, özellikle yüksek eksenel yüke maruz %8 oranında eleman için %50'lik olasılıksal sınırın dahi sağlanamadığı belirlenmiştir.

ASCE 41-17'de *Can Güvenliği* (LS) performans düzeyi için tanımlanan plastik dönme açısı (θ_p^{LS}), eksenel göçmeye göre %10'luk aşılma olasılığı öngörülerek belirlenmektedir. Buna göre TBDY'deki KH sınırı ile ASCE'deki LS sınırı (Şekil 19b yeşil çizgi) karşılaştırıldığında; incelenen elemanların %83'ünde, TBDY'de öngörülen *Kontrollü Hasar* sınırının eksenel göçmeye göre %10'luk aşılma olasılığını sağladığı görülmektedir. Ancak yüksek eksenel yüke maruz %4 oranında elemanda, %50'lik olasıksal sınırın dahi sağlanamadığı belirlenmiştir.

TBDY-2018 tasarım koşullarını sağlayan elemanlar bakımından değerlendirildiğinde; TBDY'deki $\theta_p^{GÖ}$ dönme açısı için hemen hemen tüm elemanlarda eksenel göçmeye göre %25'lik aşılma olasılığının sağlandığı, TBDY'deki θ_p^{KH} dönme açısı için ise eksenel göçmeye göre %10'luk aşılma olasılığının sağlandığı görülmektedir (Şekil 19). Buna göre TBDY-2018 uyumlu elemanlarda TBDY'deki KH sınırının, ASCE'de LS sınırı için öngörülen risk düzeyini sağladığı ifade edilebilmektedir. Bununla birlikte, TBDY'deki θ_p^{KH} ve $\theta_p^{GÖ}$ dönme açılarının çok büyük bölümünün %10'luk aşılma olasılığından çok daha güvenli olduğu görülmektedir. Aşırı güvenli olan bu elemanların çoğunluğunu düşük eksenel yüke ve güçlü eksende eğilmeye maruz kolonlar oluşturmuştur.

5. SONUÇLAR VE ÖNERİLER

TBDY-2018'de plastik dönme açısını esas alan performans düzeyleri (hasar sınırları), ASCE/SEI 41-17'deki aşılma olasılığı esaslı kolon performans kriterleri ile karşılaştırılarak değerlendirilmiştir. Çalışmada enkesit boyutu, eksenel kuvvet ve kesme kuvveti düzeyi, sargı donatısı oranı, boyuna donatı oranı ve beton dayanımı bakımından farklı özelliklerdeki kolon örneklerine ait karakteristik plastik dönme açıları üzerinde sayısal karşılaştırmalar yapılmıştır.

Her iki standartda da eğilme kapasitesine ait karakteristik sınırı ifade eden TBDY $\theta_p^{GÖ}$ ve ASCE θ_p^a dönme açılarının karşılaştırmasından aşağıdaki sonuçlara ulaşılmıştır.

- Çalışma kapsamında incelenen elemanların çok büyük bölümü (%83) için TBDY plastik dönme açıları ($\theta_p^{GÖ}$), ASCE'dekilere (θ_p^a) göre daha düşük elde edilmiştir.

- İncelenen tüm parametreler dönme açıları üzerinde farklı düzeylerde etkili olmakla birlikte, iki standart arasındaki önemli farkların oluşmasında enkesit boyutunun ve eksenel yük düzeyinin etkisi belirleyici olmuştur. Genel olarak, düşük eksenel yük ve güçlü eksende eğilmeye maruz elemanlarda TBDY, ASCE'ye göre çok daha düşük dönme açıları verirken,

yüksek eksenel yüke ve zayıf eksende eğilmeye maruz elemanlarda daha büyük dönme açıları vermiştir.

• Sargı düzeyinin ve boyuna donatı oranının dönme açıları üzerindeki etkinliği bakımından TBDY ve ASCE sonuçları arasında önemli eğilim farkları gözlenmiştir. ASCE'de sargı oranı arttıkça boyuna donatı oranının dönme açıları üzerindeki etkinliği önemli ölçüde azalırken, TBDY'de genel bunun tersi eğilim gerçekleşmiştir.

• TBDY ve ASCE yaklaşımları arasındaki farkların oluşmasında, TBDY'de donatı sıyrılmasını temsil eden amprik ifadenin, ASCE'de ise kesme düzeyini temsil eden ifadenin önemli derecede etkili olduğu belirlenmiştir. Diğer bir etken de, yüksek düzeyde sargılı ve düşük eksenel yüke maruz elemanlarda, TBDY dönme açılarının belirlenmesinde beton kısalması yerine donatı uzamasının etkili olarak dönme açılarını azaltmış olmasıdır. Bu tür elemanlarda, ASCE'de gözönüne alınan bağıntı gereği eksenel yük azalmasıyla orantılı olarak dönme kapasitelerinde artış görülürken, TBDY'ye göre elde edilen dönme açılarında ise azalma görülmüştür.

• TBDY'de mevcut yapılar için yüksek kesme kuvveti durumunda uygulanması öngörülen kesme katsayısı yaklaşımı, dönme açıları üzerinde ASCE ile benzer eğilimleri sağlamakla birlikte, sargı etkisini içermemesi nedeniyle, dönme açılarındaki kesme etkisinin mertebesi bakımından iki yaklaşım arasında önemli farklılıklara sebep olmuştur. Ayrıca TBDY-2018'e göre, yeni yapılacak bina elemanlarında kesme etkisinin gözönüne alınmamasına karşın, ASCE'ye göre, yüksek kesme etkisi altındaki elemanlarda TBDY-2018 tasarım koşulları sağlansa dahi dönme kapasitelerinin azaldığı belirlenmiştir.

TBDY performans düzeyleri için ASCE'deki aşılma olasılıkları referans alınarak yapılan değerlendirmelerden aşağıdaki sonuçlara ulaşılmıştır.

• ASCE'de, eğilme kapasitesine ait karakteristik sınırı ifade eden plastik dönme açısına (θ_p^a) göre yapılan değerlendirmelerde; TBDY'ye göre elde edilen performans düzeylerinin, özellikle düşük eksenel yüke ve güçlü eksende eğilmeye maruz elemanların büyük bölümünde ASCE'deki risk düzeylerinin çok altında, aşırı güvenli olduğu belirlenmiştir. Bununla birlikte, özellikle yüksek eksenel yüke ve zayıf eksende eğilmeye maruz elemanlar için yüksek riskli durumlar oluşabildiği görülmüştür. Güncel tasarım koşullarını sağlayan elemanlar için ise yüksek riskli elemanların oranı büyük ölçüde azalarak %8'e düşmüştür.

• ASCE'deki eksenel göçme kriterine (θ_p^b) göre yapılan değerlendirmelerde; TBDY'ye göre elde edilen performans düzeylerinin, TBDY-2018 tasarım koşullarına uygun elemanlar için ASCE'de öngörülen risk düzeyi sınırlarını sağladığı, hatta bu elemanların büyük bölümünün aşırı güvenli olduğu belirlenmiştir. Ancak, güncel tasarım koşullarını sağlamayan özellikle yüksek eksenel yüke ve zayıf eksende eğilmeye maruz elemanlarda ASCE'de öngörülen risk düzeyinin önemli ölçüde aşılabildiği görülmüştür.

ASCE yaklaşımının geniş kapsamlı deneysel veri tabanına dayandığı gözönünde bulundurulduğunda; TBDY'deki plastik dönme açısını esas alan yaklaşımın, aşırı güvenli sonuçlar doğurabileceği gibi, aynı zamanda riskli sonuçlara da sebep olabileceği anlaşılmaktadır. Bu nedenle, TBDY'deki performans düzeylerinin özellikle bu çalışmada öne çıkan sonuçlar doğrultusunda, mevcut deneysel veri tabanları ile doğrudan karşılaştırmalar yapılarak değerlendirilmesi gerektiği düşünülmektedir. Bununla birlikte kolon elemanlar ölçeğinde ve dönme kapasiteleri çerçevesinde yapılan bu tür değerlendirmelerin, deprem

dönme taleplerini ve genel bina performansını da içerecek şekilde bina ölçeğine genişletilmesi gerekmektedir. Ayrıca çeşitli sebeplerle aderans yetersizliği bulunan ve/veya düz yüzeyli donatılar içeren betonarme elemanlar için benzer çalışmaların yapılması, yönetmeliğin mevcut yapılarla ilgili bölümüne önemli katkılar sağlayacaktır.

Semboller

a ; L_s	:	Kesme açıklığı
a_i	:	Yatayda bir etriye kolu veya çiroz tarafından mesnetlenen boyuna donatıların eksenleri arasındaki uzaklık
A_c	:	Brüt enkesit alanı
A_s	:	Boyuna donatı alanı
A_{sh}	:	Enine donatı alanı
b	:	Enkesit genişliği
b_0	:	Göbek betonu sargılayan etriyelerin eksenleri arasında kalan kesit boyutu
b_k	:	Çekirdek boyutu (en dıştaki enine donatı eksenleri arasındaki uzaklık)
c	:	Eksenel göçme kapasitesine ulaşmış elemandaki artık eğilme kapasitesi oranı
d	:	Enkesit faydalı yüksekliği
d_b	:	Boyuna donatı çapı
f_c	:	Sargısız beton basınç dayanımı
f_{cc}	:	Sargılı beton basınç dayanımı
f_{ct}	:	Beton çekme dayanımı
f_y	:	Boyuna donatı akma dayanımı
f_u	:	Donatı kopma dayanımı
f_{yw}	:	Enine donatının akma dayanımı
h	:	Kesit yüksekliği
h_0	:	Göbek betonunu sargılayan etriyelerin eksenleri arasında kalan kesit boyutu
k_{nl}	:	Deplasman sünekliği talebine bağlı katsayı
L_p	:	Plastik mafsal boyu
M_y	:	Enkesit akma momenti
M_u	:	Moment taşıma kapasitesi
N	:	Kolondaki eksenel basınç kuvveti

s	: Sargı donatısı aralığı
V_e	: Kesme tasarım dayanımı
V_r	: Kesme kuvveti taşıma kapasitesi
V_y	: Akma momentine karşılık gelen kesme kuvveti
w_{we}	: Etkin sargı donatısının mekanik donatı oranı
α_{col}	: Donatı etkinlik katsayısı
α_{sh}	: Sargı donatısının etkinlik katsayısı
ε_c	: Beton birim kısalması
ε_{cu}	: Sargılı beton maksimum birim kısalması
$\varepsilon_c^{SH}, \varepsilon_c^{KH}, \varepsilon_c^{GÖ}$	: TBDY Performans düzeylerine karşılık gelen sargılı beton birim kısalmaları
ε_s	: Donatı birim uzaması
ε_{su}	: Maksimum dayanıma karşılık gelen donatı birim uzaması
$\varepsilon_s^{SH}, \varepsilon_s^{KH}, \varepsilon_s^{GÖ}$	: TBDY Performans düzeylerine karşılık gelen donatı birim uzamaları
θ_p	: Plastik dönme
$\theta_p^{SH}; \theta_p^{KH}; \theta_p^{KH}$	: TBDY-2018 peformans düzeylerine karşılık gelen plastik dönme açıları
$\theta_p^{IO}; \theta_p^{LS}; \theta_p^{CP}$	: ASCE/SEI 41-17 peformans düzeylerine karşılık gelen plastik dönme açıları
$\theta_p^a; \theta_p^b$	: ASCE 41-17 kolon davranışını temsil eden karakteristik plastik dönme açıları
$\theta_p^{a,\%10}; \theta_p^{a,\%40}$	: ASCE θ_p^a dönme açısının %10 ve %40'lık aşılma olasılıklarına karşılık gelen değerleri
λ	: Beton özelliğini ifade eden katsayı
ρ	: Boyuna donatı oranı
ρ_t	: ASCE 41-17'ye göre kesitin eğilme doğrultusundaki enine donatı oranı
ρ_{sh}	: TBDY-2018'e göre enine donatı oranı
σ_c	: Beton basınç gerilmesi
φ_y	: Akma eğriliği
φ_u	: *Göçmenin Önlenmesi* performans düzeyini tanımlayan eğrilik

Kaynaklar

[1] Türkiye Bina Deprem Yönetmeliği, T.C. Çevre ve Şehircilik Bakanlığı, Ankara, 2018.

[2] Structural Engineers Association of California (SEOAC), Performance Based Seismic Engineering of Buildings: Vision 2000, USA, 1995.

[3] Applied Technology Council (ATC), Seismic Evaluation and Retrofit of Concrete Buildings: ATC 40, Vol. 1, Washington DC., USA, 1996.

[4] Federal Emergency Management Agency (FEMA), NEHRP Guidelines for the Seismic Rehabilitation of Buildings: FEMA 273, Washington, D.C., USA, 1997.

[5] Comité Européen de Normalisation (CEN), European Standard EN 1998-3 Eurocode 8: Design of Structures for Earthquake Resistance–Part 3: Assessment and Retrofitting of Buildings, Bruxelles, 2005.

[6] American Society of Civil Engineers, Seismic Evaluation and Retrofit of Existing Buildings: ASCE Standard ASCE/SEI 41-17, Reston, VA, USA, 2017.

[7] American Society of Civil Engineers, Seismic Evaluation and Retrofit of Existing Buildings: ASCE Standard ASCE/SEI 41-06, Reston, VA, USA, 2006.

[8] American Society of Civil Engineers, Seismic Evaluation and Retrofit of Existing Buildings: ASCE Standard ASCE/SEI 41-13, Reston, VA, USA, 2013.

[9] Bayındırlık ve İskan Bakanlığı, Deprem Bölgelerinde Yapılacak Binalar Hakkında Yönetmelik, Ankara, 2007.

[10] Priestley, M.J.N., Calvi, G.M., Concepts and Procedures for Direct Displacement Based Design and Assessment, Seismic Design Methodologies for the Next Generation of Codes,Proceedings of International Conference at Bled, Slovenia, A.A. Balkema, Rotterdam, 1997.

[11] Priestley, M.J.N., Kowalsky, M.J. Direct Displacement-Based Seismic Design of Concrete Buildings, Bulletin of the New Zealand National Society for Earthquake Engineering, 33(4), 421-444, 2000.

[12] Acun, B, Sucuoğlu, H., Betonarme Kolonların Şekildeğiştirme Performans Sınırlarının Deneysel Gözlemlerle Değerlendirilmesi.*İMO Teknik Dergi, 22(108), 5523-5541, 2011.

[13] Kazaz İ., Gülkan P., Süneklik Düzeyi Yüksek Betonarme Perdelerdeki Hasar Sınırları. Teknik Dergi, 23(114), 6113-6140, 2012.

[14] Özdemir, M.A., Kazaz İ., Özkaya, S. G., Evaluation of Deformation Limits in Codes for Reinforced Concrete (RC) Columns, 4. Uluslararası Deprem Mühendisliği ve Sismoloji Konferansı, 11-13 Ekim, Anadolu Üniversitesi, Eskişehir, 2017.

[15] Fardis, M. N., Seismic Design, Assessment and Retrofitting of Concrete Buildings: Based on EN-Eurocode 8 (Vol. 8), Berlin, Springer, 2009.

[16] Biskinis, D.E., Resistance and Deformation Capacity of Concrete Members With or Without Retrofitting, Doctoral Thesis, Civil Engineering Department, University of Patras, Patras, 2007.

[17] Cansız, S., Aydemir, C., Arslan, G., Comparison of displacement capacity of reinforced concrete columns with seismic codes, Advances in Concrete Construction, 8(4), 295-304, 2019.

[18] Değer, Z.T, Başdoğan, Ç., Nonlinear modeling and damage limits of reinforced concrete shear walls based on lumped plasticity behavior, Gazi Üniversitesi Mühendislik Mimarlık Fakültesi Dergisi, 36(2), 641-653, 2021.

[19] Li, Y., Elwood, K.J., Hwang, S., Assessment of ASCE/SEI 41 Concrete Column Provisions using Shaking Table Tests. ACI Special Publication, 297, 1-22, 2014.

[20] Ghannoum, W.M., Matamoros, A.B., Nonlinear Modeling Parameters and Acceptance Criteria for Concrete Columns. ACI Special Publication, 1, 1-24, 2014.

[21] Ghannoum, W.M., Updates to Modeling Parameters and Acceptance Criteria for Non-Ductile and Splice-Deficient Concrete Columns, 16th World Conference on Earthquake Engineering, Santiago, Chile, No:1010, 2017.

[22] Applied Technology Council, Recommended Modeling Parameters and Acceptance Criteria for Nonlinear Analysis in Support of Seismic Evaluation, Retrofit, and Design: NIST GCR 17-917-45, Applied Technology Council, Redwood City, CA, USA, 2017.

[23] Eyitayo, O., Elwood K.J., Comparative Study on Acceptance Criteria for Non-Ductile Reinforced Concrete Columns. Bulletin of the New Zealand Society for Earthquake Engineering, 51 (4), 2018.

[24] Ghannoum, W.M. and B. Sivaramakrishnan, ACI 369 Rectangular Column Database, Network for Earthquake Engineering Simulation (database).

[25] Haselton, C. B., Liel, A. B., Lange, S. T., Deierlein, G. G., Beam-Column Element Model Calibrated for Predicting Flexural Response Leading to Global Collapse of RC Frame Buildings. Berkeley, California: Pacific Earthquake Engineering Research Center, USA, 2008.

[26] Ghannoum, W.M., B. Sivaramakrishnan, ACI 369 Circular Column Database, Network for Earthquake Engineering Simulation (database), 2012.

[27] Türk Standartları Enstitüsü, Betonarme Yapıların Tasarım ve Yapım Kuralları :TS 500, Bakanlıklar, Ankara, 2000.

Turkish Journal of Civil Engineering (formerly Teknik Dergi) Manuscript Drafting Rules

1. The whole manuscript (text, charts, equations, drawings etc.) should be arranged in Word and submitted in ready to print format. The article should be typed on A4 (210 x 297 mm) size paper using 10 pt (main title 15 pt) Times New Roman font, single spacing. Margins should be 40 mm on the left and right sides and 52.5 mm at the top and bottom of the page.

2. Including drawings and tables, articles should not exceed 25 pages, technical notes 10 pages.

3. Your contributed manuscript must be sent over the DergiPark system. (http://dergipark.gov.tr/tekderg)

4. The text must be written in a clear and understandable language, conform to the grammar rules. Third singular person and passive tense must be used, and no inverted sentences should be contained.

5. Title must be short (10 words maximum) and clear, and reflect the content of the paper.

6. Sections should be arranged as: (i) abstract and keywords, (ii) title, abstract and keywords in the other language, (iii) main text, (iv) symbols, (v) acknowledgements (if required) and (vi) references.

7. Both abstracts should briefly describe the object, scope, method and conclusions of the work and should not exceed 100 words. If necessary, abstracts may be re-written without consulting the author. At least three keywords must be given. Titles, abstracts and keywords must be fitted in the first page leaving ten line space at the bottom of the first page and the main text must start in the second page.

8. Section and sub-section titles must be numbered complying with the standard TS1212.

9. Symbols must conform to the international rules; each symbol must be defined where it appears first, additionally, a list of symbols must be given in alphabetic order (first Latin, then Greek alphabets) at the end of the text (before References).

10. Equations must be numbered and these numbers must be shown in brackets at the end of the line.

11. Tables, drawings and photographs must be placed inside the text, each one should have a number and title and titles should be written above the tables and below the drawings and photographs.

12. Only SI units must be used in the manuscripts.

13. Quotes must be given in inverted commas and the source must be indicated with a reference number.

14. Acknowledgement must be short and mention the people/ institutions contributed or assisted the study.

15. References must be numbered (in brackets) in the text referring to the reference list arranged in the order of appearance in the text. References must include the following information:

    If the reference is an article: Author's surname, his/her initials, other authors, full title of the article, name of the journal, volume, issue, starting and ending pages, year of publication.

       Example : Naghdi, P. M., Kalnins, A., On Vibrations of Elastic Spherical Shells. J. Appl. Mech., 29, 65-72, 1962.

    If the reference is a book: Author's surname, his/her initials, other authors, title of the book, volume number, editor if available, place of publication, year of publication.

       Example : Kraus. H., Thin Elastic Shells, New York. Wiley, 1967.

    If the reference is a conference paper: Author's surname, his/her initials, other authors, title of the paper, title of the conference, location and year.

    If the source is a thesis: Author's surname, his/her initials, thesis title, level, university, year.

    If the source is a report: Author's surname, his/her initials, other authors, title of the report, type, number, institution it is submitted to, publication place, year.

16. Discussions to an article published in Turkish Journal of Civil Engineering (formerly Teknik Dergi) should not exceed two pages, must briefly express the addressed points, must criticize the content, not the author and must be written in a polite language. Authors' closing remarks must also follow the above rules.

17. A separate note should accompany the manuscript. The note should include, (i) authors' names, business and home addresses and phone numbers, (ii) brief resumes of the authors and (iii) a statement "I declare in honesty that this article is the product of a genuinely original study and that a similar version of the article has not been previously published anywhere else" signed by all authors.

18. Copyright has to be transferred to UCTEA Turkish Chamber of Civil Engineers. The standard copyright form signed by the authorised author should therefore be submitted together with the manuscript.